The Pennsylvania State University

The Graduate School

Department of Mechanical and Nuclear Engineering

VIBRATION-BASED STRUCTURAL DAMAGE IDENTIFICATION ENHANCEMENT VIA PIEZOELECTRIC CIRCUITRY NETWORK AND ACTIVE FEEDBACK CONTROL

A Thesis in

Mechanical Engineering

by

Lijun Jiang

Submitted in Partial Fulfillment
of the Requirements
for the Degree of

Doctor of Philosophy

December 2007

The thesis of Lijun Jiang was reviewed and approved* by the following:

Kon-Well Wang
William E. Diefenderfer Chaired Professor in Mechanical Engineering
Thesis Advisor
Chair of Committee

Christopher D. Rahn
Professor of Mechanical Engineering

Edward C. Smith
Professor of Aerospace Engineering

Heath F. Hofmann
Associate Professor of Electrical Engineering

Karen A. Thole
Professor of Mechanical Engineering
Head of the Department of Mechanical and Nuclear Engineering

*Signatures are on file in the Graduate School

ABSTRACT

Vibration-based structural damage identification has been quite popular in recent years. Among all the vibration-based damage identification methods, the frequency-shift-based method is more preferred due to its simplicity and reliability. However, the current practice of frequency-shift-based damage identification encounters two severe limitations, namely, deficiency of frequency measurement data and low sensitivity of frequency shift to damage effects. Therefore, this thesis aims to advance the state-of-the-art of the frequency-shift-based damage identification by addressing the aforementioned two limitations of this method.

First, a novel approach utilizing tunable piezoelectric circuitry is proposed to address the issue of deficiency of frequency measurement data. The key idea of this approach is to use the tunable piezoelectric circuitries coupled to the mechanical structure to favorably alter the dynamics of the electro-mechanical integrated system. On one hand, the integration of piezoelectric circuitries can introduce *additional* resonant frequencies and vibration modes into the frequency response function. On the other hand, tuning the circuitry elements (i.e., the inductors) may alter the dynamic characteristics of the electro-mechanical integrated system, and hence results in a *family* of frequency response function measurements. Thus, by integrating tunable piezoelectric circuitries to the structure and appropriately tuning the circuitry elements, one can obtain a much enlarged dataset of natural frequency measurements for damage identification. Guidelines on favorable inductance tuning that can yield the optimal damage identification performance are also developed. Analyses show that when the inductances

are tuned to accomplish eigenvalue curve veerings between system eigenvalue pairs, the enriched frequency measurement data can most effectively capture the damage information, and hence results in the most accurate damage identification. An iterative second-order perturbation based algorithm is developed to identify the damage features (i.e., location and severity) from the measured frequency changes before and after damage occurrence. Numerical analyses and case studies on benchmark beam and plate structures are carried out to demonstrate and verify the proposed new method. Numerical results show that the damage identification performance can be significantly improved by using the proposed new approach with favorable inductance tuning.

To address the second issue, low sensitivity of frequency shifts to damage effects, another new approach based on the concept of sensitivity-enhancing feedback control is proposed. The key idea of this approach is to use active feedback control to appropriately assign the closed-loop eigenstructure (both eigenvalues and eigenvectors) to enhance the frequency sensitivity to mass/stiffness damage. To achieve the best performance of frequency sensitivity enhancement, a constrained optimization problem is formulated to find the optimal eigenstructure assignment for the closed-loop system, which leads to the optimal sensitivity-enhancing control. In addition, multiple closed-loop systems can be obtained from different sensitivity-enhancing controls, and these closed-loop systems provide a much enlarged dataset of natural frequency measurements for damage identification. Therefore, by designing a series of sensitivity-enhancing controls and utilizing the natural frequencies of the resulting closed-loop systems for damage identification, both of the two major limitations of the frequency-shift-based damage identification are overcome. Numerical analyses and case studies on a benchmark beam

structure are carried out to demonstrate and verify the proposed new method. Results show that the frequency sensitivity to stiffness reduction in the beam can be significantly enhanced by applying sensitivity-enhancing control to the beam structure. It is also demonstrated that the proposed method is effective in damage identification and is robust against uncertainties in frequency measurements.

To fulfill the requirement of an accurate finite element model for the sensitivity-enhancing control approach of damage identification, a frequency-based iterative model updating method is developed using the same concept of sensitivity-enhancing control. With this, the sensitivity-enhancing control approach can be used for dual functions of modeling updating and damage identification. The effectiveness of this model updating method is verified through numerical analyses on an example beam structure.

A laboratory experiment is designed and conducted to verify the sensitivity-enhancing control approach for frequency-shift-based damage detection. In the experiment, a system identification technique is utilized to identify a mathematical model for controller design and system analysis, and hence frees the requirement of having an analytical model as in the original approach. The eigenstructure assignment-based constrained optimization scheme is used to design sensitivity-enhancing controls to enhance the frequency sensitivity to mass variations in the beam structure. Experimental results show that the frequency sensitivity to mass variations can be significantly enhanced by applying the designed controller to the beam structure.

Finally, future research work towards the improvement and implementation of the proposed damage identification approaches is recommended.

TABLE OF CONTENTS

LIST OF FIGURES

LIST OF TABLES

ACKNOWLEDGEMENTS

I would like to express my deepest appreciation to my thesis advisor, Professor Kon-Well Wang, for his invaluable guidance, professional advising, and constant encouragement and support throughout the course of this research. My sincere appreciation also goes to Dr. Christopher Rahn, Dr. Edward Smith, and Dr. Heath Hofmann for their serving on my doctoral committee and for their valuable comments and suggestions.

I would also like to extend my appreciation to our project collaborator, Professor Jiong Tang at the University of Connecticut, for his helpful discussions and suggestions.

I want to thank all SDCL fellow members who have always rendered help to me. Especially, I would like to thank former SDCL members, Dr. Michael Philen, Dr. Jun-Sik Kim, and Dr. Hongbiao Yu for sharing their knowledge and experience on the experimentation. In addition, I am thankful to the former and current SDCL lab managers, and all the department staffs, especially Karen Thal and Jenny Houser, for their generous help.

My sincere gratitude goes to my parents, my sister and all other family members. Without their continuous support and encouragement, this work would not have been finished. I also want to extend my appreciation to all of my friends, especially those at Penn State, who have made my stay here a memorable and valuable experience.

Finally, I want to acknowledge the National Science Foundation for providing financial support for this research.

Chapter 1

Introduction

In recent years, structural health monitoring and damage identification have received more and more attention throughout the civil, mechanical and aerospace engineering communities. On one hand, damage developed in the structure will adversely affect the current and/or future performance of the structural system, and may also reduce the expected service life of the system. On the other hand, if the damage characteristics (e.g., damage type, damage location, and damage severity) are known, we can immediately change the operating procedure and environment to maintain the structural integrity, and future maintenance plans can be scheduled to elongate the service life of the structure. Therefore, in order to guarantee the well-designed performance and the expected service life of the structural system, it is essential to monitor the state of the structure's health, and in case of damage occurrence, identify the characteristics of the damage. In recent years, extensive research work has been performed in the field of structural health monitoring and damage identification, Sohn et al. [1] presents a comprehensive literature review on the techniques developed in the field between 1996 and 2001. For more recent technical development in this discipline, one may refer to the proceedings of the International Workshop on Structural Health Monitoring at Stanford University [2-4], the Workshop on Structural Health Monitoring in Europe [5-7], the Asia-Pacific Workshop on Structural Health Monitoring [8], and the SPIE International Symposium on Non-Destructive Evaluation (NDE) for Health Monitoring and

Diagnostics [9-14], as well as journals such as the Journal of Structural Health Monitoring and the Journal of Nondestructive Evaluation.

1.1 Structural Damage, Damage Identification, and Health Monitoring

The definition of damage can be system dependent. In general, damage can be defined as changes introduced into a system that adversely affects its current and/or future performance. As implicitly indicated in this definition, a *reference* state, which represents the undamaged (healthy) state of the system, is required to characterize the occurrence of damage. When the systems that we are concerned about are limited to the structural and mechanical systems, damage can be specifically defined as changes to the material and/or geometrical properties of these systems, including changes to the joint connections and boundary conditions. Depending on the type of damage and the scenario of loading applied to the system, damage can occur and progress in different ways. In terms of *length* scale, all damage begins at the material level, and then progresses to component and system level damage at various rates depending on the loading scenarios. In terms of *time* scale, some damage (e.g. fatigue, creep and corrosion) can accumulate gradually over a long period of time, while other damage may occur suddenly in either scheduled events or unexpected events, such as aircraft landings, earthquakes, and random impact on turbine blades.

In general, damage will alter the stiffness, mass, or energy dissipation properties of a structural system, which in turn alter the dynamic response of the system. A damage identification approach can be developed to detect the presence of damage and if

possible, characterize the damage features (e.g., damage type, damage location and damage severity) by using the measured dynamic responses of the system before and after damage occurrence. During the normal operational period of the structural system, the damage identification process is periodically performed to capture the degradation of the structure's health due to the inevitable aging and degradation resulting from operational environments. When extreme events (e.g., earthquake, random impact and blast loading) happen, the damage identification process can be used to perform a real-time evaluation of the integrity of the structure.

The process of implementing a structural damage identification approach in an engineering structure involves the following steps [1]: (1) operational evaluation, (2) data acquisition and signal processing, (3) feature extraction and damage identification.

Operational evaluation aims to provide preliminary information for the implementation of structural damage identification. The main issues involved in operational evaluation include:

- The economic and/or life safety motives for performing health monitoring and damage identification. For example, the prohibitive cost of removing pipe insulation with visual inspection stimulated the research of using Lamb waves to detect pipeline corrosion for the oil, chemical and petrochemical industries [15], the intention to enhance the safety, reliability and durability of civil infrastructures such as bridges and highways motivated the development of structural health monitoring system for those infrastructures [16-18], and both the direct cost of carrying out preventive inspections and indirect cost

associated with the interrupted service stimulated the development of structural health monitoring systems for aircraft [19,20].

- The type and features of the damage that is to be identified. For example, the health monitoring of pipelines for the oil, chemical and petrochemical industries is concerned with corrosion under insulation [15], the health monitoring of reinforced laminated composites is mainly concerned with layer delamination that could substantially reduce the stiffness and the bulking load capacity [21,22], and multiple crack damages that causes reduction of bending stiffness are the common target when monitoring the health of beam structures [23-26].
- The operational and environmental conditions under which the system being monitored is working. For example, the measurement noise and environmental effects such as temperature variation may severely deteriorate the damage identification results when resonant frequencies are used as the information carrier [27], the detection of delamination in composite plate may be obscured by the performance variation of the piezoelectric sensors under temperature change and ambient vibration [28].
- The limitations on acquiring data in the operational environment. For example, Garibaldi et al. [29] demonstrated that the lack of sufficient instrument and limitations of measurement points of a bridge testing could deteriorate the reliability and credibility of damage identification results for the bridge.

Data acquisition for structural health monitoring process involves selecting an excitation mechanism for vibration testing, selecting the physical quantities to be measured as information carrier, choosing an appropriate type of the sensor and configuring the placement of sensory system on the structure being monitored, and the data acquisition/storage/processing hardware. The most commonly used excitation methods include ambient excitation and forced excitation. In terms of forced excitation for structural testing, a variety of forcing techniques, such as actuator, shaker and impact, has been utilized for different applications. Those physical quantities, which are most relevant and sensitive to the structural properties that are being monitored to reflect the effect of damage, should be selected as the measurement quantities for the structural health monitoring process. For example, the most commonly measured quantities in vibration-based damage identification include acceleration, strain and displacement. In some cases, measurements of other quantities such as temperature, humidity, and wind are also required to quantify the environmental conditions of the structural system. Based on the physical quantities selected for measurements and the geometrical configuration of the structural system, the type of sensor and the configuration of sensor placement can be subsequently determined.

Feature extraction and damage identification is the part of structural health monitoring that receives the most attention in the technical literature. The process of feature extraction aims at identifying damage-sensitive properties from the measured structural response, based on which one may distinguish the damaged state of a structure from the healthy (undamaged) state. The best features for damage detection are typically application specific. The most commonly used features for structural health monitoring

in the technical literature include vibration signature such as resonant frequencies, mode shapes, mode shape curvature, dynamic flexibility and damping properties [30,31], electro-mechanical impedance [32], wave propagation properties [33,34] and nonlinear dynamic features such as chaotic response and local attractors [35-38]. Structural health monitoring and damage identification based on vibration signature will be reviewed in detail in the next subsection. The process of damage identification aims at determining the damage state of the structure based on the extracted features from the measurements. Different damage identification approaches have different levels of capability in characterizing the damage features. According to the damage information that can be obtained through the process of damage identification, the methods can be roughly classified into four levels [39],

Level 1: Determination of the presence of damage in the structure;

Level 2: Level 1 plus determination of the damage location;

Level 3: Level 2 plus quantification of the damage severity;

Level 4: Level 3 plus prediction of the remaining service life of the structural system.

Most of the current damage identification methods developed in the literature belong to the first three levels, while very few methods cover the fourth level since the prediction of remaining service life is more related to the field of fracture mechanics and fatigue-life analysis, and it requires information about the loading scenario applied to the structural system in the future.

1.2 Literature Review on Vibration-Based Structural Damage Identification

Structural damage identification using vibration test data has been quite popular in recent years and numerous schemes based on different vibration signature have been developed in the literature [1,30,31]. The overwhelming interest in vibration-based damage identification is due to its unique advantages as compared with those traditional nondestructive evaluation techniques. The traditional nondestructive evaluation techniques such as ultrasonic methods, magnetic field methods, radiography, eddy-current methods and thermal field methods [40], require that the damage location is known *a priori* and the vicinity of damage site is accessible for local measurement. Thus, these traditional techniques can only be utilized to detect damage on or near the surface of the structure. On the other hand, the vibration-based methods utilize measurements of global structural response, and thus oftentimes do not require the direct accessibility to the damaged spot, which could be advantageous in many applications. The basic idea of vibration-based damage identification is that damage in the structure will change the structural properties (mass, stiffness and damping) and these changes will result in changes in the dynamic characteristics of the global structural response, such as natural frequencies, mode shapes, and damping ratios.

There are several ways to classify the vibration-based damage identification approaches. One of them is based on different types of vibration signatures used for damage identification, such as natural frequencies, mode shapes, mode shape curvature, frequency response functions, and dynamically measured flexibility. Another way to characterize vibration-based approaches is whether the approach is model-based or non-

model-based. Non-model-based approaches simply compare the measured response of the potentially damaged structure with that of the healthy structure, and thus they only provide Level 1 damage identification and, in some cases, Level 1 and Level 2 damage identification. On the other hand, model-based methods require not only the measured responses of the healthy and damaged structures, but also require an accurate model (usually finite element model) of the undamaged structure. In general, model-based methods utilize a model updating process to solve for the damage-induced perturbations in structural model matrices to reproduce as closely as possible the measured response of the damaged structural system. The most commonly used model updating methods include optimal matrix update method, sensitivity-based update method, and eigenstructure assignment method.

1.2.1 Damage Identification Based on Changes in Vibration Signature

Extensive research work has been performed to develop systematic schemes toward identifying structural damage based on changes in vibration signature [1,30,31]. The most commonly used vibration signature for structural damage identification includes natural frequencies, mode shapes, mode shape curvature/strain mode shape, frequency response functions, and dynamically measured flexibility.

1.2.1.1 Natural Frequencies

Natural frequency was the first modal property exploited in the field of damage identification, and extensive research work has been performed over the past several decades. Salawu [41] presents an excellent review on utilizing changes in measured natural frequencies for structural damage identification. Some representative research work performed at the early stage is briefly reviewed in the following.

Cawley and Adams [42] presented a method based on measured frequency shifts to detect damage in composite materials. For each potential damage location, the frequency shift ratios ($\delta\omega_i / \delta\omega_j$) between a number of mode pairs are calculated from the analytic model by assuming a local stiffness reduction at that location. To identify the damage location, an error term is used to correlate the measured frequency shits to those predicted from the analytic model. By comparing the resulting errors for all potential damage locations, the actual location of damage is indicated by the lowest error. However, this method is only applicable for detection of a single damage location.

Stubbs and Osegueda [43,44] developed a sensitivity-based method for damage identification using measured frequency changes. A sensitivity-based equation is used to describe the relation between the normalized changes of squared frequencies $\{\delta\lambda\}$, the fractional elemental stiffness reduction $\{\delta\alpha\}$ and the fractional elemental mass reduction $\{\delta\beta\}$,

$$\{\delta\lambda\} = [S_k]\{\delta\alpha\} - [S_m]\{\delta\beta\} \qquad (1.1)$$

where $[S_k]$ and $[S_m]$ are the sensitivity matrices of eigenvalue change with respect to variation in elemental stiffness and mass parameters, respectively. If the damage is only related to stiffness reduction in some structural elements while the mass properties are not affected, the damage-induced stiffness reduction can be identified by solving the general inverse problem,

$$\{\delta\alpha\} = [S_k]^{+} \{\delta\lambda\} \tag{1.2}$$

The authors demonstrated that this sensitivity-based equation may be significantly underdetermined when the number of measured frequencies is much smaller than that of the damage parameters. The pseudo-inverse solution becomes ill-conditioned if the system is significantly underdetermined.

An alternative sensitivity-based approach is proposed by Richardson and Mannan [45]. This method requires frequency and mode shape measurements before damage and frequency measurements after damage. Following the same assumption that damage is limited to changes in stiffness, a sensitivity equation can be obtained for each mode by subtracting two orthogonality equations for the healthy and damaged structures,

$$\begin{aligned} \{\varphi_i + \delta\varphi_i\}^T [\Delta K] \{\varphi_i + \delta\varphi_i\} + 2\{\delta\varphi_i\}^T [\Delta K] \{\varphi_i\} \\ + \{\delta\varphi_i\}^T [\Delta K] \{\delta\varphi_i\} = \left(\omega_i^d\right)^2 - \left(\omega_i^h\right)^2 \end{aligned} \tag{1.3}$$

Neglecting the changes in mode shapes, the sensitivity equation reduces to

$$\{\varphi_i\}^T [\Delta K] \{\varphi_i\} = \left(\omega_i^d\right)^2 - \left(\omega_i^h\right)^2 \tag{1.4}$$

This method has the same difficulty as pointed out by Stubbs and Osegueda [43]. It typically leads to a set of underdetermined equations due to an insufficient number of

frequency measurements, and a pseudo-inverse search routine is required for evaluating the changes in stiffness.

Hearn and Testa [46] utilize the ratio of changes in squared natural frequency for various modes to identify damage. Assuming that the damage results in only stiffness change and neglecting high-order terms, the relation between the ith natural frequency change and stiffness change can be described as

$$\Delta\omega_i^2 = \frac{\{\varphi_i\}^T [\Delta K]\{\varphi_i\}}{\{\varphi_i\}^T [M]\{\varphi_i\}} \tag{1.5}$$

For the case of single element damage in the nth structural element, the effects of damage on the natural frequency shifts of various modes can be reduced to a function of the damage location only as

$$\frac{\Delta\omega_i^2}{\Delta\omega_j^2} = \left(\frac{\{\varphi_i\}^T \left[\tilde{K}_n^e\right]\{\varphi_i\}}{\{\varphi_i\}^T [M]\{\varphi_i\}} \right) \Bigg/ \left(\frac{\{\varphi_j\}^T \left[\tilde{K}_n^e\right]\{\varphi_j\}}{\{\varphi_j\}^T [M]\{\varphi_j\}} \right) \tag{1.6}$$

where $\left[\tilde{K}_n^e\right]$ is the elemental stiffness matrix positioned in the global stiffness matrix $[K]$. Based on this equation, a two-step procedure can be performed to correlate the ratios of the measured frequency changes with the damage location.

Williams and Messina [47] introduced a new approach called Multiple Damage Location Assurance Criterion (MDLAC), which utilizes a correlation coefficient to identify the damage vector representing damage-induced stiffness reduction. The correlation coefficient is formulated to match the patterns of two sets of frequency changes, $\{\delta f\}$ and $\{\Delta f\}$,

$$MDLAC(\delta D) = \frac{\left|\{\delta f\}^T \{\Delta f\}\right|^2}{\left(\{\delta f\}^T \{\delta f\}\right)\left(\{\Delta f\}^T \{\Delta f\}\right)} \quad (1.7)$$

where $\{\delta f\}$ is the frequency changes predicted from a frequency-sensitivity model derived from a finite element model, and $\{\Delta f\}$ is the actual frequency changes from experimental measurements. This MDLAC is similar to the Modal Assurance Criterion (MAC) used for comparing mode shapes, and it takes the value of 1.0 for an exact pattern match and 0.0 for patterns that are uncorrelated. From the experimental verification of MDLAC method, the authors found that 10 to 15 resonance frequencies are needed to provide sufficient information about damage and in practice, errors in frequency measurements can affect the ability of the MDLAC approach to give a correct prediction.

1.2.1.2 Mode Shapes

The potential of using mode shape information to detect structural damage has been investigated by many researchers. A classical approach of using mode shape information to localize the structural damage was presented by West [48]. In this approach, modal assurance criterion (MAC) is used to evaluate the level of correlation between the mode shapes of the healthy structure and the potentially damaged structure. Damage location can be identified by partitioning the mode shapes and observing changes in MAC over each partition.

Later, this classical approach has been extended by several researchers. Kim et al. [49] introduced the use of Partial MAC (PMAC) to compare the MAC values of

coordinate subsets of the modal vectors. The Partial MAC (PMAC) is used in conjunction with the Coordinate MAC (COMAC) to isolate the damaged area of the structure. Salawu and Williams [50] pointed out that the most important factor for damage detection using mode shape changes is the selection of the modes used in the analysis, and they show that the MAC values can be used to indicate which modes are being affected most by the damage. Ko et al. [51] presented a method that uses a combination of MAC, COMAC and sensitivity analysis to detect damage in steel framed structures. Sensitivity analysis is performed to determine the degrees of freedom (DOF) that are most relevant under particular damage condition, and the most relevant mode pairs are selected by analyzing the MAC between the measured modes of the undamaged and damaged structure. The authors demonstrate that the most effective indicator of damage is the COMAC computed on the selected modes and degrees of freedom (DOF) that are most relevant to the damage condition.

1.2.1.3 Mode Shape Curvature/Strain Mode Shape

An alternative way of using mode shape information for structural damage identification is to use mode shape curvature or strain mode shape. Pandey et al. [52] demonstrated that the absolute changes in mode shape curvature can be used as an effective indicator of damage for beam structures. The central difference operator is used to compute the mode shape curvature based on the displacement mode shape.

Stubbs et al. [53] presented a method based on the decrease in modal strain energy between two structural DOF, as defined by the curvature of the measured mode

shapes. For a linear elastic beam structure, the damage index for one structural element is defined as the ratio of fractional strain energy stored in that element after and before damage occurs, and large value of damage index indicates possible damage in that element. Based on the fractional strain energy term, a parameter representing the fractional change in bending stiffness can also be defined to quantify the damage severity.

Chance et al. [54] found that numerical calculation of curvature from mode shapes resulted in unacceptable errors. The authors show that the results can be dramatically improved by using the measured strains instead of using numerically calculated curvature for mode shapes. Later, Ho and Ewins [55] proposed another effective way of computing mode shape derivative when the authors use the mode shape slope squared as a feature to identify damage. To compute the derivative of the mode shape, a local polynomial is fit through every four consecutive measurement points and the obtained polynomial is then differentiated. It has been shown that this way of computing mode shape derivatives is subject to smaller variations than those typical methods using finite difference approximation.

1.2.1.4 Frequency Response Functions

Instead of using basic modal properties extracted from the frequency response function (FRF) data for damage detection, the measured FRF data itself can be directly used for damage detection. A typical FRF-based damage detection method involves minimizing the difference between the analytical and measured FRFs. Wang et al. [56]

formulated a damage detection algorithm utilizing FRF data measured prior and posterior to damage occurrence as well as an original analytical model for structural damage detection. The algorithm is derived based on so-called nonlinear perturbation equations of receptance FRF data. The developed algorithm leads to a solution of the damage vector indicating both the location and severity of the damage. The case of incomplete measurement on FRF data in terms of coordinates is also addressed by incorporating an iterative scheme with the proposed algorithm.

Trendafilova [57] also used the receptance FRF as damage-sensitive feature for structural damage detection. First, a feature vector is formed by calculating the differences between the FRFs of the healthy and the damaged structures at different frequency values. Next, the dimension of this feature vector can be reduced by removing these degrees of freedom (DOFs) and frequency areas where the sensitivity of FRF to damage is below a certain threshold value. Finally, the discriminant functions can be constructed to localize and quantify the damage.

Agneni, Crema and Mastroddi [58] utilized the measured frequency response functions (FRFs) for both model updating and damage detection. The measured FRFs are used to estimate the mass and stiffness matrices. The authors also investigated the effects of truncation on FRF data and the time signal on the performance of the proposed damage detection method.

Park and Park [59] proposed a method to identify damage locations using a reduced dynamic system, which is an inverse of the measured frequency responses. The presented method only needs incompletely measured frequency responses, and more importantly, it does not need an accurate analytical mode. Although an accurate

analytical model is not required, this method is very sensitive to the frequency data used. To overcome this limitation, the authors tested a weighting function idea for frequency selection.

1.2.1.5 Dynamically Measured Flexibility

Another class of damage identification methods uses the dynamically measured flexibility matrix to estimate changes in the static behavior of the structure. The flexibility matrix, which is defined as the inverse of the static stiffness matrix, relates the applied static force and resulting structural displacement. Each column of the flexibility matrix represents the displacement pattern of the structure subjected to a unit force applied at the corresponding degree of freedom. An approximation of the measured flexibility matrix can be calculated from the mass-normalized measured mode shapes and frequencies.

A typical approach of using flexibility matrix for damage identification is to compare the flexibility matrix synthesized using the modes of the damaged structure to the flexibility matrix synthesized using the modes of the undamaged structure or the flexibility matrix from a FEM [60-63].

Alternative methods have also been developed by many researchers, such as the unity check method based on the pseudo-inverse relationship between the dynamically measured flexibility matrix and the structural stiffness matrix [64-66], the stiffness error matrix method based on an error matrix defined as a function of the flexibility change in the structure and the undamaged stiffness matrix [67-68], and methods based on changes

in the dynamically measured stiffness matrix (the pseudo-inverse of the dynamically measured flexibility matrix) and dynamically measured mass matrix [69-70].

1.2.2 Damage Identification Using Model Update Methods

A significant part of research work in vibration-based damage identification is contributed to model updating methods, which normally use a finite element model. The basic idea of model updating methods is to solve for the perturbations of structural model matrices such as mass, stiffness and damping to reproduce as closely as possible the measured response of the damaged system. The perturbations of structural model matrices, as an indicator of damage, can be used to quantify the location and extent of the damage.

The model updating methods are fundamentally optimization methods, since they normally use a constrained optimization scheme to solve for the updated model matrices or perturbations of the nominal model matrices. The difference between various model update algorithms are from the objective function, the constraints, and the numerical scheme used to implement the optimization. One common feature that can be used as both objective function and constraint for various methods is the *modal force error* or *residual force*, $\{E_i\}$, which can be defined as

$$\left(\left(\lambda_i^d\right)^2\left[M^h\right]+\left(\lambda_i^d\right)\left[C^h\right]+\left[K^h\right]\right)\left\{\varphi^d\right\}_i=\{E\}_i \qquad (1.8)$$

where λ_i^d and $\{\varphi^d\}_i$ are the *i*th eigenvalue and eigenvector of the damaged structure, respectively. A physical meaning of this *modal force error* vector is that it represents the required harmonic force excitation applied to the healthy structure ($[M^h]$, $[C^h]$, and $[K^h]$) at the frequency of λ_i^d so that the structure would respond with mode shape [71]. The damage-induced matrix perturbations, $[\Delta M]$, $[\Delta C]$ and $[\Delta K]$, can be obtained through solving the following equation

$$\left(\left(\lambda_i^d\right)^2[\Delta M]+\left(\lambda_i^d\right)[\Delta C]+[\Delta K]\right)\{\varphi^d\}_i=\{E\}_i \qquad (1.9)$$

Typical constraints for the optimization problem include preservation of the property matrix symmetry, preservation of the property matrix sparsity, and preservation of the matrix positivity.

Various model update/damage detection methods have been developed, and they can be classified into three distinct groups: optimal matrix update method, sensitivity based method, and eigenstructure assignment method.

1.2.2.1 Optimal Matrix Update Method

The goal of optimal matrix update approach is to find a minimal perturbation to each of the original system matrix, or an updated matrix closest to the original one so that the updated matrices reproduce the measured modal properties. The optimal matrix update methods use a closed-form direct solution to solve for the system matrices of the damaged structure or the matrix perturbations due to the damage. One may refer to

Zimmerman and Smith [72], Hemez [73], and Kaouk [74] for reviews of this class of methods. The problem of optimal matrix update is generally formulated as a Lagrange multiplier or penalty-based optimization, which can be written as

$$\underset{\Delta M,\Delta C,\Delta K}{Minimize}\left\{J\left(\Delta M,\Delta C,\Delta K\right)+\lambda R\left(\Delta M,\Delta C,\Delta K\right)\right\} \tag{1.10}$$

where J is the objective function, R is the constraint function, and λ is the Lagrange multiplier or penalty constant.

The most common formulation of optimal matrix update problem, presented by Kabe [75] and Berman and Nagy [76], is to minimize the Frobenius norm of parameter matrix perturbations under the constraints of zero modal force error and preservation of property matrix symmetry. Later, Smith and Beattie [77] extend this common formulation by including a sparsity preservation constraint, and reformulating the problem as minimizing both the perturbation matrix norm and the modal force error norm subject to the symmetry and sparsity constraints. An alternative approach is presented by Kammer [78], where the optimization problem is formulated as minimization of modal force error with a constraint on property matrix symmetry. The symmetry constraint is used to preserve the reciprocity condition in the updated structural model.

Another type of approach to the optimal matrix update problem is formulated as to minimize the rank of the perturbation matrix instead of the norm of the perturbation matrix. The basic idea of this approach is that the perturbation matrices are in small rank since the damage is generally concentrated in a few structural members. The solution of the perturbation matrices is based on the theory that there exists a unique minimum rank matrix solution for an underdetermined system if a symmetry constraint is applied.

This approach, called the minimum rank perturbation theory (MRPT), has been extensively studied. First, Zimmerman and Kaouk [79] present the basic MRPT algorithm, where a nonzero entry in the damage vector is used as indicator of damage location. Later this algorithm is further developed to simultaneously estimate the perturbations of two property matrices by using complex conjugates of the modal force error equation [80]. Kaouk and Zimmerman [81] further extend the MRPT algorithm to simultaneously estimate the mass, stiffness, and proportional damping perturbation matrices. Kaouk and Zimmerman [82] introduce a partitioning scheme into the MRPT algorithm to reduce the rank of the unknown perturbation matrices, and thus reduce the number of modes required to successfully locate the damage. Zimmerman et al. [83] extend the theory to determine matrix perturbations directly from measured FRFs. The benefits of this enhanced theory include releasing the need to match modes between FEM and test, reducing the number of frequency measurements in the test, and releasing the need to perform modal parameter identification. Zimmerman et al. [84] addressed some practical issues for implementing the MRPT techniques to detect damage, such as determining the number of measured modes, filtering of the eignvectors and the damage vector, and decomposition of the damage vector into contributions from individual property matrices.

1.2.2.2 Sensitivity Based Model Update Method

Sensitivity based model update methods are based on the solution of a first-order Taylor series that minimizes an error function of the matrix perturbations. Reviews of

the various sensitivity-based model update techniques are given by Mottershead and Friswell [85], Firswell and Mottershead [86] and Link [87].

One class of sensitivity based model update methods involves the eigen-sensitivity, i.e., the derivative of eigenvalues and mode shapes with respect to physical design parameters. The eigen-sensitivity can be calculated from either the experimental data [88] or the analytical modal data [89,90]. Ricles [91] presented a model update method based on a hybrid analytical/experimental sensitivity matrix, where the modal parameter sensitivities are computed from the experimental data, and the matrix sensitivities are computed from the analytical model. Hemez [92] presented another update procedure based on sensitivity formulation at the element level, which significantly reduces the computational cost compared to formulation at the global matrix level. Jung [93] developed an eigen-sensitivity based method for finite element (FE) model updating method, and the FE model are updated iteratively using pseudo-inverse of the sensitivity matrix, which is calculated using analytical modal data. Later, Lin et al. [94] improved this eigen-sensitivity based model update method by addressing the issue of non-unique inverse solution of the sensitivity matrix, due to its underdetermined or ill-conditioned nature.

Another class of sensitivity based model update methods utilizes the sensitivity of frequency response function (FRF) with respect to physical parameters. Lin and Ewins [95,96] developed an effective model update method, where a sensitivity-based equation is formulated by utilizing the correlation between analytical and measured frequency response function data. Considering the practical difficulty of measuring FRF data at all the coordinates specified in the analytical model, the method is extended to the case of

incomplete measurement by introducing an iteration scheme in the update process. It has been shown that the proposed method using FRF data outperforms the method using modal data, since the measured FRF data provides much more information in a desired frequency range than the modal data. They also claim that the methods using modal data are discrete versions of the methods using FRF data.

1.2.2.3 Eigenstructure Assignment Based Method

Another class of model update methods is eigenstructure assignment based method. The core of this type of methods is to design a fictitious/virtual feedback controller to produce the measured modal properties of the damaged structure, and then interpret the control gains as damage-induced matrix perturbations applied to the initial finite element model. Inman and Minas [97] and Zimmerman and Widengren [98] used the eigenstructure assignment techniques for refinement/correction of an analytical model. Later, Zimmerman and Kaouk [99] extended this eigenstructure assignment-based model refinement/correction technique by introducing a subspace rotation algorithm to enhance eigenvector assignability and an iterative algorithm to enforce the load path preservation, and the extended technique was applied to the problem of structural damage detection. To avoid the additional step of identifying the damaged structural members from matrix coefficient changes, Lim [100] introduced a method based on the concept of best achievable eigenvector, which can directly identify the damaged structural members. Specifically, the Euclidean distance between the measured mode shape and the best achievable eigenvector is used to locate damage, and the

eigenstructure assignment technique is used to estimate the magnitude of the damage by requiring the best achievable eigenvectors, undamaged modal matrices, and the fictitious controller satisfying the modal force error equation. Lim [101] applied a constrained eigenstructure technique experimentally to a 20-bay planar truss structure. The concept of best achievable eigenvector is employed to perform the expansion of test mode shapes so that the measured mode shapes are not required to be comprehensive of all degree-of-freedoms, and the burden of measurement instruments can be relieved.

1.3 Problem Statement and Research Objective

Vibration-based damage identification methods have been quite popular in recent years. As a type of global damage detection method, the vibration-based methods do not require that the vicinity of the damage spot be known *a priori* or the damage site be accessible for inspection, and thus could be advantageous for many practical applications. In current practice of vibration-based damage identification, natural frequencies (eigenvalues) and mode shapes (eigenvectors) have been the most frequently used vibration signature to carry the damage information. Most of the approaches developed in the literature, such as the model updating methods using modal data, require both natural frequency and mode shape measurements to update or reconstruct the mass and stiffness parameters. However, mode shape measurement is usually incomplete since it requires a large number of sensors or a sensory network to approximate the infinite number of degrees of freedom (DOF) in real distributed parameter structures, and the mode expansion or model reduction techniques inevitably deteriorate the solution of the

eigenvalue equation through the inverse approaches [102,103]. Moreover, the mode shape measurement is very sensitive to noise and environmental uncertainty [104]. On the other hand, the measurement of natural frequencies is quite straight forward, and they are much less sensitive to measurement errors compared with mode shape measurement [105]. Thus, natural frequencies give more reliable evidence of damage in a structure, and these damage identification methods that require only measured natural frequencies (hereafter referred as frequency-shift-based methods [41]) are generally more preferred than those that require both measured natural frequencies and mode shapes.

Although easy to implement and robust to measurement noise and uncertainty, the frequency-shift-based methods have severe practical limitations for real applications. One of the limitations is related to the deficiency of frequency measurement data, i.e., the number of measurable natural frequencies is usually much smaller than the number of physical parameters that are required to characterize the damage state. This issue has been clearly demonstrated and verified by many researchers in different types of approaches. Stubbs and Osegueda [43,44] demonstrated that the sensitivity equation may be severely underdetermined due to an insufficient number of frequency measurements, and the solution resulted from the pseudo-inverse search routine may be ill-conditioned. Richardsom and Mannan [45] also reported that the sensitivity equation may be underdetermined due to an insufficient number of frequency measurements when they use an alternative sensitivity based approach for damage detection. The issue of an underdetermined problem also exists for the eigen-sensitivity based model update methods [93,94]. Due to an insufficient number of measured frequencies, the resulting sensitivity matrix may be underdetermined or ill-conditioned, and thus the inverse

operation on the sensitivity matrix that is critical for model parameter updating may not have a unique solution. The number of frequency measurements required to avoid the underdetermined problem is generally much larger than the number of natural frequencies that can be accurately identified from the experimental modal analysis in real practice. For example, Williams and Messina [47] found that 10 to 15 resonance frequencies are needed to provide sufficient information about damage, when they use Multiple Damage Location Assurance Criterion (MDLAC) to identify stiffness reduction due to damage. Messina et al. [106] pointed out that more than 10 measured modal frequencies are required for detecting multiple damage locations, when they use a sensitivity-based method in combination with statistical correlation to detect damages in truss and three-beam test structures. Therefore, the insufficient number of frequency measurements could be the severe bottleneck for the implementation of frequency-shift-based damage identification method in real applications.

Another severe limitation of the frequency-shift-based damage identification methods is related to the low sensitivity of natural frequency shift with respect to damage effects. This issue has been demonstrated both analytically and experimentally. For example, Swamidas and Chen [107] use finite element method to study the resonant frequencies of a cracked cantilevered plate, and results show that a surface crack near the root of the plate with a width of 40% of plate width and depth of 70% of plate thickness produces frequency shifts in the first two bending modes of 0.68% and 0.27%, respectively. The low sensitivity of frequency shift to damage effect has also been experimental illustrated. Adams et al. [108] studied the shifts in resonant frequencies of an aluminum bar under axial loading when it is artificially damaged by two saw cuts on

opposite sides of the bar. When damage is located at the center of the bar and thirty percent of the cross-sectional area is removed, the resonant frequencies of the first three modes are only reduced by 0.8%, 0.0%, and 0.8%, respectively. With the same level of damage located at the end of the bar, frequency shifts of the first three modes are still as low as 0.7%, 1.3% and 1.0%, respectively. Experimental tests conducted on the I-40 bridge over the Rio Grande by Farrar et al. [**109**] also demonstrate this point. No significant changes in the modal frequencies were observed even when the cross-sectional stiffness at the center of a main plate girder had been reduced 96.4%, which leads to a 21% reduction on the bending stiffness of the overall bridge cross-section. Due to the low sensitivity of frequency shifts to damage effects, it requires either very precise measurement or a large level of damage to make the frequency shifts observable. Since measurement noise is inevitable in real situations, the measured frequency shifts for small levels of damage may be severely distorted by the effects of measurement noise, or even can not be observed in some cases. Therefore, either the mission of detecting damage at its early stage becomes impossible, or if possible, the obtained damage detection results may not be reliable due to the noise effects on the measured natural frequency changes.

From reviewing the previous practice and findings, the objective of this thesis is to advance the state-of-the-art of the frequency-shift-based damage identification by addressing the aforementioned two limitations of this method, i.e., the deficiency of frequency measurement data and low sensitivity of frequency shifts to damage effects.

First, a novel approach utilizing piezoelectric transducer circuitry with tunable inductance is developed to address the issue of deficiency of frequency measurement data for damage identification. The key idea is to use a tunable piezoelectric circuitry coupled

to the mechanical structure to favorably alter the dynamics of the electro-mechanical integrated system. First, the circuitry can be tailored to change the system frequency/modal distribution by introducing additional resonant frequencies and vibration modes. Second, through tuning the circuitry elements (i.e., the inductors), one can obtain a much enlarged dataset consisting of a *family* of frequency response functions (under different circuitry tunings) as compared to the original single frequency response of the mechanical structure without circuit. Therefore, by integrating tunable piezoelectric circuitry to the structure and favorably tuning the circuitry elements, we can obtain a much enlarged dataset of natural frequency measurements for damage identification.

To address the sensitivity issue, another new approach utilizing sensitivity-enhancing feedback control is then proposed. This new approach has the potential of simultaneously solving the two major limitations of the frequency-shift-based damage identification. The basic idea of this approach is to use active feedback control to appropriately assign the closed-loop eigenvalues and eigenvectors so that the sensitivity of frequency shift to damage effects can be enhanced. Meanwhile, multiple closed-loop systems can be obtained from different sensitivity-enhancing controls, and these closed-loop systems provide a much enlarged dataset of natural frequency measurements for damage identification. Therefore, by designing a series of sensitivity-enhancing controls and utilizing the natural frequencies of the resulting closed-loop systems for damage identification, both of the aforementioned limitations of the frequency-shift-based damage identification can be overcome.

The major issue of implementing the above two enhanced damage identification methods is that they require an accurate finite element model for circuit/controller design and system analysis. There are two ways to address this issue: (1) one way is to use model updating techniques to obtain an accurate finite element model, and hence satisfy this requirement; (2) the other way is to use system identification techniques to identify a model directly from experimental data, and hence frees the requirement of having an analytical model.

In fact, both of the proposed two damage identification methods can be extended for the application of structural model updating. With this, we can use the same set of hardware setup and measure the same physical quantity (i.e., natural frequency) for both functions of model updating and damage identification. Without loss of generality, this thesis only focuses on extending the sensitivity-enhancing control approach for structural model updating.

A laboratory experiment is designed and conducted to verify the sensitivity-enhancing control approach for frequency-shift-based damage detection. In the experiment, a system identification technique is utilized to identify a mathematical model directly from test data for controller design and system analysis, and hence does not need an analytical model as in the original approach.

1.4 Organization of the Thesis

This thesis consists of six chapters, and they are organized as follows:

Chapter 1 introduces the background and motivation for the research presented in this thesis. A comprehensive review of the literature related to the research topics in this thesis is provided, problems of the current approaches are described, and the research objective of this thesis is stated.

Chapter 2 presents the enhanced frequency-shift-based damage identification method using tunable piezoelectric circuitry. The fundamental mechanism of using tunable piezoelectric circuitry to enhance frequency measurement data for damage identification is described. Guidelines on how to tune the circuitry elements (i.e., inductors) to achieve the best performance of damage identification are developed. An iterative second-order perturbation based damage identification algorithm is developed to identify the damage features from the measured frequency changes before and after damage occurrence. Numerical analyses and case studies are carried out to demonstrate and verify the proposed method.

Chapter 3 presents another enhanced frequency-shift-based damage identification method using sensitivity-enhancing feedback control. The original concept of sensitivity-enhancing control is extended through eigen-sensitivity analysis of a multi-DOF system. An eigenstructure assignment based constrained optimization scheme is developed to design the optimal sensitivity-enhancing control to achieve the best performance of sensitivity enhancement. Numerical analyses and case studies are carried out to verify the concept of sensitivity-enhancing control, and demonstrate the effectiveness of the associated damage identification method.

Chapter 4 presents a model updating method to fulfill the requirement of an accurate finite element model for the sensitivity-enhancing control approach of damage

identification. A frequency-based model updating method is developed using the same concept of sensitivity-enhancing control as used for damage identification. With this, the sensitivity-enhancing control approach can be used for dual functions of model updating and damage identification.

In Chapter 5, a laboratory experiment is designed and carried out to verify the sensitivity-enhancing control approach for damage detection. The experiment uses a system identification technique to identify a mathematical model for controller design and system analysis, and hence does not require an analytical finite element model (which is needed in the original approach).

Finally, Chapter 6 concludes the research work presented in this thesis and recommends future directions towards the improvement and implementation of the damage identification methods developed in this thesis.

Chapter 2

An Enhanced Frequency-Shift-Based Damage Identification Method Using Tunable Piezoelectric Transducer Circuitry Network

2.1 Introduction

Although the frequency-shift-based damage identification methods have been quite popular in recent years, the current practice of frequency-shift-based damage identification methods, nevertheless, has severe limitations. One common limitation for most frequency-shift-based methods, either inverse approach or model update approach, is the deficiency of frequency measurement data for the process of damage identification. When the number of measured natural frequencies is much smaller than the number of physical parameters required to completely characterize the damage, the sensitivity based equation becomes severely underdetermined and the pseudo-inverse approach may lead to an ill-conditioned solution. Therefore, the deficiency of frequency measurement data could be the severe bottleneck for the implementation of frequency-shift-based damage identification method in real applications.

To address this issue, several methods aiming to enrich frequency measurement data have been proposed in the literature. For example, Trivailo et al. [110] proposed the use of "Twin" structures, where an auxiliary structure is attached to the test structure, to generate more modal information. Cha and Gu [111] explored a mass addition technique to enrich the modal data for structural parameter updating. They show that the mass matrix can be corrected by adding known masses to a multi-spring-mass system and

measuring its new eigendata, and subsequently, the stiffness matrix can also be updated by constructing a new mass-added system and equating the associated eigenvalue equations. Nalitolela et al. [112] studied the feasibility of adding a mass or stiffness to extract additional resonant frequencies. However, it is worth mentioning that the direct addition of mass/stiffness to a structure might be difficult to implement for many applications and encounter physical restrictions. To overcome this difficulty, Lew and Juang [113] introduced a new concept of using virtual passive controller to enrich the modal frequency measurement. They show that both output and dynamic feedback controllers can be incorporated to the original structure to generate additional closed-loop modal frequencies. In this approach, while no physical mass or stiffness are attached to the structure, it requires a complex sensor-actuator-controller architecture and a certain amount of external input energy as controller source.

In this chapter, a novel approach utilizing piezoelectric transducer circuitry with tunable inductance to enrich frequency measurement data is proposed. The key idea is to use a tunable piezoelectric circuitry coupled to the mechanical structure to favorably alter the dynamics of the electro-mechanical integrated system. First, the circuitry can be tailored to change the system frequency/modal distribution by introducing additional resonant frequencies and vibration modes. Second, through tuning the circuitry elements (i.e., the inductors), one can obtain a much enlarged dataset consisting of a *family* of frequency response functions (under different circuitry tunings) as compared to the original single frequency response of the mechanical structure without circuit. This approach is analogous to adding extra mechanical spring-mass elements to the structure [111,112]. However, electrical tailoring with variable circuitry is much easier to

implement than mechanical tailoring in real systems. On the other hand, compared with the schemes based on active feedback control [113], while the proposed approach also requires attachment of additional physical element (i.e., piezoelectric transducers) to the structure, it does not require a complex sensor-actuator-controller architecture and significant external energy source.

The organization of this chapter is as follows. First, the new idea of integrating tunable piezoelectric transducer circuitry is described. The fundamental mechanism of using piezoelectric transducer circuitry with tunable inductance to enrich frequency measurement data is illustrated. Second, an iterative second-order perturbation based damage identification algorithm is formulated. This algorithm takes into account the damage-induced mode shape changes by including high order terms into the eigenvalue perturbation formulation, and actual measurements of mode shapes before and after damage are not required for this algorithm. Third, guidelines on favorable inductance tuning that can yield optimal damage identification performance are developed. The enrichment of frequency measurement data can most effectively capture the damage information when the inductances are tuned to accomplish eigenvalue curve veerings between system eigenvalue pairs. Finally, numerical analyses on benchmark beam and plate structures are carried out to verify the improvement of damage identification performance by using the proposed approach.

2.2 New Idea of Integrating Tunable Piezoelectric Circuitry

Piezoelectric materials have been explored extensively for structural dynamics applications because of their electro-mechanical coupling characteristics. The direct effect of producing an electrical charge when stressed mechanically has been often used in sensors to sense structural deformation, while the converse effect of producing a mechanical strain under electrical field has been used in actuators to alter the dynamic response of the structural system. Due to such two-way electro-mechanical coupling, piezoelectric materials have been widely used for both active and passive vibration control applications. In a purely active arrangement, electrical field or charge is applied to the piezoelectric actuators (either surface bonded to or embedded in the host structure) to generate control force/moment. In a passive situation, an external shunt circuit is usually integrated to the piezoelectric material [114-116]. Shunting the piezoelectric materials, on the other hand, does not preclude the simultaneous use of the shunted piezoelectric materials as active actuators [117]. In fact, a well designed active-passive hybrid piezoelectric actuator network [118-121] not only could enhance the active control authority, but also could increase the system passive damping.

While previous work in this area was mostly limited to actuation improvement and damping augmentation for vibration control applications, in this paper we will develop a new paradigm for damage identification using piezoelectric transducers integrated with tunable inductance circuitry. The tunable inductance can be easily achieved by utilizing synthetic inductors [122-126]. The synthetic inductors are normally designed as small-size electronic devices, and they can provide a wide range of

inductance tuning up to thousands of Henries, with high accuracy and high robustness against system and environmental variations. As explained in the following paragraphs, this new idea will effectively address the limitations of current frequency-shift based damage identification approaches.

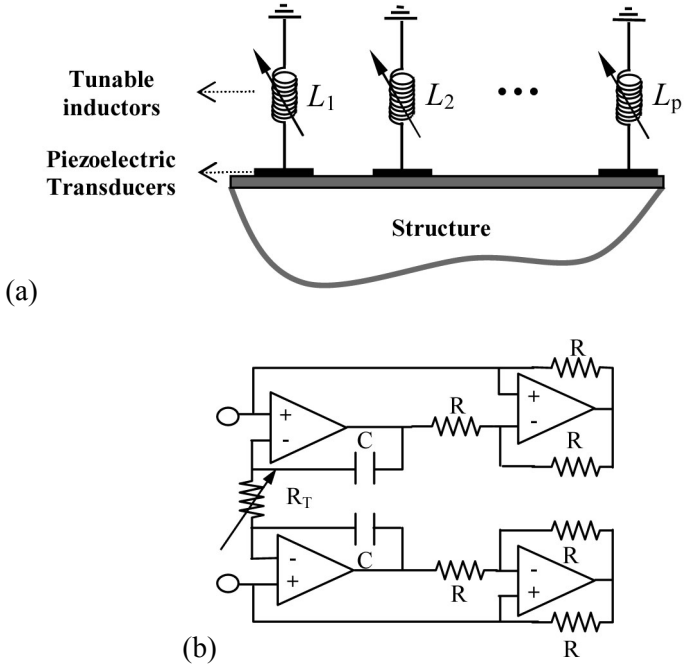

Figure 2.1. (a) Structure integrated with piezoelectric transducer circuitry with tunable inductance (b) Op-amp based circuit realization of tunable inductance, where inductance can be varied by adjusting RT.

A schematic of the electro-mechanical integrated system with piezoelectric transducer circuitries is shown in Figure 2.1(a), where each transducer is connected with a circuit consisting of a tunable inductor. Figure 2.1(b) shows the circuit diagram of an op-amp based synthetic inductor, where the inductance can be varied by adjusting the resistance R_T. The equation of motion for a general electro-mechanical integrated system shown in Figure 2.1(a) can be written as [118-121]

$$\begin{bmatrix} \boldsymbol{M}_s & \boldsymbol{0} \\ \boldsymbol{0} & \boldsymbol{L} \end{bmatrix} \begin{Bmatrix} \ddot{\boldsymbol{q}} \\ \ddot{\boldsymbol{Q}} \end{Bmatrix} + \begin{bmatrix} \boldsymbol{C} & \boldsymbol{0} \\ \boldsymbol{0} & \boldsymbol{R} \end{bmatrix} \begin{Bmatrix} \dot{\boldsymbol{q}} \\ \dot{\boldsymbol{Q}} \end{Bmatrix} + \begin{bmatrix} \boldsymbol{K}_s & \boldsymbol{K}_c \\ \boldsymbol{K}_c^T & \boldsymbol{K}_p \end{bmatrix} \begin{Bmatrix} \boldsymbol{q} \\ \boldsymbol{Q} \end{Bmatrix} = \begin{Bmatrix} \boldsymbol{F}_d \\ \boldsymbol{0} \end{Bmatrix} \qquad (2.1)$$

where $\boldsymbol{q}$ is the displacement vector of the structure, $\boldsymbol{Q}$ is the electrical charge flow vector in the circuit, $\boldsymbol{M}_s$, $\boldsymbol{C}$, and $\boldsymbol{K}_s$ are the mass, damping and stiffness matrices of the mechanical structure, respectively, $\boldsymbol{L}$, $\boldsymbol{R}$, and $\boldsymbol{K}_p$ are the inductance, resistance, and inverse capacitance matrices of the circuit, $\boldsymbol{K}_c$ is the coupling term between the mechanical and electrical fields, $\boldsymbol{F}_d$ is the excitation input.

In this research we use the shifts of natural frequencies as the information carrier for structural damage identification. The key concept of the proposed approach is to use the tunable piezoelectric circuitry to enrich the modal frequency measurement. First, the circuitry can be tailored to change the system frequency/modal distribution by introducing additional resonant frequencies and vibration modes. Second, through tuning the circuitry elements (e.g., inductors), one can further obtain a much enlarged data set consisting of a family of frequency response functions (under different circuitry tunings) as compared to the original single frequency response of the structure without circuit. These features are clearly illustrated in Figure 2.2 and Figure 2.3, where the frequency response functions of the pure mechanical structures and the associated electro-mechanical integrated systems are compared.

First, we study the effect of integrating single tunable piezoelectric circuitry on the frequency response function of the resulting integrated system. A cantilevered beam integrated with single tunable piezoelectric circuitry (this system, as shown in Figure 2.5, will be analyzed in detail in Section 2.4.1) is used as an example system.

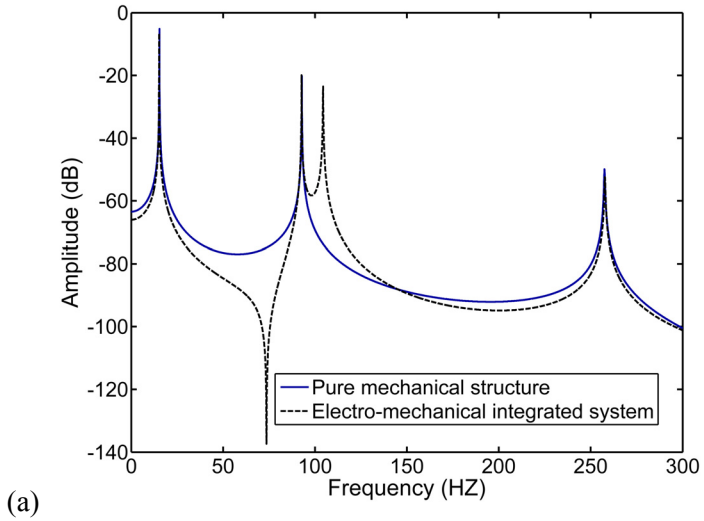

(a)

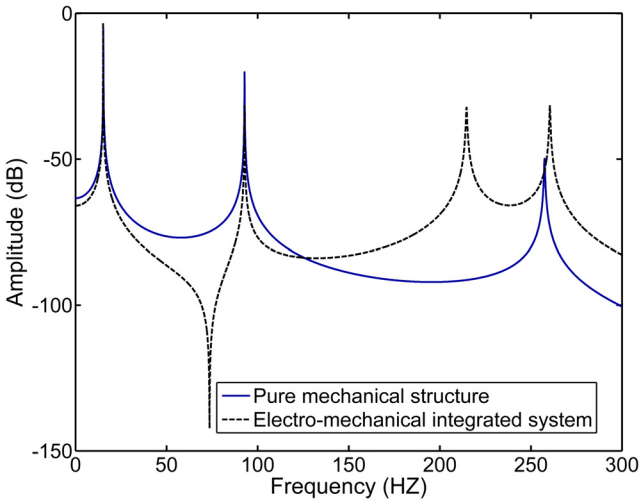

(b)

Figure **2.2**. Frequency response comparisons between the pure beam structure and the electro-mechanical integrated system with single tunable piezoelectric circuitry: (a) $L = 6.5\,\mathrm{H}$; (b) $L = 1.5\,\mathrm{H}$.

Figure **2.2** compares the frequency response functions of the pure beam structure and the integrated system with single piezoelectric circuitry. For the pure beam structure, the input excitation is a nodal force at the fourth node, and output measurement is the transverse displacement at the free-end of the beam. For the electro-mechanical integrated system, the same output measurement is used, while a voltage source in the

circuit is used as the input excitation. Observing Figure 2.2(a), we can clearly see that an additional resonant peak contributed by the circuitry dynamics is introduced into the frequency response function near the second structural resonant frequency. The frequency response function of the integrated system with a different inductance value is shown in Figure 2.2(b), where the additional resonant peak shifts to the neighborhood of the third structural resonant frequency.

In order to illustrate the effect of integrating multiple tunable piezoelectric circuitries on the frequency response function of the resulting integrated system, a cantilevered plate structure integrated with three tunable piezoelectric circuitries (this system, as shown in Figure 2.11, will be analyzed in detail in Section 2.4.2) is used as an example system. The frequency response functions of the pure plate structure and the resulting integrated system are compared in Figure 2.3. As shown in Figure 2.3(a), three additional resonant peaks contributed by the dynamics of three piezoelectric circuitries, respectively, are introduced into the frequency response function near the third, fourth, and fifth resonant frequencies of the original plate structure, respectively. The frequency response function of the integrated system with a different set of inductance values is shown in Figure 2.3(b), where the additional three peaks shift to the neighborhood of first, second and third structural resonant frequencies, respectively.

In current practices, damage identification using frequency-shift information is usually a severely under-determined problem. Since it is generally difficult to measure the resonant frequencies at high-frequency band, in current approaches the number of measurable resonant frequencies is much smaller than the number of degrees of freedom required to accurately characterize the structural damage. Clearly, the proposed method

of using tunable piezoelectric circuitry can significantly enlarge the data set and address this issue. As will be shown later, this new idea, when coupled with an identification algorithm presented in what follows, will yield much more accurate damage detection results.

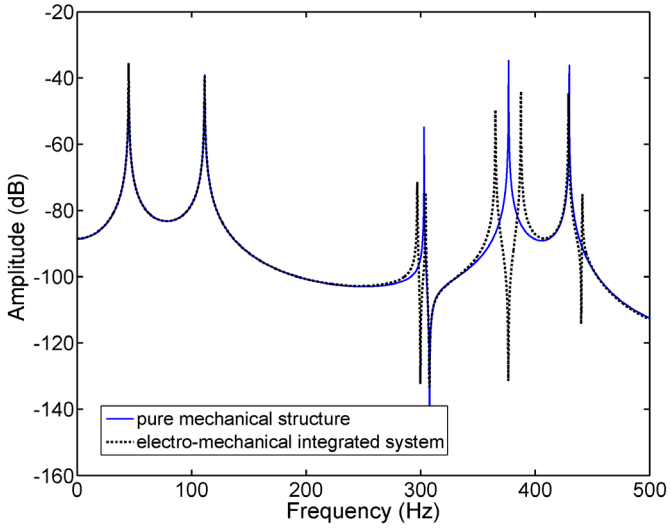

(a)

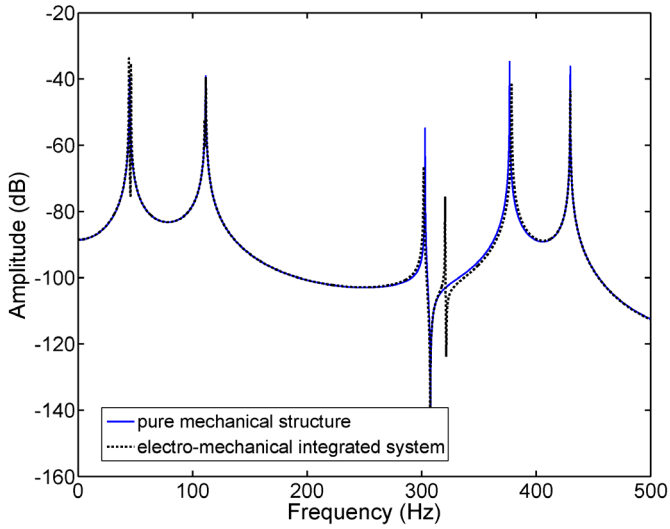

(b)

Figure **2.3**: Frequency response comparisons between the pure plate structure and the electro-mechanical integrated system with multiple tunable piezoelectric circuitries: (a) $L_1 = 0.91\,\mathrm{H}$, $L_2 = 1.25\,\mathrm{H}$, $L_3 = 1.96\mathrm{H}$; (b) $L_1 = 84.6\,\mathrm{H}$, $L_2 = 1.7\,\mathrm{H}$, $L_3 = 14.3\,\mathrm{H}$.

2.3 Iterative Second-Order Perturbation Based Damage Identification Algorithm

In this section, the concept of integrating tunable piezoelectric transducer circuitry is incorporated into a sensitivity-based model updating scheme to form the damage identification algorithm, which is used to identify both the locations and severities of the structural damages. From Eq. (2.1), the generalized mass and stiffness matrices of the electro-mechanical integrated system as shown in Figure 2.1(a) are given as

$$\tilde{\boldsymbol{M}} = \begin{bmatrix} \boldsymbol{M}_s & \boldsymbol{0} \\ \boldsymbol{0} & \boldsymbol{L} \end{bmatrix} \tag{2.2}$$

$$\tilde{\boldsymbol{K}} = \begin{bmatrix} \boldsymbol{K}_s & \boldsymbol{K}_c \\ \boldsymbol{K}_c^T & \boldsymbol{K}_p \end{bmatrix} \tag{2.3}$$

Neglecting damping, we can obtain the eigenvalue problem of the integrated system associated with the undamaged (healthy) structure,

$$\left(-\lambda_i \tilde{\boldsymbol{M}} + \tilde{\boldsymbol{K}}\right)\boldsymbol{\varphi}_i = 0 \ , \quad \text{where } i = 1, \cdots, N \tag{2.4}$$

where λ_i and $\boldsymbol{\varphi}_i$ are the ith eigenvalue and eigenvector of the undamaged system, respectively.

Following the common assumption used in literature, the structural damage is assumed to be only related to the structure stiffness. Therefore, the stiffness matrix of the integrated system has a change of $\delta\tilde{\boldsymbol{K}}$ after the structure is damaged, while the mass matrix of the integrated system remains the same, i.e.,

$$\tilde{\boldsymbol{M}}^d = \tilde{\boldsymbol{M}} \tag{2.5}$$

$$\tilde{\boldsymbol{K}}^d = \tilde{\boldsymbol{K}} + \delta\tilde{\boldsymbol{K}} \tag{2.6}$$

The eigenvalue problem of the integrated system associated with the damaged structure can be written as

$$\left(-\lambda_i^d \tilde{\boldsymbol{M}} + \tilde{\boldsymbol{K}}^d\right)\boldsymbol{\varphi}_i^d = 0, \qquad \text{where } i = 1,\cdots,N \tag{2.7}$$

where λ_i^d and $\boldsymbol{\varphi}_i^d$ are the *i*th eigenvalue and eigenvector of the damaged system, respectively, and can be expressed as

$$\lambda_i^d = \lambda_i + \delta\lambda_i \tag{2.8}$$

$$\boldsymbol{\varphi}_i^d = \boldsymbol{\varphi}_i + \delta\boldsymbol{\varphi}_i \tag{2.9}$$

2.3.1 First-Order Approximation-Based Damage Identification Algorithm

Substituting Eqs. (2.5), (2.6), (2.8) and (2.9) into Eq. (2.7), and neglecting the high order terms, we may obtain the first-order approximation of the eigenvalue change,

$$\delta\lambda_i = \boldsymbol{\varphi}_i^T \delta\tilde{\boldsymbol{K}}\boldsymbol{\varphi}_i \tag{2.10}$$

In a finite element model (FEM), the global stiffness matrix of the mechanical structure can be expressed as the direct summation of all elemental stiffness matrices

$$\boldsymbol{K}_s = \sum_{j=1}^{n_e} \boldsymbol{K}_j^e \alpha_j \tag{2.11}$$

where $\boldsymbol{K}_j^e$ is the elemental stiffness matrix of the *j*th element positioned within the global stiffness matrix $\boldsymbol{K}_s$, n_e is the number of elements used to discretize the structure, and α_j is the associated elemental stiffness parameter, which is defined as such that $\alpha_j = 1$ indicates no damage. Assuming that the unknown damage inside the structure causes

variations of elemental stiffness parameter by $\delta\alpha_j \left(j = 1, \cdots, n_e\right)$, we may express the global stiffness matrix of the damaged mechanical structure as

$$\boldsymbol{K}_s^d = \sum_{j=1}^{n_e} \boldsymbol{K}_j^e (\alpha_j + \delta\alpha_j) \tag{2.12}$$

Observe Eq. (2.3) which is the expression of the generalized stiffness matrix of the integrated system, clearly, the inverse capacitance matrix of the inductive circuit $\boldsymbol{K}_p$ and the coupling term $\boldsymbol{K}_c$ both remain the same after the structural damage occurs. Therefore, the change of the generalized stiffness matrix of the integrated system is only caused by the change of the global stiffness matrix of the mechanical structure, and can be expressed as

$$\delta\tilde{\boldsymbol{K}} = \begin{bmatrix} \delta\boldsymbol{K}_s & \boldsymbol{0} \\ \boldsymbol{0} & \boldsymbol{0} \end{bmatrix} = \begin{bmatrix} \sum_{j=1}^{n_e} \delta\alpha_j \boldsymbol{K}_j^e & \boldsymbol{0} \\ \boldsymbol{0} & \boldsymbol{0} \end{bmatrix} = \sum_{j=1}^{n_e} \delta\alpha_j \tilde{\boldsymbol{K}}_j^e \tag{2.13}$$

where $\tilde{\boldsymbol{K}}_j^e$ is the elemental stiffness matrix of the *j*th element positioned within the generalized stiffness matrix of the integrated system $\tilde{\boldsymbol{K}}$. Substituting Eq. (2.13) into Eq. (2.10), we can obtain the following relation,

$$\delta\lambda_i = \sum_{j=1}^{n_e} \delta\alpha_j \boldsymbol{\varphi}_i^T \tilde{\boldsymbol{K}}_j^e \boldsymbol{\varphi}_i \tag{2.14}$$

Eq. (2.14) is the relation for the *i*th eigenvalue change. Collecting the available changes of respective eigenvalues, we may obtain,

$$\boldsymbol{S}\delta\boldsymbol{\alpha} = \delta\boldsymbol{\lambda} \tag{2.15}$$

where

$$\delta\boldsymbol{\lambda} = \begin{bmatrix} \delta\lambda_1 & \delta\lambda_2 & \cdots & \delta\lambda_m \end{bmatrix}^T \tag{2.16}$$

$$\delta\boldsymbol{\alpha} = \begin{bmatrix} \delta\alpha_1 & \delta\alpha_2 & \cdots & \delta\alpha_{n_e} \end{bmatrix}^T \tag{2.17}$$

Which, respectively, are the vector of the damage-induced eigenvalue changes and the vector of damage-induced stiffness parameter variations. Here $\boldsymbol{S}$ is the sensitivity matrix whose elements can be expressed as

$$S_{ij} = \boldsymbol{\varphi}_i^T \tilde{\boldsymbol{K}}_j^e \boldsymbol{\varphi}_i, \quad \text{where } i = 1, 2, \cdots, m \text{ and } j = 1, 2, \cdots, n_e \tag{2.18}$$

In above expressions, m is the number of measured (available) resonant frequencies of the integrated system, and n_e is the number of elements used in the finite element model of the structure.

At this point, it is obvious that the identification of the location and severity of the unknown structural damage is equivalent to solving for $\delta\boldsymbol{\alpha}$, the vector of elemental stiffness parameter variations. Because the number of measured frequencies m is in general much smaller than the total number of structural elements n_e, Eq. (2.15) is usually a significantly underdetermined problem and one normally resort to approximate solutions through a pseudo inverse search routine [43-45].

One of the key features of integrating tunable piezoelectric transducer circuitry to the structure is that we will be able to obtain multiple frequency response functions (with different inductances) and their changes due to (the same) damage. Note that Eq. (2.15) is derived for a single set of inductance values, we may obtain a series of such equations corresponding to different sets of inductance values, which leads to a much enlarged

dataset for damage identification. Let the inductances in the piezoelectric transducer circuitry network be tuned to form a sequence $\boldsymbol{L}^{(i)}\left(i=1,2,\cdots,n\right)$

$$\begin{bmatrix} \boldsymbol{L}^{(1)} \\ \boldsymbol{L}^{(2)} \\ \vdots \\ \boldsymbol{L}^{(n)} \end{bmatrix} = \begin{bmatrix} L_1^{(1)} & L_2^{(1)} & \cdots & L_p^{(1)} \\ L_1^{(2)} & L_2^{(2)} & \cdots & L_p^{(2)} \\ \vdots & \vdots & \vdots & \vdots \\ L_1^{(n)} & L_2^{(n)} & \cdots & L_p^{(n)} \end{bmatrix} \tag{2.19}$$

where the number of columns, p, represents the number of tunable piezoelectric transducer circuitries integrated to the mechanical structure, and the number of rows, n, represents the number of inductance tuning sets. A set of simultaneous equations similar to Eq. (2.15) can then be obtained and these equations can be written in the matrix form as follows

$$\begin{bmatrix} \delta\boldsymbol{\lambda}(\boldsymbol{L}^{(1)}) \\ \delta\boldsymbol{\lambda}(\boldsymbol{L}^{(2)}) \\ \vdots \\ \delta\boldsymbol{\lambda}(\boldsymbol{L}^{(n)}) \end{bmatrix} = \begin{bmatrix} \boldsymbol{S}(\boldsymbol{L}^{(1)}) \\ \boldsymbol{S}(\boldsymbol{L}^{(2)}) \\ \vdots \\ \boldsymbol{S}(\boldsymbol{L}^{(n)}) \end{bmatrix} \cdot \delta\boldsymbol{\alpha} \tag{2.20}$$

This formulation clearly illustrates the advantage of using tunable piezoelectric circuitry. We can now significantly increase the number of measurements in eigenvalue changes (or frequency shifts) and thus increase the number of simultaneous equations that characterize the damage features. In other words, we can make the problem much less underdetermined.

2.3.2 Iterative Perturbation-Based Damage Identification Algorithm

The main limitation of the first-order approximation-based algorithm is that the information regarding the change in eigenvectors (mode shapes) is not included. Although mode shape changes can be neglected in some cases, it deteriorates the accuracy of damage identification when the damage level is high or when the mode shapes are sensitive to the damage. Therefore, an improved algorithm which includes the information about the change in mode shape is highly desirable. Wong et al. [127] developed a general high-order perturbation expression for the eigenvalue problem with changes in stiffness, and the perturbation method is used iteratively in conjunction with an optimization method to identify the stiffness parameters of the structure. In what follows, we use a second-order perturbation to describe the changes of eigenvalues, which leads to the inclusion of the information of damage-induced mode shape changes. The changes of the kth eigenvalue of the integrated system after damage occurrence can be expressed as

$$\delta\lambda_k = \sum_{i=1}^{n_e} \frac{\partial \lambda_k}{\partial \alpha_i}\delta\alpha_i + \sum_{i=1}^{n_e}\sum_{j=1}^{n_e} \frac{\partial^2 \lambda_k}{\partial \alpha_i \partial \alpha_j}\delta\alpha_i\delta\alpha_j = \boldsymbol{S}_k^{(1)}\delta\boldsymbol{\alpha} + \delta\boldsymbol{\alpha}^T\boldsymbol{S}_k^{(2)}\delta\boldsymbol{\alpha} \tag{2.21}$$

where $\boldsymbol{S}_k^{(1)}$, $\boldsymbol{S}_k^{(2)}$ are the first and second order perturbation coefficients for the kth eigenvalue, respectively. They can be expressed as

$$\boldsymbol{S}_k^{(1)}(i) = (\boldsymbol{\varphi}_k)^T\,\tilde{\boldsymbol{K}}_i^e\,(\boldsymbol{\varphi}_k) \tag{2.22}$$

$$\boldsymbol{S}_k^{(2)}(i,j) = \frac{1}{2!}(\boldsymbol{\varphi}_k)^T\left\{\tilde{\boldsymbol{K}}_i^e\boldsymbol{D}_k^{(1)}(j) + \tilde{\boldsymbol{K}}_j^e\boldsymbol{D}_k^{(1)}(i)\right\} \tag{2.23}$$

where $\boldsymbol{D}_k^{(1)}(i)$ is the coefficient vector of the first-order perturbation for the kth mass-

normalized eigenvector

$$\delta\boldsymbol{\varphi}_k = \sum_{i=1}^{n_e} \frac{\partial \boldsymbol{\varphi}_k}{\partial \alpha_i} \delta\alpha_i = \sum_{i=1}^{n_e} \boldsymbol{D}_k^{(1)}(i)\delta\alpha_i \tag{2.24}$$

and can be calculated as follows,

$$\boldsymbol{D}_k^{(1)}(i) = \sum_{j=1}^{m} \boldsymbol{P}_k^{(1)}(i,j)\boldsymbol{\varphi}_j \tag{2.25}$$

$$\boldsymbol{P}_k^{(1)}(i,j) = \begin{cases} 0 & j = k; \\ \dfrac{1}{\lambda_k - \lambda_j}\left(\boldsymbol{\varphi}_j\right)^T \tilde{\boldsymbol{K}}_i^e\left(\boldsymbol{\varphi}_k\right) & j \neq k; \end{cases} \tag{2.26}$$

For a given set of inductance values, $\boldsymbol{L}^{(0)} = \begin{bmatrix} L_1^{(0)} & L_2^{(0)} & \cdots & L_p^{(0)} \end{bmatrix}$, a second-order perturbation based equation can be obtained as

$$\begin{aligned} \delta\boldsymbol{\lambda}(\boldsymbol{L}^{(0)}) &= \begin{Bmatrix} \delta\lambda_1(\boldsymbol{L}^{(0)}) \\ \delta\lambda_2(\boldsymbol{L}^{(0)}) \\ \vdots \\ \delta\lambda_k(\boldsymbol{L}^{(0)}) \end{Bmatrix} = \begin{bmatrix} \boldsymbol{S}_1^{(1)} \\ \boldsymbol{S}_2^{(1)} \\ \vdots \\ \boldsymbol{S}_k^{(1)} \end{bmatrix} \cdot \delta\boldsymbol{\alpha} + \begin{bmatrix} (\delta\boldsymbol{\alpha})^T \boldsymbol{S}_1^{(2)}(\delta\boldsymbol{\alpha}) \\ (\delta\boldsymbol{\alpha})^T \boldsymbol{S}_2^{(2)}(\delta\boldsymbol{\alpha}) \\ \vdots \\ (\delta\boldsymbol{\alpha})^T \boldsymbol{S}_k^{(2)}(\delta\boldsymbol{\alpha}) \end{bmatrix} \\ &= \boldsymbol{S}^{(1)}(\boldsymbol{L}^{(0)}) \cdot \delta\boldsymbol{\alpha} + \boldsymbol{P}\left\{\boldsymbol{S}^{(2)}(\boldsymbol{L}^{(0)}), \delta\boldsymbol{\alpha}\right\} \end{aligned} \tag{2.27}$$

When we tune the inductances to form a sequence as $\boldsymbol{L}^{(i)}\left(i = 1, 2, \cdots, n\right)$ and perform frequency (eigenvalue) measurements, correspondingly we may obtain a series of eigenvalue change equations, which, collectively, lead to a set of equations in the following form,

$$\begin{bmatrix} \delta\boldsymbol{\lambda}(\boldsymbol{L}^{(1)}) \\ \delta\boldsymbol{\lambda}(\boldsymbol{L}^{(2)}) \\ \vdots \\ \delta\boldsymbol{\lambda}(\boldsymbol{L}^{(n)}) \end{bmatrix} = \begin{bmatrix} \boldsymbol{S}^{(1)}(\boldsymbol{L}^{(1)}) \\ \boldsymbol{S}^{(1)}(\boldsymbol{L}^{(2)}) \\ \vdots \\ \boldsymbol{S}^{(1)}(\boldsymbol{L}^{(n)}) \end{bmatrix} \cdot \delta\boldsymbol{\alpha} + \begin{bmatrix} \boldsymbol{P}\left\{\boldsymbol{S}^{(2)}(\boldsymbol{L}^{(1)}), \delta\boldsymbol{\alpha}\right\} \\ \boldsymbol{P}\left\{\boldsymbol{S}^{(2)}(\boldsymbol{L}^{(2)}), \delta\boldsymbol{\alpha}\right\} \\ \vdots \\ \boldsymbol{P}\left\{\boldsymbol{S}^{(2)}(\boldsymbol{L}^{(n)}), \delta\boldsymbol{\alpha}\right\} \end{bmatrix} \tag{2.28}$$

For the nonlinear equation, Eq. (2.28), a constrained optimization method is needed to find the approximate solution of $\delta\boldsymbol{\alpha}$. The constrained optimization problem is formulated to minimize the norm of the difference between the actual eigenvalue change ($\delta\boldsymbol{\lambda}^{actual}$) from the frequency response measurement, and $\delta\boldsymbol{\lambda}(\delta\boldsymbol{\alpha})$, the eigenvalue change produced by the estimated stiffness parameter variation $\delta\boldsymbol{\alpha}$, in the following manner:

$$\begin{aligned} &\text{Minimize} && \left\| \delta\boldsymbol{\lambda}(\delta\boldsymbol{\alpha}) - \delta\boldsymbol{\lambda}^{actual} \right\| \\ &\text{subject to} && -1 < \delta\alpha_j \le 0 \text{, where } j = 1, 2, \cdots, n_e \end{aligned} \qquad (2.29)$$

In order to further improve the performance of damage identification, the perturbation method is used iteratively in conjunction with a constrained optimization scheme, namely, an iterative second-order perturbation based damage identification algorithm. A detailed flow chart of this algorithm is shown in Figure 2.4.

From the measurements of frequency response functions of the integrated system with actual structural damage, system eigenvalues corresponding to different inductance values, $\boldsymbol{\lambda}^d(\boldsymbol{L}^{(1)}), \boldsymbol{\lambda}^d(\boldsymbol{L}^{(2)}), \cdots, \boldsymbol{\lambda}^d(\boldsymbol{L}^{(n)})$, are obtained. In the first iteration, the baseline system is set to be the integrated system with no structural damage, i.e., $\delta\alpha_j^{(1)} = 0$, where $j = 1, 2, \cdots, n_e$.

In each iteration, the eigenvalues of the baseline system corresponding to different inductance values $\boldsymbol{\lambda}^{(k)}(\boldsymbol{L}^{(1)}), \boldsymbol{\lambda}^{(k)}(\boldsymbol{L}^{(2)}), \cdots, \boldsymbol{\lambda}^{(k)}(\boldsymbol{L}^{(n)})$, where k denotes the iteration number, can be calculated from the formulated eigenvalue problem based on the finite element model that has been developed before damage occurred. Then the eigenvalue differences between the actual damaged system and the baseline system can be easily

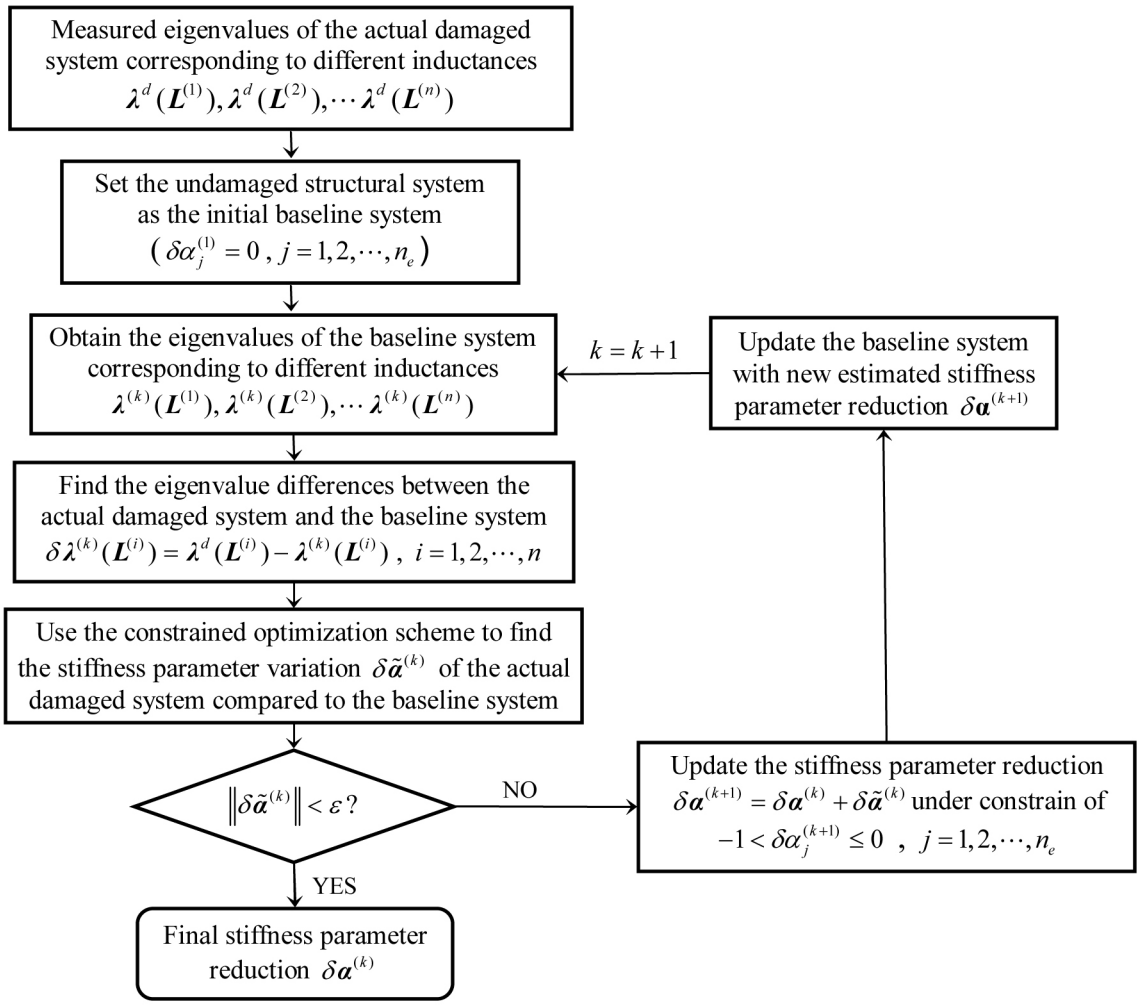

Figure 2.4: Flowchart of the iterative second-order perturbation based damage identification algorithm

found through the equation $\delta\lambda^{(k)}(L^{(i)}) = \lambda^d(L^{(i)}) - \lambda^{(k)}(L^{(i)})$, where $i = 1,2,\cdots,n$. In the next step, the stiffness parameter variation $\delta\tilde{\alpha}^{(k)}$ is found by using the constrained optimization scheme, which is realized by the standard constrained minimum subroutine FMINCON provided by MATLAB. Then the estimated stiffness parameter variation is updated by using $\delta\alpha^{(k+1)} = \delta\alpha^{(k)} + \delta\tilde{\alpha}^{(k)}$ under the constraint $-1 < \delta\alpha_j^{(k+1)} \le 0$, and the baseline system is also updated to represent the system with the new estimated stiffness

parameter variation $\delta\boldsymbol{\alpha}^{(k+1)}$. This process continues until the termination criterion, $\left\|\delta\tilde{\boldsymbol{\alpha}}^{(k)}\right\| < \varepsilon$, is satisfied, where ε is a sufficiently small constant.

2.4 Formulation of Favorable Inductance Tuning

A fundamental issue of the proposed tunable piezoelectric circuitry concept is how to tune the inductances to best enhance the performance of damage identification. In this section, we present the guidelines of forming a favorable inductance tuning sequence based on the analysis on how the inductance tuning affects the characteristics of system dynamics and the damage-induced eigenvalue changes. First, a benchmark beam structure integrated with a single tunable piezoelectric transducer circuitry is used to obtain the fundamental understandings of the effects of inductance tuning. Then, a more complicated plate structure integrated with multiple piezoelectric transducer circuitries is studied to verify and extend the observations to multiple inductance tunings.

2.4.1 Integrated System With Single Tunable Piezoelectric Circuitry

We first study a benchmark example of a cantilevered beam integrated with a single tunable piezoelectric transducer circuitry (Figure 2.5). A circuit with tunable inductor is integrated to a homogenous cantilevered beam through the piezoelectric transducer, which is bonded on the upper surface of the beam from x_1 to x_2. Using Galerkin's method to discretize the partial differential equations, we can obtain a set of ordinary differential equations in the form of Eq. (2.1) [119].

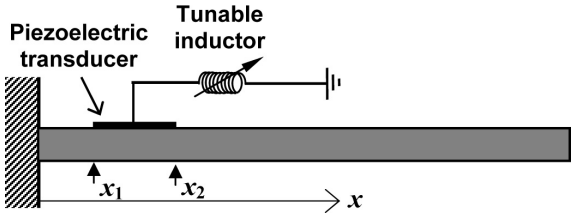

Figure 2.5: Configuration of a cantilevered beam integrated with a single tunable piezoelectric transducer circuitry

2.4.1.1 Simplified Two-DOF System Analysis

If only the first mode is used in the Galerkin's method, the integrated system can be modeled as a 2-DOF system and the eigenvalue problem of this simplified system is given as

$$\left(\begin{bmatrix} k_{11} & k_c \\ k_c & k_p \end{bmatrix} - \lambda \begin{bmatrix} m_{11} & 0 \\ 0 & L \end{bmatrix} \right) \{\boldsymbol{\varphi}_i\} = \begin{Bmatrix} 0 \\ 0 \end{Bmatrix} \tag{2.30}$$

which yields two eigenvalues,

$$\lambda_{1,2} = \frac{(k_{11}L + k_p m_{11}) \pm \sqrt{(k_{11}L - k_p m_{11})^2 + 4m_{11}Lk_c^2}}{2m_{11}L} \tag{2.31}$$

The difference between these two eigenvalues is

$$\lambda_1 - \lambda_2 = \frac{\sqrt{(k_{11}L - k_p m_{11})^2 + 4m_{11}Lk_c^2}}{m_{11}L} \tag{2.32}$$

From Eq. (2.32) we can derive and conclude that the difference of the two eigenvalues reaches its minimum or, in other words, the two eigenvalues are the closest, when the inductance takes the value of

$$L^* = \frac{k_p m_{11}}{k_{11}} \left(\frac{1}{1 - 2k_c^2 / (k_{11} k_p)} \right) \tag{2.33}$$

Hereafter this is referred to as the "critical" inductance value. If we assume that $k_c^2 \le k_{11} k_p$, Eq. (2.33) can be simplified as

$$L^* \approx \frac{k_p m_{11}}{k_{11}} \tag{2.34}$$

Table 2.1: System parameters for the integrated system of beam structure

Beam structure		Piezoelectric material	
Density:	$\rho_b = 2700\,\text{kg/m}^3$	Density:	$\rho_p = 7800\,\text{kg/m}^3$
Length:	$L_b = 0.4184\,\text{m}$	Young's modulus:	$E_p = 6.6\times10^{10}\ \text{N/m}^2$
Thickness:	$h_b = 3.175\,\text{mm}$	Thickness:	$h_p = 0.191\,\text{mm}$
Width:	$b = 0.0381\,\text{m}$	Dielectric constant:	$\beta_{33} = 7.1445\times10^7\ \text{V}\cdot\text{m/C}$
Young's modulus:	$E_b = 7.1\times10^{10}\ \text{N/m}^2$	Piezoelectric constant:	$h_{31} = 1.0707\times10^9\ \text{N/C}$

Let the left and right ends of the piezoelectric transducer be $x_1 = 0.04184\,\text{m}$ and $x_2 = 0.08368\,\text{m}$. All other system parameters of this illustrative case are specified in Table 2.1. The variation of the two system eigenvalues with respect to the inductance tuning is plotted in Figure 2.6. In this figure, the horizontal axis denotes the normalized inductance ξ, which is defined as the ratio between the actual inductance to the critical inductance L^* given in Eq. (2.33),

$$\xi = \frac{L}{L^*} = \frac{L}{(k_p \cdot m_{11}) / k_{11}} \tag{2.35}$$

From Figure 2.6, we can see that the loci of the two eigenvalues approach each other in the first stage, and then diverge abruptly when we continuously increase the inductance. This phenomenon of rapid changes of system eigenvalues with respect to the system parameter (inductance L) indicates the occurrence of eigenvalue curve veering [128-131].

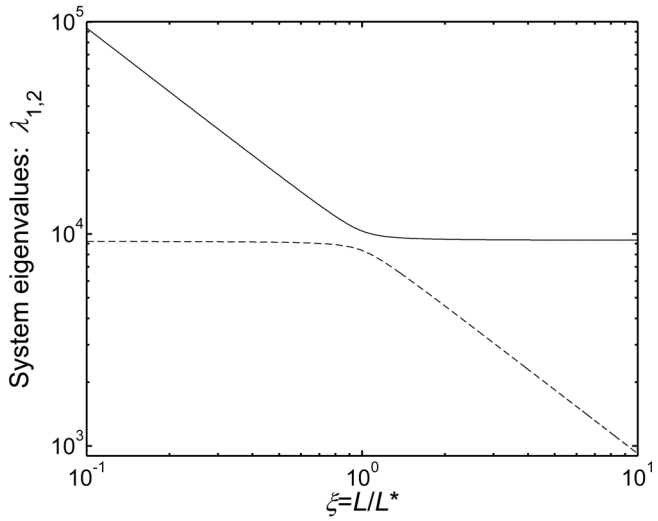

Figure 2.6: System eigenvalues versus the normalized inductance when using the simplified 2-DOF system model for the integrated beam system. —— λ_1, ---- λ_2.

Liu [132] examined the derivatives of the eigenvalues and eigenvectors for the phenomena of eigenvalue curve veering and mode localization. In this paper, we are concerned with the sensitivity of damage-induced eigenvalue change with respect to inductance tuning, since a favorable tuning of the inductance value should yield a system in which the eigenvalue change is very sensitive to the damage occurrence (causing stiffness parameter change). This sensitivity can be expressed as the second-order derivatives of the system eigenvalues with respect to stiffness parameter ($G = E_b I_b$) and inductance (L),

$$\frac{\partial(\delta\lambda_{1,2})}{\partial L}=\frac{\partial}{\partial L}\left(\frac{\partial\lambda_{1,2}}{\partial G}\delta G\right)=\frac{\partial^2\lambda_{1,2}}{\partial L\partial G}\delta G \tag{2.36}$$

The derivatives of the eigenvalues with respect to stiffness parameter change can be solved as

$$\frac{\partial\lambda_{1,2}}{\partial G}=\frac{\partial\lambda_{1,2}}{\partial k_{11}}\cdot\frac{\partial k_{11}}{\partial G}=\frac{1}{2m_{11}}\left[1\pm\frac{k_{11}L-k_p m_{11}}{\sqrt{(k_{11}L-k_p m_{11})^2+4m_{11}Lk_c^2}}\right]\cdot\frac{\partial k_{11}}{\partial G} \tag{2.37}$$

Substituting Eq. (2.37) into Eq. (2.36), we can obtain the derivative of damage-induced eigenvalue changes ($\delta\lambda_1$ and $\delta\lambda_2$) with respect to inductance (L) as

$$\frac{\partial(\delta\lambda_{1,2})}{\partial L}=\pm\frac{Lk_{11}k_c^2+m_{11}k_p k_c^2}{\left[(k_{11}L-k_p m_{11})^2+4m_{11}Lk_c^2\right]^{\frac{3}{2}}}\cdot\left(\frac{\partial k_{11}}{\partial G}\delta G\right) \tag{2.38}$$

For a specific damage scenario, $\left(\partial k_{11}/\partial G\right)\delta G$ on the right hand side of Eq. (2.38) is fixed, and the inductance value which yields the maximum of $\partial(\delta\lambda_{1,2})/\partial L$ can be easily solved by letting the derivative of the fractional part on the right hand side of Eq. (2.38) with respect to the inductance (L) be zero,

$$L^*=\frac{m_{11}k_p}{2k_{11}}\cdot\left[\left(9-\frac{10k_c^2}{k_{11}k_p}+\frac{k_c^4}{k_{11}^2k_p^2}\right)^{\frac{1}{2}}-\left(1-\frac{k_c^2}{k_{11}k_p}\right)\right] \tag{2.39}$$

If we assume that $k_c^2\le k_{11}k_p$, Eq. (2.39) can be simplified as

$$L^*\approx\frac{k_p m_{11}}{k_{11}} \tag{2.40}$$

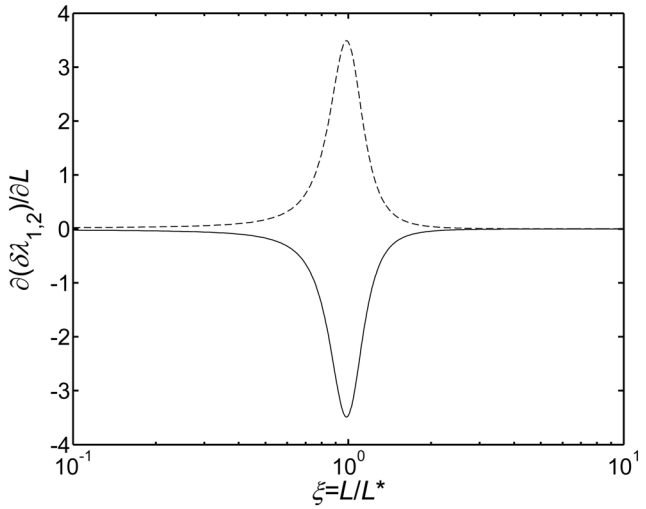

Figure **2.7**: Sensitivities of the damage-induced eigenvalue changes with respect to the normalized inductance when using the simplified 2-DOF system model for the integrated beam system. —— $\partial\left(\delta\lambda_1\right)/\partial L$, ---- $\partial\left(\delta\lambda_2\right)/\partial L$.

Assuming that the damage-induced stiffness reduction is $\delta G = -0.15G$, we can plot the derivative of the damage-induced eigenvalue changes ($\delta\lambda_1$ and $\delta\lambda_2$) with respect to inductance (L), as shown in Figure **2.7**. From this figure, we can see that the sensitivities of the two eigenvalue changes with respect to inductance reach their maximal absolute values when the inductance is tuned near the critical value, $L^* = k_p \cdot m_{11}/k_{11}$, and the sensitivities decreases dramatically when the inductance is tuned away from this critical value. Recall Eq. (**2.34**) and note that eigenvalue curve veering occurs when the inductance is tuned around $L^* = k_p \cdot m_{11}/k_{11}$ (Figure **2.6**). We can conclude that the occurrence of eigenvalue curve veering not only suggests rapid changes of system eigenvalues (characteristics of system dynamics) with respect to inductance tuning, but also produces an inductance tuning range in which high sensitivity of damaged-induced eigenvalue changes with respect to inductance tuning can be

expected. Therefore, when the inductance is tuned around L^*, multiple sets of frequency-shift measurements with different sensitivity relations to the potential damage can be obtained. This can greatly enrich the frequency data available for damage identification and help to more completely capture the information about the damage occurrence.

2.4.1.2 Multiple-DOF System Analysis

The above observations for the 2-DOF system are based on the analytical sensitivity analysis of the damage-induced eigenvalue changes with respect to inductance tuning. In this sub-section we extend this sensitivity analysis to multi-DOF systems. The cantilevered beam shown in Figure 2.5 is now analyzed using the finite element method. As shown in Figure 2.16, the beam is evenly discretized into 10 elements, and the piezoelectric transducer is bonded on the upper surface of the beam from the second element to the fourth element. The relevant system parameters are the same as specified in Table 2.1.

First, we examine how the inductance tuning alters the characteristics of system dynamics (i.e., system eigenvalues). Figure 2.8 shows the variations of the first four system eigenvalues with respect to inductance tuning. From this figure, we can see that eigenvalue curve veering occurs between each two consecutive system eigenvalues from low mode to high mode when the inductance is tuned from $1500\,\mathrm{H}$ down to $0.3\,\mathrm{H}$. In each eigenvalue curve veering, only the two associated system eigenvalues change dramatically with respect to inductance tuning, while other system eigenvalues are hardly affected. Meanwhile, as a well-known phenomenon associated with the curve veering,

during the eigenvalue curve veering the eigenvectors corresponding to the veering eigenvalues will interchange in a rapid but continuous way [128-131].

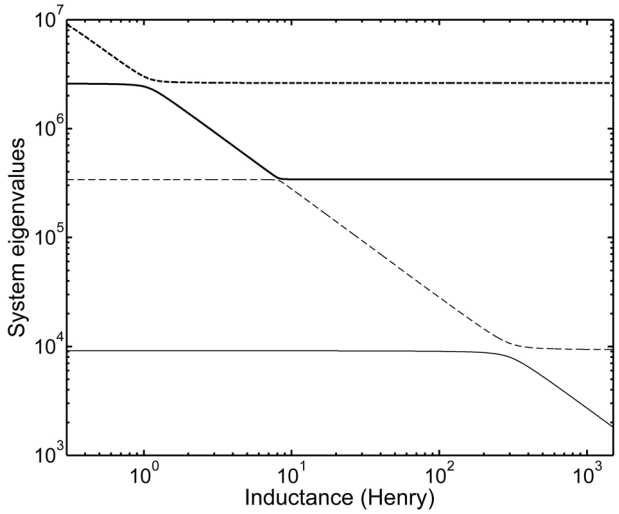

Figure 2.8: System eigenvalues versus inductance when using the multiple-DOF system model for the integrated beam system. —— λ_1, ---- λ_2, ▬▬ λ_3, ▬ ▬ λ_4.

It has been shown that for the 2-DOF system (Figure 2.6 and Figure 2.7) the occurrence of eigenvalue curve veering is realized by an inductance tuning range with high sensitivity of damage-induced eigenvalue changes. In order to examine the case of a multiple-DOF system, we calculate the sensitivities of the damage-induced eigenvalue changes with respect to inductance L, as plotted in Figure 2.9 where (a)-(c) correspond to the first, second and third eigenvalue changes, respectively. The structural damage is assumed to be on the second beam element and the damage causes a 25% stiffness reduction. As shown in Figure 2.9(a), there is only one peak region indicating high sensitivity of the first eigenvalue change with respect to inductance tuning, and this region corresponds to eigenvalue curve veering between the first and second system eigenvalues. In Figure 2.9(b), two peak regions with high sensitivity of eigenvalue

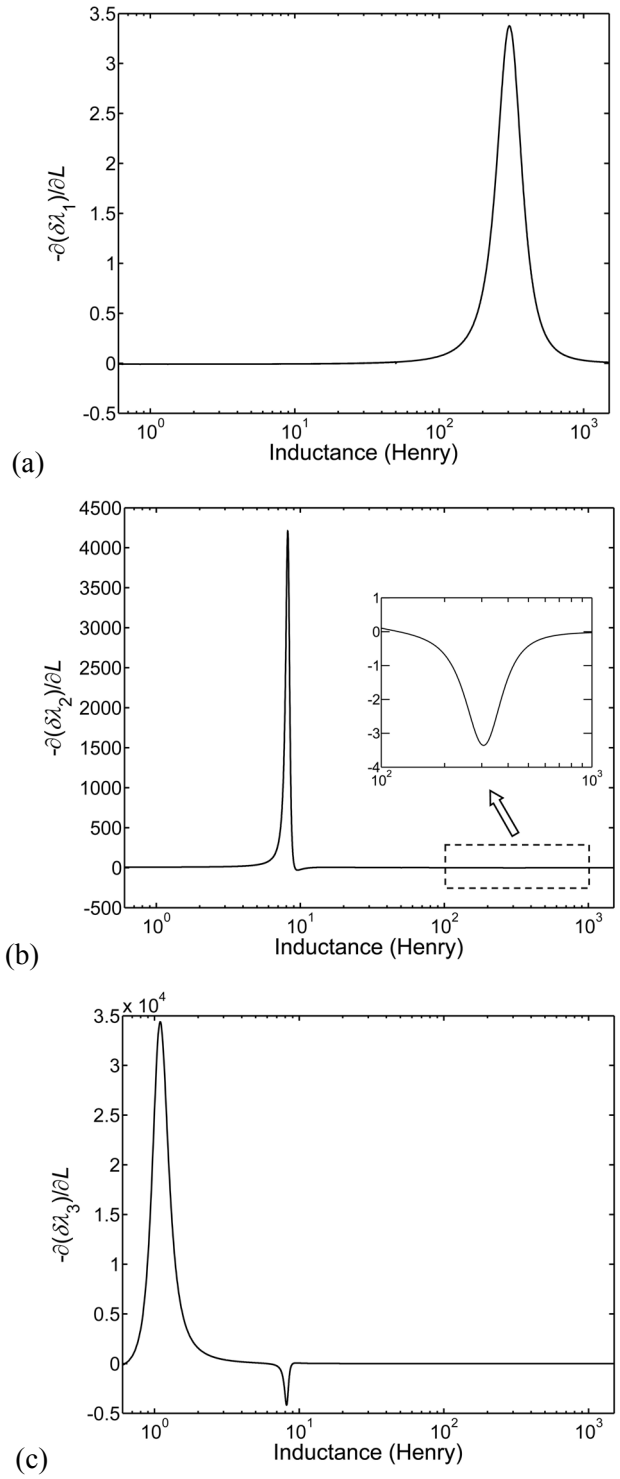

Figure **2.9**: Sensitivities of the damage-induced eigenvalue changes with respect to inductance when using the multiple-DOF system model for the integrated beam system: (a) Sensitivity of the first eigenvalue change; (b) Sensitivity of the second eigenvalue change; (c) Sensitivity of the third eigenvalue change.

change with respect to inductance tuning are found, and it is easy to verify that these two regions correspond to the eigenvalue curve veering between two pairs of system eigenvalues (the first and second, and the second and third), respectively. Similar conclusion can be drawn in Figure 2.9(c), where two peak regions with high sensitivity are achieved when the third system eigenvalue has curve veering with the second and fourth system eigenvalues.

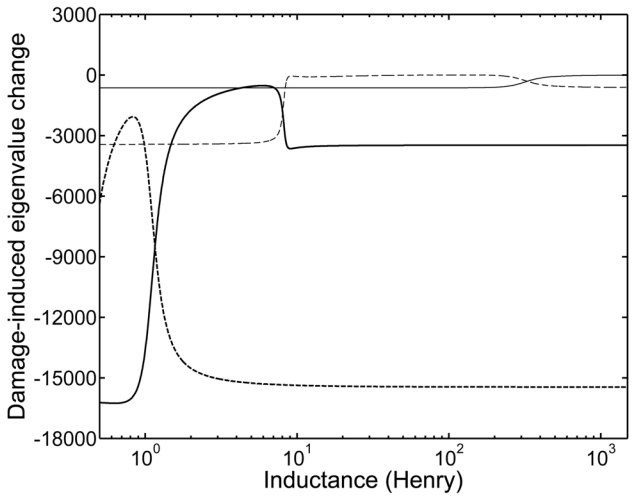

Figure 2.10: Variation of the damage-induced eigenvalue changes with respect to inductance when using the multiple-DOF system model for the integrated beam system. —— $\delta\lambda_1$, ---- $\delta\lambda_2$, ▬▬ $\delta\lambda_3$, ▬ ▬ ▬ ▬ $\delta\lambda_4$.

Figure 2.10 shows the variation of the damage-induced eigenvalue changes with respect to inductance tuning when the second element is damaged with a 25% stiffness reduction. If the inductance is tuned around each of the eigenvalue curve veering value, the damage-induced changes of the two system eigenvalues associated with the two loci in that curve veering vary significantly with respect to inductance. Therefore, if the inductance is tuned around values corresponding to eigenvalue curve veering, multiple sets of frequency-shift measurement with dramatically different sensitivity relations to

the damage can be obtained. Again, this will greatly enrich the modal data measurement available for damage identification.

2.4.2 Integrated System With Multiple Tunable Piezoelectric Circuitries

The previous example concerns the integration of a single tunable piezoelectric circuitry onto a homogeneous beam structure. For more complicated structures, it can be envisioned that multiple tunable circuitries could be more beneficial for damage identification. In this sub-section, we use a plate structure, as shown in Figure **2.11**, to explore the tuning of multiple tunable piezoelectric transducer circuitries. For this benchmark plate, the left edge of the plate is clamped and the other three edges have free boundary conditions. The plate is discretized into 25 elements, and the element numbers are labeled as shown in the figure. Three piezoelectric transducers are bonded onto the 7th, 13th and 19th elements, respectively. Each piezoelectric transducer patch has a size of 5 cm x 5 cm. Three piezoelectric circuitries with tunable inductances (L_1, L_2 and L_3) are integrated to the plate structure through three piezoelectric transducers, respectively. The parameters of the system including the plate structure and piezoelectric material are listed in Table **2.2**.

In the case of single piezoelectric circuitry, only one eigenvalue curve veering can be achieved under certain inductance tuning, and all other eigenvalues are much less affected. On the other hand, multiple piezoelectric transducer circuitries make it possible for multiple pairs of system eigenvalues to achieve curve veering simultaneously. Such multiple curve-veering phenomena could further enhance the system response sensitivity

with respect to inductance tunings. When multiple piezoelectric circuitries are integrated with the mechanical structure, these circuitries are not only directly coupled with the mechanical structure, but also coupled indirectly with other circuitries through energy exchange within the entire electro-mechanical integrated system. In other words, when tuning the inductance in one electric circuit, the interactions between the mechanical structure and other electric circuitries are also affected even if the inductances in those circuitries remain the same. Therefore, it is not feasible to tune each of the inductances separately. We need to tune these inductances simultaneously to achieve the desired set of eigenvalue curve veering concurrently. Since there are three tunable piezoelectric transducer circuitries in this plate example, these circuits can be tuned to accomplish at least three eigenvalue curve veerings. In each curve veering, one additional resonance frequency, due to the dynamics of one piezoelectric circuitry, is introduced into the frequency response function near the structural resonance frequency corresponding to that veering.

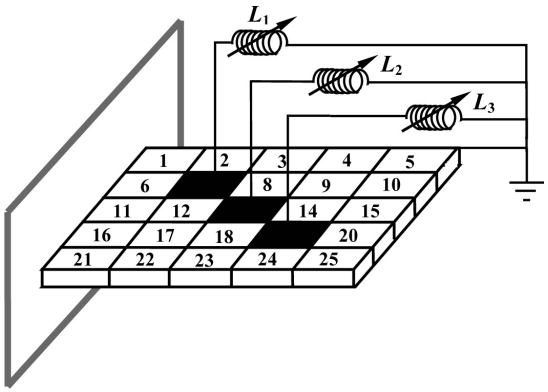

Figure 2.11: Configuration of a cantilevered plate integrated with multiple tunable piezoelectric transducer circuitries.

Table 2.2: System parameters for the integrated system of plate structure

Plate structure		Piezoelectric material	
Density:	$\rho_s = 2700\,\text{kg/m}^3$	Density:	$\rho_p = 7800\,\text{kg/m}^3$
Length:	$a = 0.25\,\text{m}$	Young's modulus:	$E_p = 6.9\times10^{10}\ \text{N/m}^2$
Width:	$b = 0.25\,\text{m}$	Thickness	$h_p = 0.25\,\text{mm}$
Thickness:	$h_s = 5\,\text{mm}$	Dielectric constant:	$\beta_{33} = 7.1445\times10^7\ \text{V}\cdot\text{m/C}$
Young's modulus:	$E_s = 30\times10^9\ \text{N/m}^2$	Piezoelectric constant:	$h_{31} = 7.664\times10^8\ \text{N/C}$
Element size:	$5\,\text{cm}\times5\,\text{cm}$	Patch size:	$5\,\text{cm}\times5\,\text{cm}$

Typically, clustered eigenvalues or close natural frequencies in a dynamic system are related to eigenvalue curve veering [128-132]. Indeed, the occurrence of close eigenvalues is an indication of eigenvalue curve veering and thus can be used as the criterion for tuning the inductances to realize multiple eigenvalue curve-veering phenomena. In this research, an optimization scheme is formulated to find the critical values of three inductances $\langle L_1^*, L_2^*, L_3^* \rangle$ which yield three pairs of close eigenvalues. That is, three eigenvalue curve veerings are realized simultaneously when the inductances are tuned around their respective critical values. The objective function to be minimized is defined as the summation of the difference between each pair of system eigenvalues that are targeted for eigenvalue curve veering.

2.4.2.1 Option 1 of Inductance Tuning

The integrated system has a large number of eigenvalues/natural frequencies, which can all be potential candidates for eigenvalue curve veering. We first formulate an

optimization problem to find the critical values of three inductances to achieve eigenvalue curve veerings between the 1st and 2nd eigenvalues, the 3rd and 4th eigenvalues, and the 5th and 6th eigenvalues respectively and simultaneously. The objective function is defined as

$$J_1 = \sum_{i=1}^{3} \left| \lambda_{2i-1} - \lambda_{2i} \right| \qquad (2.41)$$

By using the standard constrained minimum subroutine, FMINCON, provided by MATLAB, the minimization of the above objective function yields the following critical inductance values

$$L_1^* = 84.6\,\mathrm{H}\,,\ L_2^* = 1.91\,\mathrm{H}\,,\ L_3^* = 14.5\,\mathrm{H} \qquad (2.42)$$

Utilizing the above critical values as center values and expanding the inductance on both sides by $20.0\,\mathrm{H}$, $0.5\,\mathrm{H}$ and $4.0\,\mathrm{H}$, respectively, the tuning ranges for the three inductances can be formulated as

$$L_1 \in [64.6\,\mathrm{H}, 104.6\,\mathrm{H}],\ L_2 \in [1.41\,\mathrm{H}, 2.41\,\mathrm{H}],\ L_3 \in [10.5\,\mathrm{H}, 18.5\,\mathrm{H}] \qquad (2.43)$$

Figure 2.12 shows the variation of the first six eigenvalues with respect to inductance tuning. The horizontal axis only shows the change of the inductance L_3, while it should be noted that inductances L_1 and L_2 are actually tuned synchronously when tuning L_3 (This statement holds for all the following figures in the same category). It is shown in this figure that three eigenvalue curve veerings occur between the 1st and 2nd eigenvalues, the 3rd and 4th eigenvalues, and the 5th and 6th eigenvalues, respectively and simultaneously.

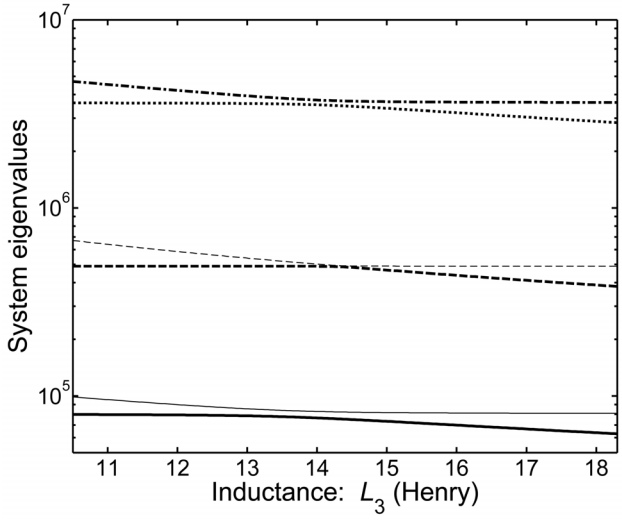

Figure **2.12**: System eigenvalues versus inductance L_3 for the integrated plate system when using option 1 of inductance tuning. —— λ_1, —— λ_2, - - - - λ_3, - - - - λ_4, ····· λ_5, -·-·- λ_6.

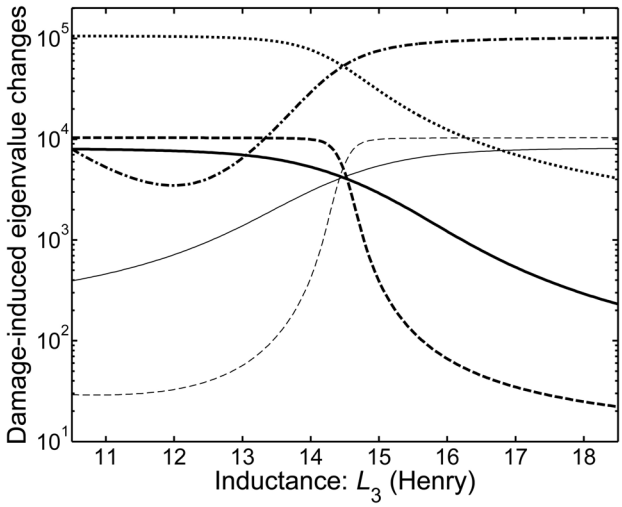

Figure **2.13**: Variation of the damage-induced eigenvalue changes with respect to inductance L_3 for the integrated plate system when using option 1 of inductance tuning. —— $(-\delta\lambda_1)$, —— $(-\delta\lambda_2)$, - - - - $(-\delta\lambda_3)$, - - - - $(-\delta\lambda_4)$, ····· $(-\delta\lambda_5)$, -·-·- $(-\delta\lambda_6)$.

Figure 2.13 shows the variation of the damage-induced eigenvalue changes with respect to inductance tuning inside the proposed inductance tuning ranges. The structural damages are assumed to result in 20%, 30%, 10%, and 20% of stiffness parameter reductions on the 6th, 11th, 12th, and 16th elements, respectively. It can be easily observed from the figure that the damage-induced changes of the three eigenvalue pairs vary significantly around the curve veering values of the inductances.

2.4.2.2 Option 2 of Inductance Tuning

In order to examine the general effect of eigenvalue curve veering, here we investigate an alternative option of inductance tuning, i.e., we aim at achieving eigenvalue curve veering between the 3rd and 4th eigenvalues, the 5th and 6th eigenvalues, and the 7th and 8th eigenvalues, respectively and simultaneously. The objective function is then defined as

$$J_2 = \sum_{i=1}^{3} \left| \lambda_{2i+1} - \lambda_{2i+2} \right| \tag{2.44}$$

The minimization of the above objective function yields

$$L_1^* = 0.96\,\mathrm{H}, \quad L_2^* = 1.25\,\mathrm{H}, \quad L_3^* = 1.91\,\mathrm{H} \tag{2.45}$$

The tuning ranges for three inductances can be determined as

$$L_1 \in [0.51\,\mathrm{H}, 1.41\,\mathrm{H}], \quad L_2 \in [0.65\,\mathrm{H}, 1.85\,\mathrm{H}], \quad L_3 \in [1.16\,\mathrm{H}, 2.66\,\mathrm{H}] \tag{2.46}$$

The variation of the 3rd, 4th, 5th, 6th, 7th and 8th system eigenvalues with respect to inductance tuning inside the proposed tuning ranges are shown in Figure 2.14. It can

be observed from this figure that the eigenvalue curve veerings are achieved not only between those desired pairs of system eigenvalues (the 3rd and 4th, the 5th and 6th, and the 7th and 8th), but also between the 4th and 5th, and the 6th and 7th system eigenvalues. The reason for this phenomenon is that the three circuitry modes are tuned to accomplish curve veerings with three twisting-bending modes (3rd-5th) of the plate structure, and the resonance frequencies of these twisting-bending modes are close to each other, which makes the veering more sensitive to inductance tuning. As a result, it now becomes possible for one eigenvalue to veer with its two adjacent eigenvalues successively inside the inductance tuning ranges.

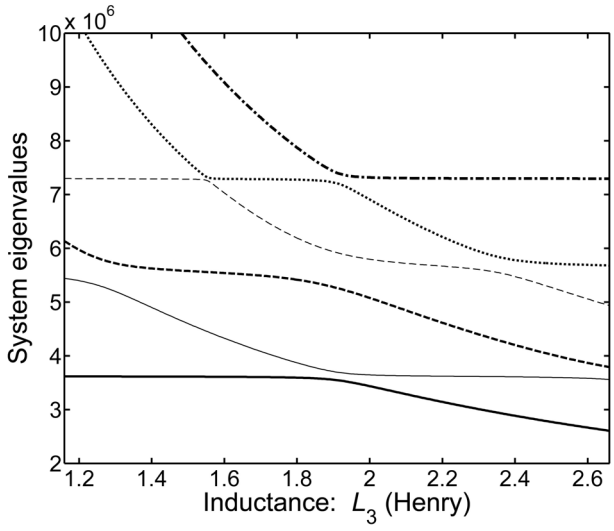

Figure 2.14: System eigenvalues versus inductance L_3 for the integrated plate system when using option 2 of inductance tuning. ——— λ_3, —— λ_4, - - - - λ_5, - - - - λ_6, ····· λ_7, -·-·- λ_8.

For the same damage scenario as used in Figure 2.13, the variations of the damage-induced eigenvalue changes with respect to inductance tuning inside the tuning ranges are plotted in Figure 2.15. It can be easily seen that the variation of the damage-

induced eigenvalue changes is more noticeable than that in Figure **2.13** produced (under tuning option 1), and the reason for this is that additional eigenvalue veerings occur under tuning option 2, as shown in Figure **2.14**. Overall, we can conclude that by integrating multiple tunable piezoelectric transducer circuitries to the mechanical structure being inspected, the frequency measurement data available for damage identification can be further enriched by formulating inductance tuning sequence to accomplish eigenvalue curve veering between different pairs of system eigenvalues.

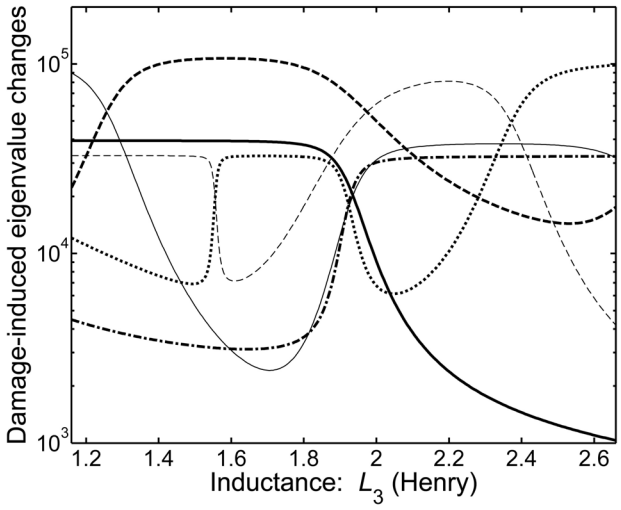

Figure **2.15**: Variation of the damage-induced eigenvalue changes with respect to inductance L_3 for the integrated plate system when using option 2 of inductance tuning. —— $(-\delta\lambda_3)$, —— $(-\delta\lambda_4)$, - - - - $(-\delta\lambda_5)$, - - - - $(-\delta\lambda_6)$, ····· $(-\delta\lambda_7)$, -·-·- $(-\delta\lambda_8)$.

2.5 Damage Identification Analyses and Case Studies

The preceding sections have outlined the basis of eigenvalue curve veerings under inductance tuning and illustrated such phenomena. In this section, we perform analyses on damage identification in beam and plate structures to demonstrate the performance

improvement with the proposed new methodology. Specifically, we will directly utilize the favorable inductance tuning results obtained in Section 2.4.

2.5.1 Damage Identification in Beam Structure With Single Tunable Piezoelectric Circuitry

The configuration of the integrated example system is shown in Figure 2.16. The cantilever beam is evenly divided into 10 elements. The piezoelectric transducer is bonded onto the upper surface of the beam from the second to the fourth element, and the piezoelectric transducer is connected in series to a tunable inductive circuit, a schematic of which is shown in Figure 2.1(b). All system parameters of the beam structure and piezoelectric material are listed in Table 2.1.

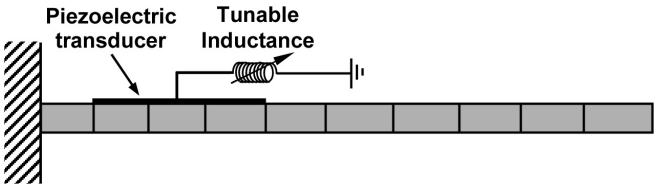

Figure 2.16: Cantilevered beam structure integrated with tunable piezoelectric transducer circuitry

The Young's modulus is assumed to be constant over each beam element and the elemental stiffness parameter of each beam element can be expressed as

$$G_i = E_b I_b (1 - \delta\alpha_i), \text{ where } i = 1, 2, \cdots, 10 \qquad (2.47)$$

where E_b and I_b are the Young's modulus and moment of inertia of the undamaged beam element, and $\delta\alpha_i$ denotes the damage-induced stiffness parameter reduction of the ith element.

The standard assembly process is used to construct the global mass and stiffness matrices of the beam structure, $\boldsymbol{M}_s \in \boldsymbol{R}^{20\times 20}$ and $\boldsymbol{K}_s \in \boldsymbol{R}^{20\times 20}$. Based on these global matrices, the first three modal frequencies of the cantilever beam without the tunable piezoelectric transducer circuitry are

$$\omega_1 = 96.51 \text{ rad/s}, \ \omega_2 = 578.58 \text{ rad/s}, \ \omega_3 = 1616.1 \text{ rad/s} \qquad (2.48)$$

After the integration of tunable piezoelectric transducer circuitry to the structure, one additional degree-of-freedom resulted from the charge flow in the circuit is added to the system, the electro-mechanical integrated system yields generalized mass and stiffness matrices, $\tilde{\boldsymbol{M}} \in \boldsymbol{R}^{21\times 21}$ and $\tilde{\boldsymbol{K}} \in \boldsymbol{R}^{21\times 21}$.

Table 2.3: First three resonant frequencies of the integrated system with respect to inductance

Inductance: L $(Henry)$	1st modal frequency: ω_1 (rad/s)	2nd modal frequency: ω_2 (rad/s)	3rd modal frequency: ω_3 (rad/s)
7.50	95.45	581.40	611.99
7.75	95.45	580.55	602.94
8.00	95.45	578.81	595.25
8.25	95.45	575.20	589.87
8.50	95.45	569.37	587.10
225	93.05	114.33	583.40
250	92.13	109.54	583.40
275	90.85	105.91	583.40
300	89.18	103.31	583.40
325	87.17	101.54	583.40

According to the analysis and results obtained in section 3.1, a favorable inductance tuning sequence can be selected as follows:

$$\boldsymbol{L} = [7.50 \quad 7.75 \quad 8.00 \quad 8.25 \quad 8.50 \quad 225 \quad 250 \quad 275 \quad 300 \quad 325]\ \text{H} \qquad (2.49)$$

In the above tuning sequence, the first 5 values are selected from the curve veering between the second and third system eigenvalues, and the last 5 values are selected from the curve veering between the first and second system eigenvalues. The first three resonant frequencies of the integrated system with respect to these inductance values are given in Table 2.3. From the table, it can be easily seen that the second and third modal frequencies of the integrated system vary significantly when the inductance is tuned around 8.0H, and the 1st and 2nd modal frequencies vary significantly when the inductance is tuned around 275H. Since the same structural damage will result in different frequency shifts for systems with different dynamic characteristics, clearly, much enriched information about frequency shifts can be expected with such tunable piezoelectric circuitry.

In order to illustrate the performance improvement of using tunable piezoelectric transducer circuitry network and verify the guidelines on favorable inductance tuning obtained in Section 2.4.1, here we compare the damage identification results under three different approaches: (1) traditional method (iterative second-order perturbation based algorithm without integration of tunable piezoelectric circuitry); (2) the proposed new method (iterative second-order perturbation based algorithm with integration of tunable piezoelectric circuitry) with *ad hoc* inductance tuning; and (3) the proposed new method with *favorable* inductance tuning. For a fair comparison, we assume that only the

frequencies below 1000 rad/sec are available for accurate measurement. This means that only the first two natural frequencies can be measured for damage identification when we use the traditional method without tunable piezoelectric circuitry, and only the first three modal frequencies, of which the additional one comes from the dynamics of the piezoelectric circuitry, are available when using the proposed new method.

Table **2.4**: Damage-induced modal frequency changes under inductance tuning

Inductance L (H)	1st modal frequency change: $\delta\omega_1$ (rad/s)	2nd modal frequency change: $\delta\omega_2$ (rad/s)	3rd modal frequency change: $\delta\omega_3$ (rad/s)
7.50	-3.42	-2.52	-0.69
7.75	-3.42	-2.27	-0.93
8.00	-3.42	-1.75	-1.44
8.25	-3.42	-0.90	-2.29
8.50	-3.42	-0.28	-2.90
225	-3.21	-0.19	-2.99
250	-3.02	-0.38	-2.99
275	-2.72	-0.68	-2.99
300	-2.32	-1.08	-2.99
325	-1.88	-1.51	-2.99

The first case we examine is to identify single element damage. The damage in the beam is assumed to be on the second element and results in a 25% stiffness reduction. The damage-induced natural frequency-shifts under 10 different inductance values specified in Eq. (**2.49**) are listed in Table **2.4**. From this table, we can see that the changes of the second and third natural frequencies vary significantly when the inductance is tuned at around $8.0\,\mathrm{H}$. Meanwhile, when the inductance is tuned at around

$275.0\,\mathrm{H}$, the changes of the first and second natural frequencies vary significantly. Compared to only one set of frequency-shifts when using the traditional method without tunable piezoelectric circuitry, we can now obtain as many sets of frequency-shift measurement as the number of tuned inductance sequence.

Figure **2.17** shows the predictions of structural damage by using the traditional method and the proposed new method with *ad hoc* and *favorable* inductance tuning. From this figure, we can see that the prediction using the traditional method has significant error because the major damage is predicted to be on the third element and the predicted damage severity of the second element is much less than the actual value. When the proposed new method with tunable piezoelectric circuitry is used, no obvious improvement is observed in the case of *ad hoc* inductance tuning ($L_i = 100 + 10 \times i$, where $i = 1, 2, \cdots, 10$), while a quite accurate prediction is achieved when using the *favorable* inductance tuning. This clearly demonstrates the necessity of employing the proposed tuning methodology.

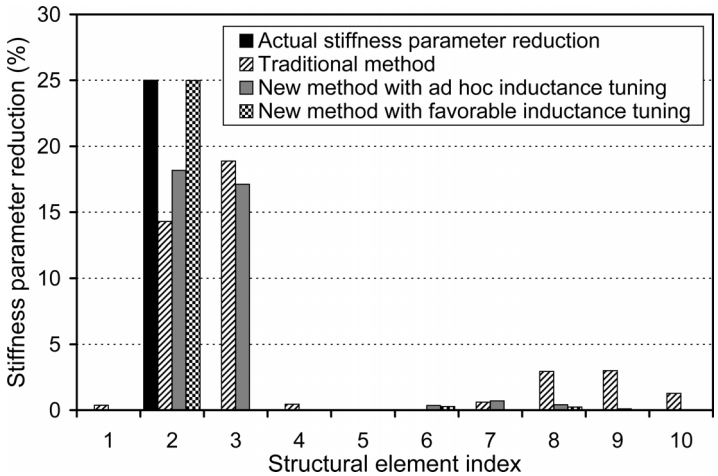

Figure **2.17**: Identification of structural damage on the second element of the beam structure

Another example of identifying single element damage is given in Figure **2.18**, where the actual structural damage is on the fifth element and causes 25% reduction of the elemental stiffness. As can be seen from the figure, the traditional method predicts major stiffness reductions on the fifth, sixth, seventh and eighth structural elements, and the prediction is not acceptable. When the proposed new method with *ad hoc* inductance tuning is used, a major damage is predicted on the fifth element and the prediction is much better than that of the traditional method; however, the predicted severity of the damage on the fifth element is much lower then the actual one, and a false damage is predicted on the seventh element. Finally, when we use the *favorable* inductance tuning given in Eq. (**2.49**), both the location and severity of the structural damage are accurately predicted.

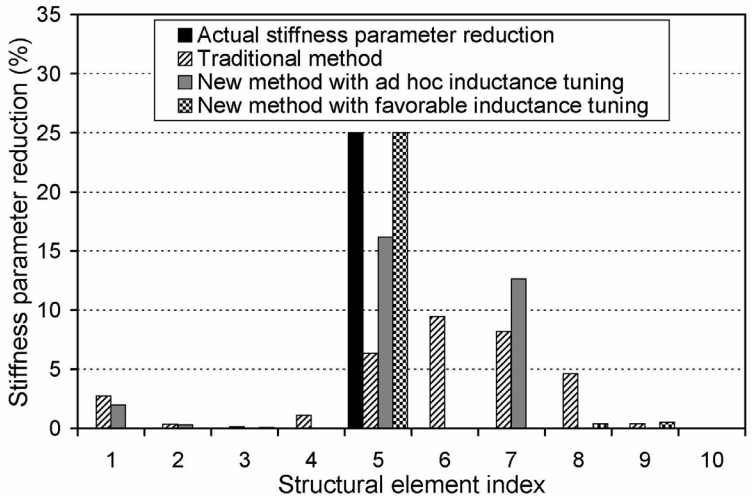

Figure **2.18**: Identification of structural damage on the fifth element of the beam structure

In order to quantitatively evaluate the performance of damage identification using different methods, the root-mean-square deviation (RMSD) between the predicted

stiffness parameter reduction using one specific method ($\delta\boldsymbol{\alpha}^{p}$) and the actual damage-induced stiffness parameter reduction ($\delta\boldsymbol{\alpha}^{a}$), is used as a metric to quantify the prediction

$$RMSD(\%) = \sqrt{\sum_{i=1}^{N_e}\left(\delta\alpha_i^{p} - \delta\alpha_i^{a}\right)^2 \Big/ \sum_{i=1}^{N_e}\left(\delta\alpha_i^{a}\right)^2} \times 100 \qquad (2.50)$$

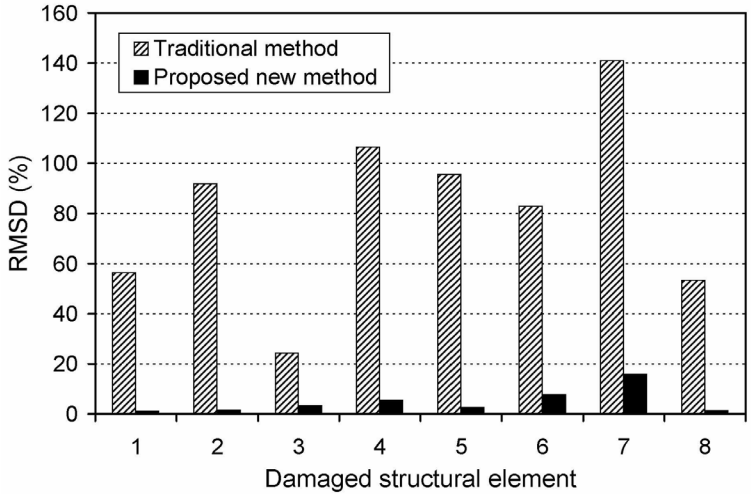

Figure 2.19: Comparison of RMSD for identifying single element damage in beam structure by using the tradition method and the proposed new method with favorable inductance tuning

A comparison of RMSD for identifying single element damage by using the traditional method and the proposed new method with *favorable* inductance tuning is provided in Figure 2.19. The horizontal axis indicates the index of the structural element that has damage, and it is assumed that the damage cause a 25% stiffness reduction of the corresponding element. That is, successively we let an element in the beam structure have a 25% stiffness loss damage in each case studied. The vertical axis indicates the RMSD between the predicted and actual stiffness parameter reduction. We can see that the RMSD of the predictions obtained from the traditional method has a maximum value

of 141% when identifying damage on the 7th element, and even the minimum value is larger than 24%. On the other hand, when the proposed new method with *favorable* inductance tuning is used, the RMSD of the obtained predictions are greatly reduced, with a maximum value 16% when identifying damage on the 7th element. It can be concluded that the proposed new method with *favorable* inductance tuning significantly outperforms the traditional method when it is used to identify single element damage.

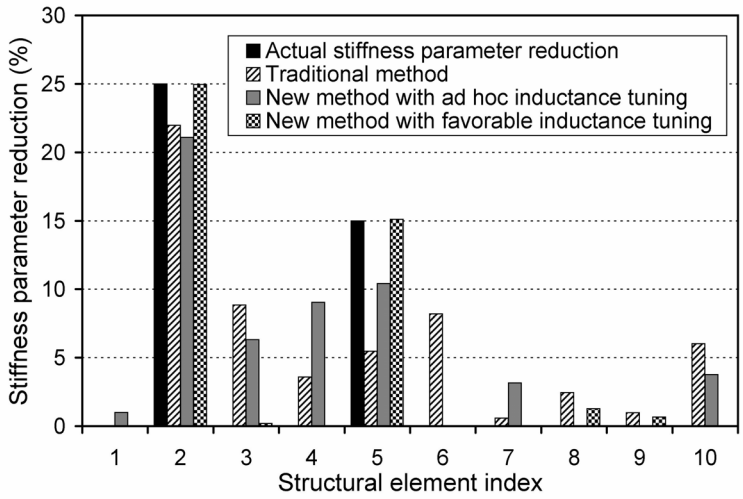

Figure **2.20**: Identification of structural damages on the second and fifth elements of the beam structure

The proposed method can be also used to detect multiple element damages in the beam structure. An example of damage identification is given in Figure **2.20**, where the actual structural damages are assumed to be on the 2nd and 5th elements with 25% and 15% damage-induced stiffness reductions, respectively. Neither the traditional method nor the new method with *ad hoc* inductance tuning gives an accurate prediction of the actual damage situation. When the proposed new method with the *favorable* inductance tuning is used, both the locations and severities of the two damages are accurately

predicted. In terms of the RMSD of the different methods, the prediction obtained from the traditional method results in a RMSD of 60%, and the predictions obtained from the proposed new method with *ad hoc* inductance tuning and *favorable* inductance tuning have RMSD errors of 45% and 5%, respectively.

2.5.2 Damage Identification in Plate Structure with Multiple Tunable Piezoelectric Circuitries

In this second case study, we will examine the performance improvement of using multiple tunable piezoelectric circuitries to detect damages in a more complicated plate structure, and we also compare the damage detection performance by using different tuning options. In this example, we assume that only the frequencies under 4000rad/sec are available for accurate measurement. Therefore, only the first five natural frequencies can be used for damage identification when we use the traditional method without tunable piezoelectric circuitry, and only the first eight modal frequencies, of which the additional three come from the inductance circuit connected to the piezoelectric transducer, are available when using the enhanced method with integration of tunable piezoelectric circuitry. According to the two tuning options derived in the previous section, the first set of inductance tuning sequence can be selected from the inductance tuning ranges obtained for tuning option 1,

$$\begin{Bmatrix} \boldsymbol{L}^{(1)} \\ \boldsymbol{L}^{(2)} \\ \boldsymbol{L}^{(3)} \\ \boldsymbol{L}^{(4)} \\ \boldsymbol{L}^{(5)} \end{Bmatrix} = \begin{bmatrix} L_1^{(1)} & L_2^{(1)} & L_3^{(1)} \\ L_1^{(2)} & L_2^{(2)} & L_3^{(2)} \\ L_1^{(3)} & L_2^{(3)} & L_3^{(3)} \\ L_1^{(4)} & L_2^{(4)} & L_3^{(4)} \\ L_1^{(5)} & L_2^{(5)} & L_3^{(5)} \end{bmatrix} = \begin{bmatrix} 78.6 & 1.51 & 14.00 \\ 81.6 & 1.61 & 14.15 \\ 84.6 & 1.71 & 14.30 \\ 87.6 & 1.81 & 14.45 \\ 90.6 & 1.91 & 14.60 \end{bmatrix} \text{H} \qquad (2.51)$$

A second set of inductance tuning sequence is selected from the inductance tuning ranges obtained for tuning option 2

$$\begin{Bmatrix} \boldsymbol{L}^{(1)} \\ \boldsymbol{L}^{(2)} \\ \boldsymbol{L}^{(3)} \\ \boldsymbol{L}^{(4)} \\ \boldsymbol{L}^{(5)} \end{Bmatrix} = \begin{bmatrix} L_1^{(1)} & L_2^{(1)} & L_3^{(1)} \\ L_1^{(2)} & L_2^{(2)} & L_3^{(2)} \\ L_1^{(3)} & L_2^{(3)} & L_3^{(3)} \\ L_1^{(4)} & L_2^{(4)} & L_3^{(4)} \\ L_1^{(5)} & L_2^{(5)} & L_3^{(5)} \end{bmatrix} = \begin{bmatrix} 0.51 & 0.65 & 1.16 \\ 0.71 & 0.95 & 1.56 \\ 0.91 & 1.25 & 1.96 \\ 1.16 & 1.55 & 2.36 \\ 1.41 & 1.85 & 2.66 \end{bmatrix} \text{H} \tag{2.52}$$

As shown in Figure 2.12 and Figure 2.14, respectively, each set of the inductance tuning sequence formulated above achieves one set of eigenvalue curve veerings between different pairs of system eigenvalues, and the ability of accomplishing multiple sets of eigenvalue curve veering is exactly the additional benefit offered by integrating multiple piezoelectric circuitries. Therefore, to utilize multiple sets of eigenvalue curve veering to further enrich the frequency measurement data for damage detection, the inductances should be tuned according to a combined inductance tuning sequence, which can be obtained by assembling the two sets of inductance tuning sequences in Eq. (2.51) and Eq. (2.52),

$$\begin{bmatrix} L_1^{(1)} & L_1^{(2)} & \cdots & L_1^{(10)} \\ L_2^{(1)} & L_2^{(2)} & \cdots & L_2^{(10)} \\ L_3^{(1)} & L_3^{(2)} & \cdots & L_3^{(10)} \end{bmatrix} = \begin{bmatrix} 78.6 & 81.6 & 84.6 & 87.6 & 90.6 & 0.51 & 0.71 & 0.91 & 1.16 & 1.41 \\ 1.51 & 1.61 & 1.71 & 1.81 & 1.91 & 0.65 & 0.95 & 1.25 & 1.55 & 1.85 \\ 14.00 & 14.15 & 14.30 & 14.45 & 14.60 & 1.16 & 1.56 & 1.96 & 2.36 & 2.66 \end{bmatrix} \text{H} \tag{2.53}$$

Unless otherwise specified, hereafter this combined inductance tuning sequence is used as the favorable tuning sequence in the proposed new method for damage identification.

The variation of the first eight natural frequencies with respect to inductance tuning sequence in Eq. (2.53) is shown in Table 2.5. In the first 5 rows in this table, the

first 6 natural frequencies vary significantly with respect to inductance tuning. This is because the corresponding inductance tuning sequence is selected from tuning option 1 where eigenvalue curve veering occur between the 1st and 2nd, the 3rd and 4th, and the 5th and 6th system eigenvalues. In the last 5 rows, the 3rd through the 8th natural frequencies vary significantly with respect to inductance tuning because the inductance tuning sequence is selected from tuning option 2 where eigenvalue curve veering occur between the 3rd through the 8th system eigenvalues.

Table 2.5: Natural frequencies of the integrated plate system with respect to inductance tuning

Inductance (Henry)			System natural frequencies (rad/s)							
L_1	L_2	L_3	ω_1	ω_2	ω_3	ω_4	ω_5	ω_6	ω_7	ω_8
78.6	1.51	14.00	281.46	299.38	698.57	704.98	1900.0	2132.4	2385.8	2700.2
81.6	1.61	14.15	280.70	294.64	697.85	702.14	1898.9	2070.5	2381.2	2700.2
84.6	1.71	14.30	279.34	290.76	694.98	701.43	1896.6	2014.0	2378.4	2700.0
87.6	1.81	14.45	277.11	288.05	692.10	700.71	1891.0	1964.7	2376.8	2700.0
90.6	1.91	14.60	273.99	286.44	688.48	700.71	1874.8	1930.3	2375.3	2700.0
0.51	0.65	1.16	283.23	699.86	1901.6	2331.1	2471.8	2700.9	3279.3	3689.9
0.71	0.95	1.56	283.23	699.86	1900.0	2101.9	2358.0	2698.3	2725.6	3130.8
0.91	1.25	1.96	283.23	699.86	1866.8	1912.1	2295.4	2434.7	2695.7	2771.6
1.16	1.55	2.36	283.23	699.86	1710.6	1901.1	2107.1	2373.0	2460.3	2701.5
1.41	1.85	2.66	283.23	699.86	1612.5	1887.1	1948.6	2215.6	2383.3	2700.7

The first example of damage detection is shown in Figure 2.21. The actual structural damages, denoted by the solid black bars in this figure, are assumed to be on the 11th, 16th, and 21st elements with 10%, 15%, and 20% stiffness reductions, respectively. The variation of damage-induced frequency shift with respect to inductance

tuning sequence is shown in Table **2.6**. Compared to only one set of frequency-shifts when using the traditional method without tunable piezoelectric circuitry, we can now obtain as many sets of frequency-shift measurement as the number of tuned inductance sequence. As shown in Figure **2.21**, the prediction by using the traditional method has a significant RMSD error of 86%, which is not acceptable. Although the new method with *ad hoc* inductance tuning ($\tilde{L}_1^{(i)} = (i)$ H, $\tilde{L}_2^{(i)} = (2\times i - 1)$ H, $\tilde{L}_3^{(i)} = (3\times i - 2)$ H, where $i = 1, 2, \cdots, 10$) successfully locates all three damaged elements, the predicted damage severities are not accurate and have a RMSD error of 28%. When the new method with *favorable* inductance tuning is used, the three locations of the structural damages are exactly identified, and the predicted damage severities are very close to the actual stiffness parameter reductions. The RMSD error of the prediction by using the *favorable* inductance tuning is only 2%.

A second example of detecting damages in the plate structure is given in Figure **2.22**, where the actual structural damages are assumed to be on the first, seventh and thirteenth elements with 25%, 15% and 10% stiffness reduction, respectively. The prediction obtained from the traditional method, which yield a RMSD error of 90.5%, is not acceptable. Although the new method with *ad hoc* inductance tuning gives better prediction, the associated RMSD error of the prediction is still as high as 77.7%. When the proposed new method with *favorable* inductance tuning is used, both of the locations and severities of all three element damages are accurately identified. The RMSD error of the prediction by the proposed new method with *favorable* inductance tuning is as low as 1.2%.

Table 2.6: Damage-induced natural frequency changes of the integrated plate system with respect to inductance tuning. The damages are assumed to cause 10%, 15% and 20% stiffness reductions on the 11th, 16th and 21st elements, respectively.

Inductance (Henry)			Damage-induced natural frequency changes (rad/s)							
L_1	L_2	L_3	$\delta\omega_1$	$\delta\omega_2$	$\delta\omega_3$	$\delta\omega_4$	$\delta\omega_5$	$\delta\omega_6$	$\delta\omega_7$	$\delta\omega_8$
78.6	1.51	14.00	-7.62	-0.67	-8.64	-0.71	-23.57	-0.94	-7.56	-24.55
81.6	1.61	14.15	-7.18	-1.12	-7.93	-1.43	-23.58	-0.97	-7.78	-24.55
84.6	1.71	14.30	-6.34	-1.95	-5.05	-4.29	-23.08	-1.49	-7.79	-24.37
87.6	1.81	14.45	-4.97	-3.35	-2.89	-6.45	-21.00	-3.06	-8.22	-24.37
90.6	1.91	14.60	-3.29	-5.00	-0.73	-8.62	-14.46	-9.87	-8.01	-24.56
0.51	0.65	1.16	-8.28	-9.28	-24.08	-6.66	-1.62	-24.55	-0.15	-0.27
0.71	0.95	1.56	-8.28	-9.28	-23.83	-0.48	-7.65	-23.82	-1.28	-0.32
0.91	1.25	1.96	-8.28	-9.28	-8.86	-14.96	-4.36	-4.11	-23.85	-1.08
1.16	1.55	2.36	-8.28	-9.28	-0.29	-23.29	-0.95	-6.75	-1.22	-24.36
1.41	1.85	2.66	-8.28	-9.27	-0.31	-19.17	-5.14	-0.68	-7.78	-24.55

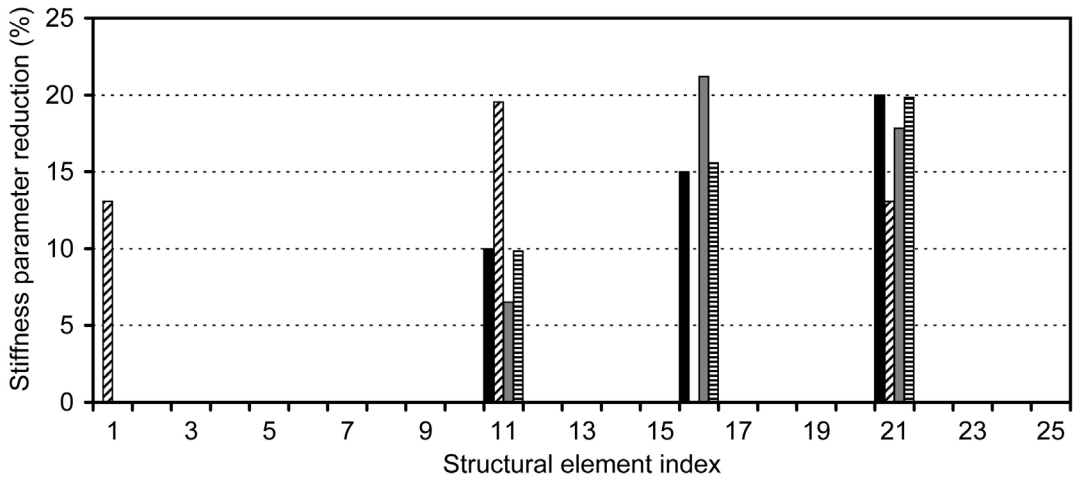

Figure 2.21: Identification of damages on the 11th, 16th and 21st elements of the plate structure with 10%, 15% and 20% stiffness parameter reductions, respectively. ■ Actual stiffness parameter reduction, ▨ Prediction using the traditional method, ▩ Prediction using the new method with ad hoc inductance tuning, ▤ Prediction using the new method with favorable inductance tuning.

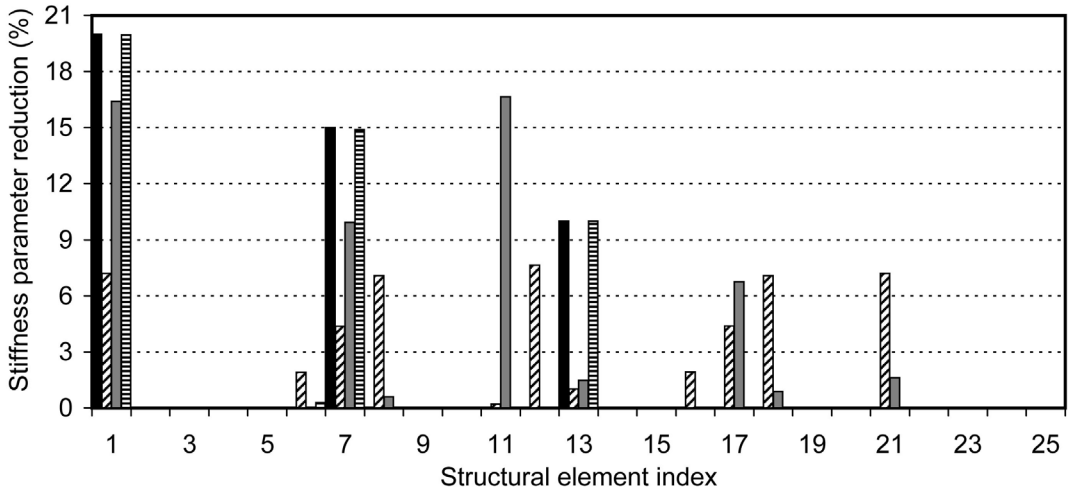

Figure 2.22: Identification of damages on the 1st, 7th and 13th elements of the plate structure with 20%, 15% and 10% stiffness parameter reductions, respectively. ■ Actual stiffness parameter reduction, ▨ Prediction using the traditional method, ■ Prediction using the new method with ad hoc inductance tuning, ▤ Prediction using the new method with favorable inductance tuning.

In order to further examine the effects of inductance tuning sequence on the performance of damage detection, the predictions using three different sets of inductance tuning sequences are compared in Figure 2.23. The first set of inductance tuning sequence is selected from tuning option 1, as shown in Eq. (2.51), the second set of tuning sequence is selected from tuning option 2, as shown in Eq. (2.52), and the third set is the combination of the first two sets, as given by Eq. (2.53). As shown in the Figure 2.23, the locations of the three damaged elements are accurately predicted by using any set of the inductance tuning sequence. However, the predicted severities of the three damages have a RMSD error of 22% when using the tuning option 1. When tuning option 2 is used, the predicted severities are much more accurate and the prediction error in terms of RMSD decreases to 7%. The performance improvement is not only because the eigenvalue curve veering is achieved for high order system eigenvalues which are

usually more sensitive to structural damage than low eigenvalues, but also because of the more noticeable variation of damage-induced eigenvalue change with respect to inductance tuning as shown in Figure **2.15**. Finally, when the combined tuning sequence is used, the accuracy of the predicted damage severity is further improved with a prediction error of 2%.

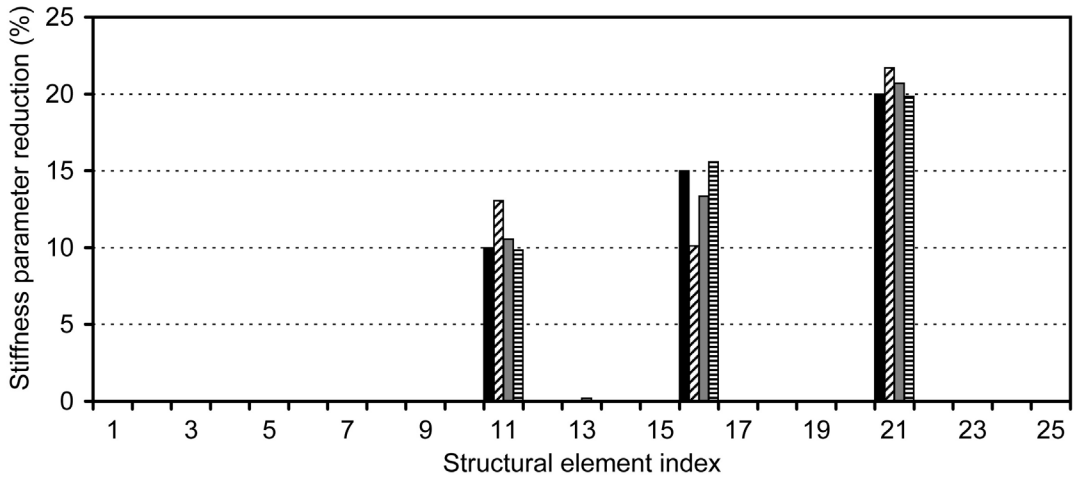

Figure **2.23**: Effects of different inductance tuning sequences on the performance of damage identification for the plate structure. ■ Actual stiffness parameter reduction, ▨ Prediction using tuning option 1, ▩ Prediction using tuning option 2, ▤ Prediction using the combined tuning option.

The above case study clearly demonstrates the merits of using multiple piezoelectric transducer circuitries to detect damage. To best benefit the damage identification process, the *favorable* inductance tuning sequence for the tunable piezoelectric circuitry network can be formed by accomplishing a "comprehensive" set of eigenvalue curve veering in the sense that each of the measurable modal frequencies is under curve veering at least once.

2.6 Summary

In this chapter, an enhanced frequency-shift-based damage identification method using tunable piezoelectric transducer circuitry is developed. The key idea is to use tunable piezoelectric circuitries coupled to the mechanical structure to favorably alter the dynamics of the electro-mechanical integrated system. First, the circuitry can be tailored to change the system frequency/modal distribution by introducing additional resonant frequencies and vibration modes. Second, through tuning the circuitry elements (i.e., the inductors), one can obtain a much enlarged dataset consisting of a *family* of frequency response functions (under different circuitry tunings) as compared to the original single frequency response of the mechanical structure without circuit. Guidelines on favorable inductance tuning that can yield the optimal damage identification performance are also developed. Analyses show that when the inductances are tuned to accomplish eigenvalue curve veerings between system eigenvalue pairs, the enriched frequency measurement data can most effectively capture the damage information. An iterative second-order perturbation based algorithm is developed to find the damaged-induced stiffness parameter reduction based on the system eigenvalue changes (frequency shift) before and after the structural damage occurred. The major advantage of using this algorithm is that it takes into account the damage-induced mode shape changes without the actual measurement of the modes. Numerical analyses and case studies on benchmark beam and plate structures are carried out to demonstrate and verify the proposed new method. Numerical results show that the damage identification performance can be significantly improved by using the proposed new approach with favorable inductance tuning.

Chapter 3

Optimal Sensitivity-Enhancing Feedback Control via Eigenstructure Assignment for Structural Damage Identification

3.1 Introduction

As described in the section of problem statement in Chapter 1, the frequency-shift-based damage identification methods encounter two major limitations: deficiency of frequency measurement data and low sensitivity of frequency shift to damage effects [105]. To tackle the issue of insufficient number of frequency measurement data, various techniques such as "twin" structure technique [110], mass/stiffness addition technique [111,112], and virtual passive controller approach [113], have been proposed in the literature. In Chapter 2, a new concept of integrating tunable piezoelectric transducer circuitry to the original structure to enrich frequency measurement data has been proposed. Compared with other techniques proposed in the literature, this new technique has certain advantages toward the implementation in real applications. For example, the electrical tailoring used in this approach is much easier to realize than the mechanical tailoring used in mass/stiffness addition technique [111,112], and it does not require a complicated sensor-actuator-controller architecture and significant external power source that are necessary for the virtual passive controller approach [113]. However, similar to those previous techniques in the literature, although this approach can effectively solve the problem of insufficient frequency measurement data, it has not explicitly addressed another severe issue of frequency-shift-based damage identification methods, namely,

low sensitivity of frequency shift to damage effects. Therefore, this chapter aims to develop a new approach that can simultaneously overcome the aforementioned two limitations of frequency-shift-based damage identification methods.

To address the sensitivity issue of frequency-shift-based damage identification methods, a new concept of sensitivity-enhancing control (SEC) was introduced by Ray and Tian [**133**]. The basic idea is to use feedback control to place the closed-loop natural frequencies at appropriate locations such that their sensitivities toward mass/stiffness damage can be enhanced. Using a cantilevered beam example, they developed a control law to enhance the detection sensitivity by reducing the first three natural frequencies using a single point force actuator. Later, this concept was validated through a laboratory experiment [**134**]. More recently, Koh and Ray [**135**] advanced this concept by applying sensitivity-enhancing control to multi-input systems. A minimum-gain eigenstructure assignment method is used to design the multi-input control laws. In that study, it has also been shown that multiple independent closed-loop systems can be obtained by developing a series of sensitivity-enhancing controls, and these multiple closed-loop systems will lead to a much enlarged dataset of frequency measurement, which will significantly improve the performance of frequency-shift-based damage identification.

Although the aforementioned studies have shown promising features for improving the performance of frequency-shift-based methods, certain important issues have not been addressed. While it has been theoretically shown that reducing/increasing the closed-loop natural frequency can enhance the sensitivity toward stiffness/mass damage in a single DOF system [**133**], it becomes less obvious in a multiple-DOF system. In previous studies, either a pole placement technique or a minimum-gain

eigenstructure assignment technique is used to design the feedback controller with the purpose of reducing the closed-loop eigenvalues to desired positions, whereas the role of the closed-loop eigenvectors has not been considered. On the other hand, it is well-known that, with multiple control inputs/actuators, one may have the freedom of assigning closed-loop eigenvalues and eigenvectors simultaneously. The possibility of using eigenvector assignment to further enhance the frequency-shift sensitivity has not been explored.

The objective of this research is to advance the state-of-the-art of sensitivity-enhancing feedback control for damage identification by developing a new eigenstructure assignment based approach. Eigenvalue sensitivity analysis of a multi-DOF system indicates that the closed-loop eigenvalue sensitivity depends on both the closed-loop eigenvalues and eigenvectors. Therefore, optimal assignment of eigenvalues and eigenvectors need to be performed to achieve the best sensitivity enhancement result. In this research, the classical eigenvector assignment via the singular value decomposition (SVD) technique is utilized for the process of eigenstructure assignment, and a constrained optimization problem is formulated to find the closed-loop control law. On the other hand, similar to the strategy presented in Ref. [**135**], different feedback control gains designed by activating different combinations of actuators result in a series of sensitivity enhanced closed-loop systems, which lead to a much enlarged dataset of frequency measurement for damage identification. The effectiveness of the methodology is demonstrated through numerical studies on a beam structure example. The importance of closed-loop eigenvector assignment to the sensitivity enhancement is demonstrated.

The improvement of damage identification performance by using the proposed approach is verified, and the effect of measurement noise is examined.

3.2 Concept of Sensitivity-Enhancing Feedback Control

In this section, the underlying mechanism of sensitivity-enhancing feedback control is outlined using a single degree-of-freedom (DOF) system and then expanded to a multiple-DOF system based on eigenvalue sensitivity analysis of the closed-loop system.

3.2.1 Sensitivity-Enhancing Feedback Control for Single DOF System

The concept of sensitivity-enhancing feedback control for structural damage identification was initially introduced by Ray and Tian [133]. The key idea is to enhance the sensitivity of (closed-loop) natural frequencies with respect to changes in structural parameters by using feedback control. In Ref. [133], a single DOF system is used to illustrate this concept. Consider a lightly-damped second-order system,

$$\begin{bmatrix} \dot{x} \\ \ddot{x} \end{bmatrix} = \begin{bmatrix} 0 & 1 \\ -k/m & -b/m \end{bmatrix} \begin{bmatrix} x \\ \dot{x} \end{bmatrix} + \begin{bmatrix} 0 \\ 1/m \end{bmatrix} u \tag{3.1}$$

For the original structure, the sensitivity of the natural frequency ω_n to changes in stiffness parameter (k) and mass parameter (m) are, respectively,

$$\frac{\partial \omega_n}{\partial k} = \frac{\omega_n}{2k} = \frac{1}{2\sqrt{mk}} \tag{3.2}$$

$$\frac{\partial \omega_n}{\partial m} = -\frac{\omega_n}{2m} = -\frac{\sqrt{k}}{2\sqrt{m^3}} \tag{3.3}$$

Applying feedback control with control input $u = -\begin{bmatrix} K_1 & K_2 \end{bmatrix}\begin{bmatrix} x & \dot{x} \end{bmatrix}^T$ to the original structure, we then obtain a closed-loop system. The natural frequency of the closed-loop system is $\omega_n^c = \sqrt{(k+K_1)/m}$, and its sensitivities with respect to stiffness and mass changes can be solved as, respectively,

$$\frac{\partial \omega_n^c}{\partial k} = \frac{\omega_n^c}{2(k+K_1)} = \frac{1}{2\sqrt{m(k+K_1)}} \tag{3.4}$$

$$\frac{\partial \omega_n^c}{\partial m} = -\frac{\omega_n^c}{2m} = -\frac{\sqrt{(k+K_1)}}{2\sqrt{m^3}} \tag{3.5}$$

Comparing Eq. (3.4) with Eq. (3.2) and Eq. (3.5) with Eq. (3.3), we may readily conclude that the sensitivity of the closed-loop natural frequency to the stiffness change can be enhanced by letting the control gain K_1 be negative ($-k < K_1 < 0$), thus reducing the natural frequency, and one should increase the natural frequency (let K_1 be positive) to enhance the sensitivity to the mass change.

3.2.2 Sensitivity-Enhancing Feedback Control for Multi-DOF System

While the illustration of sensitivity-enhancing feedback control in a single DOF system is straightforward, applying this idea to a multiple-DOF system with multiple inputs is more intriguing. In what follows, we will extend the concept of sensitivity-enhancing feedback control to a multiple-DOF system with multiple inputs based on

eigen-solution sensitivity analysis of the corresponding closed-loop system. For such a system, the equation of motion can be written as

$$\boldsymbol{M}\ddot{\boldsymbol{x}} + \boldsymbol{C}\dot{\boldsymbol{x}} + \boldsymbol{K}\boldsymbol{x} = \bar{\boldsymbol{B}}_1\boldsymbol{u} + \bar{\boldsymbol{B}}_0\boldsymbol{f} \tag{3.6}$$

where $\boldsymbol{M} \in \Re^{n\times n}$, $\boldsymbol{C} \in \Re^{n\times n}$ and $\boldsymbol{K} \in \Re^{n\times n}$ are the mass, damping, and stiffness matrices, respectively, and $\bar{\boldsymbol{B}}_1 \in \Re^{n\times r}$ and $\bar{\boldsymbol{B}}_0 \in \Re^{n\times p}$ are the input matrices of control action $\boldsymbol{u}$ and the external disturbance $\boldsymbol{f}$, respectively. For the open-loop system without control, the eigenvalue problem is given as

$$\left(\lambda_j^2\boldsymbol{M} + \lambda_j\boldsymbol{C} + \boldsymbol{K}\right)\boldsymbol{u}_j = \boldsymbol{0} \tag{3.7}$$

where λ_j and $\boldsymbol{u}_j$ are the *j*th eigenvalue and eigenvector of the open-loop system. If we assume that the damping is sufficiently small and thus can be neglected, the sensitivity of the open-loop eigenvalue λ_j with respect to a structural parameter α can be expressed as

$$\frac{\partial\lambda_j}{\partial\alpha} = -\frac{\lambda_j\boldsymbol{u}_j^T\dfrac{\partial\boldsymbol{M}}{\partial\alpha}\boldsymbol{u}_j}{2\boldsymbol{u}_j^T\boldsymbol{M}\boldsymbol{u}_j} - \frac{\boldsymbol{u}_j^T\dfrac{\partial\boldsymbol{K}}{\partial\alpha}\boldsymbol{u}_j}{2\lambda_j\boldsymbol{u}_j^T\boldsymbol{M}\boldsymbol{u}_j} \tag{3.8}$$

Let the control input be

$$\boldsymbol{u} = \boldsymbol{K}_{c1}\boldsymbol{x} + \boldsymbol{K}_{c2}\dot{\boldsymbol{x}} \tag{3.9}$$

where $\boldsymbol{K}_{c1} \in \Re^{r\times n}$ and $\boldsymbol{K}_{c2} \in \Re^{r\times n}$ are the control gain matrices corresponding to the displacement and velocity vectors, respectively. The equation of motion of the closed-loop system is given as

$$\boldsymbol{M}\ddot{\boldsymbol{x}} + \tilde{\boldsymbol{C}}\dot{\boldsymbol{x}} + \tilde{\boldsymbol{K}}\boldsymbol{x} = \bar{\boldsymbol{B}}_0\boldsymbol{f} \tag{3.10}$$

where the closed-loop damping and stiffness matrices are, respectively,

$$\tilde{\boldsymbol{C}} = \left[\boldsymbol{C} - \bar{\boldsymbol{B}}_1 \boldsymbol{K}_{c2} \right] \tag{3.11}$$

$$\tilde{\boldsymbol{K}} = \left[\boldsymbol{K} - \bar{\boldsymbol{B}}_1 \boldsymbol{K}_{c1} \right] \tag{3.12}$$

Clearly, these closed-loop matrices may no longer be symmetric. Due to this asymmetric property, both the right and left eigenvectors will be involved in the eigen-solution sensitivity analysis [136-138]. The right and left eigenvalue problems of the closed-loop damped system can be written as, respectively,

$$\left[\left(\lambda_j^c \right)^2 \boldsymbol{M} + \lambda_j^c \tilde{\boldsymbol{C}} + \tilde{\boldsymbol{K}} \right] \boldsymbol{u}_j^c = \boldsymbol{0} \tag{3.13}$$

$$\left(\boldsymbol{v}_j^c \right)^T \left[\left(\lambda_j^c \right)^2 \boldsymbol{M} + \lambda_j^c \tilde{\boldsymbol{C}} + \tilde{\boldsymbol{K}} \right] = \boldsymbol{0} \tag{3.14}$$

where λ_j^c, $\boldsymbol{u}_j^c$ and $\boldsymbol{v}_j^c$ are the jth eigenvalue and the corresponding right and left eigenvectors of the closed-loop system. Taking the derivative of Eq. (3.13) with respect to structural parameter α and utilizing Eq. (3.14), we may obtain the sensitivity of the closed-loop eigenvalue λ_j^c with respect to α as

$$\frac{\partial \lambda_j^c}{\partial \alpha} = - \frac{\left(\boldsymbol{v}_j^c \right)^T \left[\left(\lambda_j^c \right)^2 \dfrac{\partial \boldsymbol{M}}{\partial \alpha} + \lambda_j^c \dfrac{\partial \tilde{\boldsymbol{C}}}{\partial \alpha} + \dfrac{\partial \tilde{\boldsymbol{K}}}{\partial \alpha} \right] \boldsymbol{u}_j^c}{\left(\boldsymbol{v}_j^c \right)^T \left[2 \lambda_j^c \boldsymbol{M} + \tilde{\boldsymbol{C}} \right] \boldsymbol{u}_j^c} \tag{3.15}$$

Note that for a given feedback controller, the control input matrix ($\bar{\boldsymbol{B}}_1$) and control gain matrices ($\boldsymbol{K}_{c1}$ and $\boldsymbol{K}_{c2}$) in Eqs. (3.11) and (3.12) do not change with the variation of α. Therefore, we have

$$\frac{\partial \tilde{\boldsymbol{C}}}{\partial \alpha} = \frac{\partial \boldsymbol{C}}{\partial \alpha} \tag{3.16}$$

$$\frac{\partial \tilde{\boldsymbol{K}}}{\partial \alpha} = \frac{\partial \boldsymbol{K}}{\partial \alpha} \tag{3.17}$$

Thus, Eq. (3.15) can be rewritten as

$$\frac{\partial \lambda_j^c}{\partial \alpha} = -\frac{\left(\boldsymbol{v}_j^c\right)^T \left[\left(\lambda_j^c\right)^2 \frac{\partial \boldsymbol{M}}{\partial \alpha} + \lambda_j^c \frac{\partial \boldsymbol{C}}{\partial \alpha} + \frac{\partial \boldsymbol{K}}{\partial \alpha}\right] \boldsymbol{u}_j^c}{\left(\boldsymbol{v}_j^c\right)^T \left[2\lambda_j^c \boldsymbol{M} + \tilde{\boldsymbol{C}}\right] \boldsymbol{u}_j^c} \tag{3.18}$$

Since the system eigenvalue is usually complex, we may have $\lambda_j^c = -\sigma_j^c + i\omega_j^c$, with the real part indicting the damping effect and the imaginary part indicating the modal/natural frequency ($\sigma_j^c \ll \omega_j^c$ for a lightly-damped system). The imaginary part of Eq. (3.18) represents the sensitivity of modal frequency ω_j^c to structural parameter α,

$$\frac{\partial \omega_j^c}{\partial \alpha} = \mathrm{Im}\left[\frac{\partial \lambda_j^c}{\partial \alpha}\right] \tag{3.19}$$

while the real part $\mathrm{Re}\left[\partial \lambda_j^c / \partial \alpha\right]$ represents the sensitivity of closed-loop damping effect to the variation of α.

From Eqs. (3.18) and (3.19), we can see that for a multiple-DOF system, the sensitivity of the closed-loop natural frequency change with respect to the mass or stiffness parameter variation not only depends on the closed-loop eigenvalue (λ_j^c), but also depends on the eigenvectors of the closed-loop system ($\boldsymbol{u}_j^c$ and $\boldsymbol{v}_j^c$). In other words, the sensitivity of natural frequency change to structural parameter variation can be enhanced by appropriately assigning the closed-loop eigenvalues and eigenvectors. Note

that with this observation, we have extended beyond the conclusions from previous investigations on single DOF structures [133]. If we assume that the damping is sufficiently small so that the contribution of the damping matrix to eigenvalue sensitivity can be neglected, Eq. (3.18) can be approximated as

$$\lambda_{j,\alpha}^{c} \approx -\frac{\lambda_j^c \left(\boldsymbol{v}_j^c\right)^T \boldsymbol{M}_{,\alpha} \boldsymbol{u}_j^c}{2\left(\boldsymbol{v}_j^c\right)^T \boldsymbol{M}\boldsymbol{u}_j^c} - \frac{\left(\boldsymbol{v}_j^c\right)^T \boldsymbol{K}_{,\alpha} \boldsymbol{u}_j^c}{2\lambda_j^c \left(\boldsymbol{v}_j^c\right)^T \boldsymbol{M}\boldsymbol{u}_j^c} \tag{3.20}$$

Compare Eq. (3.20) with Eq. (3.8). If we assume that the closed-loop eigenvectors are kept the same (or as close as possible) as those of the open-loop system, the sensitivity of the closed-loop natural frequency with respect to stiffness change can be enhanced by reducing the closed-loop eigenvalue λ_j^c, while increasing the closed-loop eigenvalue λ_j^c results in enhancement of sensitivity with respect to mass change. Under such a condition, the observation coincides with conclusions from previous studies [133].

3.3 Sensitivity-Based Damage Identification Using Closed-Loop Natural Frequency Measurements

In general, damage occurring in the structure will change the mass or stiffness properties and hence the dynamic characteristics of the global structural response. Given a healthy structure with equation of motion shown in Eq. (3.6), we may assume that the structural damage induces the following structural parameter variation

$$\delta\alpha_i = \alpha_i^d - \alpha_i^h \quad (i = 1, 2, \cdots, n_e) \tag{3.21}$$

where α_i^h and α_i^d are the structure parameter values before and after damage occurrence,

and n_e represents the number of structural parameters required to characterize the damage occurrence. The mass and stiffness matrices of the damaged structure can then be expressed as the summation of their corresponding model matrices of the undamaged (healthy) structure and first-order perturbations with respect to structural parameters (α_i)

$$\boldsymbol{M}^d = \boldsymbol{M}^h + \sum_{i=1}^{n_e} \delta\alpha_i \frac{\partial \boldsymbol{M}^h}{\partial \alpha_i} \tag{3.22}$$

$$\boldsymbol{K}^d = \boldsymbol{K}^h + \sum_{i=1}^{n_e} \delta\alpha_i \frac{\partial \boldsymbol{K}^h}{\partial \alpha_i} \tag{3.23}$$

For a given closed-loop control applied to the structure, the damage-induced changes of the closed-loop natural frequencies can be denoted as

$$\delta\omega_j^c = {}^d\omega_j^c - {}^h\omega_j^c \quad (j = 1, 2, \cdots, q) \tag{3.24}$$

where ${}^h\omega_j^c$ and ${}^d\omega_j^c$ are measured natural frequencies of the closed-loop systems associated with the healthy and damaged structures, respectively, and q represents the number of measurable natural frequencies from the frequency response functions. A first-order approximation can be used to linearize the nonlinear relation between $\delta\omega_j^c$ and $\delta\alpha_i$ $(i = 1, 2, \cdots, n_e)$,

$$\delta\omega_j^c = \sum_{i=1}^{n_e} \frac{\partial \omega_j^c}{\partial \alpha_i} \delta\alpha_i \tag{3.25}$$

By collecting the equations for all measurable natural frequencies of the closed-loop system, a first-order sensitivity-based equation in the matrix form can be obtained as follows:

$$\begin{Bmatrix} \delta\omega_1^c \\ \delta\omega_2^c \\ \vdots \\ \delta\omega_q^c \end{Bmatrix} = \left[S^c(j,i) \right] \begin{Bmatrix} \delta\alpha_1 \\ \delta\alpha_2 \\ \vdots \\ \delta\alpha_{n_e} \end{Bmatrix} \quad \text{or} \quad \delta\boldsymbol{\omega}^c = \boldsymbol{S}^c \cdot \delta\boldsymbol{\alpha} \tag{3.26}$$

where $\delta\omega_j^c$ represents the damage-induced change of the jth closed-loop natural frequency, $\delta\alpha_i$ represents the damage-induced variation of the ith structural parameter α_i, $\boldsymbol{S}^c$ is the so-called sensitivity matrix which has dimension of $q \times n_e$. Using Eqs. (3.18) and (3.19) we may calculate the elements of the sensitivity matrix $\boldsymbol{S}^c$ as,

$$S^c(j,i) = \frac{\partial \omega_j^c}{\partial \alpha_i} = \mathrm{Im}\left[\frac{\partial \lambda_j^c}{\partial \alpha_i} \right] \tag{3.27}$$

Even though the sensitivity of frequency change to structural damage can be enhanced by incorporating appropriately designed feedback control (a design approach will be described in the next section), the number of natural frequencies available from the frequency response measurement of single closed-loop system is still usually much smaller than the number of structural parameters needed to characterize the damage occurrence. Therefore, Eq. (3.26) is generally an under-determined problem, and the damage-induced structural parameter variations $\delta\alpha_i (i = 1, 2, \cdots, n_e)$ cannot be accurately determined through that equation. However, this issue can actually be improved by collecting frequency measurements from multiple closed-loop systems. That is, we may activate different combinations of the actuators in the control system to design a series of closed-loop controls, which lead to a series of closed-loop systems. The frequency measurements from these multiple closed-loop systems for the same structure (with damage) will significantly enrich the frequency measurement data available for damage

identification. For each designed feedback controller, an equation relating the measured frequency changes to structure parameter variation, as shown in Eq. (3.26), can be obtained, and the equations for all designed controllers can be combined together as follows

$$\begin{bmatrix} \delta\boldsymbol{\omega}^{c1} \\ \delta\boldsymbol{\omega}^{c2} \\ \vdots \\ \delta\boldsymbol{\omega}^{ct} \end{bmatrix} = \begin{bmatrix} \boldsymbol{S}^{c1} \\ \boldsymbol{S}^{c2} \\ \vdots \\ \boldsymbol{S}^{ct} \end{bmatrix} \cdot \delta\boldsymbol{\alpha} \quad \text{or} \quad \delta\tilde{\boldsymbol{\omega}}^{c} = \boldsymbol{S}^{tot} \cdot \delta\boldsymbol{\alpha} \tag{3.28}$$

where $\boldsymbol{S}^{ci}$ and $\delta\boldsymbol{\omega}^{ci}$ $(i = 1, 2, \cdots, t)$ are the sensitivity matrix and measured frequency changes under the *i*th closed-loop system design. It can be clearly seen that the number of frequency measurement data increases from the original q to qt, whereas the number of system parameters being determined does not change. In addition, the combined sensitivity matrix $\boldsymbol{S}^{tot}$ has dimension of $qt \times n_e$, and the original problem can be improved into a much less undetermined problem by increasing the number of rows (constraint equations) in Eq. (3.28). To achieve this goal, the sensitivity-enhancing feedback controllers should be properly designed in the sense that each feedback controller produces different pattern of sensitivity enhancement so that the condition number of the combined sensitivity matrix $\boldsymbol{S}^{tot}$ can be improved.

The damage-induced structural parameter variation $\delta\boldsymbol{\alpha}$ can be estimated by using the following performance index

$$J(\delta\boldsymbol{\alpha}) = \left(\delta\tilde{\boldsymbol{\omega}}^{c} - \boldsymbol{S}^{tot}\delta\boldsymbol{\alpha}\right)^{T}\left(\delta\tilde{\boldsymbol{\omega}}^{c} - \boldsymbol{S}^{tot}\delta\boldsymbol{\alpha}\right) \tag{3.29}$$

where $\delta\tilde{\boldsymbol{\omega}}^{c}$ represents the actual measured frequency changes.

3.4 Optimal Design of Sensitivity-Enhancing Feedback Control

The proposed optimal sensitivity-enhancing feedback control is built upon the simultaneous placement/assignment of the closed-loop eigenvalues and eigenvectors. In this section, the classical eigenstructure assignment via SVD (singular value decomposition) technique is summarized at first, and then a constrained optimization problem is formulated to find the optimal eigenstructure assignment for the closed-loop system to achieve the best performance of sensitivity enhancement.

3.4.1 Eigenstructure Assignment via SVD

The eigenstructure assignment via SVD technique has been extensively explored and previously utilized to achieve modal control [139], mode localization [140,141], vibration confinement [142], and vibration isolation [143]. A brief review of the SVD based eigenstructure assignment technique is provided in the following. A state space form of the closed-loop system given in Eq. (3.10) can be written as

$$\dot{\boldsymbol{z}} = (\boldsymbol{A} + \boldsymbol{B}_1 \boldsymbol{K}_c)\boldsymbol{z} + \boldsymbol{B}_0 \boldsymbol{f}(t) \tag{3.30}$$

where $\boldsymbol{z} = \begin{bmatrix} \boldsymbol{x} \\ \dot{\boldsymbol{x}} \end{bmatrix} \in \Re^{N\times 1}$ ($N = 2n$) is the state vector, $\boldsymbol{f} \in \Re^{p\times 1}$ is the excitation input vector, and $\boldsymbol{A} = \begin{bmatrix} \boldsymbol{0}_{n\times n} & \boldsymbol{I}_{n\times n} \\ -\boldsymbol{M}^{-1}\boldsymbol{K} & -\boldsymbol{M}^{-1}\boldsymbol{C} \end{bmatrix} \in \Re^{N\times N}$, $\boldsymbol{B}_1 = \begin{bmatrix} \boldsymbol{0}_{n\times 1} \\ \boldsymbol{M}^{-1}\bar{\boldsymbol{B}}_1 \end{bmatrix} \in \Re^{N\times r}$, $\boldsymbol{K}_c = \begin{bmatrix} -\boldsymbol{K}_{c1} \\ -\boldsymbol{K}_{c2} \end{bmatrix} \in R^{r\times N}$ and $\boldsymbol{B}_0 = \begin{bmatrix} \boldsymbol{0}_{n\times 1} \\ \boldsymbol{M}^{-1}\bar{\boldsymbol{B}}_0 \end{bmatrix} \in \Re^{N\times p}$ are the system matrix, control input matrix, control gain matrix and excitation input matrix, respectively.

The eigenvalue equation of the closed-loop system can be written as

$$\left(\boldsymbol{A}+\boldsymbol{B}_1\boldsymbol{K}_c\right)\boldsymbol{\varphi}_j=\lambda_j^c\boldsymbol{\varphi}_j \tag{3.31}$$

where $\boldsymbol{\varphi}_j$ represents the jth eigenvector corresponding to the assigned or desired closed-loop eigenvalue λ_j^c. Eq. (3.31) can be written in an alternative form as

$$\left[\boldsymbol{A}-\lambda_j^c\boldsymbol{I}_N \mid \boldsymbol{B}_1\right]\begin{Bmatrix}\boldsymbol{\varphi}_j\\ \boldsymbol{K}_c\boldsymbol{\varphi}_j\end{Bmatrix}=\boldsymbol{0} \tag{3.32}$$

which means $\begin{Bmatrix}\boldsymbol{\varphi}_j\\ \boldsymbol{K}_c\boldsymbol{\varphi}_j\end{Bmatrix}$ must fall into the null space of the matrix $\left[\boldsymbol{A}-\lambda_j^c\boldsymbol{I}_N \mid \boldsymbol{B}_1\right]$.

We define

$$\boldsymbol{S}_{\lambda_j^c}=\left[\boldsymbol{A}-\lambda_j^c\boldsymbol{I}_N \mid \boldsymbol{B}_1\right] \tag{3.33}$$

Applying singular value decomposition (SVD) to $\boldsymbol{S}_{\lambda_j^c}$ leads to

$$\boldsymbol{S}_{\lambda_j^c}=\left[\boldsymbol{A}-\lambda_j^c\boldsymbol{I}_N \mid \boldsymbol{B}_1\right]=\boldsymbol{U}_j\left[\boldsymbol{D}_j \mid \boldsymbol{0}_{N\times r}\right]\boldsymbol{V}_j^* \tag{3.34}$$

where $\boldsymbol{D}_j$ is a positive definite diagonal matrix containing all the singular values of $\boldsymbol{S}_{\lambda_j^c}$, the columns of $\boldsymbol{U}_j$ contain the set of orthonormal left singular vectors, and the columns of $\boldsymbol{V}_j$ contain the set of orthonormal right singular vectors. The right singular vector matrix $\boldsymbol{V}_j$ can be partitioned in the following form

$$\boldsymbol{V}_j=\begin{bmatrix}\boldsymbol{V}_{11}^{(j)} & \boldsymbol{V}_{12}^{(j)}\\ \boldsymbol{V}_{21}^{(j)} & \boldsymbol{V}_{22}^{(j)}\end{bmatrix} \tag{3.35}$$

where $\boldsymbol{V}_{11}^{(j)}$, $\boldsymbol{V}_{12}^{(j)}$, $\boldsymbol{V}_{21}^{(j)}$ and $\boldsymbol{V}_{22}^{(j)}$ are $N\times N$, $N\times r$, $r\times N$, and $r\times r$ sub-matrices,

respectively. Post-multiplying Eq. (3.34) by $\begin{bmatrix} \boldsymbol{V}_{12}^{(j)} \\ \boldsymbol{V}_{22}^{(j)} \end{bmatrix}$ and utilizing the unitary condition for the singular vector matrices, one obtains

$$\left[\boldsymbol{A} - \lambda_j^c \boldsymbol{I}_N \mid \boldsymbol{B} \right] \begin{bmatrix} \boldsymbol{V}_{12}^{(j)} \\ \boldsymbol{V}_{22}^{(j)} \end{bmatrix} = \boldsymbol{0} \tag{3.36}$$

Obviously the linearly independent column vectors of matrix $\begin{bmatrix} \boldsymbol{V}_{12}^{(j)} \\ \boldsymbol{V}_{22}^{(j)} \end{bmatrix}$ span the null space of $\boldsymbol{S}_{\lambda_j^c}$, hence any *achievable* closed-loop eigenvector must be a linear combination of the column vectors of $\boldsymbol{V}_{12}^{(j)}$. Therefore, within the admissible subspace, we may assign an eigenvector by properly choosing the linear combination coefficient vector. In other words, the assigned right eigenvector of the closed-loop system can be expressed as

$$\boldsymbol{\varphi}_j^a = \boldsymbol{V}_{12}^{(j)} \boldsymbol{\beta}_j \tag{3.37}$$

where $\boldsymbol{\beta}_j$ is the coefficient vector used to span the column vectors of $\boldsymbol{V}_{12}^{(j)}$ to achieve $\boldsymbol{\varphi}_j^a$, and the following equation holds

$$\boldsymbol{K}_c \boldsymbol{\varphi}_j^a = \boldsymbol{V}_{22}^{(j)} \boldsymbol{\beta}_j \tag{3.38}$$

By collecting Eq. (3.38) for all desired right eigen-solutions, finally we have

$$\boldsymbol{K}_c \boldsymbol{\Phi}^a = \boldsymbol{W} \tag{3.39}$$

where

$$\boldsymbol{\Phi}^a = \begin{bmatrix} \boldsymbol{\varphi}_1^a & \boldsymbol{\varphi}_2^a & \cdots & \boldsymbol{\varphi}_N^a \end{bmatrix}, \ \boldsymbol{\varphi}_j^a = \boldsymbol{V}_{12}^{(j)} \boldsymbol{\beta}_j \tag{3.40}$$

$$\boldsymbol{W} = \begin{bmatrix} \boldsymbol{w}_1 & \boldsymbol{w}_2 & \cdots & \boldsymbol{w}_N \end{bmatrix}, \ \boldsymbol{w}_j = \boldsymbol{V}_{22}^{(j)} \boldsymbol{\beta}_j \tag{3.41}$$

Thus the gain matrix can be obtained as

$$\boldsymbol{K}_c = \boldsymbol{W}(\boldsymbol{\Phi}^a)^{-1} \tag{3.42}$$

3.4.2 Constrained Optimization for Optimal Sensitivity-Enhancing Control Design

Assume that the closed-loop eigenvalues are assigned as follows:

$$\lambda_j^c = \begin{cases} \gamma_j \times \lambda_j^o & j = 1,2,\cdots,q \\ \lambda_j^o & j = q+1, q+2,\cdots,n \end{cases} \tag{3.43}$$

where λ_j^o is the jth eigenvalue of the open-loop system and q is the total number of eigenvalues to be placed/adjusted during eigenstructure assignment (or the total number of the measurable natural frequencies). Thus, the closed-loop eigenvectors can also be assigned in their corresponding admissible space

$$\boldsymbol{\varphi}_j^c = \begin{cases} \boldsymbol{V}_{12}^{(j)} \boldsymbol{\beta}_j & j = 1,2,\cdots,q \\ \boldsymbol{V}_{12}^{(j)} \tilde{\boldsymbol{\beta}}_j & j = q+1, q+2,\cdots,n \end{cases} \tag{3.44}$$

where the column vectors of $\boldsymbol{V}_{12}^{(j)}$ span the admissible space for the jth eigenvector assignment, and $\boldsymbol{\beta}_j$ or $\tilde{\boldsymbol{\beta}}_j$ is the corresponding coefficient vector to express $\boldsymbol{\varphi}_j^c$ in the column space of $\boldsymbol{V}_{12}^{(j)}$. Here $\boldsymbol{\beta}_j$ ($j = 1,2,\cdots,q$) are the design variables in the optimization procedure to achieve sensitivity enhancement, whereas $\tilde{\boldsymbol{\beta}}_j$ ($j = q+1, q+2,\cdots,n$) are selected so that the actual closed-loop eigenvectors $\boldsymbol{\varphi}_j^c$ ($j = q+1, q+2,\cdots,n$) are as close as possible to their corresponding open-loop eigenvectors $\boldsymbol{\varphi}_j^o$. The coefficient vectors, $\tilde{\boldsymbol{\beta}}_j$ ($j = q+1, q+2,\cdots,n$), can be determined by

minimizing the following performance index

$$J_{f_j} = \left\| \boldsymbol{\varphi}_j^o - \boldsymbol{V}_{12}^{(j)} \tilde{\boldsymbol{\beta}}_j \right\|^2 \tag{3.45}$$

By letting $dJ_{f_j} / d\tilde{\beta}_j = 0$, $\tilde{\boldsymbol{\beta}}_j$ ($j = q+1, q+2, \cdots, n$) can be solved as

$$\tilde{\boldsymbol{\beta}}_j = \left(\boldsymbol{V}_{12}^{(j)*} \boldsymbol{V}_{12}^{(j)} \right)^{-1} \boldsymbol{V}_{12}^{(j)*} \boldsymbol{\varphi}_j^o \tag{3.46}$$

Therefore, the "closest" achievable closed-loop eigenvector is

$$\boldsymbol{\varphi}_j^c = \boldsymbol{V}_{12}^{(j)} \left(\boldsymbol{V}_{12}^{(j)*} \boldsymbol{V}_{12}^{(j)} \right)^{-1} \boldsymbol{V}_{12}^{(j)*} \boldsymbol{\varphi}_j^o, \quad \text{where } j = q+1, q+2, \cdots, n \tag{3.47}$$

At this point, it is clear that the design of the optimal feedback controller for sensitivity enhancement is equivalent to finding the optimal values of eigenvalue reducing ratios γ_j ($j = 1, 2, \cdots, q$) and those coefficient vectors for closed-loop eigenvector assignment $\boldsymbol{\beta}_j$ ($j = 1, 2, \cdots, q$) to best enhance the sensitivity of the targeted natural frequency changes to the specified type of structural damages. The overall control objective is to achieve the best performance of sensitivity enhancement with minimum control effort required for the corresponding feedback control.

The total control effort required for the feedback control can be calculated by

$$W_{contr} = trace\left(\boldsymbol{K}_c \boldsymbol{P}_l \boldsymbol{K}_c^T \right) \tag{3.48}$$

where $\boldsymbol{K}_c$ is the control gain matrix, and $\boldsymbol{P}_l$ is the solution to the following Lyapunov equation

$$\boldsymbol{A}_{cl} \boldsymbol{P}_l + \boldsymbol{P}_l \boldsymbol{A}_{cl}^T + \boldsymbol{Z} = \boldsymbol{0} \tag{3.49}$$

in which $\boldsymbol{Z}$ is the variance matrix of the excitation input. And the performance index of

the sensitivity enhancement for a closed-loop system can be defined as the summation of the element-to-element ratios between the closed-loop sensitivity matrix and the open-loop sensitivity matrix

$$SE = \sum_{j=1}^{q} \left[\bar{w}_j \sum_{i=1}^{n_e} \left| \frac{S^c(j,i)}{S^o(j,i)} \right| \right] \tag{3.50}$$

where $\boldsymbol{S}^c$ and $\boldsymbol{S}^o$ are the sensitivity matrices of the closed-loop and open-loop systems, respectively, and $\bar{w}_j$ is the weight factor on the sensitivity enhancement of the jth natural frequency change.

Finally, the optimization problem is formulated as follows: we want to find the optimal values of the design variables

$$\begin{aligned} \boldsymbol{p} &= \left\{ \gamma_1, \gamma_2, \cdots, \gamma_q, \boldsymbol{\beta}_1, \boldsymbol{\beta}_2, \cdots, \boldsymbol{\beta}_q \right\} \\ &= \left\{ \boldsymbol{\gamma}, \boldsymbol{\beta}_1, \boldsymbol{\beta}_2, \cdots, \boldsymbol{\beta}_q \right\} \in \Re^{(r+1)q} \end{aligned} \tag{3.51}$$

that can minimize the following fitness function:

$$J(\boldsymbol{p}) = \frac{C_0}{SE} + W_{contr} \tag{3.52}$$

under the constraints of

$$\mathrm{Re}\left[\frac{\partial \lambda_j^c}{\partial \alpha_i} \right] \geq \varepsilon_j, \qquad (j = 1, 2, \cdots, q,\ i = 1, 2, \cdots, n_e) \tag{3.53}$$

where ε_j is a small negative number and C_0 in the fitness function is a constant to adjust the relative weighting between the performance of sensitivity enhancement and the required control effort. The purpose of these constraints is to guarantee the stability of the closed-loop system as long as the damage occurred is under some specified level, in

other words, we do not want the closed-loop system to be so sensitive that even small damages lead to an unstable system.

In this research, an elite-based simplex-GA hybrid approach developed by Yen et al. [144] is used to find the solution for the constrained optimization problem formulated above. This is a hybrid approach by combining a concurrent probabilistic simplex method with simple GA, thus offering a better trade-off between computation cost, convergence rate and the optimality of the solution found.

3.5 Numerical Analysis and Results

In this section, a cantilevered beam is used as the illustrative structure to demonstrate the performance of sensitivity-enhancing feedback control. The feasibility and effectiveness of using multiple closed-loop systems with different sensitivity-enhancing controls to identify structural damage are examined, and the effect of measurement noise on the damage identification performance is evaluated.

A schematic of the system model used for numerical analysis is given in Figure 3.1. The aluminum cantilevered beam is assumed to be homogenous, and evenly discretized into 10 elements. The piezoelectric actuators bonded on the upper surface of the second, fourth, sixth and eighth beam elements are used as control input actuators, and are actuated by the control voltage sources V_1, V_2, V_3 and V_4, respectively. The piezoelectric actuator bonded on the bottom surface of the second element is used as an input actuator to excite the structure for frequency response measurement, where V_0 is the excitation input voltage. V_0 is in the form of Gaussian white noise with zero mean

and 50V standard deviation. The values of key system parameters are specified as shown in Table 3.1.

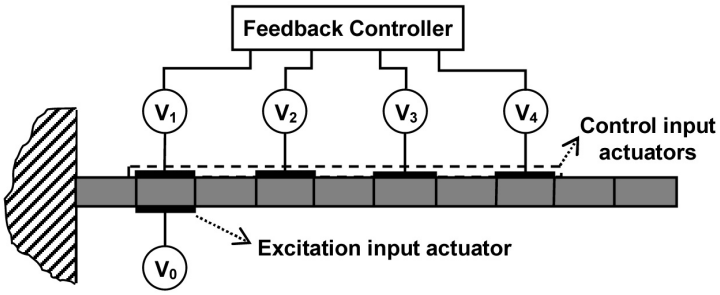

Figure 3.1: Schematic of the system model

Table 3.1: System parameters

Beam structure		Piezoelectric material	
Density:	$\rho_b = 2410 kg/m^3$	Density:	$\rho_p = 7600 kg/m^3$
Length:	$L_b = 0.40m$	Young's modulus:	$E_p = 5.9\times10^{10} N/m^2$
Thickness:	$h_b = 3.4mm$	Thickness:	$h_p = 0.3mm$
Width:	$b = 0.026m$	Width:	$b_p = 0.02m$
Young's modulus:	$E_b = 6.6\times10^{10} N/m^2$	Piezoelectric constant:	$d_{31} = -276\times10^{-12} m/V$

Without loss of generality, we will consider the type of damages that cause only stiffness change to the structure. We also assume that a high-fidelity finite element model (FEM) of the structure has been developed before damage occurrence. The structural parameter $\alpha_i (i = 1, 2, \cdots, 10)$ is defined as the stiffness parameter of the *i*th structural element such that $\alpha_i (EI)_i$ denotes the actual elemental stiffness and $\delta\alpha_i \times 100\%$ represents the damage-induced stiffness parameter variation in percentage of

the corresponding element. For example, $\alpha_i = 1.0$ means that the ith element is undamaged while $\alpha_i = 0.95$ indicates a 5% stiffness reduction on that element.

3.5.1 Sensitivity-Enhancing Control Design

Assuming that only the first 3 natural frequencies can be accurately measured from the frequency responses, we are therefore concerned about the sensitivities of these three frequencies to possible damage in any of the structural elements. For this specific example, we assign the first three closed-loop eigenvalues and their corresponding eigenvectors to design the feedback controller for the sensitivity enhancement of these first three natural frequencies. Combining the frequency reduction ratios and the coefficient vectors for the eigenvector assignment, we have 15 design variables in total

$$\boldsymbol{p} = \left\{ \gamma_1, \gamma_2, \gamma_3, \boldsymbol{\beta}_1 \in \Re^{4\times 1}, \boldsymbol{\beta}_2 \in \Re^{4\times 1}, \boldsymbol{\beta}_3 \in \Re^{4\times 1} \right\} \tag{3.54}$$

The optimal values of these design variables can be found by using the constrained optimization process formulated in Section 3.4. The GA parameters in the optimization process are set as follows: population size 80, crossover rate 0.6, and mutation rate 0.01. The optimization process returns the optimal values of the design variables, $\boldsymbol{\gamma}^*$, $\boldsymbol{\beta}_1^*$, $\boldsymbol{\beta}_2^*$ and $\boldsymbol{\beta}_3^*$, which are given in the first row of Table 3.2. Based on these values, the gain matrix for the closed-loop control can be obtained by using Eq. (3.42). For the resulting optimal closed-loop system, the first three natural frequencies are reduced by 5%, 11%, and 33% respectively when compared with their corresponding open-loop values, as given by $\boldsymbol{\gamma}^*$. The coefficient vectors for the optimal

eigenvector assignment are given by $\boldsymbol{\beta}_1^*$, $\boldsymbol{\beta}_2^*$ and $\boldsymbol{\beta}_3^*$, and the first three left and right eigenvectors of the optimal closed-loop system are plotted and compared with their corresponding open-loop ones, as shown in Figure **3.2**.

To evaluate the performance of sensitivity enhancement by incorporating the optimal feedback controller with the original open-loop system, we compare the frequency shift of the open-loop and closed-loop systems induced by the same damage, as shown in Figure **3.3**. The subplots (a), (b) and (c) compare the first, second and third natural frequency shifts, respectively, due to a 5% stiffness reduction in each structural element. For example, the bars in subplot (a) represent the first natural frequency shift of the open-loop or closed-loop systems due to a 5% stiffness reduction on each structural element shown as the horizontal-axis label. From the figures, we can see that: (1) the structural damage may induce either an increase or decrease in the natural frequencies of the closed-loop system, while the frequencies of the open-loop system are always reduced; and (2) the damage-induced frequency changes of the closed-loop system are much larger than those of the open-loop system. For example, a maximum enhancement ratio of 4026 is achieved for the first frequency shift when the eighth structural element is damaged, a maximum ratio of 61 is obtained for the second frequency shift by damage on the fourth element, and the third frequency shift achieves a maximum enhancement ratio of 83 when the damage occurs on the sixth element. Moreover, by incorporating the optimal sensitivity-enhancing feedback control with the original structure, not only the sensitivity of frequency shift to structural damage can be greatly enhanced, but also the condition of the sensitivity matrix is improved given that the condition number of the

closed-loop sensitivity matrix is much smaller that of the open-loop sensitivity matrix, i.e., $COND(\boldsymbol{S}^c) = 8.7$ and $COND(\boldsymbol{S}^o) = 20.1$.

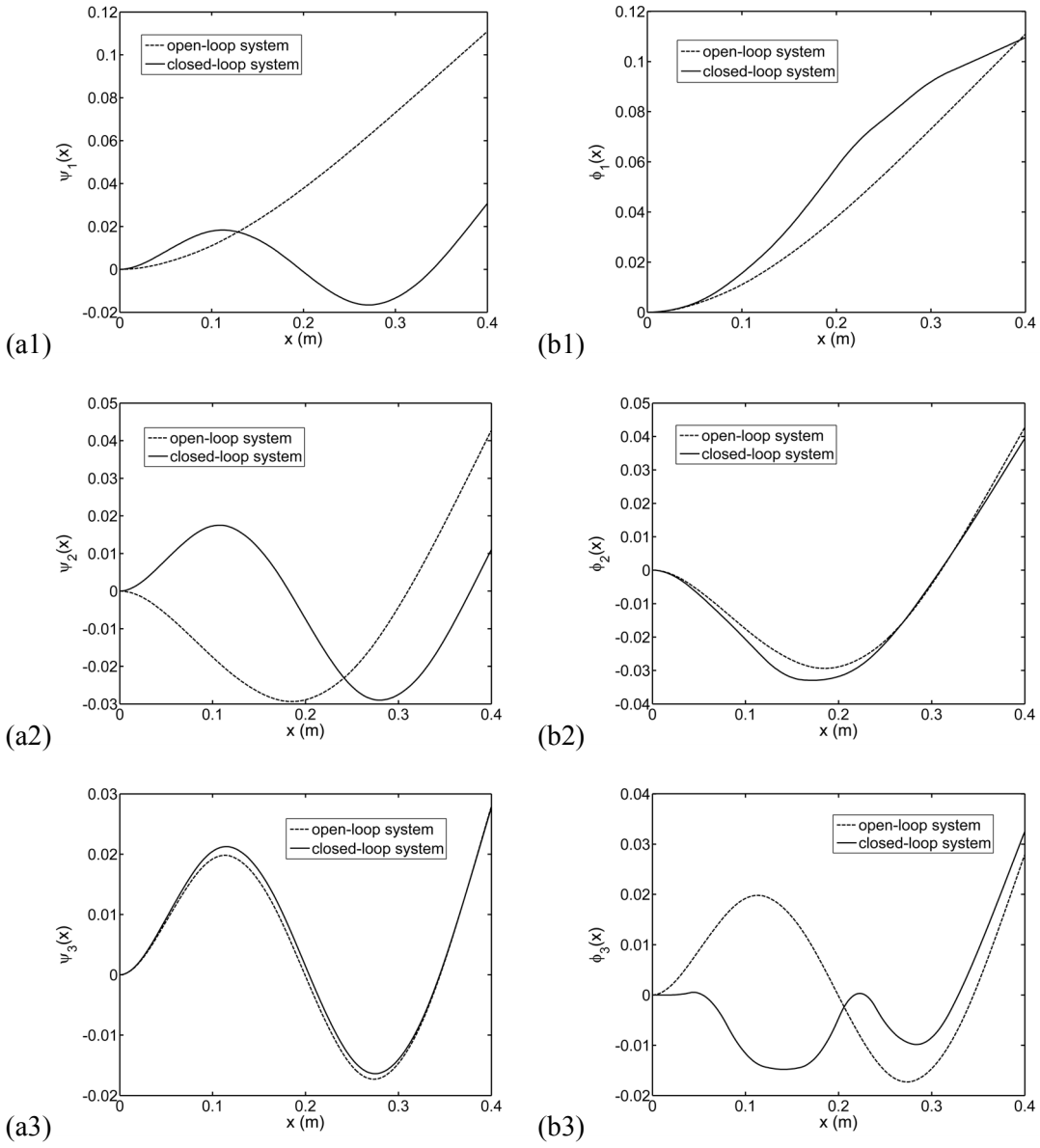

Figure 3.2: Comparison of the left and right eigenvectors of the open-loop and closed-loop systems: (a1-a3) Comparison of the first, second and third left eigenvectors, respectively; (b1-b3) Comparison of the first, second and third right eigenvectors, respectively

In order to highlight the importance of optimal eigenvector assignment to the sensitivity enhancement performance, we compare the first three natural frequency shifts of the above optimal closed-loop system with those of the two *ad hoc* closed-loop systems for the same damage. The *ad hoc closed-loop system (a)* has the same eigenvalues as those of the optimal closed-loop system, while its eigenvectors are assigned as the "closest" achievable eigenvectors to their corresponding open-loop ones. This type of eigenvector assignment can be achieved by using Eq. (**3.46**) and Eq. (**3.47**). In the *ad hoc closed-loop system (b)*, the first three natural frequencies are further reduced to 40% of their corresponding open-loop values, and its eigenvectors are also assigned as the "closest" achievable eigenvectors to their corresponding open-loop ones. Therefore, these ad hoc closed-loop systems are designed by only reducing the closed-loop eigenvalues while maintaining the open-loop eigenvectors as much as possible.

Figure **3.4** shows the comparison results. Similar to Figure **3.3**, each bar in the figure represents the corresponding natural frequency shift due to 5% stiffness reduction on the element as specified by the horizontal-axis label. From the figure, we can see that the *ad hoc closed-loop system (a)* achieves much less sensitivity enhancement, although its eigenvalues are reduced to the same values as the optimally designed closed-loop system. Even if we further reduce the closed-loop eigenvalues to the ratio of 0.4 in the *ad hoc closed-loop system (b)*, the performance of sensitivity enhancement is still not comparable to that of the optimal closed-loop system. Therefore, one may conclude that, in order to achieve the best performance of sensitivity enhancement, both the closed-loop eigenvalues and eigenvectors should be simultaneously optimized (optimal eigenstructure assignment) instead of only reducing the eigenvalues of the closed-loop system.

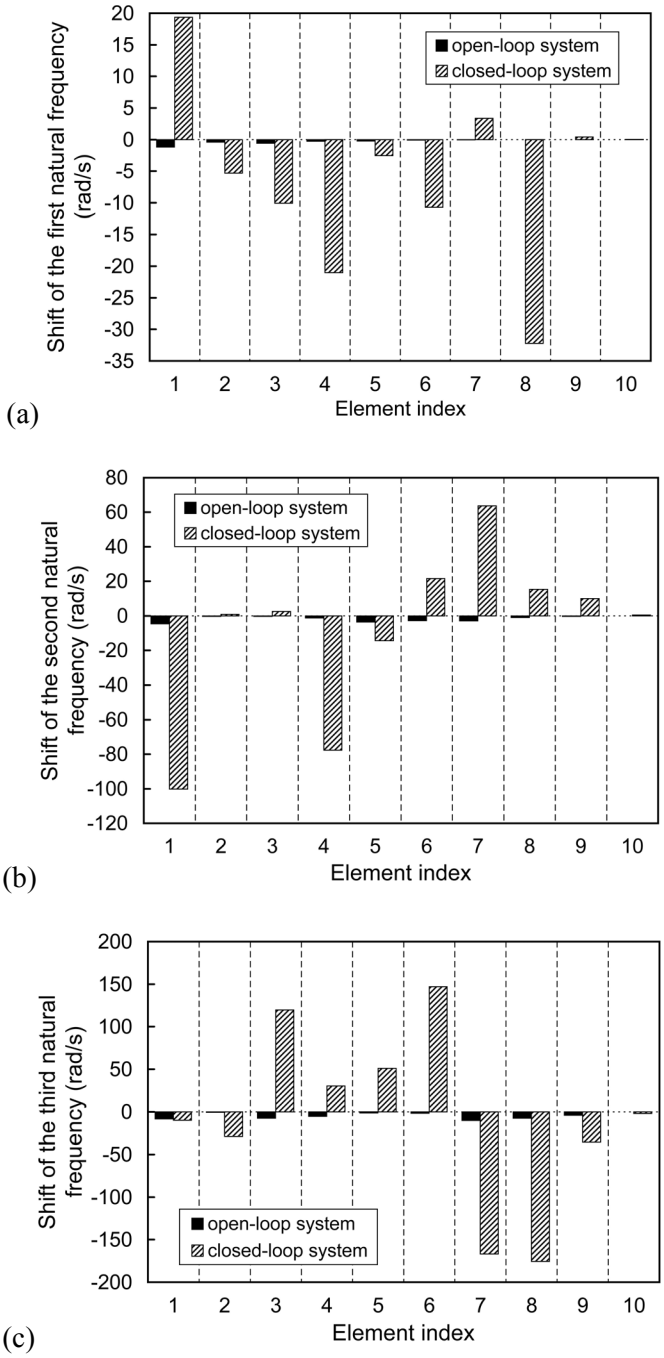

Figure **3.3**: Comparison of the damage-induced natural frequency shifts of the open-loop and closed-loop systems: (a) Comparison of the first natural frequency shift; (b) Comparison of the second natural frequency shift; (c) Comparison of the third natural frequency shift.

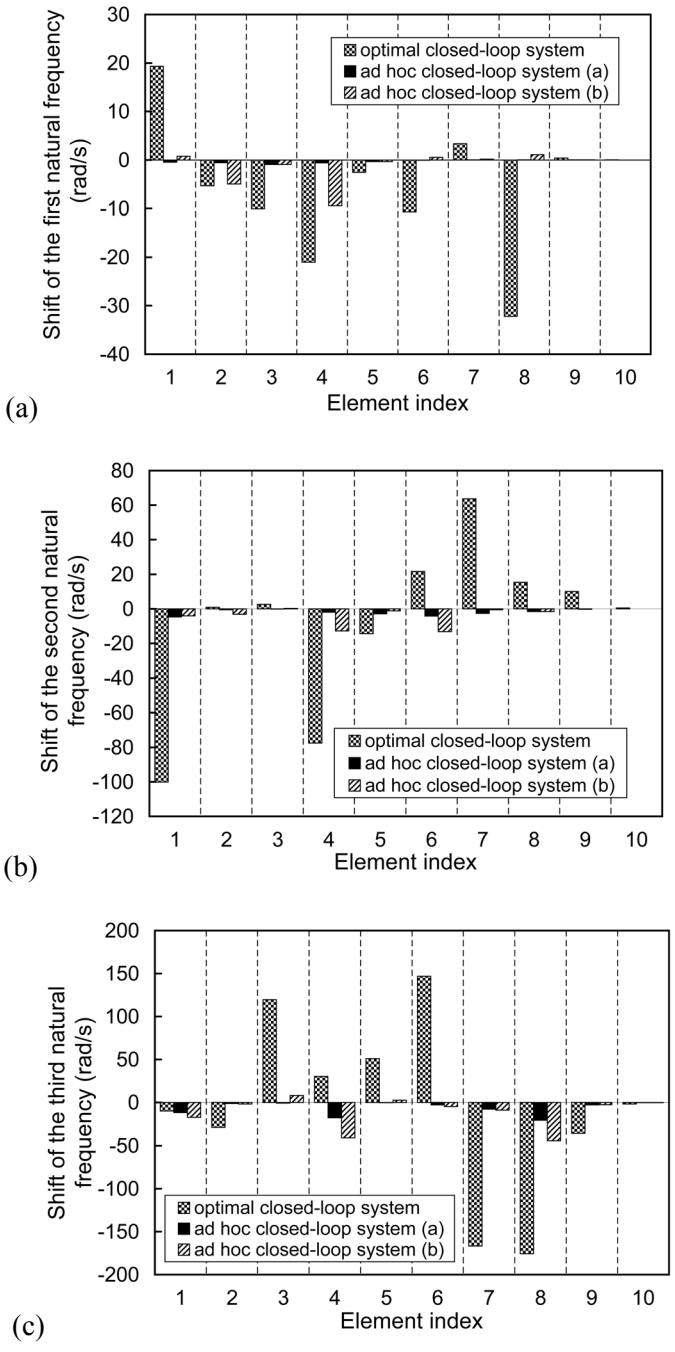

Figure **3.4**: Comparison of the damage-induced natural frequency shifts of the optimal closed-loop system and the ad hoc closed-loop systems: (a) Comparison of the first natural frequency shift; (b) Comparison of the second natural frequency shift; (c) Comparison of the third natural frequency shift.

3.5.2 Damage Identification Using Measured Natural Frequencies of the Sensitivity-Enhanced Closed-Loop Systems

In the previous subsection, it has been demonstrated that the sensitivity of natural frequency shift to stiffness reduction can be significantly enhanced by using the optimal sensitivity-enhancing feedback control. In this subsection we will examine the damage identification performance by using natural frequency measurements of the sensitivity enhanced closed-loop systems. It is worth emphasizing that, for this problem, a single closed-loop system only provides 3 measurable natural frequencies; hence the number of frequency measurements is still highly deficient for sensitivity-based damage identification. In order to tackle this issue, multiple closed-loop systems with different feedback controllers are designed to enrich the frequency measurement data as proposed in Section 3.3.

3.5.2.1 Design of Multiple Sensitivity-Enhanced Closed-Loop Systems

In addition to the optimal sensitivity enhanced closed-loop system presented in last subsection (CLS-1), three alternative optimally-designed closed-loop systems (CLS-2, CLS-3, CLS-4) are obtained by activating different combinations of actuators in the given hardware setup. As shown in Table 3.2, CLS-2 uses actuators on the second, fourth and sixth structural elements, CLS-3 uses actuators on the second, fourth and eighth elements, and only the actuators on the second and fourth elements are used in designing CLS-4. The optimal closed-loop eigenvalues and coefficient vectors of the

optimal closed-loop eigenvectors for each closed-loop system are obtained as given in Table 3.2.

Table 3.2: Design parameters and optimization results of multiple sensitivity-enhancing feedback controllers

System index	Actuator locations	Optimization setting	Optimal closed-loop eigenvalues	Coefficient vectors of the optimal closed-loop eigenvectors
CLS-1	2,4,6,8	$C_0 = 1.0e15$ $\bar{w}_j = 1.0$	$\lambda_1^c = 0.95\lambda_1^o$ $\lambda_2^c = 0.89\lambda_2^o$ $\lambda_3^c = 0.67\lambda_3^o$	$\boldsymbol{\beta}_1^* = [-0.42 \quad -0.29 \quad 0.94 \quad 0.64]$ $\boldsymbol{\beta}_2^* = [0.13 \quad 0.55 \quad 0.23 \quad -0.09]$ $\boldsymbol{\beta}_3^* = [-0.26 \quad -0.09 \quad -0.45 \quad 0.09]$
CLS-2	2,4,6	$C_0 = 1.0e14$ $\bar{w}_j = 1.0$	$\lambda_1^c = 0.99\lambda_1^o$ $\lambda_2^c = 0.87\lambda_2^o$ $\lambda_3^c = 0.62\lambda_3^o$	$\boldsymbol{\beta}_1^* = [-0.48 \quad 0.73 \quad 0.53]$ $\boldsymbol{\beta}_2^* = [-0.07 \quad -0.33 \quad 0.01]$ $\boldsymbol{\beta}_3^* = [-0.96 \quad -0.17 \quad -0.68]$
CLS-3	2,4,8	$C_0 = 1.0e14$ $\bar{w}_j = 1.0$	$\lambda_1^c = 0.91\lambda_1^o$ $\lambda_2^c = 0.85\lambda_2^o$ $\lambda_3^c = 0.83\lambda_3^o$	$\boldsymbol{\beta}_1^* = [0.14 \quad 0.09 \quad -0.69]$ $\boldsymbol{\beta}_2^* = [-0.93 \quad -0.90 \quad 0.51]$ $\boldsymbol{\beta}_3^* = [-0.59 \quad -0.69 \quad -0.44]$
CLS-4	2,4	$C_0 = 5.0e13$ $\bar{w}_j = 1.0$	$\lambda_1^c = 1.00\lambda_1^o$ $\lambda_2^c = 0.93\lambda_2^o$ $\lambda_3^c = 0.76\lambda_3^o$	$\boldsymbol{\beta}_1^* = [0.56 \quad -0.85]$ $\boldsymbol{\beta}_2^* = [1.00 \quad 0.45]$ $\boldsymbol{\beta}_3^* = [0.94 \quad -0.28]$

In order to show the sensitivity enhancement performance of these alternative closed-loop systems (CLS-2, CLS-3, CLS-4), the first three natural frequency changes of these closed-loop systems are compared with the frequency changes of the open-loop system (OLS) induced by the same damage, as given in Table 3.3. In this table, each row gives the first three natural frequency changes of the OLS (open-loop system), CLS-2, CLS-3 and CLS-4, induced by 5% stiffness reduction on one structural element as indicated in the first column of the table. From the table, we can clearly see that the

damage-induced frequency changes of these alternative closed-loop systems are generally much larger than those of the open-loop system, and thus these alternative closed-loop systems also achieve significant enhancement of frequency-shift sensitivity to stiffness reduction.

Table 3.3: Natural frequency changes of the open-loop and closed-loop systems due to single element damage

Damaged element	First natural frequency change (rad/s)				Second natural frequency change (rad/s)				Third natural frequency change (rad/s)			
	OLS	CLS-2	CLS-3	CLS-4	OLS	CLS-2	CLS-3	CLS-4	OLS	CLS-2	CLS-3	CLS-4
1	-1.175	32.04	14.61	45.37	-4.672	-106.2	-90.40	-166.7	-8.340	-94.11	20.87	-94.76
2	-0.412	-2.843	-0.503	-2.382	-0.367	0.373	3.186	-27.76	-0.604	-65.19	-6.102	-8.097
3	-0.586	-14.14	-5.628	-14.28	-0.276	6.897	29.19	71.67	-7.586	142.2	-2.469	23.02
4	-0.250	-18.31	-13.92	-11.29	-1.272	-94.12	-89.42	-65.19	-5.313	36.87	20.46	61.55
5	-0.214	-3.567	-3.313	-5.446	-3.613	-8.544	20.79	30.27	-1.487	47.88	-17.53	-2.485
6	-0.072	3.243	-0.472	1.422	-2.732	7.309	4.332	-12.06	-1.780	111.5	-14.62	1.098
7	-0.043	5.858	0.499	4.572	-2.970	41.40	-2.754	-36.61	-10.29	-140.6	-16.08	14.98
8	-0.008	2.127	-21.42	1.791	-0.917	16.63	-25.18	-16.67	-7.524	-60.77	7.740	11.04
9	-0.002	0.746	0.120	0.649	-0.305	6.611	-1.449	-6.82	-4.078	-25.24	-1.496	5.840
10	-0.000	0.033	0.006	0.029	-0.013	0.322	-0.080	-0.337	-0.024	-1.273	-0.06	0.335

3.5.2.2 Numerical Results and Case Studies of Damage Identification

As assumed, each of the optimal sensitivity-enhanced closed-loop systems given in Table 3.2 provides 3 measurable natural frequencies; hence by using these four closed-loop systems, we have 12 natural frequency measurements in total for sensitivity based damage identification process formulated in Section 3.3. In order to illustrate the performance improvement, the damage identification results are compared to those using

frequency measurements from the open-loop system and frequency measurements from a set of ad hoc closed-loop systems (AHCLS-1, AHCLS-2, AHCLS-3, AHCLS-4). The ad hoc closed-loop system, AHCLS-*i* (*i*=1,2,3,4), has the same closed-loop eigenvalues as those of the optimal closed-loop system, CLS-*i*, while its eigenvectors are not optimally assigned (assigned as the "closest" achievable eigenvectors to their corresponding open-loop ones). It is worth mentioning that this set of ad hoc closed-loop systems also provides 12 natural frequency measurements (3 from each system) for damage identification. However, we only have three natural frequency measurements available for damage identification when the open-loop system is utilized.

Figure **3.5**(a-h) shows the results of damage identification by using noise-free natural frequencies of the open-loop system, ad hoc closed-loop systems, and the optimal closed-loop systems. Each subplot in the figure compares the damage identification results for one case of detecting single element damage. The horizontal axis and vertical axis indicate the index of structural element and its associated stiffness reduction in percentage, respectively. As shown in the figure, when the three frequency measurements of the open-loop system are used for damage identification, the predicted stiffness reductions generally do not match with the actual stiffness reduction, and the obtained predictions have significant errors. When the twelve frequency measurements from the ad hoc closed-loop systems or optimal closed-loop systems are used for damage identification, an obvious improvement of damage identification results can be observed. In each case, the actual damaged element is always predicted to have the most severe stiffness reduction, in other words; the structural damage in each case is successfully localized. Also, the corresponding damage severity in each case is nearly accurately

predicted. Therefore, by utilizing the enlarged dataset of frequency measurement from a series of closed-loop systems, we can significantly improve the performance of damage identification.

Since measurement noise is inevitable in the natural frequency measurements, it is necessary to examine the performance of the proposed approach under the influence of measurement noise. Here we assume that the measured natural frequencies of the damaged closed-loop systems are contaminated with measurement noise. The noise-contaminated frequency measurement is simulated by using the following equation

$$\tilde{\boldsymbol{\omega}}_d^c = \boldsymbol{\omega}_d^c + v\boldsymbol{R}\boldsymbol{\omega}_d^c \qquad (3.55)$$

where $\tilde{\boldsymbol{\omega}}_d^c$ and $\boldsymbol{\omega}_d^c$ are the noise-contaminated and noise-free natural frequency measurements of the damaged closed-loop system, respectively, and $\boldsymbol{R}$ is a diagonal matrix whose diagonal entries are independent, normally distributed random numbers with mean 0, variance 1, and standard deviation 1, and $v \in [0, 1]$ represents the noise level. Two different levels of measurement noise, $v = 0.5\%$ and $v = 2.0\%$, are considered in the following case studies.

Figure 3.6 shows the damage identification results by using noise-contaminated natural frequencies of the open-loop system, the ad hoc closed-loop systems, and the optimal closed-loop systems. We first assume that the level of the measurement noise is 0.5%, i.e., $v = 0.5\%$. Each subplot in the figure compares the damage identification results for one case of detecting single element damage. The horizontal axis and vertical axis indicate the index of structural element and its associated stiffness parameter reduction in percentage, respectively. For each case of damage identification, 200

independent sets of simulated measurement noise are generated and added to the frequency measurements, then the resulting 200 sets of noise-contaminated natural frequencies (from the open-loop system, the ad hoc closed-loop systems, or the optimal closed-loop systems) are used to perform damage identification, respectively. By doing so, 200 predictions of elemental stiffness parameter reductions are obtained. The average of the resulting 200 predictions of the elemental stiffness reductions is represented by different patterns of bars in each subplot, and the 'T' marker added on the top of the bars represents the standard deviation of the obtained 200 predictions. As shown in the figure, when the natural frequencies of the open-loop system are utilized for damage identification, even the structural damage cannot be accurately located for most cases, and thus the damage identification performance is quite poor. The performance of damage identification can be improved by using the natural frequencies of the ad hoc closed-loop systems, however, the resulting damage identification results are still not satisfactory. Finally, when the natural frequencies from the optimal closed-loop systems are utilized, both the location and severity of the structural damage are successfully identified in each case. Moreover, under such situation, the standard deviation of the damage identification results due to uncertainties in frequency measurement is much smaller. This clearly indicates that the damage identification results using the optimal closed-loop systems are more robust against uncertainties in frequency measurement.

When the noise level increases to $v = 2.0\%$, the resulting damage identification results by using natural frequencies from different systems are presented in Figure **3.7**. Here we use the same damage scenario for each subplot as that used in Figure **3.6**. As can be observed in Figure **3.7**, the performance of damage identification using natural

frequencies of the open-loop system remains poor. Unlike the case studies for noise level $v = 0.5\%$, there is no improvement of damage identification results when the natural frequencies of the ad hoc closed-loop systems are used. That is, the performance of damage identification using the ad hoc closed-loop systems becomes poor when the noise level increase to $v = 2.0\%$. When the natural frequencies of the optimal closed-loop systems are used for damage identification, the structural damage can still be successfully identified in each case, and the standard deviation of the detection results only increases marginally under the higher noise level, which again demonstrates the improvement in both detection accuracy and robustness. The above case studies clearly show that the damage identification by using natural frequencies of the optimal closed-loop systems outperforms that by using those of either the open-loop system or the ad hoc closed-loop systems.

3.6 Summary

In this chapter, an enhanced frequency-shift-based damage identification method using sensitivity-enhancing feedback control is developed. A feedback controller can be designed to enhance the sensitivity of frequency shift to structural damage, which would benefit the process of damage identification. In order to obtain the best performance of sensitivity enhancement in the closed-loop system, both the closed-loop eigenvalues and eigenvectors should be treated as design variables in the controller synthesis process. In this research, we formulate an algorithm to optimally assign the eigenvalues and eigenvectors that yield enhanced closed-loop natural frequency sensitivity, which leads to

improved damage identification performance. The problem that is common in frequency-shift-based damage identification, namely deficiency of frequency measurement data, is also addressed by using multiple closed-loop systems with different feedback controller design. A series of numerical studies are performed on an example structure. It is shown that, in order to achieve the best performance of sensitivity enhancement, both the closed-loop eigenvalues and eigenvectors should be simultaneously optimized. It is also demonstrated that the proposed method is effective in damage identification and is robust against uncertainties in frequency measurements.

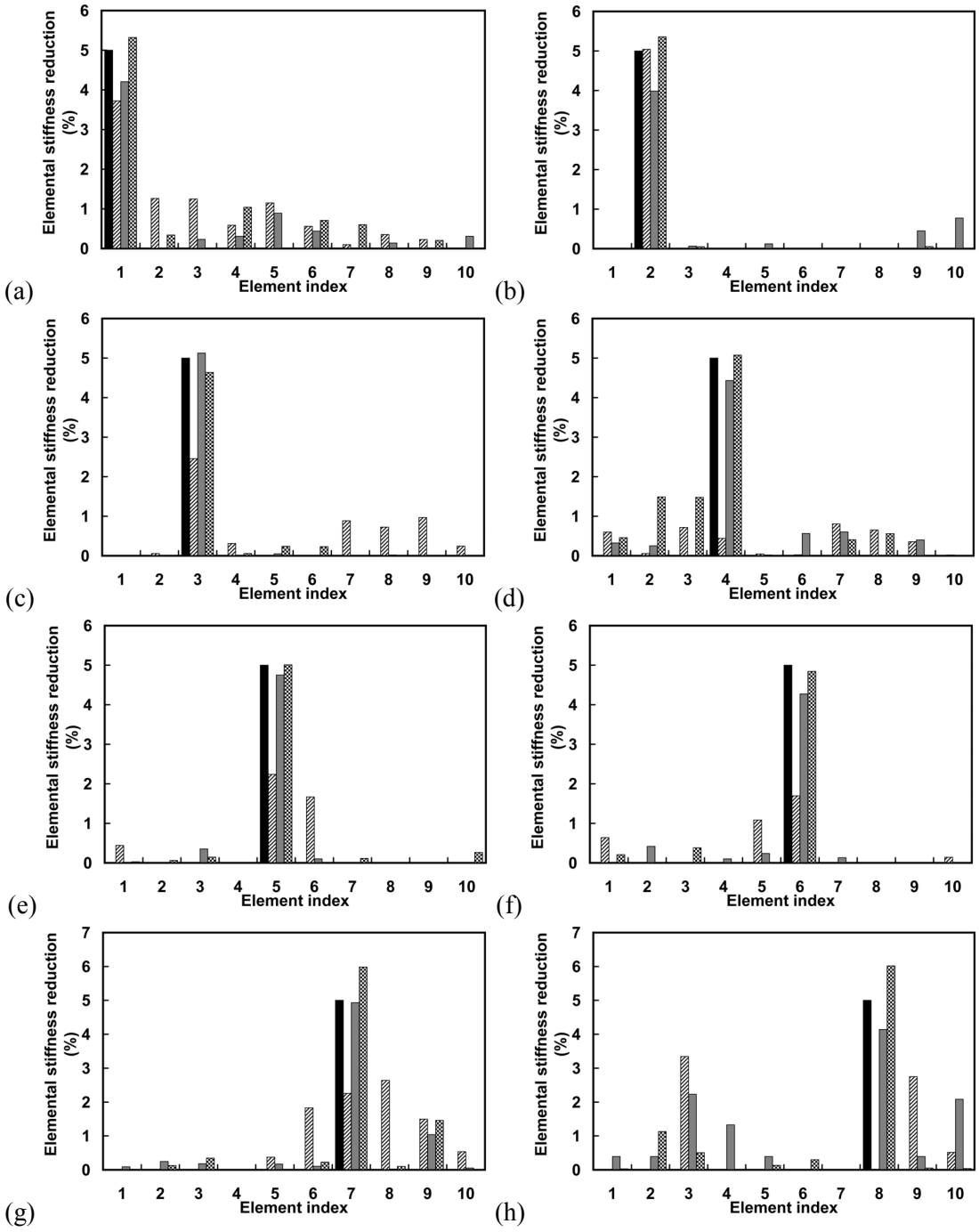

Figure 3.5: Damage identification results using noise-free natural frequencies. ■ Actual stiffness reduction; ▨ Prediction using noise-free natural frequencies of the open-loop system; ■ Prediction using noise-free natural frequencies of the ad hoc closed-loop systems; ▩ Prediction using noise-free natural frequencies of the optimal closed-loop systems.

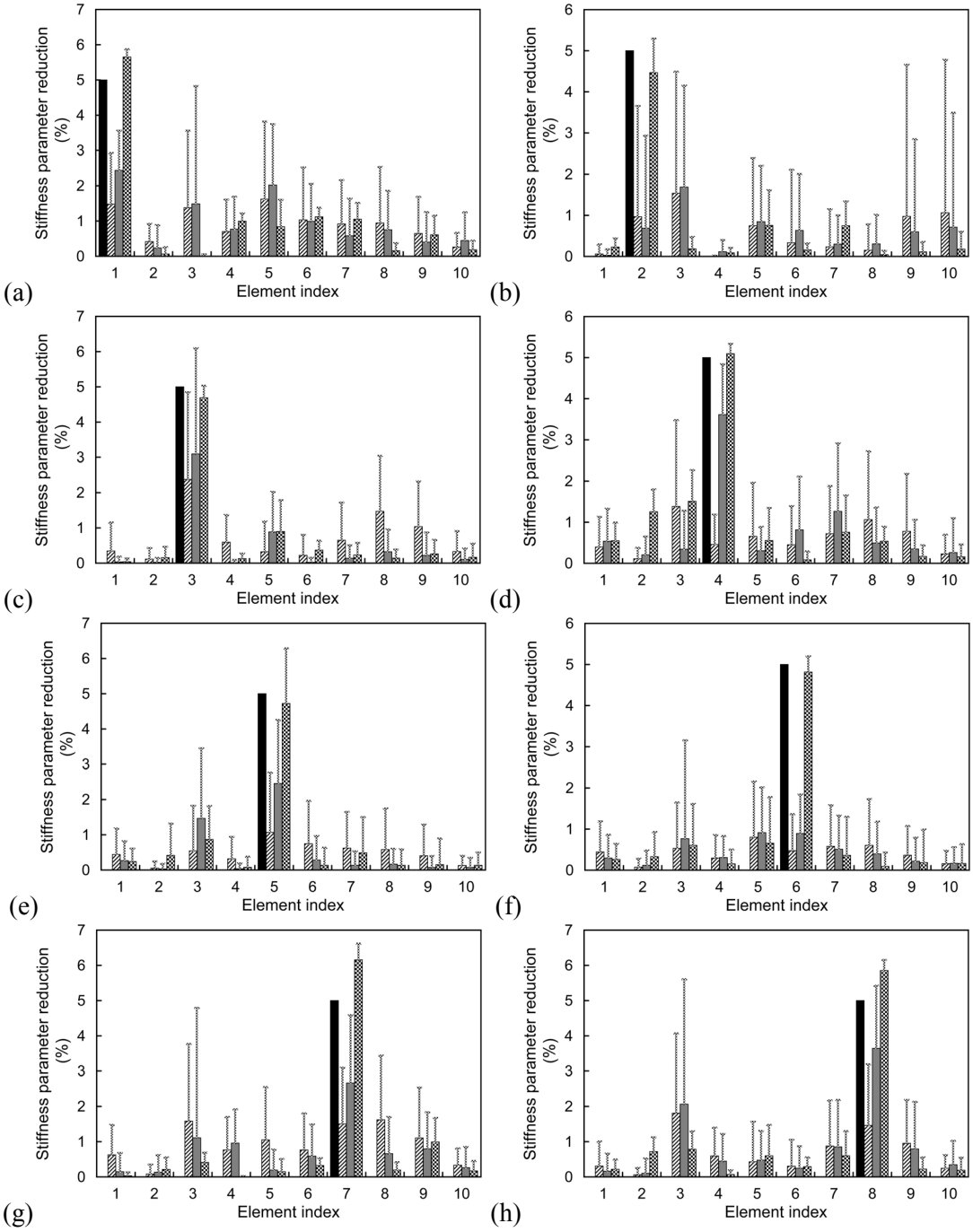

Figure **3.6**: Damage identification results using noise-contaminated natural frequencies. The noise level is v=0.5%. ■ Actual stiffness reduction; ▨ Prediction using noise-contaminated natural frequencies of the open-loop system; ▩ Prediction using noise-contaminated natural frequencies of the ad hoc closed-loop systems; ◘ Prediction using noise-contaminated natural frequencies of the optimal closed-loop systems.

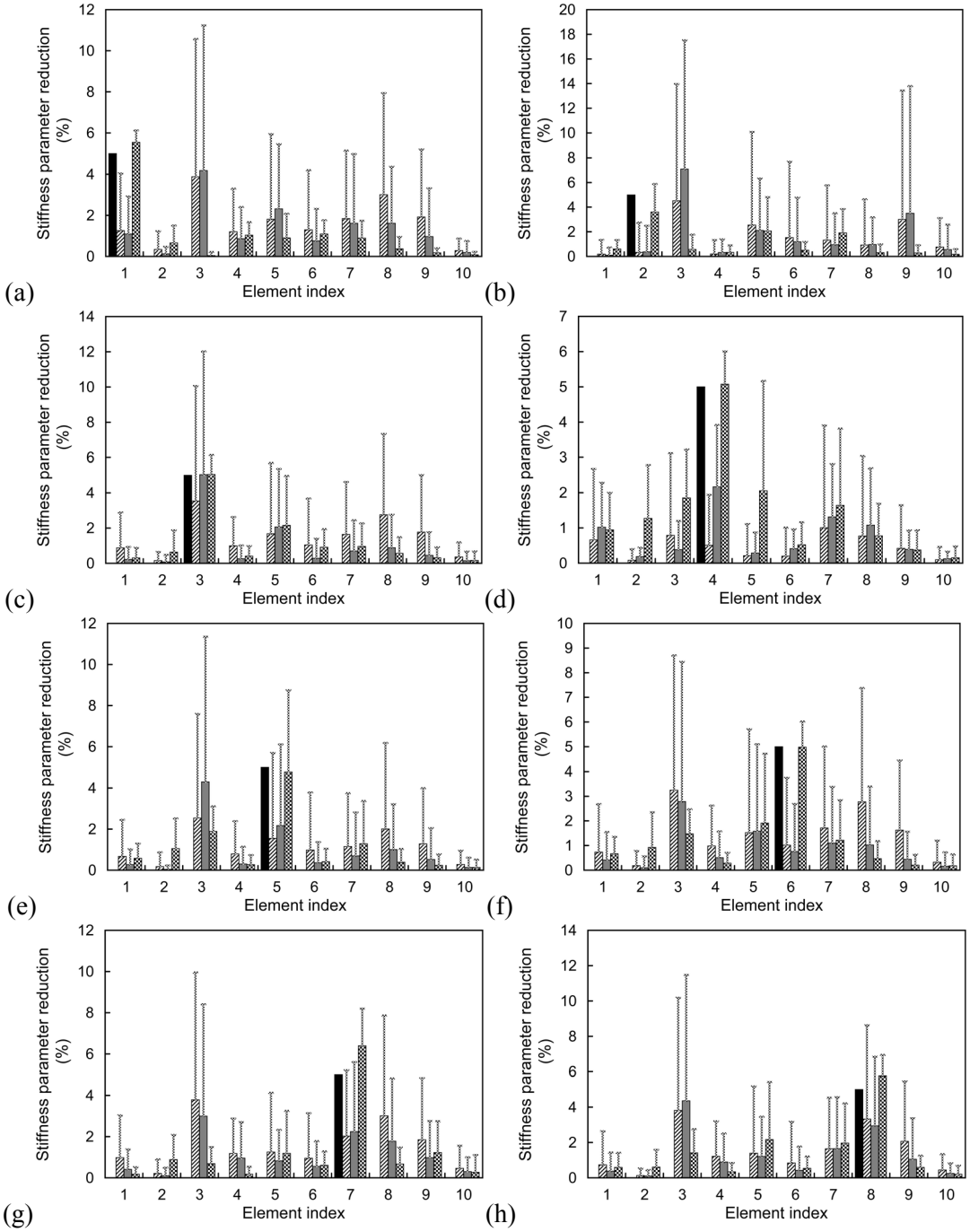

Figure 3.7: Damage identification results using noise-contaminated natural frequencies. The noise level is v=2.0%. ■ Actual stiffness reduction; ▨ Prediction using noise-contaminated natural frequencies of the open-loop system; ▩ Prediction using noise-contaminated natural frequencies of the ad hoc closed-loop systems; ▣ Prediction using noise-contaminated natural frequencies of the optimal closed-loop systems.

Chapter 4

Sensitivity-Enhancing Control Approach for Structural Model Updating

The major issue of implementing the two enhanced damage identification methods proposed in Chapter 2 and Chapter 3, is that both of them require an accurate finite element model of the structure for circuit/controller design and system analysis. There are two ways to address this issue: (1) one way is to use model updating techniques to obtain an accurate finite element model, and hence satisfy this requirement; (2) the other way is to use system identification techniques to identify a model directly from experimental data for circuit/controller design and system analysis, and hence frees the requirement of having an analytical model. This chapter focuses on the first method of using the model updating techniques, and the second method of using system identification techniques will be discussed in Chapter 5.

Although there are a variety of techniques available for model updating, it is preferred that the process of model updating utilizes the same hardware setup and physical quantity measurement as used for damage identification, which will greatly save the time and cost involved in the whole process. In fact, both of the proposed two damage identification methods can be extended for the application of structural model updating. With this, we can use the same set of hardware setup (i.e., integration of piezoelectric circuitry for the tunable circuitry approach or sensor-controller-actuator architecture for the sensitivity-enhancing control approach) and measure the same physical quantity (i.e., natural frequency) for both functions of model updating and

damage identification. Without loss of generality, this thesis will only focus on extending the sensitivity-enhancing control approach for structural model updating.

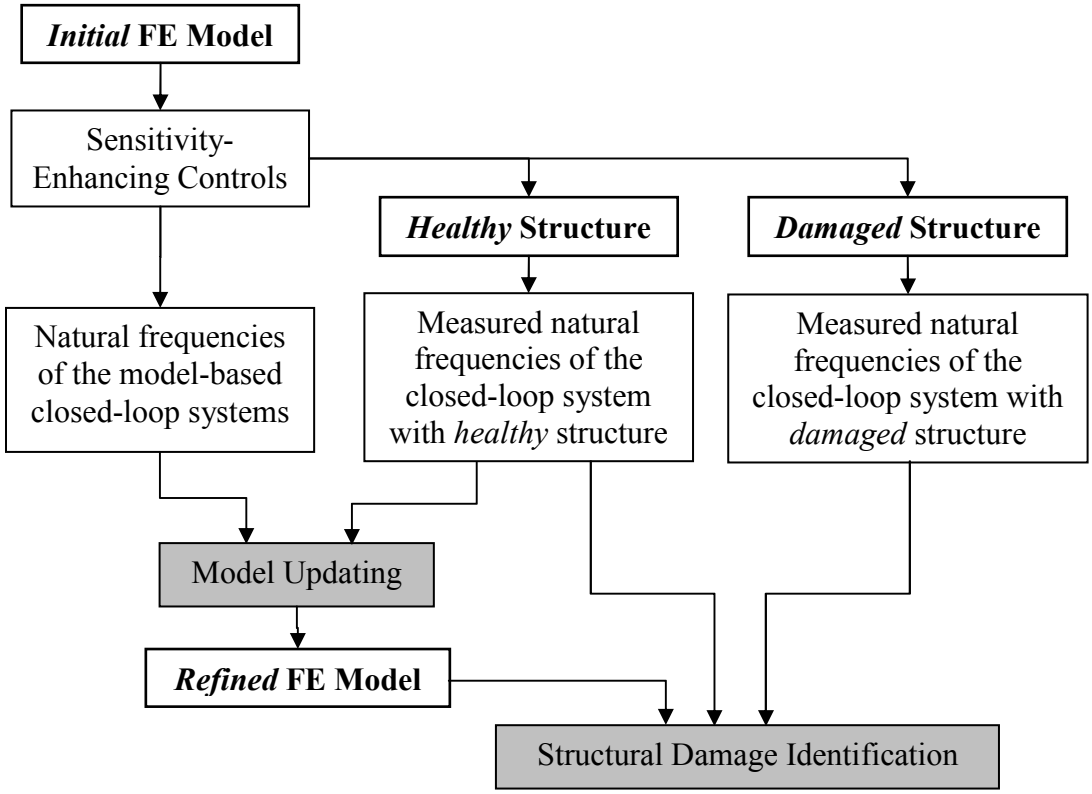

Figure 4.1: Schematic of the sensitivity-enhancing control approach for dual functions of structural model updating and damage identification

Therefore, the purpose of this chapter is to utilize the same concept of sensitivity-enhancing control as used for damage identification in Chapter 3 to develop a model updating scheme, so that we can use the same hardware setup (i.e., sensor-controller-actuator architecture) and measure the same physical quantity (i.e., natural frequency) for both functions of structural model updating and damage identification. Figure 4.1 shows the schematic of the sensitivity-enhancing control approach for dual functions of structural model updating and damage identification. From the initial finite element (FE)

model, a series of sensitivity-enhancing controls can be designed to enhance the frequency sensitivities to the updating structural parameters and/or damage parameters. The natural frequencies of the model-based closed-loop systems and those measured from the closed-loop systems associated with the healthy structure, can be used to update the initial FE model to obtain a refined FE model. The refined FE model, together with the measured frequency changes of the closed-loop systems before and after damage occurrence, can then be used to realize structural damage identification.

Since the structural damage identification using sensitivity-enhancing control with a refined FE model has been described in detail and numerically verified in Chapter 3, this chapter will only focus on the model updating process using sensitivity-enhancing controls.

4.1 Introduction

In structural dynamic analysis and control design problems, it is a common task for engineers to establish a mathematical model of the structure of interest. In many cases, the finite element method (FEM) is utilized to construct the mathematical model. However, it is well known from experience that an initial finite element model always differs from the actual structure due to the inevitable modeling errors in material properties, geometrical properties, and boundary conditions. Therefore, to obtain a reliable and high-fidelity model, it is imperative to refine the initial finite element model by correlating it with the experimentally measured data. This process is often called *model updating*, *model correlation*, or *model refinement*. The model updating process

involves modifications of the mass, stiffness and damping matrices of the mathematical model to achieve an improved agreement between the model predictions and the experimentally measured data from the actual structure.

From reviewing the basic concept of model updating, we realize that the problem of model updating is quite similar to the problem of damage identification. Both of them aim to identify the discrepancies in structural parameters that are responsible for the discrepancies observed in the measurement data. Structural damage identification aims to identify the damage (e.g., cracks, erosions, and delaminations) induced changes in structural parameters, based on the observed changes in the measurement data before and after damage occurrence. Similarly, structural model updating aims to find out the modeling errors in structural parameters based on the discrepancies between the model predictions and the experimentally measured data from the actual structure. Due to their similarity, the methods developed for structural damage identification can be easily extended for the application of model updating.

Similar to the practice of damage identification, the most commonly used experimental data for model updating is the modal information (i.e., natural frequencies and mode shapes) from vibration tests. However, it has been pointed out that the use of mode shape information for model updating entails three major difficulties [**85**,**86**]: (a) the mode shape measurement is more sensitive to measurement noise and carries more errors than frequency measurement [**104**,**105**]; (b) the measured mode shapes are in general incomplete in terms of spatial co-ordinates, and this would require either an expansion on the measured mode shapes or an reduction on the FE model, both of which may introduce additional errors to the measured data or the model; (c) the calculation of

mode shape sensitivities is more difficult than that of frequency sensitivities. Therefore, those techniques that require only the measured natural frequencies are more preferred for model updating. However, these techniques encounter the same limitations as encountered by the frequency-shift-based damage identification methods, and these limitations are, (a) deficiency of frequency measurement data; and (b) low sensitivity of natural frequency to the updating structural parameters [85,86,104,105].

From reviewing the above limitations of the natural frequency-based model updating techniques, one may realize that we can use the same concept of sensitivity-enhancing control as proposed in Chapter 3 to overcome these limitations. Therefore, the purpose of this chapter is to develop an enhanced frequency-based model updating method using the concept of sensitivity-enhancing control. First, the natural frequency sensitivity to model errors in structural parameters can be enhanced by integrating sensitivity-enhancing control to the structure. Second, by including the natural frequencies from a series of sensitivity-enhanced closed-loop systems, we can significantly enrich the frequency measurement data available for model updating.

4.2 Iterative Model Updating Method Using the Natural Frequencies of Sensitivity-Enhanced Closed-Loop Systems

In this section, a novel iterative model updating process using the concept of sensitivity-enhancing control is presented. First, the model updating process using the open-loop natural frequency is briefly summarized, and its limitations for the current practice are discussed. Second, the concept of sensitivity-enhancing control proposed in

Chapter 3, is utilized to develop an enhanced model updating method using natural frequencies of the sensitivity-enhanced closed-loop systems.

4.2.1 Model Updating Using the Open-Loop Natural Frequencies

For a flexible structure, an initial mathematical model can be constructed by using finite element method. The global mass matrix and stiffness matrix, $\boldsymbol{M}_0$ and $\boldsymbol{K}_0$, can be expressed as

$$\boldsymbol{M}_0 = \sum_{j=1}^{n} \boldsymbol{M}_j^e \tag{4.1}$$

$$\boldsymbol{K}_0 = \sum_{j=1}^{n} \boldsymbol{K}_j^e \tag{4.2}$$

Where $\boldsymbol{M}_j^e$ and $\boldsymbol{K}_j^e$ are the elemental mass matrix and stiffness matrix of the *j*th element. The natural frequencies associated with this model can be obtained by solving the following eigenvalue problem

$$\left(\boldsymbol{K}_0 - \omega_i^2 \boldsymbol{M}_0\right)\boldsymbol{u}_i = \boldsymbol{0} \tag{4.3}$$

Due to the idealizations involved in modeling the material properties, geometrical properties and boundary conditions, the mathematical model may differ from the actual structure. Thus, there are always discrepancies between the model parameters (such as stiffness and inertial) used in the mathematical model and those of the actual structure.

The process of model updating seeks to modify the mass and stiffness matrices of the initial model so that the updated mass and stiffness matrices will reproduce the

measured modal data from the actual structure as close as possible. The updated mass and stiffness matrices can be expressed as the summation of the initial values from the finite element (FE) model, $\boldsymbol{M}_0$ and $\boldsymbol{K}_0$, and their first perturbations with respect to updating parameters θ_j

$$\boldsymbol{M} = \boldsymbol{M}_0 + \sum_{j=1}^{l} \frac{\partial \boldsymbol{M}}{\partial \theta_j} \delta\theta_j \tag{4.4}$$

$$\boldsymbol{K} = \boldsymbol{K}_0 + \sum_{j=1}^{l} \frac{\partial \boldsymbol{K}}{\partial \theta_j} \delta\theta_j \tag{4.5}$$

where l is the total number of physical parameters that need to be updated, $\delta\theta_j$ is the model error of the physical parameter θ_j. The sensitivity of mass and stiffness matrices to updating parameters, $\partial \boldsymbol{M} / \partial \theta_j$ and $\partial \boldsymbol{K} / \partial \theta_j$, can be calculated from the initial mathematical model.

Given the natural frequency discrepancy between the initial model and the actual structure

$$\delta\boldsymbol{\omega} = \begin{pmatrix} \delta\omega_1 & \delta\omega_2 & \cdots & \delta\omega_q \end{pmatrix}^T \tag{4.6}$$

where q denotes the total number of measured natural frequencies, a first-order sensitivity based equation can be formulated to relate the frequency discrepancy vector $\delta\boldsymbol{\omega}$ and parameter modeling error vector $\delta\boldsymbol{\theta}$

$$\delta\boldsymbol{\omega} = \boldsymbol{S}\delta\boldsymbol{\theta} \tag{4.7}$$

where $\boldsymbol{S} \in \Re^{q \times l}$ is the frequency sensitivity matrix with respect to the updating parameters, and can be computed by using the following equation

$$\boldsymbol{S}(i,j) = \frac{\partial \omega_i}{\partial \theta_j} = \boldsymbol{u}_i^T \left[\frac{1}{2\omega_i} \frac{\partial \boldsymbol{K}}{\partial \theta_j} - \frac{\omega_i}{2} \frac{\partial \boldsymbol{M}}{\partial \theta_j} \right] \boldsymbol{u}_i \tag{4.8}$$

Since the number of measured natural frequencies (q) is usually much smaller than the number of physical parameters that need to be updated (l), Eq. (4.7) often results in a significantly underdetermined problem, and may not lead to an accurate solution of the modeling error vector of $\delta\boldsymbol{\theta}$. Moreover, due to the low sensitivity of natural frequency to parameter variation, the frequency difference between the mathematical model and the actual structure may not be accurately measured in the presence of noise. Because of these, the practice of model updating based on measured open-loop natural frequencies often encounters severe limitations.

4.2.2 Iterative Model Updating Method Using the Natural Frequencies of the Sensitivity-Enhanced Closed-Loop Systems

From reviewing the above limitations of model updating using open-loop natural frequency measurements, one may realize that the same concept of sensitivity-enhancing control as proposed for damage identification in Chapter 3, can be utilized to overcome both of the aforementioned limitations. In this subsection, we present a novel iterative model updating scheme that utilizes the natural frequencies of the sensitivity-enhanced closed-loop systems.

As demonstrated and verified in Chapter 3, an appropriately designed active feedback control can be applied to the structure to increase the sensitivity of natural frequencies to the structural parameters that need to be updated. Here we use the same controller design scheme as proposed in Section **3.4** of Chapter 3; namely, the eigenstructure assignment-based constrained optimization scheme, to design the sensitivity-enhancing feedback control for model updating. The details of this controller design scheme will not be reiterated here, one may refer to Section **3.4** in Chapter 3.

Assuming that we have designed a set of closed-loop systems with enhanced frequency sensitivities to updating parameters, the process of updating the structural parameters using the closed-loop natural frequencies is illustrated as follows. For each closed-loop system, a sensitivity-based equation can be obtained as

$$\delta\boldsymbol{\omega}^{ci} = \boldsymbol{S}^{ci}\delta\boldsymbol{\theta} \tag{4.9}$$

where $\delta\boldsymbol{\theta}$ is a vector of modeling errors in physical parameters, $\delta\boldsymbol{\omega}^{ci}$ is the frequency difference between the model and actual structure when the ith feedback control is applied, and $\boldsymbol{S}^{ci}$ is the frequency sensitivity matrix of the ith closed-loop system, whose elements can be calculated using

$$\boldsymbol{S}^{c}(i,j) = \frac{\partial\omega_i^c}{\partial\theta_j} = \left(\boldsymbol{v}_i^c\right)^T\left[\frac{1}{2\omega_i^c}\frac{\partial\boldsymbol{K}}{\partial\theta_j} - \frac{\omega_i^c}{2}\frac{\partial\boldsymbol{M}}{\partial\theta_j}\right]\boldsymbol{u}_i^c \tag{4.10}$$

where λ_i^c, $\boldsymbol{u}_i^c$ and $\boldsymbol{v}_i^c$ are the ith eigenvalue and its associated right and left eigenvectors of the closed-loop system.

Collecting the equations for all closed-loop systems, a combined equation is obtained as follows

$$\begin{Bmatrix} \delta\boldsymbol{\omega}^{c1} \\ \delta\boldsymbol{\omega}^{c2} \\ \vdots \\ \delta\boldsymbol{\omega}^{cp} \end{Bmatrix} = \begin{bmatrix} \boldsymbol{S}^{c1} \\ \boldsymbol{S}^{c2} \\ \vdots \\ \boldsymbol{S}^{cp} \end{bmatrix} \delta\boldsymbol{\theta} \quad \text{or} \quad \delta\boldsymbol{\omega}^{c} = \boldsymbol{S}^{c}\delta\boldsymbol{\theta} \tag{4.11}$$

where p is total number of closed-loop systems that have been designed. Note that by utilizing p closed-loop systems, the total number of frequency measurement data for model updating is increased by p times compared with the case of using the open-loop natural frequencies, whereas the number of updating parameters (i.e, dimension of $\delta\boldsymbol{\theta}$) does not change. This means that the deficiency of frequency measurement data can be greatly improved by including the natural frequencies from a series of closed-loop systems.

Based on Eq. (4.11), the modeling error vector $\delta\boldsymbol{\theta}$ can be estimated by minimizing the following performance index

$$J\left(\delta\boldsymbol{\theta}\right) = \left(\delta\boldsymbol{\omega}^{c} - \boldsymbol{S}^{c}\delta\boldsymbol{\theta}\right)^{T}\left(\delta\boldsymbol{\omega}^{c} - \boldsymbol{S}^{c}\delta\boldsymbol{\theta}\right) \tag{4.12}$$

The least-square solution of this minimization problem is obtained using the generalized inverse as follows

$$\delta\boldsymbol{\theta} = \left(\boldsymbol{S}^{c}\right)^{+}\delta\boldsymbol{\omega}^{c} \tag{4.13}$$

The above solution is based on a first-order linear approximation between the frequency discrepancies and parameter variations; this, however, may become inadequate when high sensitivity is introduced by the closed-loop control, which renders the second and higher order effects important. To obtain a more accurate estimation of the modeling errors, an iterative parameter updating process is used to compensate for the nonlinearity

of the relation between the frequency discrepancies and the modeling errors. A schematic diagram of the iterative process is given in Figure 4.2.

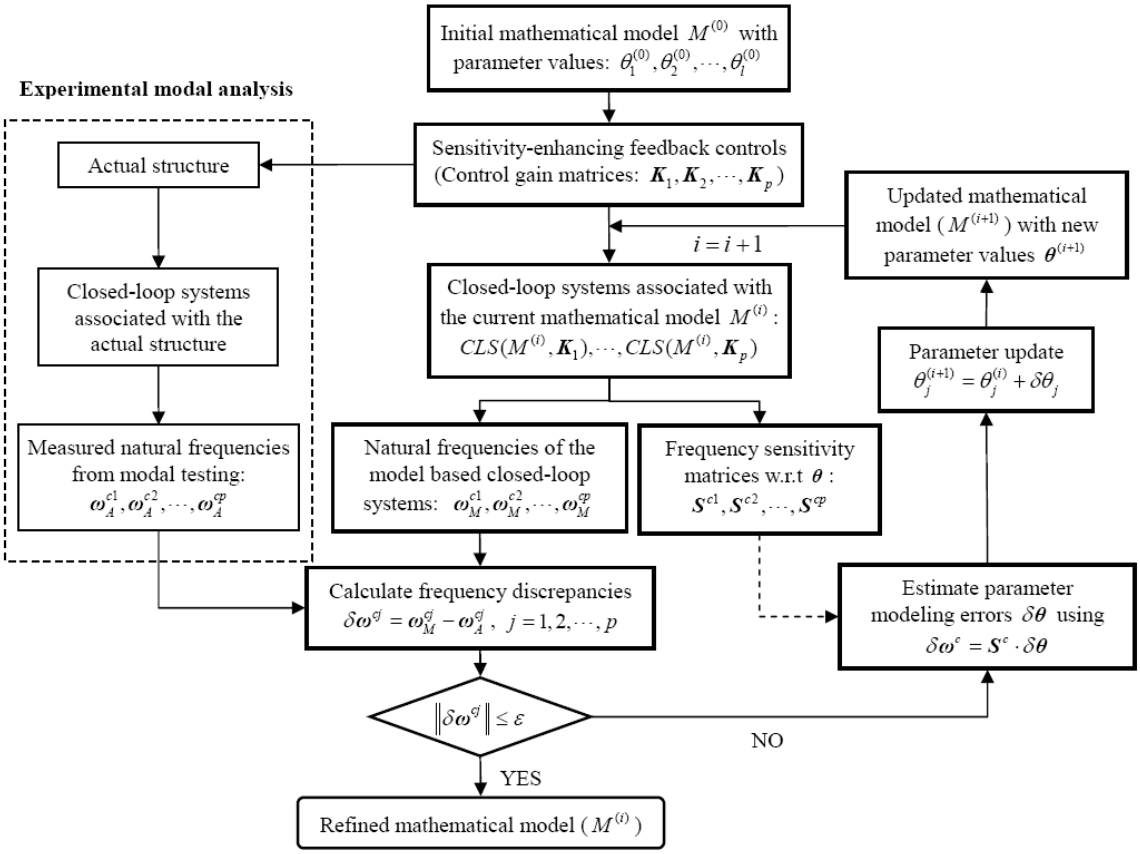

Figure 4.2: Schematic representation of the iterative process

The major steps involved in the iterative process are described as follows:

1. An initial mathematical model ($M^{(0)}$) is constructed. The physical parameters that need to be updated are θ_j ($j = 1, 2, \cdots, l$), and their initial values are $\theta_j^{(0)}$.

2. Based on the initial mathematical model ($M^{(0)}$), a series of closed-loop controls are designed to enhance the frequency sensitivity to the updating

parameters θ_j. The corresponding gain matrices of the closed-loop controls are $\boldsymbol{K}_1, \boldsymbol{K}_2, \cdots, \boldsymbol{K}_p$.

3. Apply the closed-loop controls designed in Step 2 to the actual structure, and measure the natural frequencies of the resulting closed-loop systems, $\boldsymbol{\omega}_A^{c1}, \boldsymbol{\omega}_A^{c2}, \cdots, \boldsymbol{\omega}_A^{cp}$.

4. Find the model-predicted natural frequencies under the aforementioned series of closed-loop controls. With the current mathematical model $M^{(i)}$ ($i = 0$ for the first iteration), the natural frequencies of these closed-loop systems, $\boldsymbol{\omega}_M^{c1}, \boldsymbol{\omega}_M^{c2}, \cdots, \boldsymbol{\omega}_M^{cp}$, are solved based on the corresponding eigenvalue problems. Using the modal data obtained for each closed-loop system, the frequency sensitivity matrix to the updating parameters θ_j can be calculated by utilizing Eq. (**4.10**), and they are denoted as $\boldsymbol{S}^{c1}, \boldsymbol{S}^{c2}, \cdots, \boldsymbol{S}^{cp}$.

5. Compare the closed-loop natural frequencies measured from the actual structure with those predicted from the model-based closed-loop systems,

   5.1 If the discrepancies are sufficiently small, an updated mathematical model that is sufficiently close to the actual structure is obtained, and the iterative process stops;

   5.2 If the discrepancies do not satisfy the criterion, a sensitivity-based equation is utilized to estimate the parameter modeling errors in the current mathematical model $M^{(i)}$.

6. We update the physical parameters using $\theta_j^{(i+1)} = \theta_j^{(i)} + \delta\theta_j$, and an updated mathematical model $M^{(i+1)}$ is obtained with the new parameter values, $\boldsymbol{\theta}^{(i+1)}$.
7. Repeat Steps 4-6.

4.3 Illustrative Example of Model Updating

In this section, a cantilevered beam is used as an illustrative example to demonstrate and verify the proposed model updating method.

4.3.1 Schematic of the Illustrative Example

A schematic of the system model used for numerical analysis is given in Figure 4.3. The cantilevered beam is evenly discretized into 10 elements. Four piezoelectric actuators bonded on the upper surface of the beam are used as control input actuators, and they are located on the second, fourth, sixth, and eighth beam elements, respectively. The control voltage sources for these four control input actuators are V_1, V_2, V_3, and V_4, respectively. Another piezoelectric transducer bonded on the bottom surface of the second element is used to excite the structure for frequency response measurement, where V_0 is the excitation input voltage. V_0 is in the form of Gaussian white noise with zero mean and 50V standard deviation. The mass density, Young's modulus, and piezoelectric constant of the piezoelectric actuators are, respectively, $\rho_p = 7.6\times10^3\,\text{kg/m}^3$, $E_p = 5.9\times10^{10}\,\text{N/m}^2$, and $d_{31} = -2.76\times10^{-10}\,\text{N/C}$.

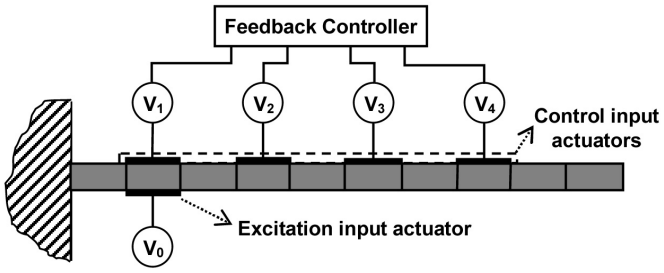

Figure **4.3**: Schematic of the system model

An initial mathematical model of the cantilevered beam is constructed by using the FE method. The global mass and stiffness matrices of the FE model can be written as

$$\boldsymbol{M}_0 = \sum_{j=1}^{n} m_j \boldsymbol{M}_j^e \text{, and } \boldsymbol{K}_0 = \sum_{j=1}^{n} k_j \boldsymbol{K}_j^e \qquad (4.14)$$

where $\boldsymbol{M}_j^e$ and $\boldsymbol{K}_j^e$ are the elemental mass matrix and stiffness matrix of the *j*th structural element. m_j and k_j are the mass parameter and stiffness parameter of the *j*th structural element, and are defined as

$$m_j = (\rho A)_j, \quad k_j = (EI)_j \qquad (4.15)$$

where ρ is the material density, A is the beam section area, E is the Young's modulus, and I is the second moment of area. The initial values of the mass and stiffness parameters are calculated using the nominal values of the following structural parameters: beam length $L = 0.40m$, beam width $w = 2.6cm$, beam thickness $t = 3.4mm$, material density $\rho = 2410kg/m^3$, and elastic modulus $E = 6.6 \times 10^{10} N/m^2$.

Due to the idealizations involved in modeling the material and geometry properties, the mass and stiffness parameters, m_j and k_j, may not be a true

representation of the actual structure. To obtain a more accurate FE model of the structure, we need to find out the model errors in mass and stiffness parameters, i.e., δm_j and δk_j, so that the updated system matrices

$$\boldsymbol{M} = \sum_{j=1}^{n} \left(m_j + \delta m_j \right) \boldsymbol{M}_j^e \text{, and } \boldsymbol{K} = \sum_{j=1}^{n} \left(k_j + \delta k_j \right) \boldsymbol{K}_j^e \tag{4.16}$$

reproduce the measured modal data from the actual structure as close as possible.

In the following, the proposed model updating method is used to update the FE model by identifying the model errors in the mass and stiffness parameters. More specifically, a series of closed-loop controls are designed to enhance the frequency sensitivities to mass or stiffness parameters. Then the natural frequencies of these sensitivity-enhanced closed-loop systems are utilized to update the mass and stiffness parameters in the initial FE model.

4.3.2 Design of Sensitivity-Enhancing Controls for Model Updating

In the FE model, the derivatives of the mass and stiffness matrices with respect to the mass parameter m_j and stiffness parameter k_j, respectively, can be solved as

$$\frac{\partial \boldsymbol{M}_0}{\partial m_j} = \boldsymbol{M}_j^e, \quad \frac{\partial \boldsymbol{K}_0}{\partial m_j} = \boldsymbol{K}_j^e \tag{4.17}$$

where $\boldsymbol{M}_j^e$ and $\boldsymbol{K}_j^e$ are the elemental mass matrix and stiffness matrix of the jth element, respectively. Using Eq. (4.8), the sensitivities of the open-loop natural frequency ω_i^o with respect to the mass and stiffness parameters can be obtained as

$$\frac{\partial \omega_i^o}{\partial m_j} = -\frac{\omega_i^o}{2}\left(\boldsymbol{u}_i\right)^T \boldsymbol{M}_j^e \left(\boldsymbol{u}_i\right) \tag{4.18}$$

$$\frac{\partial \omega_i^o}{\partial k_j} = \frac{1}{2\omega_i^o}\left(\boldsymbol{u}_i\right)^T \boldsymbol{K}_j^e \left(\boldsymbol{u}_i\right) \tag{4.19}$$

Then the frequency sensitivity matrices to the mass and stiffness parameters for the open-loop system can be constructed as

$$\boldsymbol{S}_m^o\left(i,j\right) = \frac{\partial \omega_i^o}{\partial m_j}, \qquad \boldsymbol{S}_k^o\left(i,j\right) = \frac{\partial \omega_i^o}{\partial k_j} \tag{4.20}$$

For the closed-loop system, the sensitivities of closed-loop natural frequency ω_i^c with respect to the mass and stiffness parameters can be obtained using Eq. (4.10)

$$\frac{\partial \omega_i^c}{\partial m_j} = -\frac{\omega_i^c}{2}\left(\boldsymbol{v}_i^c\right)^T \boldsymbol{M}_j^e \left(\boldsymbol{u}_i^c\right) \tag{4.21}$$

$$\frac{\partial \omega_i^c}{\partial k_j} = \frac{1}{2\omega_i^c}\left(\boldsymbol{v}_i^c\right)^T \boldsymbol{K}_j^e \left(\boldsymbol{u}_i^c\right) \tag{4.22}$$

where $\boldsymbol{u}_i^c$ and $\boldsymbol{v}_i^c$ are the *i*th right and left eigenvector of the closed-loop system. The frequency sensitivity matrices to the mass and stiffness parameters for the closed-loop system can be constructed as

$$\boldsymbol{S}_m^c\left(i,j\right) = \frac{\partial \omega_i^c}{\partial m_j}, \qquad \boldsymbol{S}_k^c\left(i,j\right) = \frac{\partial \omega_i^c}{\partial k_j} \tag{4.23}$$

Table 4.1: Closed-loop systems with enhanced frequency sensitivities to mass parameters

System ID	Actuator locations	Optimization parameters	First three closed-loop eigenvalues
CLS-1	2,4,6,8	$C_0 = 1.0e13$, $\bar{w}_i = 1.0$	$\lambda_1^c = 2.70\lambda_1^o$, $\lambda_2^c = 1.89\lambda_2^o$, $\lambda_3^c = 1.30\lambda_3^o$
CLS-2	2,4,6,8	$C_0 = 1.0e14$, $\bar{w}_i = 1.0$	$\lambda_1^c = 2.99\lambda_1^o$, $\lambda_2^c = 1.62\lambda_2^o$, $\lambda_3^c = 1.52\lambda_3^o$
CLS-3	2,4,6	$C_0 = 1.0e13$, $\bar{w}_i = 1.0$	$\lambda_1^c = 3.00\lambda_1^o$, $\lambda_2^c = 1.54\lambda_2^o$, $\lambda_3^c = 1.28\lambda_3^o$
CLS-4	2,4,6	$C_0 = 1.0e14$, $\bar{w}_i = 1.0$	$\lambda_1^c = 2.75\lambda_1^o$, $\lambda_2^c = 1.11\lambda_2^o$, $\lambda_3^c = 1.26\lambda_3^o$
CLS-5	2,4,8	$C_0 = 1.0e13$, $\bar{w}_i = 1.0$	$\lambda_1^c = 2.71\lambda_1^o$, $\lambda_2^c = 1.79\lambda_2^o$, $\lambda_3^c = 1.46\lambda_3^o$
CLS-6	2,4,8	$C_0 = 1.0e14$, $\bar{w}_i = 1.0$	$\lambda_1^c = 3.00\lambda_1^o$, $\lambda_2^c = 1.43\lambda_2^o$, $\lambda_3^c = 1.23\lambda_3^o$

Table 4.2: Closed-loop systems with enhanced frequency sensitivities to stiffness parameters

System ID	Actuator locations	Optimization parameters	First three closed-loop eigenvalues
CLS-7	2,4,6,8	$C_0 = 1.0e14$, $\bar{w}_i = 1.0$	$\lambda_1^c = 0.91\lambda_1^o$, $\lambda_2^c = 0.98\lambda_2^o$, $\lambda_3^c = 0.65\lambda_3^o$
CLS-8	2,4,6,8	$C_0 = 1.0e15$, $\bar{w}_i = 1.0$	$\lambda_1^c = 0.95\lambda_1^o$, $\lambda_2^c = 0.89\lambda_2^o$, $\lambda_3^c = 0.67\lambda_3^o$
CLS-9	2,4,6	$C_0 = 1.0e14$, $\bar{w}_i = 1.0$	$\lambda_1^c = 0.99\lambda_1^o$, $\lambda_2^c = 0.87\lambda_2^o$, $\lambda_3^c = 0.62\lambda_3^o$
CLS-10	2,4,6	$C_0 = 1.0e15$, $\bar{w}_i = 1.0$	$\lambda_1^c = 0.97\lambda_1^o$, $\lambda_2^c = 0.41\lambda_2^o$, $\lambda_3^c = 0.67\lambda_3^o$
CLS-11	2,4,8	$C_0 = 1.0e14$, $\bar{w}_i = 1.0$	$\lambda_1^c = 0.91\lambda_1^o$, $\lambda_2^c = 0.85\lambda_2^o$, $\lambda_3^c = 0.83\lambda_3^o$
CLS-12	2,4,8	$C_0 = 1.0e15$, $\bar{w}_i = 1.0$	$\lambda_1^c = 0.91\lambda_1^o$, $\lambda_2^c = 0.82\lambda_2^o$, $\lambda_3^c = 0.83\lambda_3^o$

The eigenstructure assignment based method described in Section 3.4 of Chapter 3 is used to design the closed-loop controls to enhance the sensitivities of natural frequencies to mass and stiffness parameters. Six closed-loop controls are designed to enhance the frequency sensitivities to mass parameters, and the resulting sensitivity-enhanced closed-loop systems are listed in Table 4.1. In the table, the first column gives the system ID, the second column provides information about the use of actuators for

each closed-loop system, the third column gives the parameter setting for the optimization process, and the fourth column shows the first three eigenvalues of the closed-loop system (i.e., ratios to their corresponding open-loop ones). Another six closed-loop controls are designed to enhance the frequency sensitivities to stiffness parameters, and the resulting sensitivity-enhanced closed-loop systems are listed in Table 4.2. For each closed-loop system, the associated actuator usage, parameter setting for the optimization process, and the first three eigenvalues are given in the second, third, and fourth columns, respectively.

4.3.3 Model Updating Using the Closed-Loop Natural Frequencies

In this subsection, we will use the natural frequencies of sensitivity-enhanced closed-loop systems in Table 4.1 and Table 4.2 to update the mass and stiffness parameters of the initial FE model. In our numerical analysis, only the first three natural frequencies of each closed-loop system are utilized for the model updating process.

As proposed, an iterative process is utilized to update the mass and stiffness parameters based on the frequency difference between the model and the actual structure. In each iteration, the mass and stiffness parameters are updated by estimating the parameter errors in the current model. The modeling errors of mass and stiffness parameters can be estimated by solving the following sensitivity-based equation

$$\begin{Bmatrix} \delta\boldsymbol{\omega}^{c1} \\ \delta\boldsymbol{\omega}^{c2} \\ \vdots \\ \delta\boldsymbol{\omega}^{c12} \end{Bmatrix} = \begin{bmatrix} \boldsymbol{S}_m^{c1} & \boldsymbol{S}_k^{c1} \\ \boldsymbol{S}_m^{c2} & \boldsymbol{S}_k^{c2} \\ \vdots & \vdots \\ \boldsymbol{S}_m^{c12} & \boldsymbol{S}_k^{c12} \end{bmatrix} \begin{Bmatrix} \delta\boldsymbol{m} \\ \delta\boldsymbol{k} \end{Bmatrix} \tag{4.24}$$

where $\delta\boldsymbol{\omega}^{ci} \in \Re^{3\times 1}$ $(i = 1, 2, \cdots, 12)$ is the frequency difference of the ith closed-loop system (CLS-i) between the current FE model and the actual structure, $\boldsymbol{S}_m^{ci} \in \Re^{3\times 10}$ and $\boldsymbol{S}_k^{ci} \in \Re^{3\times 10}$ are the frequency sensitivity matrices to the mass and stiffness parameters, respectively.

In our numerical analysis, a series of random numbers are utilized to simulate the modeling errors in mass and stiffness parameters. With these modeling errors, the actual values of the mass and stiffness parameters can be obtained, and then the actual structure can be represented by the FE model with the actual values of the mass and stiffness parameters.

In the first example of model updating, the modeling errors in mass and stiffness parameters are given as follows:

$$\delta m_j / m_j = \{\text{-3.04\%} \quad \text{4.06\%} \quad \text{-2.68\%} \quad \text{4.44\%} \quad \text{-3.33\%} \quad \text{6.19\%} \quad \text{1.23\%} \quad \text{-3.92\%} \quad \text{5.15\%} \quad \text{1.50\%}\} \tag{4.25}$$

$$\delta k_j / k_j = \{\text{-2.73\%} \quad \text{3.02\%} \quad \text{-5.17\%} \quad \text{3.79\%} \quad \text{-1.80\%} \quad \text{-6.19\%} \quad \text{0.33\%} \quad \text{4.46\%} \quad \text{-3.16\%} \quad \text{0.50\%}\} \tag{4.26}$$

Note that the modeling errors are given as percentages relative to the parameters' nominal values.

For the open-loop system without active feedback control, the differences of the first three natural frequencies between the initial FE model and the actual structure are given in the first row in Table **4.3**. Then we look at the effects of modeling errors on the natural frequencies of the sensitivity-enhanced closed-loop systems listed in Table **4.1** and Table **4.2**. The closed-loop natural frequency discrepancies between the initial FE

model and the actual structure are given in Table 4.3. For each closed-loop natural frequency discrepancy, its ratio to the corresponding open-loop natural frequency discrepancy is also given as the number in the parenthesis. It can be easily seen that the frequency discrepancies of the closed-loop systems are much larger than their corresponding ones of the open-loop system. Therefore, by utilizing the sensitivity-enhancing feedback controls, the sensitivities of natural frequencies to modeling errors in the mass/stiffness parameters are significantly enhanced.

Table 4.3: Frequency discrepancies of the open-loop and closed-loop systems between the initial FE model and the actual structure

Systems	$\delta\omega_1$ (rad/s)	$\delta\omega_2$ (rad/s)	$\delta\omega_3$ (rad/s)
Open-loop	-1.85	-10.84	-13.14
CLS-1	6.00 (-3.24)	231.14 (-21.32)	-120.72 (9.19)
CLS-2	4.84 (-2.62)	17.62 (-1.63)	416.12 (-31.67)
CLS-3	2.90 (-1.57)	20.06 (-1.85)	275.98 (-21.00)
CLS-4	-62.77 (33.91)	-72.93 (6.73)	-36.72 (2.79)
CLS-5	13.31 (-7.19)	74.11 (-6.84)	-57.71 (4.39)
CLS-6	13.29 (-7.18)	19.46 (-1.79)	-27.38 (2.08)
CLS-7	-10.74 (5.80)	-74.85 (6.90)	-54.06 (4.11)
CLS-8	-1.92 (1.04)	-109.33 (10.08)	33.01 (2.51)
CLS-9	-15.10 (8.16)	-66.41 (6.13)	55.97 (-4.26)
CLS-10	27.42 (-14.81)	-33.14 (3.06)	34.32 (-2.61)
CLS-11	11.27 (-6.09)	135.27 (-12.48)	260.05 (-19.79)
CLS-12	10.61 (-5.73)	-68.84 (6.35)	72.42 (-5.51)

Then the proposed model updating method is used to update the mass and stiffness parameters of the initial FE model, and the results are presented in Figure 4.4. Figure 4.4(a) shows the estimation of the modeling errors in mass parameters, and

Figure 4.4(b) shows that estimation of the modeling errors in stiffness parameters. In each figure, the horizontal axis represent the index of structural element, the vertical axis represents the modeling error in mass/stiffness parameter of that corresponding element. It is worth mentioning that the mass parameter of the first element and the stiffness parameter of the last element are not included in the updating process. The reason is that even the closed-loop natural frequencies are insensitive to these two parameters. In each figure, the symbols of "■" represent the actual model errors, the symbols of "◊" and "□" represent the estimation of modeling errors in the first and second iteration, and the symbols of "○" represent the final estimation of the modeling errors after the iterative process converges. From these two figures, we can see that after only five iterations, the estimated modeling errors of both mass parameters and stiffness parameters match quite well with their actual values.

To illustrate the importance of enriching frequency measurement data for the model updating process, we compared the model updating results by using different numbers of closed-loop natural frequencies. Figure 4.5(a)-(b) shows the model updating results for 5 different cases, i.e., using the natural frequencies of two closed-loop system (CLS 1,2 or CLS 7,8), four closed-loop systems (CLS 1,2,7,8), eight closed-loop systems (CLS 1-4, 7-10), and twelve closed-loop systems (CLS 1-12). When we look at the results in each figure, we can easily find out that increasing the number of closed-loop systems used for model updating significantly improves the resulting estimation of the modeling errors in both mass and stiffness parameters. This also verifies the proposed idea of using multiple closed-loop controls to enrich frequency measurement data for model updating.

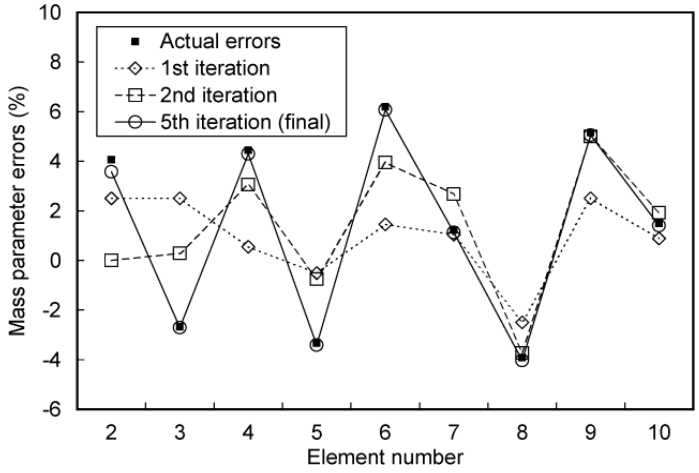

(a) Estimation of the mass parameter errors

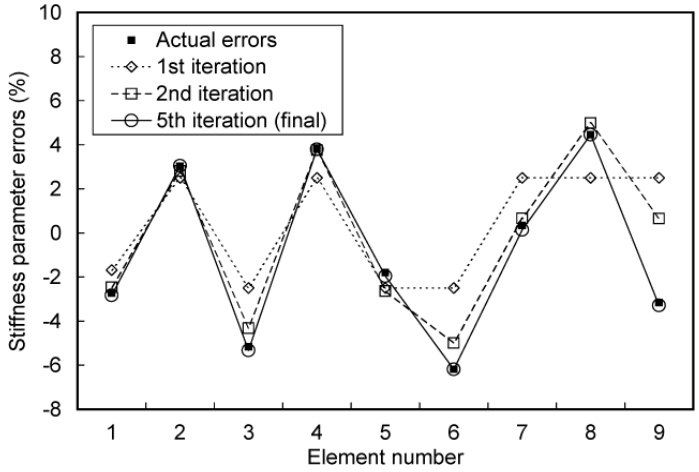

(b) Estimation of the stiffness parameter errors

Figure **4.4**: Estimation of the modeling errors in mass and stiffness parameters for case I

For a second example of model updating, the actual modeling errors of the mass and stiffness parameters are set as follows

$$\delta m_j / m_j = \{5.03\% \quad 4.77\% \quad -6.42\% \quad -4.29\% \quad 3.60\% \quad -3.49\% \quad 1.14\% \quad 4.93\% \quad -3.09\% \quad 2.61\%\} \tag{4.27}$$

$$\delta k_j / k_j = \{-3.26\% \quad -3.91\% \quad 1.07\% \quad -4.27\% \quad 2.81\% \quad -5.93\% \quad 1.45\% \quad 2.51\% \quad -3.20\% \quad -1.95\%\} \tag{4.28}$$

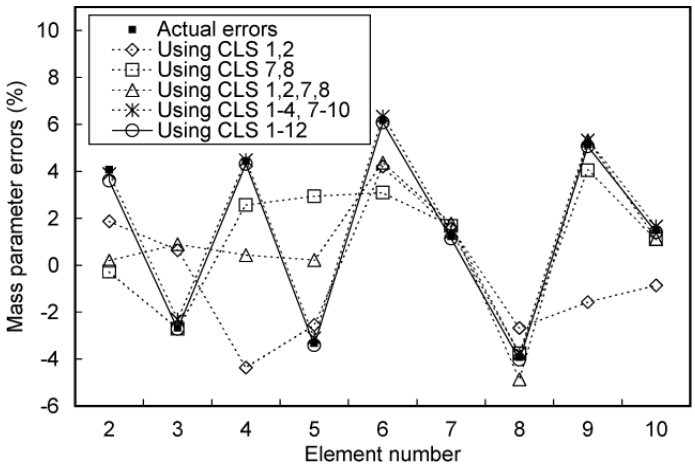

(a) Estimation of the mass parameter errors

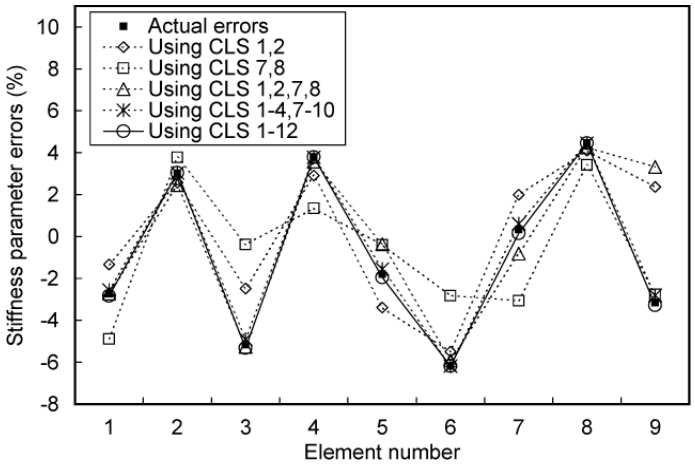

(b) Estimation of the stiffness parameter errors

Figure 4.5: Comparison of the estimated modeling errors by using different numbers of closed-loop natural frequencies

Again, the first three natural frequencies of those sensitivity-based closed-loop systems listed in Table 4.1 and Table 4.2 are utilized to update the mass and stiffness parameters of the initial FE model. The results of model updating are given in Figure 4.6, where Figure 4.6(a) shows the estimation of the mass parameter errors, and Figure 4.6(b) shows the estimation of the stiffness parameter errors. As shown in both

figures, the estimated modeling errors in mass/stiffness parameters converge to their actual values after five iterations of parameter updating.

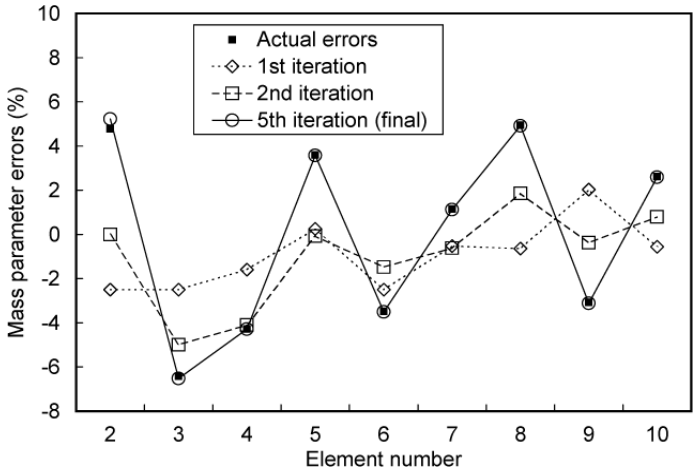

(a) Estimation of the mass parameter errors

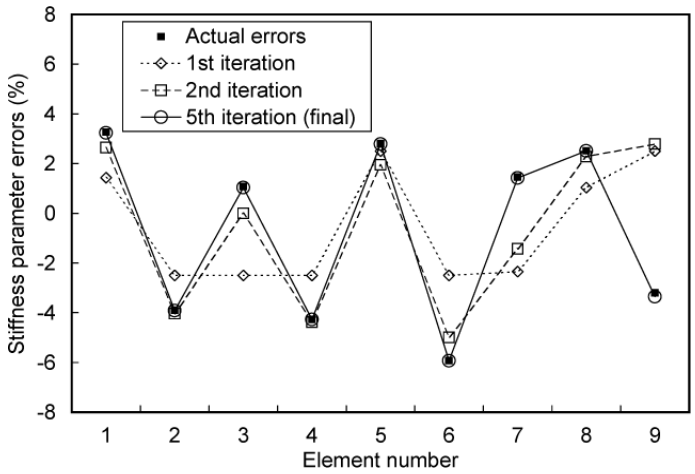

(b) Estimation of the stiffness parameter errors

Figure **4.6**: Estimation of the modeling errors in mass and stiffness parameters for case II

In real applications, the natural frequency measurements are subjected to various types of uncertainties such as the effect of measurement noise. To evaluate the robustness of the proposed model updating method with respect to uncertainties in frequency measurement, we add random noise to the frequency measurement and use

noise-contaminated natural frequencies to perform model updating. The effects of measurement noise on the measured natural frequencies are simulated using the following equation

$$\begin{bmatrix} \tilde{\boldsymbol{\omega}}_A^{c1} \\ \tilde{\boldsymbol{\omega}}_A^{c2} \\ \vdots \\ \tilde{\boldsymbol{\omega}}_A^{c12} \end{bmatrix} = \begin{bmatrix} \boldsymbol{\omega}_A^{c1} \\ \boldsymbol{\omega}_A^{c2} \\ \vdots \\ \boldsymbol{\omega}_A^{c12} \end{bmatrix} + \nu \boldsymbol{R} \begin{bmatrix} \boldsymbol{\omega}_A^{c1} \\ \boldsymbol{\omega}_A^{c2} \\ \vdots \\ \boldsymbol{\omega}_A^{c12} \end{bmatrix} \tag{4.29}$$

where $\boldsymbol{\omega}_A^{ci}$ is the noise-free natural frequencies of the ith closed-loop system (i.e., calculated from the FE model with actual mass and stiffness parameters), $\tilde{\boldsymbol{\omega}}_A^{ci}$ is the noise-contaminated natural frequencies to simulate the actual measurement from the structural system, $\boldsymbol{R}$ is a diagonal matrix whose diagonal entries are independent, normally distributed random numbers with mean 0, variance 1, and standard deviation 1, and $\nu \in [0, 1]$ represents the noise level.

As an illustrative example, here we use noise-contaminated natural frequencies to perform model updating for case I. The noise level is set to be $\nu = 0.1\%$. 200 independent sets of random numbers are generated and added to the noise-free natural frequencies to simulate the effect of measurement noise, and then the resulting 200 sets of noise-contaminated natural frequencies are used to perform model updating, respectively.

The results of model updating are presented in Figure 4.7, where the symbols of "○" represent the average of the resulting 200 estimations of parameter modeling errors, and the standard deviation of the 200 estimations are represented by the symbols of "I" across the average. From the figure, we can see that the mean of the estimated parameter

modeling errors (both mass and stiffness parameter errors) matches well with the actual modeling errors; moreover, the standard deviation of the results is within an acceptable range. Therefore, the proposed model updating method is robust against uncertainties in the natural frequency measurement.

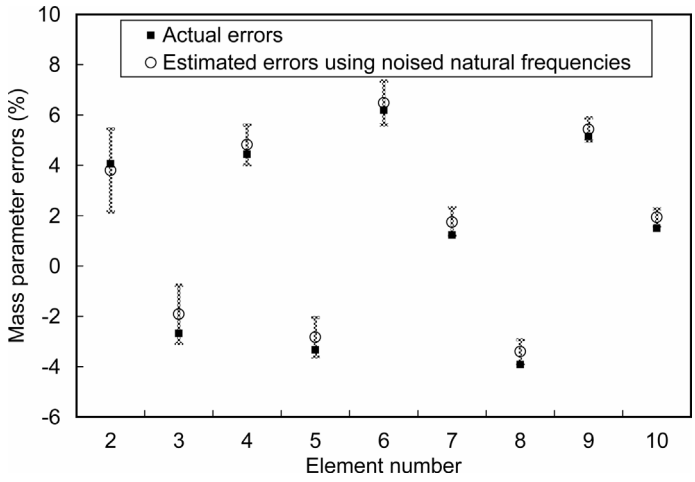

(a) Estimation of the mass parameter errors

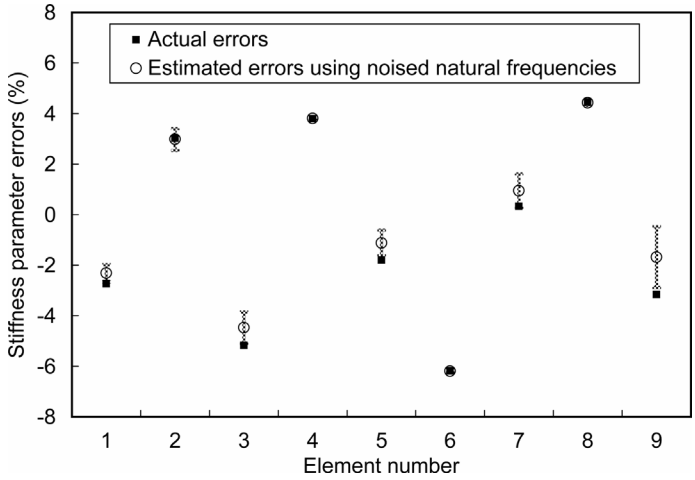

(b) Estimation of the stiffness parameter errors

Figure 4.7: Effects of measurement noise on the model updating results

4.4 Summary

In this chapter, a novel model updating method using natural frequencies of sensitivity-enhanced closed-loop system is developed. The proposed method effectively overcomes the well-known limitations of the traditional frequency-based model updating technique. First, closed-loop control is applied to the structure to enhance the frequency sensitivity to modeling errors in physical parameters. Second, the frequency measurement data available for model updating can be greatly enriched by including natural frequencies of a series of closed-loop systems. An iterative process is developed to update the physical parameters based on frequency discrepancy between the mathematical model and the actual structure. Numerical analysis on a benchmark structure is carried out to verify the proposed model updating method. Results show that the model errors in the FE model can be accurately identified by using the proposed method. The proposed method is robust to certain level of measurement noise in the frequency measurement.

Chapter 5

Experiment Investigation: Structural Damage Detection Using Sensitivity-Enhancing Feedback Control and Identified Model

In this chapter, a laboratory experiment is designed and carried out to verify the sensitivity-enhancing control approach for frequency-shift-based damage detection enhancement. In this experiment, a system identification technique is utilized to identify a mathematical model for controller design and system analysis. With this, the proposed damage detection method using sensitivity-enhancing control no longer requires an analytical model, which greatly favors the implementation of this method for applications on complex structures that are difficult to model accurately.

This chapter is organized as follows. The first section gives an overall description of the experimental system including hardware setup, experiment objective, and procedure. In the second section, a system identification technique is utilized to identify a state-space model of the structural system from the measured frequency response functions (FRF). After that, the identified model is utilized to design the sensitivity-enhancing control to enhance the frequency sensitivity to mass variations in the structure. Finally, the designed sensitivity-enhancing feedback control is implemented to the structure using Simulink/dSpace real-time interface (RTI). A series of tests are carried out to evaluate the sensitivity enhancement performance of the designed controllers.

5.1 Experimental Setup and Overall Description

The overall experimental setup is illustrated in Figure 5.1. The experimental test stand consists of a cantilevered beam structure, dynamic signal analyzer and function generator, a laser vibrometer sensing instrument, power amplifier, signal conditioner, and dSPACE data acquisition system. The manufacturer and model information of the above instruments used in this experiment is given as follows:

- Dynamic Signal Analyzer (HP 35665A)
- Laser Vibrometer Sensing Instrument (Polytec OFV 303 Sensor Head & Polytec OFV 3001S Laser Vibrometer Controller)
- Power Amplifier (PCB Piezotronics 790 Series Power Amplifier)
- Signal Conditioner (DL Instruments Model 4302 Filter)
- Data Acquisition System (dSPACE 1103)

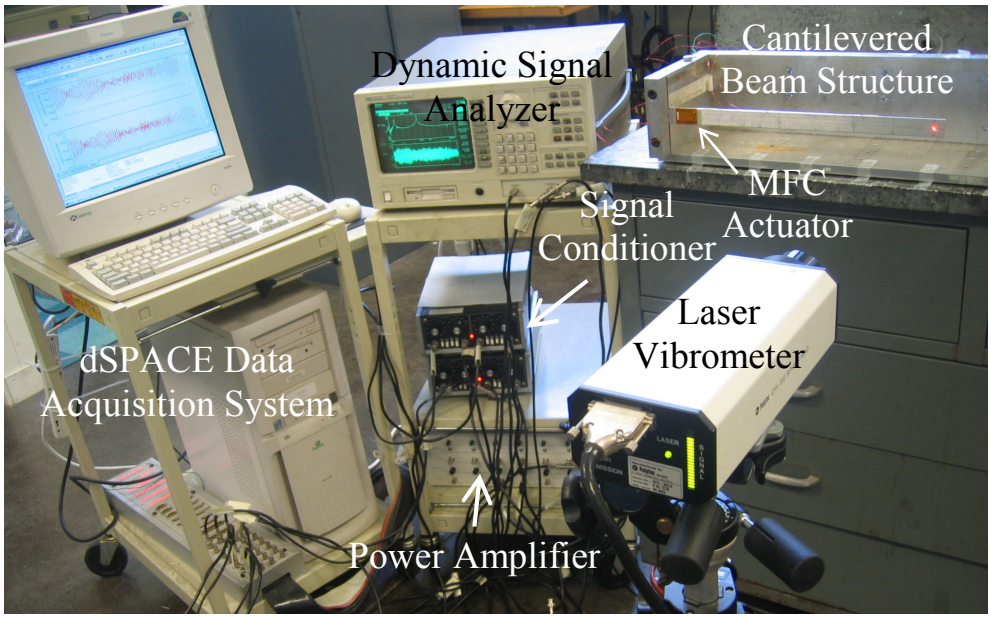

Figure 5.1: Experimental setup

Figure 5.2 shows the schematic of the experimental setup. As shown in the figure, three Macro Fiber Composite (MFC) actuators (a photograph and schematic of the MFC actuator is shown in Figure 5.3) are bonded on the bottom and top surfaces of the host beam structure. The MFC actuator boned on the bottom surface is used to excite the structure to produce vibrations, and the other two MFC actuators on the top surface are used as control actuators for active feedback control. The key properties of the beam structure and the MFC actuators are listed in Table 5.1. A non-contact laser vibrometer sensor is utilized to measure the displacement or velocity at the positions of interest on the beam. A PC-based digital control system, namely, SIMULINK/dSPACE real time interface (RTI), is used to implement the active feedback control.

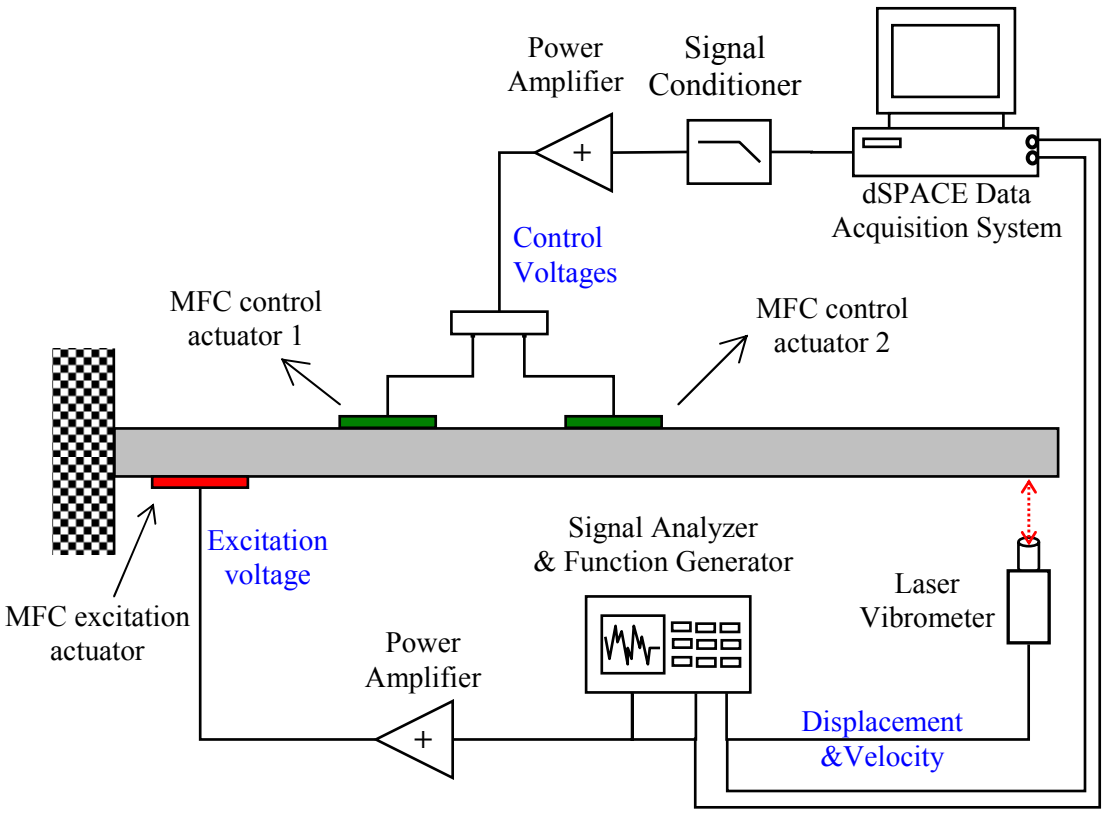

Figure 5.2: Schematic of the experimental setup

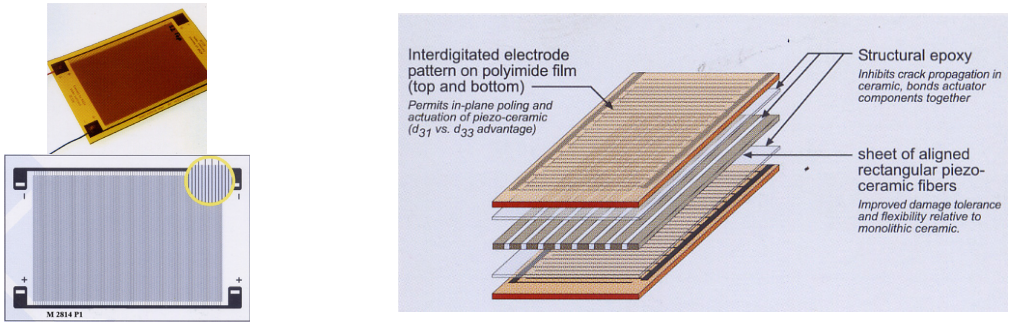

Figure **5.3**: Photograph and schematic of Macro Fiber Composite (MFC) actuator (Source: http://www.smart-material.com)

Table **5.1**: Properties of the beam structure and MFC actuator

Beam structure		MFC actuator (type: M2814 P1)	
Mass density:	$\rho_b = 2725 kg/m^3$	Piezoelectric constant:	$d_{33} = 4.0\times10^2$ pC/N
Elastic modulus:	$E_b = 6.6\times10^{10} N/m^2$	Tensile modulus:	$E_1 = 30.34\times10^9$ N/m^2
Element length:	$l = 0.42m$	Operational voltage range:	-500V $\sim +1500$V
Overall length:	$L_b = 1.4cm$	Length:	$L_a = 2.8cm$
Width:	$w_b = 25.30mm$	Width:	$w_a = 1.4cm$
Thickness:	$t_b = 3.10mm$	Thickness:	$t_a = 0.3mm$

An overall description of the signal flow in the experiment is summarized as follows. First, the excitation signal generated by the Function Generator (HP 35665A) is amplified by the Power Amplifier, and then applied to the MFC excitation actuator to excite the beam structure. The Laser Vibrometer sensor signal (displacement or velocity measurement), together with the excitation signal, is sent to the Dynamic Signal Analyzer (HP 35665A) to perform FFT analysis for frequency response function (FRF) measurement. Second, the excitation signal and Laser Vibrometer sensor signal are sent to the dSPACE data acquisition system, where a real-time controller is embedded to

calculate the required control voltages to the MFC control actuators. The dSPACE system outputs the control voltages through its DAC channels, the control voltage signals pass through the Power Amplifier and Signal Conditioner, and are then applied to the MFC control actuators.

In Chapter 3 and Chapter 4, it has been demonstrated and verified that the sensitivity-enhancing controls can be designed to enhance the frequency sensitivity to both stiffness and mass damage/variation. Stiffness changes are usually simulated by sawing a crack in the structure, which permanently damages the structure without the possibility of returning to the original healthy structure. In addition, it is impossible to quantify the amount of stiffness change. On the other hand, the mass changes are much easier to realize and the amount of mass change can be accurately quantified. Therefore, in this experiment we will focus on detecting mass changes in the beam structure. The mass changes are realized by attaching an extra point mass on the surface of the beam structure. The objective of this experiment investigation is to design sensitivity-enhancing controls to enhance the frequency sensitivity to mass changes in the beam structure, such that the mass changes will induce more significant frequency-shift of the closed-loop system than that of the open-loop system.

The major steps of the experiment are summarized as follows. First, system identification technique is utilized to identify a state-space model of the structural system using the measured frequency response functions (FRF). Then the identified state-space model is utilized to design the sensitivity-enhancing feedback control to enhance the frequency sensitivity to mass variations in the beam. Finally, the designed sensitivity-enhancing controls are implemented to the beam structure using Simulink/dSpace real

time interface (RTI). A series of tests are carried out to evaluate the sensitivity enhancement performance of the designed controllers.

5.2 System Identification Using the Measured Frequency Response Functions

The sensitivity-enhancing control approach for damage identification, proposed in Chapter 3, requires an accurate finite element (FE) model of the structure for controller design system analysis. To obtain an accurate FE model, the common way is to use the model updating techniques (e.g., the one proposed in Chapter 4 using sensitivity-enhancing controls) to refine an initial FE model by correlating the experimentally measured data with the model predictions. In this experimental investigation, a system identification technique is utilized to identify a mathematical model directly from the experimentally measured data. With this, the proposed damage detection method using sensitivity-enhancing control no longer requires an accurate finite element model, which greatly favors the implementation of this method for practical applications.

System identification methods can be broadly classified into two categories: parametric model-based methods and non-parametric methods. Parametric model-based system identification methods involve the use of mathematical models to reproduce the experimentally measured input-output data in either time or frequency domain. The benefits of using parametric models for structural identification include their direct relationship with physically meaningful quantities such as stiffness and mass, and their suitability for system analysis and control design [145]. Popular time-domain models used for system identification include linear polynomial models (e.g., ARX models and

ARMAX models), and state space model with free, canonical and structured parameterizations. Many system identification algorithms are available to estimate the parameters of such parametric models; these include prediction error method (PEM), least squares estimation (LSE), instrumental variable method (IV), maximum likelihood algorithm (MLA), subspace methods, and eigensystem realization algorithm (ERA). One may refer to Ref. [146-148] for a comprehensive overview of the system identification theory and algorithms.

In this experiment, the frequency-domain system identification technique is utilized to identify a state-space model of the beam structure integrated with MFC actuators, a schematic of which is shown in Figure 5.2. More specifically, the prediction error method (PEM), together with the experimental modal analysis technique, is utilized to identify a state-space model with structured parameterization from the measured frequency response functions (FRF).

Considering the cantilevered beam structure integrated with excitation and control actuators, as shown in Figure 5.2, the overall system can be modeled as a linear, time-invariant system (LTI system) with the equation of motion

$$\boldsymbol{M}\ddot{\boldsymbol{x}} + \boldsymbol{C}\dot{\boldsymbol{x}} + \boldsymbol{K}\boldsymbol{x} = \bar{\boldsymbol{B}}_c \boldsymbol{V}_c + \bar{\boldsymbol{B}}_e \boldsymbol{V}_e \qquad (5.1)$$

where $\boldsymbol{x} \in \Re^{n\times 1}$ is the displacement vector at the points of interest, $\boldsymbol{M} \in \Re^{n\times n}$, $\boldsymbol{C} \in \Re^{n\times n}$ and $\boldsymbol{K} \in \Re^{n\times n}$ are the mass, damping, and stiffness matrices, respectively, $\bar{\boldsymbol{B}}_e \in \Re^{n\times p}$ and $\bar{\boldsymbol{B}}_c \in \Re^{n\times r}$ are the influence matrices for the excitation input voltage $\boldsymbol{V}_e$ and the control input voltage $\boldsymbol{V}_c$, respectively.

Define the state vector as the combination of displacement and velocity, i.e., $z = \begin{bmatrix} \boldsymbol{x} \\ \dot{\boldsymbol{x}} \end{bmatrix} \in \Re^{N\times 1}$ ($N = 2n$), and assume that the system output is the displacement and velocity, the equation of motion given by Eq. (5.1) can be written in the standard state-space form

$$\begin{aligned} \dot{\boldsymbol{z}} &= \boldsymbol{A}\boldsymbol{z} + \boldsymbol{B}_c\boldsymbol{V}_c + \boldsymbol{B}_e\boldsymbol{V}_e \\ \boldsymbol{y} &= \begin{Bmatrix} \boldsymbol{x} \\ \dot{\boldsymbol{x}} \end{Bmatrix} = \boldsymbol{C}\boldsymbol{z} = \begin{bmatrix} \boldsymbol{I}_{n\times n} & \boldsymbol{0}_{n\times n} \\ \boldsymbol{0}_{n\times n} & \boldsymbol{I}_{n\times n} \end{bmatrix} \boldsymbol{z} \end{aligned} \tag{5.2}$$

where

$$\begin{aligned} \boldsymbol{A} &= \begin{bmatrix} \boldsymbol{0}_{n\times n} & \boldsymbol{I}_{n\times n} \\ -\boldsymbol{M}^{-1}\boldsymbol{K} & -\boldsymbol{M}^{-1}\boldsymbol{C} \end{bmatrix} \in \Re^{N\times N}, \\ \boldsymbol{B}_c &= \begin{bmatrix} \boldsymbol{0}_{n\times 1} \\ \boldsymbol{M}^{-1}\bar{\boldsymbol{B}}_c \end{bmatrix} \in \Re^{N\times r} \text{ and } \boldsymbol{B}_e = \begin{bmatrix} \boldsymbol{0}_{n\times 1} \\ \boldsymbol{M}^{-1}\bar{\boldsymbol{B}}_e \end{bmatrix} \in \Re^{N\times p} \end{aligned} \tag{5.3}$$

Eq. (5.1) and Eq. (5.2) can be transformed into their equivalent forms in modal coordinates. The generalized eigenvalue problem for Eq. (5.1) can be formulated as

$$\Lambda \boldsymbol{M}\Phi = \boldsymbol{K}\Phi \tag{5.4}$$

where $\Lambda = diag\left(\omega_1^2, \omega_2^2, \cdots, \omega_n^2\right)$ is a diagonal matrix containing the squares of the system's natural frequencies, and $\Phi = \begin{bmatrix} \boldsymbol{\varphi}_1 & \boldsymbol{\varphi}_2 & \cdots & \boldsymbol{\varphi}_n \end{bmatrix}$ is the eigenvector matrix.

The displacement vector $\boldsymbol{x}$ in Eq. (5.1) can be expressed in modal coordinate as $\boldsymbol{x} = \Phi\boldsymbol{q}$, where Φ is the eigenvector matrix, and $\boldsymbol{q}$ is the vector of modal coordinates. Substituting $\boldsymbol{x} = \Phi\boldsymbol{q}$ into Eq. (5.1) and pre-multiplying Φ^T on both sides of the equation, Eq. (5.1) can be transformed into its equivalent form in modal coordinates as follows

$$\left[\Phi^T\boldsymbol{M}\Phi\right]\ddot{\boldsymbol{q}} + \left[\Phi^T\boldsymbol{C}\Phi\right]\dot{\boldsymbol{q}} + \left[\Phi^T\boldsymbol{K}\Phi\right]\boldsymbol{q} = \Phi^T\bar{\boldsymbol{B}}_c\boldsymbol{V}_c + \Phi^T\bar{\boldsymbol{B}}_e\boldsymbol{V}_e \tag{5.5}$$

If the eigenvector matrix Φ is mass-matrix normalized, i.e., Φ satisfies $\Phi^T \boldsymbol{M} \Phi = \boldsymbol{I}_{n\times n}$, Eq. (5.5) can be further simplified as

$$\ddot{\boldsymbol{q}} + \begin{bmatrix} \ddots & & 0 \\ & 2\zeta_j\omega_j & \\ 0 & & \ddots \end{bmatrix} \dot{\boldsymbol{q}} + \begin{bmatrix} \ddots & & 0 \\ & \omega_j^2 & \\ 0 & & \ddots \end{bmatrix} \boldsymbol{q} = \bar{\boldsymbol{B}}_c^m \boldsymbol{V}_c + \bar{\boldsymbol{B}}_e^m \boldsymbol{V}_e \tag{5.6}$$

where ω_j and ζ_j represent the natural frequency and damping ratio of the *j*th structural mode, respectively, $\bar{\boldsymbol{B}}_e^m = \Phi^T \bar{\boldsymbol{B}}_e$ and $\bar{\boldsymbol{B}}_c^m = \Phi^T \bar{\boldsymbol{B}}_c$ are the influence matrices in modal coordinates for the excitation input voltage $\boldsymbol{V}_e$ and the control input voltage $\boldsymbol{V}_c$, respectively.

Define the state vector as $\boldsymbol{\eta} = \begin{bmatrix} \boldsymbol{q} \\ \dot{\boldsymbol{q}} \end{bmatrix} \in \Re^{N\times 1}$, Eq. (5.6) can be written in the standard state-space form

$$\begin{aligned} \dot{\boldsymbol{\eta}} &= \boldsymbol{A}^m \boldsymbol{\eta} + \boldsymbol{B}_c^m \boldsymbol{V}_c + \boldsymbol{B}_e^m \boldsymbol{V}_e \\ \boldsymbol{y} &= \boldsymbol{C}^m \boldsymbol{\eta} = \begin{bmatrix} \Phi & \boldsymbol{0}_{n\times n} \\ \boldsymbol{0}_{n\times n} & \Phi \end{bmatrix} \boldsymbol{\eta} \end{aligned} \tag{5.7}$$

where

$$\begin{aligned} \boldsymbol{A}^m &= \begin{bmatrix} \boldsymbol{0}_{n\times n} & \boldsymbol{I}_{n\times n} \\ diag\left(-\omega_1^2, -\omega_2^2, \cdots, -\omega_n^2\right) & diag\left(-2\zeta_1\omega_1, -2\zeta_2\omega_2, \cdots, -2\zeta_n\omega_n\right) \end{bmatrix} \in \Re^{N\times N}, \\ \boldsymbol{B}_c^m &= \begin{bmatrix} \boldsymbol{0}_{n\times 1} \\ \bar{\boldsymbol{B}}_c^m \end{bmatrix} \in \Re^{N\times r} \text{ and } \boldsymbol{B}_e^m = \begin{bmatrix} \boldsymbol{0}_{n\times 1} \\ \bar{\boldsymbol{B}}_e^m \end{bmatrix} \in \Re^{N\times p} \end{aligned} \tag{5.8}$$

From observing Eq. (5.7) and Eq. (5.8), one may find that the parameters in system matrix $\boldsymbol{A}^m$ and output matrix $\boldsymbol{C}^m$, i.e., natural frequencies, damping ratios and mode shapes, can be obtained from experimental modal analysis. Then the input matrices $\boldsymbol{B}_e^m$ and $\boldsymbol{B}_c^m$ can be identified using the system identification technique.

Therefore, to identify a state-space model with the structured parameterization as given by Eq. (5.7) and Eq. (5.8), it involves two major steps: (1) use the experimental modal analysis results to determine the system matrix $\boldsymbol{A}^m$ and output matrix $\boldsymbol{C}^m$; (2) use the system identification technique to determine the system input matrices, $\boldsymbol{B}_e^m$ and $\boldsymbol{B}_c^m$.

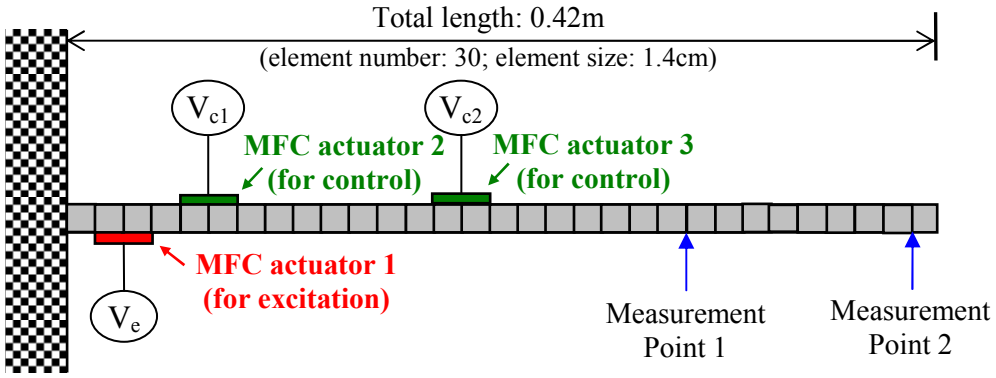

Figure 5.4: Setup of FRF measurement for system identification

The setup of FRF measurement for system identification is shown in Figure 5.4. The system inputs include the excitation voltage to the MFC excitation actuator (V_e) and two control voltages to the two MFC control actuators (V_{c1} and V_{c2}). The system outputs are the velocities at two measurement points on the beam, one is located at 12.6 cm away from the free end of the beam, and the other is located at 1.4 cm away from the free end of the beam. It is clear that the system can be described as a 3-input (one excitation voltage, two control voltages) and 2-output (velocities at two measurement points) system. For such a system, the state-space model with the same structured parameterization as given by Eq. (5.7) and Eq. (5.8), can be expressed as

$$\dot{\boldsymbol{\eta}} = \begin{bmatrix} 0 & 0 & 1 & 0 \\ 0 & 0 & 0 & 1 \\ -\omega_1^2 & 0 & -2\zeta_1\omega_1 & 0 \\ 0 & -\omega_2^2 & 0 & -2\zeta_2\omega_2 \end{bmatrix} \boldsymbol{\eta} + \begin{bmatrix} 0 & 0 & 0 \\ 0 & 0 & 0 \\ \boldsymbol{B}_e^m(3) & \boldsymbol{B}_{c1}^m(3) & \boldsymbol{B}_{c2}^m(3) \\ \boldsymbol{B}_e^m(4) & \boldsymbol{B}_{c1}^m(4) & \boldsymbol{B}_{c2}^m(4) \end{bmatrix} \begin{Bmatrix} V_e \\ V_{c1} \\ V_{c2} \end{Bmatrix} \qquad (5.9)$$

$$\boldsymbol{y} = \begin{bmatrix} 0 & 0 & \phi_1(1) & \phi_2(1) \\ 0 & 0 & \phi_1(2) & \phi_2(2) \end{bmatrix} \boldsymbol{\eta}$$

Therefore, the system identification of the integrated system shown in Figure 5.4, is equivalent to identifying the unknown parameters in the state-space model given by Eq. (5.9). The major steps involved in the system identification process are summarized as follows:

I. Use the Dynamic Signal Analyzer (DSA) to measure the frequency response functions (FRF) between each input/output pair (voltage input on each MFC actuator to velocity response at each measurement point);

II. Use the *experimental modal analysis* technique to identify modal parameters (natural frequencies, damping ratios, and mode shapes) from the measured FRFs;

III. Use the identified modal parameters to construct the system matrix $\boldsymbol{A}^m$ and output matrix $\boldsymbol{C}^m$, and use the prediction error method (PEM) in MATLAB System Identification Toolbox to estimate the input matrices $\boldsymbol{B}_e^m$ and $\boldsymbol{B}_c^m$.

IV. Validate the identified state-space model by comparing the measured FRFs with the model predictions.

First, we measure the frequency response functions from the input voltage on each MFC actuator to the velocity response at each measurement point. The total number of FRFs obtained from measurement is 3×2=6. The input voltage to MFC excitation actuator goes

through CH-1 of the power amplifier, and the input voltages to the MFC control actuators go through CH-2 and CH-3 of the power amplifier, respectively. CH-1, CH-2, and CH-3 of the power amplifier have amplification gains of 29.97, 29.80, and 29.92, respectively. The velocity response at each measurement point is measured by the Laser Vibrometer sensor, and the sensor gain is set as 10.0 mm/S/V.

Table 5.2: Experimental modal analysis results

Frequencies and Damping

Mode	Natural Frequency (HZ)	Damping (%)
1	14.31	193.57e-3
2	88.81	126.55e-3

Mode Shapes

Mode	$\phi_i(1)$	$\phi_i(2)$
1	0.91885e-3	1.46641e-3
2	1.89878e-3	-5.40915e-3

Then the FRFs obtained from the input voltage on the MFC excitation actuator to the velocity response at two measurement points are used to perform the experimental modal analysis. The commercial software STARMODAL is used to identify the natural frequencies, damping ratios, and mode shapes from the measured frequency response functions. The results of the experimental modal analysis are listed in Table 5.2. With these modal parameters, the system matrix $\boldsymbol{A}^m$ and output matrix $\boldsymbol{C}^m$ can be constructed

$$\boldsymbol{A}^m = \begin{bmatrix} 0 & 0 & 1 & 0 \\ 0 & 0 & 0 & 1 \\ -8087.395820 & 0 & -0.349729 & 0 \\ 0 & -311354.123148 & 0 & -1.330193 \end{bmatrix} \qquad (5.10)$$

$$\boldsymbol{C}^m = \begin{bmatrix} 0 & 0 & 0.515589 & 0.267187 \\ 0 & 0 & 0.824438 & -0.734553 \end{bmatrix}$$

Then the identified system matrix $\boldsymbol{A}^m$ and output matrix $\boldsymbol{C}^m$ in Eq. (5.10) are utilized to construct an initial state-space model, where the input matrices ($\boldsymbol{B}_e^m$ and $\boldsymbol{B}_c^m$) are assigned with arbitrary numbers. Then the prediction error method (PEM) in MATLAB System Identification Toolbox is utilized to identify the actual values of input matrices ($\boldsymbol{B}_e^m$ and $\boldsymbol{B}_c^m$). The identified values of the input matrices ($\boldsymbol{B}_e^m$ and $\boldsymbol{B}_c^m$) are given as follows

$$\boldsymbol{B}_e^m = \begin{bmatrix} 0 \\ 0 \\ 0.001764 \\ 0.007395 \end{bmatrix} \text{ and } \boldsymbol{B}_c^m = \begin{bmatrix} 0 & 0 \\ 0 & 0 \\ -0.001529 & -0.001010 \\ -0.002021 & 0.008596 \end{bmatrix} \tag{5.11}$$

From Eq. (5.10) and Eq. (5.11), the final state-space model obtained from system identification can be written as

$$\frac{d}{dt}\begin{Bmatrix} \eta_1 \\ \eta_2 \\ \dot{\eta}_1 \\ \dot{\eta}_2 \end{Bmatrix} = \begin{bmatrix} 0 & 0 & 1 & 0 \\ 0 & 0 & 0 & 1 \\ -8087.395820 & 0 & -0.349729 & 0 \\ 0 & -311354.123148 & 0 & -1.330193 \end{bmatrix} \begin{Bmatrix} \eta_1 \\ \eta_2 \\ \dot{\eta}_1 \\ \dot{\eta}_2 \end{Bmatrix} + \begin{bmatrix} 0 & 0 \\ 0 & 0 \\ -0.001529 & -0.001010 \\ -0.002021 & 0.008596 \end{bmatrix} \begin{Bmatrix} V_{c1} \\ V_{c2} \end{Bmatrix} + \begin{bmatrix} 0 \\ 0 \\ 0.001764 \\ 0.007395 \end{bmatrix} V_e \tag{5.12}$$

$$\boldsymbol{y}_v = \begin{bmatrix} 0 & 0 & 0.515589 & 0.267187 \\ 0 & 0 & 0.824438 & -0.734553 \end{bmatrix} \begin{Bmatrix} \eta_1 \\ \eta_2 \\ \dot{\eta}_1 \\ \dot{\eta}_2 \end{Bmatrix}$$

Figure 5.5 compares the measured frequency response functions with those predicted from the identified model. H_{ij} (i=1,2; j=1,2,3) represents the frequency

response function from the voltage input on the *j*th MFC actuator to the velocity response at the *i*th measurement point. From the figure, we can see that the frequency response functions estimated from the identified model match well with those from the experimental measurement. Therefore, the identified state-space model is quite accurate, and it can be utilized to design the sensitivity-enhancing feedback control.

5.3 Design of Sensitivity-Enhancing Feedback Control Using the Identified Model

In this section, the identified state space model (obtained in the previous section) is utilized to design the sensitivity-enhancing feedback control to increase the frequency sensitivity to mass variations of the beam. First, to comply with the type of model used for calculating frequency sensitivity, the identified state-space model in modal coordinates is transformed into its equivalent one in the actual physical coordinates (i.e., displacement and velocity at the selected measurement points). Second, the calculation of frequency sensitivity to mass variations also requires that either the mass matrix is known or the mass-normalized eigenvector is available. To achieve this, a series of tests are designed and carried out to estimate the frequency sensitivity matrix of the open-loop system, and an optimization scheme is developed to estimate the mass matrix based on the open-loop sensitivity matrix. Finally, the controller design approach presented in Section 3.4 of Chapter 3, namely, the eigenstructure assignment-based constrained optimization scheme, is utilized to design the optimal sensitivity-enhancing control to enhance the frequency sensitivity to mass variations in the beam.

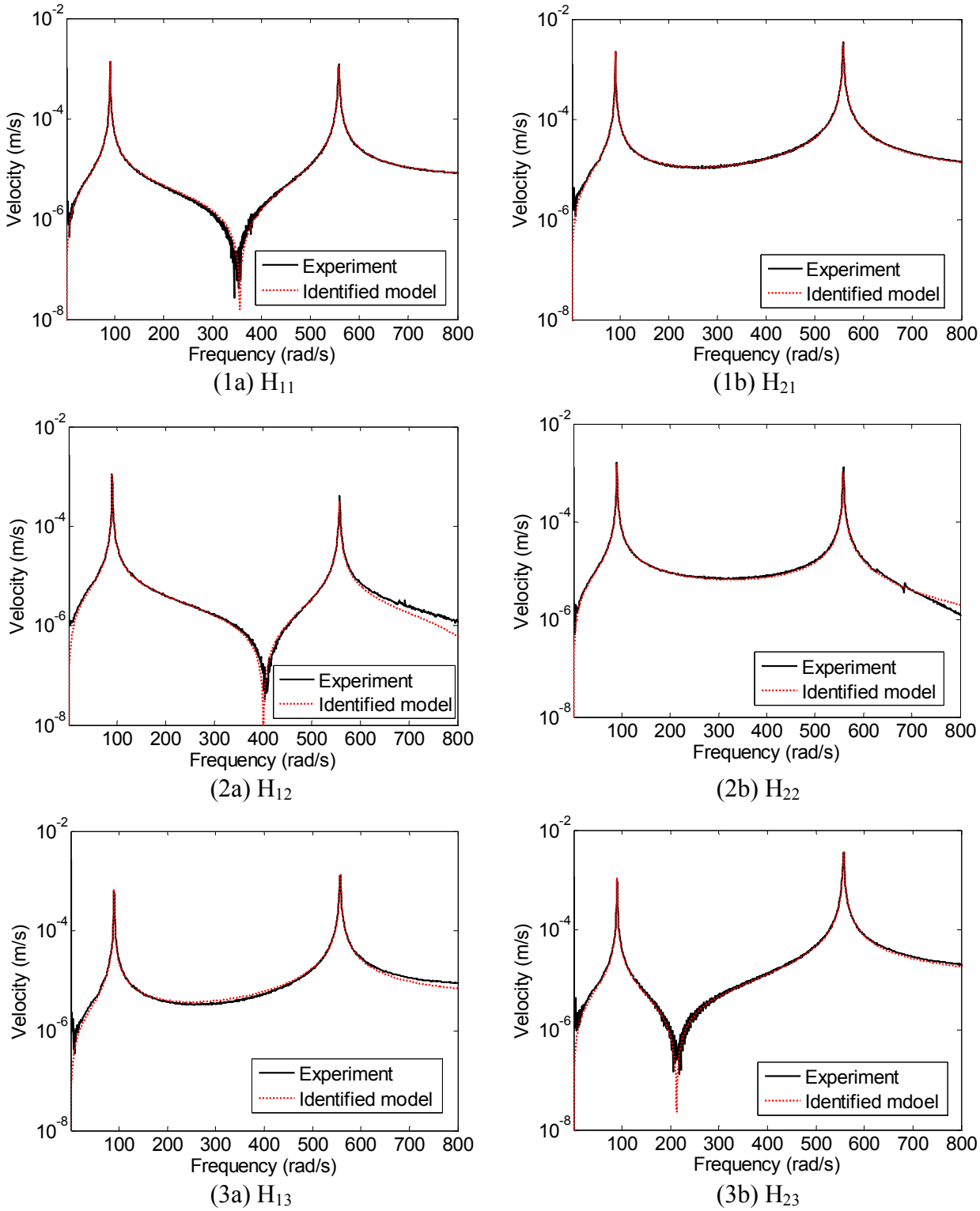

(1a) H_{11} (1b) H_{21}

(2a) H_{12} (2b) H_{22}

(3a) H_{13} (3b) H_{23}

Figure **5.5**: Comparison of the FRFs measured from the experiment and predicted from the identified model

For the 3-input 2-output system as shown in Figure 5.4, the equation of motion can be expressed as

$$\boldsymbol{M}\begin{Bmatrix}\ddot{x}_1\\ \ddot{x}_2\end{Bmatrix}+\boldsymbol{C}\begin{Bmatrix}\ddot{x}_1\\ \ddot{x}_2\end{Bmatrix}+\boldsymbol{K}\begin{Bmatrix}x_1\\ x_2\end{Bmatrix}=\bar{\boldsymbol{B}}_c\boldsymbol{V}_c+\bar{\boldsymbol{B}}_e V_e \tag{5.13}$$

where x_1 and x_2 represent the displacement at measurement points 1 and 2, $\boldsymbol{M}$, $\boldsymbol{C}$, and $\boldsymbol{K}$ are the equivalent mass, damping, and stiffness matrices, $\bar{\boldsymbol{B}}_e$ and $\bar{\boldsymbol{B}}_c$ are the influence matrices for the excitation voltage input V_e and the control voltage input $\boldsymbol{V}_c=\{V_{c1}\quad V_{c2}\}^T$, respectively. For the open-loop system, the eigenvalues and eigenvectors can be obtained by solving the following eigenvalue problem

$$\left(\boldsymbol{K}-\omega_i^2\boldsymbol{M}\right)\boldsymbol{u}_i=\boldsymbol{0}\text{, where } i=1,2 \tag{5.14}$$

where ω_i and $\boldsymbol{u}_i$ represent the ith natural frequency and its corresponding eigenvector of the open-loop system..

From the eigenvalue sensitivity analysis presented in Section 3.2.2 of Chapter 3, the sensitivity of the open-loop natural frequencies to mass variation at one specific measurement point can be obtained as

$$\frac{\partial\omega_i}{\partial m_j}=-\frac{\omega_i}{2}\frac{\boldsymbol{u}_i^T\left[\partial\boldsymbol{M}/\partial m_j\right]\boldsymbol{u}_i}{\boldsymbol{u}_i^T\boldsymbol{M}\boldsymbol{u}_i} \tag{5.15}$$

For a closed-loop system with control input $\boldsymbol{V}_c=\boldsymbol{K}_{c1}\begin{Bmatrix}x_1\\ x_2\end{Bmatrix}+\boldsymbol{K}_{c2}\begin{Bmatrix}\dot{x}_1\\ \dot{x}_2\end{Bmatrix}$, the sensitivity of the closed-loop natural frequency to mass variation at one specific measurement point can be expressed as

$$\frac{\partial \omega_i^c}{\partial m_j} = -\frac{\omega_i^c}{2} \frac{\left(\boldsymbol{v}_i^c\right)^T \left[\partial \boldsymbol{M} / \partial m_j\right] \boldsymbol{u}_i^c}{\left(\boldsymbol{v}_i^c\right)^T \boldsymbol{M} \boldsymbol{u}_i^c} \tag{5.16}$$

where ω_i^c, $\boldsymbol{u}_i^c$ and $\boldsymbol{v}_i^c$ are the ith natural frequency and the corresponding right and left eigenvectors of the closed-loop system.

From observing Eq. (5.15) and Eq. (5.16), one may notice that in order to calculate the open-loop and closed-loop natural frequency sensitivity to mass variations at the selected measurement points, it requires that: (1) the eigenvector $\boldsymbol{u}_i$ is expressed in the actual physical coordinates, i.e., the displacement or velocity at the selected measurement points; and (2) the mass matrix $\boldsymbol{M}$ is known unless the eigenvector $\boldsymbol{u}_i$ is mass-matrix normalized, i.e., $\boldsymbol{u}_i$ satisfies $\boldsymbol{u}_i^T \boldsymbol{M} \boldsymbol{u}_i = \boldsymbol{I}$. However, the identified state-space model obtained in previous section is expressed in the modal coordinates, and the eigenvector $\boldsymbol{u}_i$ obtained from experimental modal analysis normally is not mass-matrix normalized. Therefore, before we utilize the identified state space model to design the sensitivity-enhancing controls, we need to: (1) transform the identified state-space model in modal coordinate into its equivalent one in the actual physical coordinates; (2) estimate the equivalent mass matrix $\boldsymbol{M}$ associated with the identified model.

For the identified state-space model in modal coordinates, the following matrix transformations are performed to transform it into its equivalent one in the actual physical coordinates

$$\boldsymbol{A}=\begin{bmatrix}\left(\Phi^{-1}\right)^T & \boldsymbol{0}_{2\times2}\\ \boldsymbol{0}_{2\times2} & \left(\Phi^{-1}\right)^T\end{bmatrix}\boldsymbol{A}^m\begin{bmatrix}\Phi^{-1} & \boldsymbol{0}_{2\times2}\\ \boldsymbol{0}_{2\times2} & \Phi^{-1}\end{bmatrix};$$

$$\boldsymbol{B}_c=\begin{bmatrix}\left(\Phi^{-1}\right)^T & \boldsymbol{0}_{2\times2}\\ \boldsymbol{0}_{2\times2} & \left(\Phi^{-1}\right)^T\end{bmatrix}\boldsymbol{B}_c^m;\ \boldsymbol{B}_e=\begin{bmatrix}\left(\Phi^{-1}\right)^T & \boldsymbol{0}_{2\times2}\\ \boldsymbol{0}_{2\times2} & \left(\Phi^{-1}\right)^T\end{bmatrix}\boldsymbol{B}_e^m;\ \boldsymbol{C}=\boldsymbol{C}^m\begin{bmatrix}\Phi^{-1} & \boldsymbol{0}_{2\times2}\\ \boldsymbol{0}_{2\times2} & \Phi^{-1}\end{bmatrix} \tag{5.17}$$

where Φ is the right eigenvector matrix. The resulting state-space model has the states of displacement and velocity at the two measurement points, and the model is given as

$$\frac{d}{dt}\begin{Bmatrix}x_1\\x_2\\\dot{x}_1\\\dot{x}_2\end{Bmatrix}=\begin{bmatrix}0 & 0 & 1 & 0\\ 0 & 0 & 0 & 1\\ -119610.813201 & 69744.803740 & -0.710285 & 0.225486\\ 306601.610997 & -199830.705766 & 0.991245 & -0.969637\end{bmatrix}\begin{Bmatrix}x_1\\x_2\\\dot{x}_1\\\dot{x}_2\end{Bmatrix}$$
$$+\begin{bmatrix}0 & 0\\ 0 & 0\\ -0.001328 & 0.001776\\ 0.000224 & -0.007147\end{bmatrix}\begin{Bmatrix}V_{c1}\\V_{c2}\end{Bmatrix}+\begin{bmatrix}0\\0\\0.002886\\-0.003978\end{bmatrix}V_e \tag{5.18}$$

$$\boldsymbol{y}_v=\begin{bmatrix}0 & 0 & 1 & 0\\ 0 & 0 & 0 & 1\end{bmatrix}\begin{Bmatrix}x_1\\x_2\\\dot{x}_1\\\dot{x}_2\end{Bmatrix};\ \boldsymbol{y}_d=\begin{bmatrix}1 & 0 & 0 & 0\\ 0 & 1 & 0 & 0\end{bmatrix}\begin{Bmatrix}\eta_1\\\eta_2\\\dot{\eta}_1\\\dot{\eta}_2\end{Bmatrix}$$

The next step is to estimate the equivalent mass matrix $\boldsymbol{M}$ associated with the state-space model given by Eq. (5.18). The key idea for the mass matrix estimation is to minimize the difference between the open-loop frequency sensitivity matrix calculated by using Eq. (5.15), in which the mass matrix $\boldsymbol{M}$ is the only unknown, and the one estimated from a series of tests on the open-loop system with known mass addition at the measurement points.

First, a series of tests are carried out to estimate the open-loop natural frequency sensitivity to mass variations at the two measurement points. More specifically, we

successively add a small amount of mass (2 gram) to each measurement point, and measure the frequency response functions of the perturbated structure with mass addition. Comparing the natural frequencies of the perturbed structure with those of the original structure, the shift of the open-loop natural frequencies due to mass addition at each measurement position can be obtained. Table **5.3** shows the measured natural frequencies of the original structure and the perturbated structures. From the table, we can easily see that adding 2g mass to measurement point 1 induces -0.19 HZ shift in the first natural frequency and a shift of -0.34 HZ in the second natural frequency; and adding 2g mass to measurement point 2 induces -0.53 HZ shift in the first natural frequency and -2.36 HZ shift in the second natural frequencies.

Table **5.3**: Open-loop natural frequencies of the original structure and the perturbated structure with mass addition

Mode	Original structure	Perturbated structure -1 (2g mass added to measurement point 1)	Perturbated structure -2 (2g mass added to measurement point 2)
1	14.31 HZ	14.12 HZ	13.78 HZ
2	88.81HZ	88.47 HZ	86.45 HZ

On the other hand, the frequency shift of the open-loop system due to 2g mass addition at the two measurement points can be calculated using the open-loop sensitivity matrix. Based on the open-loop frequency sensitivity given in Eq. (**5.15**), the following equation can be utilized to calculate the frequency shift

$$\begin{Bmatrix} \delta\omega_1 \\ \delta\omega_2 \end{Bmatrix} = \begin{bmatrix} S(1,1) & S(1,2) \\ S(2,1) & S(2,2) \end{bmatrix} \begin{Bmatrix} \delta m_1 \\ \delta m_2 \end{Bmatrix} \tag{5.19}$$

where $\delta\omega_1$ and $\delta\omega_2$ denote the shift of the first and second natural frequency, respectively, δm_1 and δm_2 denote the mass variations at the two measurement points, respectively, and $\boldsymbol{S}$ is the open-loop frequency sensitivity matrix, whose elements can be calculated using Eq. (5.15) as

$$\boldsymbol{S}(i,j)=\frac{\partial\omega_i}{\partial m_j}=-\frac{\omega_i}{2}\frac{\boldsymbol{u}_i^T\left[\partial\boldsymbol{M}/\partial m_j\right]\boldsymbol{u}_i}{\boldsymbol{u}_i^T\boldsymbol{M}\boldsymbol{u}_i},\ \text{where } i=1,2 \text{ and } j=1,2 \tag{5.20}$$

Note that in Eq. (5.20), the natural frequency ω_i and eigenvector $\boldsymbol{u}_i$ are known from the experimental modal analysis, $\left[\partial\boldsymbol{M}/\partial m_j\right]$ can be specified as $\begin{bmatrix}1 & 0\\ 0 & 0\end{bmatrix}$ for $j=1$ and $\begin{bmatrix}0 & 0\\ 0 & 1\end{bmatrix}$ for $j=2$, and the only unknown is the mass matrix $\boldsymbol{M}$. Based on the experimental results of frequency-shift data given in Table 5.3 and the estimated frequency-shift using Eq. (5.19), an optimization scheme can be formulated to estimate the unknown mass matrix $\boldsymbol{M}$. The optimization scheme aims to minimize the difference between the frequency-shift from the experimental measurement and the frequency-shift predicted using the model-based sensitivity analysis

$$J=\left\|\begin{Bmatrix}\delta\omega_1^1\\ \delta\omega_2^1\\ \delta\omega_1^2\\ \delta\omega_2^2\end{Bmatrix}-\begin{Bmatrix}S(1,1)\times 0.002\\ S(2,1)\times 0.002\\ S(1,2)\times 0.002\\ S(2,2)\times 0.002\end{Bmatrix}\right\| \tag{5.21}$$

After the optimization process converges, it returns the optimal estimate of the mass matrix

$$\boldsymbol{M}=\begin{bmatrix}0.063404 & -0.013868\\ -0.013868 & 0.018051\end{bmatrix} \tag{5.22}$$

With the state-space model given by Eq. (5.18) and the estimated mass matrix given by Eq. (5.22), the design approach of sensitivity-enhancing control described in Section 3.4 of Chapter 3 can be utilized to design the sensitivity-enhancing controls to enhance the frequency sensitivity to mass variations at the selected measurement points.

For the open-loop system with state-space model described in Eq. (5.18), applying state feedback control with control action $\boldsymbol{V}_c = \boldsymbol{K}_c \boldsymbol{x}$, the resulting closed-loop system can be expressed as

$$\dot{\boldsymbol{z}} = (\boldsymbol{A} + \boldsymbol{B}_c \boldsymbol{K}_c)\boldsymbol{z} + \boldsymbol{B}_e V_e(t) \tag{5.23}$$

where $\boldsymbol{z} = \begin{bmatrix} x_1 & x_2 & \dot{x}_1 & \dot{x}_2 \end{bmatrix}^T$ is the state vector, $\boldsymbol{B}_e$ and $\boldsymbol{B}_c$ are the input influence matrices for the excitation voltage V_e and the control voltages $\boldsymbol{V}_c = \begin{Bmatrix} V_{c1} \\ V_{c2} \end{Bmatrix}$.

The eigenvalue problem of the closed-loop system can be formulated as

$$\left(\boldsymbol{A} + \boldsymbol{B}_c \boldsymbol{K}_c\right)\boldsymbol{\varphi}_j^c = \lambda_j^c \boldsymbol{\varphi}_j^c, \text{ where } j = 1, 2 \tag{5.24}$$

where λ_j^c and $\boldsymbol{\varphi}_j^c$ represent the jth eigenvalue and eigenvector of the closed-loop system. From the theory of eigenstructure assignment, the eigenvector $\boldsymbol{\varphi}_j^c$ associated with the closed-loop eigenvalue λ_j^c cannot be arbitrarily assigned, and the admissible space for eigenvector assignment can be found by using the singular value decomposition (SVD) technique.

Applying SVD technique to the matrix, $\boldsymbol{S}_{\lambda_j^c} = \left[\boldsymbol{A} - \lambda_j^c \boldsymbol{I}_N \mid \boldsymbol{B}_c\right]$, leads to

$$\boldsymbol{S}_{\lambda_j^c} = \left[\boldsymbol{A} - \lambda_j^c \boldsymbol{I}_N \mid \boldsymbol{B}_c\right] = \boldsymbol{U}_j \left[\boldsymbol{D}_j \mid \boldsymbol{0}_{N \times r}\right] \boldsymbol{V}_j^* \tag{5.25}$$

where $\boldsymbol{D}_j$ is a diagonal matrix containing all the singular values of $\boldsymbol{S}_{\lambda_j^c}$, the columns of $\boldsymbol{U}_j$ contain the set of orthonormal left singular vectors, and the columns of $\boldsymbol{V}_j$ contain the set of orthonormal right singular vectors. The right singular vector matrix $\boldsymbol{V}_j$ can be partitioned in the following form, $\boldsymbol{V}_j = \begin{bmatrix} \boldsymbol{V}_{11}^{(j)} & \boldsymbol{V}_{12}^{(j)} \\ \boldsymbol{V}_{21}^{(j)} & \boldsymbol{V}_{22}^{(j)} \end{bmatrix}$, where $\boldsymbol{V}_{11}^{(j)}$, $\boldsymbol{V}_{12}^{(j)}$, $\boldsymbol{V}_{21}^{(j)}$ and $\boldsymbol{V}_{22}^{(j)}$ are 4×4, 4×2, 2×4, and 2×2 sub-matrices, respectively. It can be shown that any achievable closed-loop eigenvector must be a linear combination of the column vectors of $\boldsymbol{V}_{12}^{(j)}$. Therefore, any achievable closed-loop eigenvector can be expressed as

$$\boldsymbol{\varphi}_j^a = \boldsymbol{V}_{12}^{(j)}\boldsymbol{\beta}_j, \text{ where } j = 1,2 \tag{5.26}$$

where $\boldsymbol{\beta}_j$ is the linear combination coefficient vector used to span the column vectors of $\boldsymbol{V}_{12}^{(j)}$ to achieve $\boldsymbol{\varphi}_j^a$.

Assume that the closed-loop eigenvalues are assigned as follows:

$$\lambda_j^{\mathrm{c}} = \gamma_j \times \lambda_j^{\mathrm{o}}, \ j = 1,2 \tag{5.27}$$

where λ_j^{o} is the *j*th eigenvalue of the open-loop system, and γ_j denotes the ratio between the *j*th closed-loop eigenvalue and its corresponding open-loop one. Given the closed-loop eigenvalues in Eq. (5.27), the associated closed-loop eigenvectors can be assigned in their respective admissible space

$$\boldsymbol{\varphi}_j^c = \boldsymbol{V}_{12}^{(j)}\boldsymbol{\beta}_j, \ j = 1,2 \tag{5.28}$$

where the column vectors of $\boldsymbol{V}_{12}^{(j)}$ span the admissible space for assigning the jth eigenvector, and $\boldsymbol{\beta}_j$ is the corresponding coefficient vectors for eigenvector assignment.

To achieve a closed-loop system that has the eigenvalues as given in Eq. (5.27) and eigenvectors as given in Eq. (5.28), the required control gain matrix can be determined by using the following equations

$$\boldsymbol{K}_c = \boldsymbol{W}(\boldsymbol{\Phi}^a)^{-1} \tag{5.29}$$

Where the matrices $\boldsymbol{\Phi}^a$ and $\boldsymbol{W}$ can be expressed as

$$\begin{aligned} \boldsymbol{\Phi}^a &= \begin{bmatrix} \boldsymbol{\varphi}_1^c & (\boldsymbol{\varphi}_1^c)^* & \boldsymbol{\varphi}_2^c & (\boldsymbol{\varphi}_2^c)^* \end{bmatrix}, \text{ where } \boldsymbol{\varphi}_j^c = \boldsymbol{V}_{12}^{(j)}\boldsymbol{\beta}_j \\ \boldsymbol{W} &= \begin{bmatrix} \boldsymbol{w}_1 & (\boldsymbol{w}_1)^* & \boldsymbol{w}_2 & (\boldsymbol{w}_2)^* \end{bmatrix}, \text{ where } \boldsymbol{w}_j = \boldsymbol{V}_{22}^{(j)}\boldsymbol{\beta}_j \end{aligned} \tag{5.30}$$

For the control gain matrix obtained in Eq. (5.29), the total control effort required for the closed-loop control is given by

$$W_{contr} = trace\left(\boldsymbol{K}_c \boldsymbol{P}_l \boldsymbol{K}_c^T\right) \tag{5.31}$$

where $\boldsymbol{K}_c$ is the control gain matrix, and $\boldsymbol{P}_l$ is the solution to the following Lyapunov equation

$$\left(\boldsymbol{A} + \boldsymbol{B}_c\boldsymbol{K}_c\right)\boldsymbol{P}_l + \boldsymbol{P}_l\left(\boldsymbol{A} + \boldsymbol{B}_c\boldsymbol{K}_c\right)^T + \boldsymbol{Z} = \boldsymbol{0} \tag{5.32}$$

in which $\boldsymbol{Z}$ is the variance matrix of the excitation input.

A constrained optimization scheme can be formulated to find the optimal eigenstructure assignment such that the resulting closed-loop system achieves the best performance of sensitivity enhancement with constrained control effort. More specifically, the optimization problem aims to find the optimal values of the design variables

$$\boldsymbol{p} = \{\gamma_1, \gamma_2, \boldsymbol{\beta}_1, \boldsymbol{\beta}_2\} \in \Re^6 \tag{5.33}$$

that can maximize the sensitivity enhancement performance index, which is defined as the summation of element-to-element ratios between the closed-loop and open-loop frequency sensitivity matrices,

$$J(\boldsymbol{p}) = \sum_{i=1}^{2}\left[\sum_{j=1}^{2}\left|\frac{\boldsymbol{S}^c(i,j)}{\boldsymbol{S}(i,j)}\right|\right] \tag{5.34}$$

under certain constraints on the control effort requirement.

Table 5.4: Closed-loop systems resulted from different sensitivity-enhancing controls

Closed-loop system ID	Constrains	Closed-loop eigenvalues	Closed-loop eigenvectors
CLS-1	$Max\left\|\boldsymbol{K}_c(i,j)\right\| \le 1.0e6$	$\lambda_1^c = 1.1577\lambda_1^o$ $\lambda_2^c = 1.0043\lambda_2^o$	$\boldsymbol{\beta}_1 = [-0.4794 \quad -0.2777]$ $\boldsymbol{\beta}_2 = [-0.1699 \quad -0.1548]$
CLS-2	$Max\left\|\boldsymbol{K}_c(i,j)\right\| \le 8.0e6$	$\lambda_1^c = 1.4692\lambda_1^o$ $\lambda_2^c = 1.0387\lambda_2^o$	$\boldsymbol{\beta}_1 = [-0.4220 \quad 0.0095]$ $\boldsymbol{\beta}_2 = [-0.2884 \quad -0.4594]$
CLS-3	$Max\left\|\boldsymbol{K}_c(i,j)\right\| \le 6.0e7$	$\lambda_1^c = 2.4993\lambda_1^o$ $\lambda_2^c = 0.9477\lambda_2^o$	$\boldsymbol{\beta}_1 = [-0.8166 \quad 0.4516]$ $\boldsymbol{\beta}_2 = [-0.2333 \quad -0.3740]$

In this experiment, three sensitivity-enhancing controllers are designed with different constraints on the control effort requirement. Table 5.4 gives the descriptions of these constraints and the corresponding optimal values of the parameters for eigenstructure assignment. With these parameters for eigenstructure assignment, the corresponding control gain matrix can be calculated using Eq. (5.29). The control gain matrices for the three closed-loop systems listed in Table 5.4 are given in Eq. (5.35), Eq. (5.36), and Eq. (5.37), respectively.

$$\boldsymbol{K}_{c1} = \begin{bmatrix} 9.6282e5 & 9.8370e5 & -4.3850e\text{-}2 & 4.2228e\text{-}3 \\ 3.4626e5 & 7.0469e5 & -3.3843e\text{-}2 & -1.2697e\text{-}4 \end{bmatrix} \quad (5.35)$$

$$\boldsymbol{K}_{c2} = \begin{bmatrix} 5.8845e6 & 4.8171e6 & 0.1646 & 0.6187 \\ -7.0588e6 & 2.0554e6 & 1.5531 & 0.3747 \end{bmatrix} \quad (5.36)$$

$$\boldsymbol{K}_{c3} = \begin{bmatrix} 5.7165e7 & 1.9046e7 & 7.3662 & -4.2467 \\ -1.6071e7 & -1.2520e7 & -29.5269 & -8.8395 \end{bmatrix} \quad (5.37)$$

5.4 Implementation of the Sensitivity-Enhancing Control and Experimental Results

The designed controllers for frequency sensitivity enhancement in the previous section are based on full-state feedback, and they are only feasible when all the state variables (displacement and velocity at all measurement points) are available for measurement. However, the Laser Vibrometer sensor used in this experiment can only measure the displacement or velocity at one measurement point. Therefore, to implement the designed sensitivity-enhancing feedback control, a state observer (or state estimator) must be developed to estimate the state variables based on the system input and output measurement data.

For a general second-order system written in state-space form

$$\begin{aligned} \dot{\boldsymbol{x}} &= \boldsymbol{A}\boldsymbol{x} + \boldsymbol{B}_c\boldsymbol{u} + \boldsymbol{B}_e\boldsymbol{f} \\ \boldsymbol{y} &= \boldsymbol{C}\boldsymbol{x} \end{aligned} \quad (5.38)$$

where $\boldsymbol{x}$ is the state vector, $\boldsymbol{A}$ is the system matrix, $\boldsymbol{C}$ is the output matrix, $\boldsymbol{B}_e$ and $\boldsymbol{B}_c$ are the input influence matrices for excitation input $\boldsymbol{f}$ and control input $\boldsymbol{u}$, respectively. The equation for the Luenberger state observer [149,150] is defined as

$$\dot{\bar{\boldsymbol{x}}} = \boldsymbol{A}\bar{\boldsymbol{x}} + \boldsymbol{B}_c\boldsymbol{u} + \boldsymbol{B}_e\boldsymbol{f} + \boldsymbol{L}(\boldsymbol{y} - \boldsymbol{C}\bar{\boldsymbol{x}}) \tag{5.39}$$

where $\bar{\boldsymbol{x}}$ is the estimated state vector, and $\boldsymbol{L}$ is the observer gain matrix. The Luenberger observer simulates the real system presented in Eq. (5.38) and penalizes the different between the measured output $\boldsymbol{y}$ and the estimated output $\boldsymbol{C}\bar{\boldsymbol{x}}$. From Eq. (5.38) and Eq. (5.39), the estimation error equation can be obtained as

$$\dot{\boldsymbol{e}} = \left(\boldsymbol{A} - \boldsymbol{L}\boldsymbol{C}\right)\boldsymbol{e} \tag{5.40}$$

where $\boldsymbol{e} = \boldsymbol{x} - \bar{\boldsymbol{x}}$ is the estimation error vector. From Eq. (5.40), one may notice that the estimation error $\boldsymbol{e}$ has the property that: $\boldsymbol{e}(t) \to 0$ as $t \to \infty$, for all $\boldsymbol{e}(t_0)$, if and only if the observer is asymptotically stable. In other words, the estimation error $\boldsymbol{e}$ will asymptotically approach zero if the eigenvalues of $\boldsymbol{A} - \boldsymbol{L}\boldsymbol{C}$, also named observer poles, have negative real parts. It can be also shown that if the system given in Eq. (5.38) is completely observable, one might place the observer poles arbitrarily far in the left-half complex plane to obtain fast convergence of the estimation error. This, however, generally must be achieved by make the gain matrix $\boldsymbol{L}$ quite large in magnitude, which in turn makes the observer very sensitive to the measurement noises. Hence, a compromise between the convergence rate of the estimation error and the amplification of the measurement noise effect must be found for the observer design.

Define the control input $\boldsymbol{u}$ as $\boldsymbol{u} = \boldsymbol{K}_c\bar{\boldsymbol{x}}$, assembling the system equation given by Eq. (5.38) and the observer equation given by Eq. (5.39) yields the overall equation of the coupled system

$$\frac{d}{dt}\begin{Bmatrix} \boldsymbol{x} \\ \bar{\boldsymbol{x}} \end{Bmatrix} = \begin{bmatrix} \boldsymbol{A} & \boldsymbol{B}_c\boldsymbol{K}_c \\ \boldsymbol{LC} & \boldsymbol{A}-\boldsymbol{LC}+\boldsymbol{B}_c\boldsymbol{K}_c \end{bmatrix}\begin{Bmatrix} \boldsymbol{x} \\ \bar{\boldsymbol{x}} \end{Bmatrix} + \begin{bmatrix} \boldsymbol{B}_e \\ \boldsymbol{B}_e \end{bmatrix} f$$
$$y = \begin{bmatrix} \boldsymbol{C} & \boldsymbol{0} \end{bmatrix}\begin{bmatrix} \boldsymbol{x} \\ \bar{\boldsymbol{x}} \end{bmatrix} \qquad (5.41)$$

Figure 5.6 shows the block diagram of the above coupled control system with state observer.

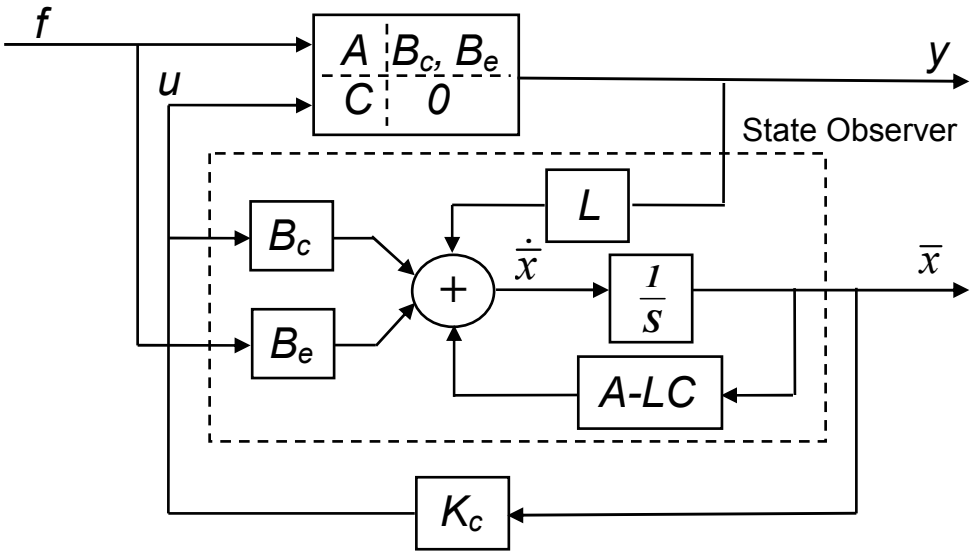

Figure 5.6: Block diagram of the coupled system with state observer

In this experiment, the Laser Vibrometer sensor is used to measure the displacement at the measurement point 2 (sensor gain: 8 μm/V), and the measured displacement together with the excitation input voltage is sent to the state observer to estimate the other states. With all the system state available, the control voltages required on the two MFC control actuators can be calculated using the control gain matrices for each controller design (given by Eq. (5.35), Eq. (5.36), and Eq. (5.37)).

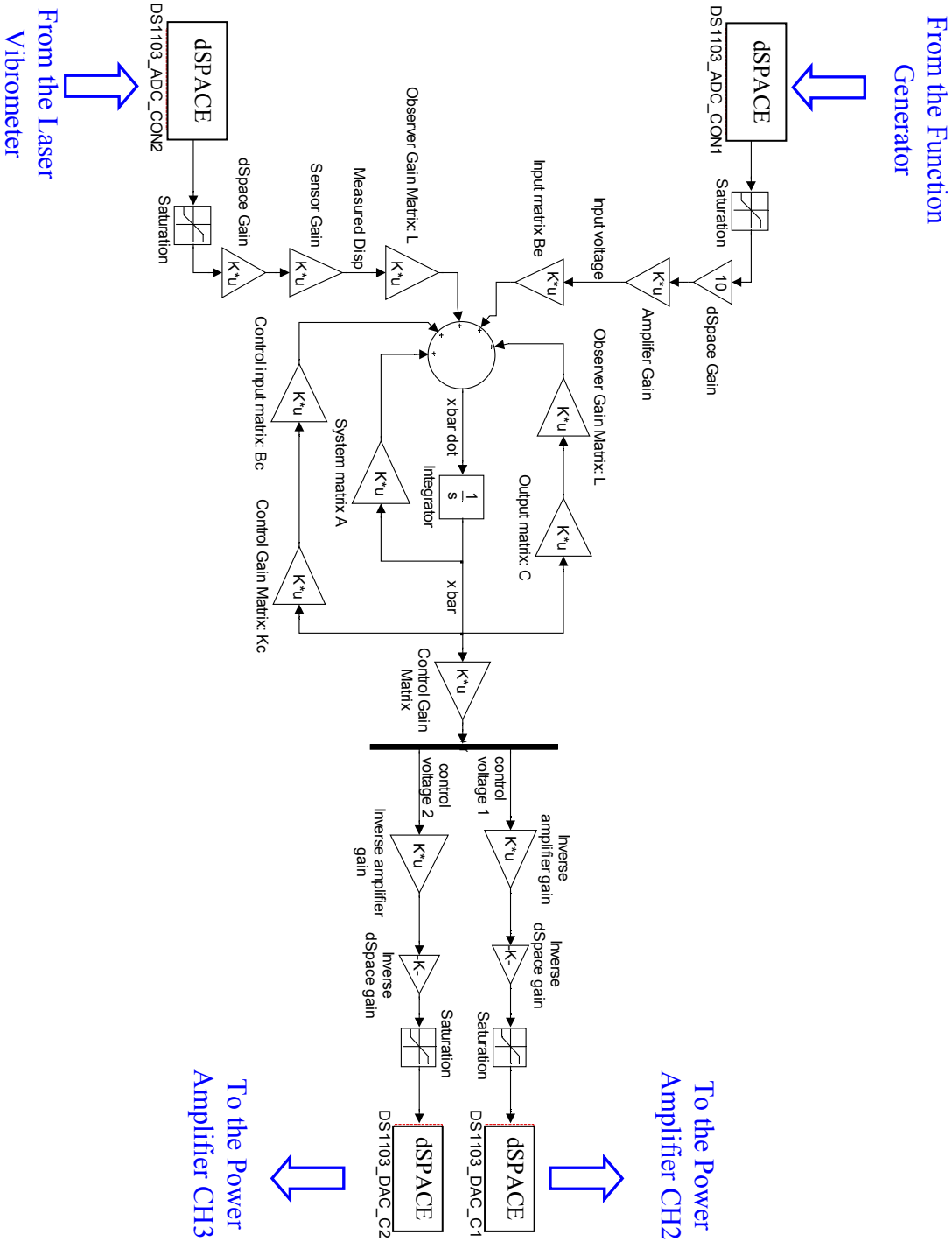

Figure **5.7**: Simulink model for implementing the state observer based controller

Figure 5.7 shows the SIMULINK model developed to implement the sensitivity-enhancing controls. The left part of the SIMULINK model functions as the state observer, where two dSPACE ADC channels (CON1-CH1 and CON2-CH5) are used to read the excitation signal from the Function Generator and the measurement signal from the Laser Vibrometer. The right part of the SIMULINK model calculates the control voltages using the estimated states and the control gain matrix. Two dSPACE DAC channels (CH1 and CH2) are used to output the control voltages to the power amplifier and ultimately to the two MFC control actuators.

With the above observer-based controller design, we can implement the designed sensitivity-enhancing controls to evaluate their performance of sensitivity enhancement. To do this, we compare the natural frequency shifts of the closed-loop systems with those of the open-loop system when a point mass is attached to the same position on the beam. More specifically, two cases of mass additions are tested for each closed-loop system, that is: (1) adding 2g point mass at the measurement point 1, and (2) adding 2g point mass at the measurement point 2. For each closed-loop system given in Table 5.4, we measured the FRFs of the closed-loop system for the original structure without mass addition, and the perturbated structures with the aforementioned two cases of mass additions.

Figure 5.8 shows the measured FRFs of the closed-loop system 1 for the original structure and the perturbated structure with 2g mass added at the measurement point 1. Figure 5.9 shows measured FRFs of the closed-loop system 1 for the original structure and the perturbated structure with 2g mass added at the measurement point 2. Similarly, the measured FRFs of the closed-loop system 2 for two cases of mass additions are

shown in Figure 5.10 and Figure 5.11, respectively; and the measured FRFs of the closed-loop system 3 for the two cases of mass additions are given in Figure 5.12 and Figure 5.13, respectively. From these figures, we can easily see that: (1) for the closed-loop system 1, which are obtained with the strictest constraints on the control gain matrix, the frequency-shift induced by two cases of mass additions are similar to those of the open-loop system, and hence almost no sensitivity enhancement is achieved; (2) for the closed-loop system 2, which corresponds to the moderate constraints on the control gain matrix, only the first frequency sensitivity to mass variation at measurement point 2 is significantly enhanced; (3) for the closed-loop system 3, which allows the maximum amount of external control input, most of the frequency sensitivities to mass variations are significantly enhanced.

To quantify the sensitivity enhancement performance of the three closed-loop system, natural frequency shifts of each closed-loop system corresponding to the two cases of mass additions are compared to those of the open-loop system. Table 5.5 shows the natural frequencies of the open-loop and the three closed-loop systems for the original structure without mass addition and the two cases of mass additions. With these frequencies, we can easily obtain the frequency-shift of the open-loop and closed-loop systems due to mass addition at the two measurement points. The results are given in Table 5.6. Again, from the table, we can see that: (1) no obvious sensitivity enhancement is achieved for closed-loop system 1; (2) closed-loop system 2 only significantly enhances the first frequency sensitivity to mass variation at measurement point 2; (3) closed-loop system 3 achieves significant enhancement on most of the frequency

sensitivities. When we use the performance index of sensitivity-enhancement defined by Eq. (5.34) to evaluate these three closed-loop systems, it gives the following results

$$SE_{c1} = 4.40\,; \quad SE_{c2} = 6.36\,; \quad SE_{c3} = 20.37\,. \tag{5.42}$$

Note that a value of 4.0 for the performance index denotes no sensitivity enhancement.

With the above observations, we can conclude that: (1) the designed controllers are effective in enhancing the frequency sensitivity to mass variations in the beam structure; (2) the more the control effort allowed for the controller design, the better the sensitivity enhancement performance achieved by the resulting closed-loop system.

Table 5.5: Measured natural frequencies of the open-loop and closed-loop system before and after mass addition

System ID	Without mass addition		With 2g mass added to measurement point 1		With 2g mass added to measurement point 2	
	ω_1 (HZ)	ω_2 (HZ)	$\tilde{\omega}_1^I$ (HZ)	$\tilde{\omega}_2^I$ (HZ)	$\tilde{\omega}_1^{II}$ (HZ)	$\tilde{\omega}_2^{II}$ (HZ)
Open-loop	14.31	88.83	14.10	88.47	13.78	86.45
Closed-loop 1	15.96	89.10	15.71	88.76	15.35	86.52
Closed-loop 2	20.46	91.47	20.26	91.04	18.74	89.25
Closed-loop 3	34.71	84.16	36.58	83.05	30.42	84.64

Table 5.6: Natural frequency changes of the open-loop and closed-loop systems due to mass addition at the two measurement points

System ID	With 2g mass added to the measurement point 1		With 2g mass added to the measurement point 2	
	$\Delta\omega_1^I = \omega_1^I - \omega_1$ (HZ)	$\Delta\omega_2^I = \omega_2^I - \omega_2$ (HZ)	$\Delta\omega_1^{II} = \omega_1^{II} - \omega_1$ (HZ)	$\Delta\omega_2^{II} = \omega_2^{II} - \omega_2$ (HZ)
Open-loop	-0.21	-0.35	-0.53	-2.38
Closed-loop 1	-0.25	-0.34	-0.61	-2.58
Closed-loop 2	-0.20	-0.43	-1.72	-2.22
Closed-loop 3	1.87	-1.11	-4.29	0.48

To have a quantitative understanding of the required control effort for each closed-loop system, the control voltages to random noise excitation for each closed-loop system are plotted in Figure **5.14**, Figure **5.15**, and Figure **5.16**, respectively. From these figures, we can see that the closed-loop system 3, which achieves the best performance of sensitivity enhancement, requires higher control voltages (more control effort) than the other two closed-loop systems.

5.5 Conclusions

In this Chapter, a laboratory experiment is designed and performed to verify the sensitivity-enhancing control approach for structural damage detection. In this experiment investigation, a system identification technique is utilized to identify a mathematic model for controller design and system analysis, and hence an accurate finite element model is not needed. The eigenstructure assignment based constrained optimization scheme is utilized to design the optimal sensitivity-enhancing controls. Experiment results show that by applying the sensitivity-enhancing controls to the structure, the frequency sensitivities to mass variations in the beam structure can be significantly enhanced.

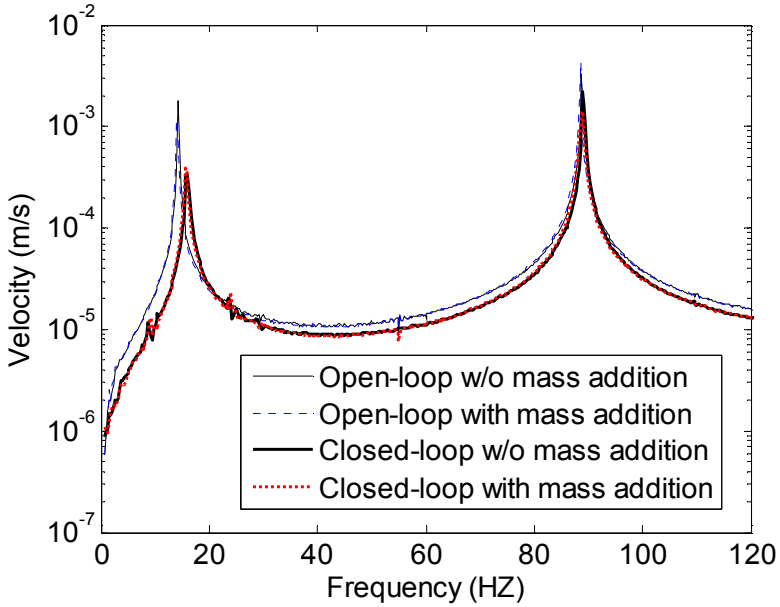

Figure **5.8**: Measured frequency response functions of the closed-loop system 1 before and after adding 2g point mass to the measurement point 1

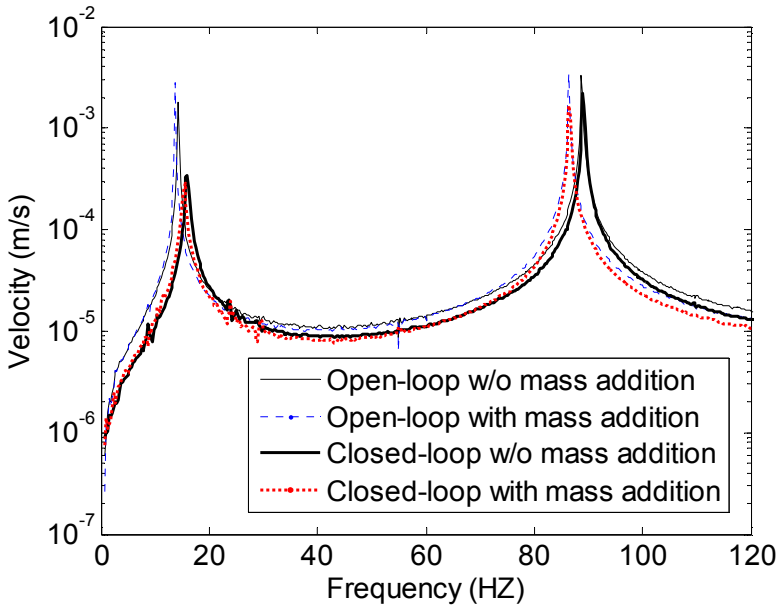

Figure **5.9**: Measured frequency response functions of the closed-loop system 1 before and after adding 2g point mass to the measurement point 2

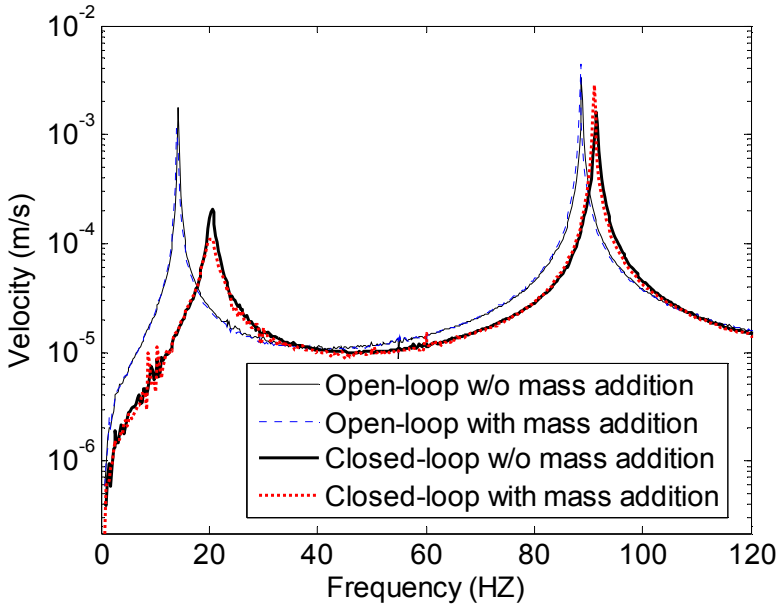

Figure **5.10**: Measured frequency response functions of the closed-loop system 2 before and after adding 2g point mass to the measurement point 1

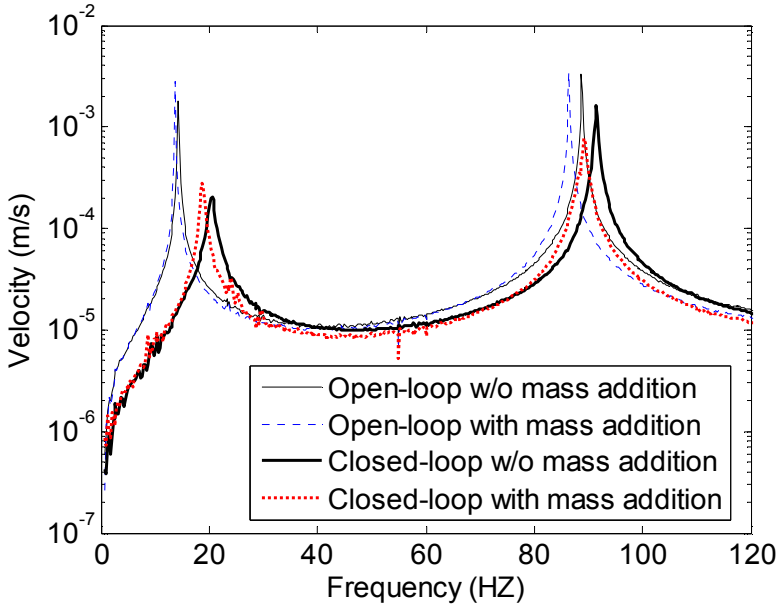

Figure **5.11**: Measured frequency response functions of the closed-loop system 2 before and after adding 2g point mass to the measurement point 2

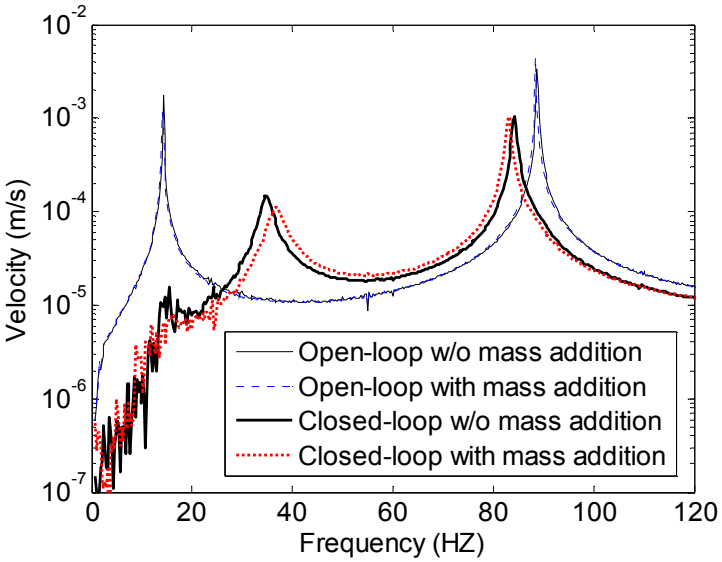

Figure **5.12**: Measured frequency response functions of the closed-loop system 3 before and after adding 2g point mass to the measurement point 1

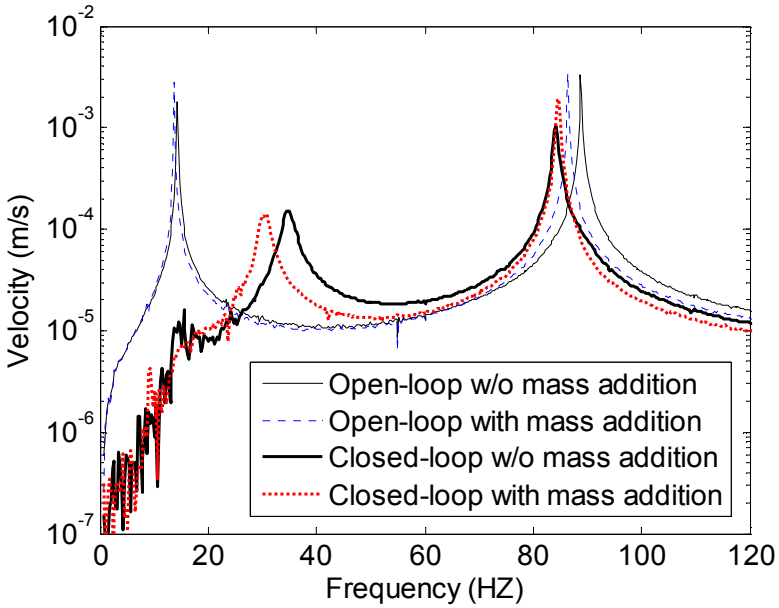

Figure **5.13**: Measured frequency response functions of the closed-loop system 3 before and after adding 2g point mass to the measurement point 2

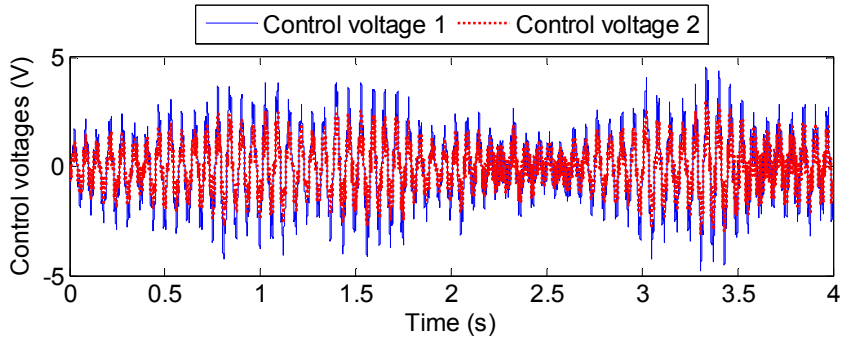

Figure **5.14**: Control voltages of the closed-loop system 1 to random noise excitation with magnitude of 3.96 V rms. (V_{c1} magnitude: 1.69 V rms, and V_{c2} magnitude: 1.05 V rms)

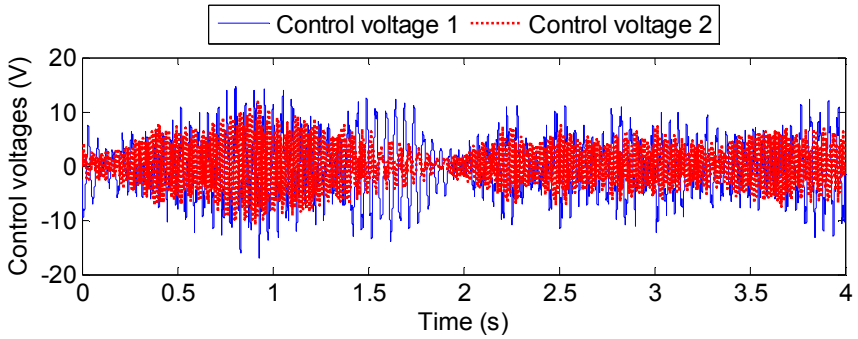

Figure **5.15**: Control voltages of the closed-loop system 2 to random noise excitation with magnitude of 4.01 V rms (V_{c1} magnitude: 5.38 V rms, and V_{c2} magnitude: 3.56 V rms)

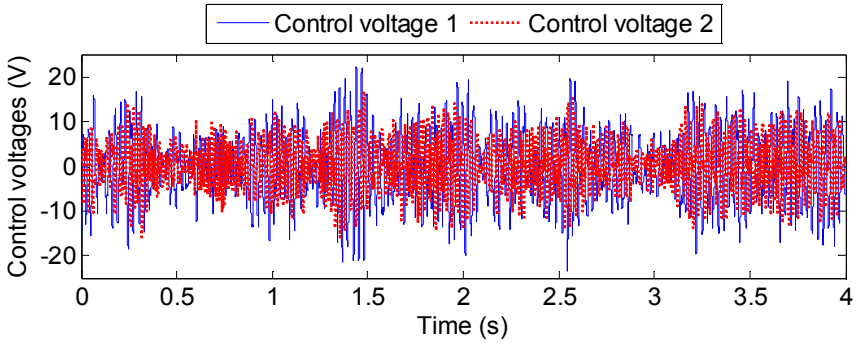

Figure **5.16**: Control voltages of the closed-loop system 3 to random noise excitation with magnitude of 3.91 V rms (V_{c1} magnitude:7.67 V rms, and V_{c2} magnitude: 5.36 V rms)

Chapter 6

Conclusions and Recommendations

The purpose of this chapter is to summarize the research efforts and achievements in this thesis, and to recommend future research directions towards the improvement and implementation of the approaches developed in this thesis.

6.1 Conclusions

In this thesis, two enhanced frequency-shift-based damage identification methods are developed to address the two major limitations of the traditional approach, namely, deficiency of frequency measurement data for damage identification and low sensitivity of frequency shift to damage effects. The first method with tunable piezoelectric circuitry network can effectively enrich the frequency measurement data for damage identification through appropriate tuning of the circuitry elements (i.e., inductors). The second method using sensitivity-enhancing controls can simultaneously achieve the enhancement of frequency sensitivity to damage effects and the enrichment of frequency measurement data for damage identification. The research efforts, achievements and discussions related to these two methods are summarized in the following two subsections.

6.1.1 Enhanced Method Using Tunable Piezoelectric Circuitry Network

(1) A new idea of using the tunable piezoelectric circuitries coupled to the mechanical structure to enrich the frequency measurement data for damage identification is proposed. By integrating tunable piezoelectric circuitries to the structure and appropriately tuning the circuitry elements, one can obtain a much enlarged dataset of natural frequency measurements for damage identification. Compared with the previous approaches that use mechanical tailoring to enrich frequency measurement data (e.g., mass/stiffness addition techniques [111, 112]), this approach utilizes electrical tailoring (i.e., circuitry tuning) to alter the system dynamics, and hence is much easier to implement.

(2) Guidelines on favorable inductance tuning that can yield the optimal damage identification performance are developed. Analyses show that when the inductances are tuned to accomplish eigenvalue curve veerings between system eigenvalue pairs, the enriched frequency measurement data can most effectively capture the damage information, and hence, results in the most accurate damage identification results.

(3) An iterative second-order perturbation-based algorithm is developed to identify the damage features (i.e., location and severity) from the measured frequency changes before and after damage occurrence. This algorithm takes into account the damage-induced mode shape changes by including high order terms into the eigenvalue perturbation formulation, while actual

measurements of mode shapes before and after damage are not required for this algorithm.

(4) Numerical analyses and case studies on benchmark beam and plate structures are carried out to demonstrate and verify the proposed new method. Numerical results show that the damage identification performance can be significantly improved by using the proposed new approach with favorable inductance tuning.

(5) Compared with the sensitivity-enhancing control approach, this approach is passive in nature; therefore system stability is guaranteed and it dose not require a sensor-controller-actuator architecture and external control inputs. On the other hand, it cannot achieve significant sensitivity enhancement as the sensitivity-enhancing control approach. Therefore, this approach is suitable for damage identification problems where the deficiency of frequency measurement data is the major concern while the frequency sensitivity issue is not so severe.

6.1.2 Enhanced Method Using Sensitivity-Enhancing Control

(1) A feedback controller can be designed to enhance the sensitivity of frequency shift to structural damage, which would benefit the process of damage identification. In order to obtain the best performance of sensitivity enhancement in the closed-loop system, both the closed-loop eigenvalues and

eigenvectors should be treated as design variables in the controller synthesis process.

(2) To achieve the best performance of frequency sensitivity enhancement, a constrained optimization problem is formulated to find the optimal eigenstructure assignment for the closed-loop system, which leads to the optimal sensitivity-enhancing control.

(3) Multiple closed-loop systems can be obtained from different sensitivity-enhancing controls, and these closed-loop systems provide a much enlarged dataset of natural frequency measurements for damage identification. Therefore, by designing a series of sensitivity-enhancing controls and utilizing the natural frequencies of the resulting closed-loop systems for damage identification, both of the two major limitations of the classical frequency-shift-based damage identification approach can be overcome.

(4) A series of numerical studies are performed on an example structure. It is shown that, in order to achieve the best performance of sensitivity enhancement, both the closed-loop eigenvalues and eigenvectors should be simultaneously optimized. It is also demonstrated that the proposed method is effective in damage identification and is robust against uncertainties in frequency measurements.

(5) This approach requires an accurate finite element model for controller design and system analysis. To fulfill this requirement, the concept of sensitivity-enhancing control is utilized to develop an iterative model updating method using only the measured natural frequencies. With this extension, the proposed approach can be used for dual functions of model updating and damage identification.

(6) A laboratory experiment is designed and carried out to verify the sensitivity-enhancing control approach for damage identification. The experiment utilizes a system identification technique to identify a mathematical model directly from test data for controller design and system analysis, and hence does not require an analytical model as needed in the original approach. Experiment results show that the frequency sensitivity to mass variations in the structure can be significantly enhanced by applying the designed sensitivity-enhancing controls to the structure.

6.2 Recommendations for Future Research Work

In this section, future research work towards the improvement and implementation of the approaches developed in this thesis, as well as other promising methods for structural health monitoring, are recommended.

6.2.1 Further Improvement to the Sensitivity-Enhancing Control Approach for Structural Damage Identification

The experimental studies presented in Chapter 5 have shown that the frequency sensitivity to mass variation can be significantly enhanced by integrating sensitivity-enhancing control to the beam structure. Through the current activities of experiment investigation, we found that in order to achieve substantial enhancement of frequency sensitivity, it always requires relatively high control gains. However, large control gains may also amplify the effect of measurement noise, and this may affect the system performance and sometime even cause the closed-loop system to be unstable. In the current experiment investigation, both the system model and the controller design are based on the assumption of deterministic system behavior, and thus the effect of model uncertainty and noise effect are neglected. Therefore, to improve the current approach, the effect of model uncertainty and measurement noise should be considered in system analysis and design. To achieve this goal, stochastic approaches of system identification and state estimation are suggested in future experimental investigations.

The stochastic system identification problem is stated as: Given input data $\boldsymbol{u}(t)$ and output measurement data $\boldsymbol{y}(t)$, find the quadruple system matrices $\{\boldsymbol{A},\boldsymbol{B},\boldsymbol{C},\boldsymbol{D}\}$ (up to within a similarity transformation) and the noise covariance matrices $\boldsymbol{W}$ and $\boldsymbol{V}$, which correspond to the process noise $w(t)$ and measurement noise $v(t)$, respectively. One popular method of system identification for the stochastic state-space model is the so-called stochastic subspace identification. A general overview of the subspace identification method (both deterministic and stochastic) is provided by Refs. [151,152].

Subspace methods identify state-space models from input and output data by applying robust numerical techniques such as QR factorization, SVD and least squares. There are two types of stochastic subspace identification methods than can be used: Covariance-Driven Stochastic Subspace Identification [153,154] and Data-Driven Stochastic Subspace Identification (SSI-DATA) [155,156].

In accordance with the stochastic system model, the state observer should also allow for stochastic uncertainties in the system. For a stochastic system model, the optimal state observer is given by the well-known Kaman-Bucy Filter (KBF) [157-160]. The Kalman-Bucy Filter is considered to be the optimal state observer in a least-square sense and allows for stochastic uncertainties in the system.

6.2.2 Multifunctional Piezoelectric Sensory Node via Power Electronic Circuit for Structural Health Monitoring

This part of future research work features the practical implementation and function extension of structural health monitoring system using variable piezoelectric circuitry networking. The key idea is to use innovative power electronics to develop multifunctional adaptive piezoelectric sensory node to realize the tunable inductance function, self-sensing actuation, and energy harvesting function. First, the power-electronics-based synthetic inductor would have the advantages of high-performance and low-power consumption when compared to the traditional op-amp based synthetic inductor [122,123]. This will greatly favor the practical implementation of structural health monitoring using variable piezoelectric circuitry networking. Second, the power electronic circuit can be implemented to realize additional functions besides the tunable

inductor for structural health monitoring, and those additional functions include self-sensing actuation [161-164] and energy harvesting [165-170].

Figure 6.1 shows the block diagram of a single sensor node. In the circuitry diagram, the switch-mode inverter circuitry serves as an efficient, general-purpose interface to the piezoelectric transducer, allowing all the aforementioned functions to be synthesized in an integrated manner [166-169]. The power electronic arrangement is coupled with a local controller. The local controller is designed to synthesize the multiple functions of the sensor node, and thus has a different goal than the overall structural system controller (shown as the global controller in Figure 6.1), which may be designed for the purpose of command following, shape control, and vibration control, etc. Voltage and current measurements used by the local controller can also be used to determine the structural strain/displacement, which enables the device's sensing ability.

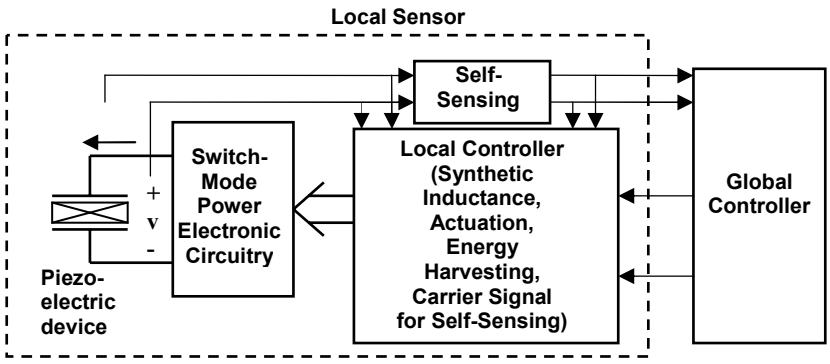

Figure 6.1: Block diagram of single sensor setup

6.2.3 Structural Health Monitoring Using the Measured Frequency Response Functions

This thesis has been focused on structural health monitoring using only the measured natural frequencies of the structural system. Another research direction is to directly use the measured frequency response function (FRF) data for structural health monitoring [171-174]. Although promising, there are some fundamental issues that need to be resolved in order to obtain accurate and reliable results of damage identification.

(1) *Selection of frequency points for damage identification*. A major advantage of using measured FRF data over using modal data (natural frequencies and mode shapes) comes from the fact that FRF data can provide much more information in a desired frequency range than modal data. However, not all the information is suitable for structural damage identification, and the accuracy and reliability of the damage identification result heavily depends on the selection of frequency points from the measured FRFs [172]. Therefore, a good research direction is to develop guidelines for frequency selection to achieve the most accurate and reliable results of damage identification. The following issues need to be considered when developing the guidelines for frequency selection, (i) the effects of modeling errors; (ii) the effects of measurement noise and errors; (iii) the sensitivity of FRF magnitude to damage effects.

(2) *Non-model based damage identification method.* The traditional FRF-based damage identification method requires an accurate finite element model and the measurement of FRFs at all the degrees-of-freedom [171-174]. However,

these two conditions are practically impossible to meet, especially for large complex structures. Therefore, another good research direction is to develop a non-model damage identification method using the measured frequency response functions. One promising solution is to use the measured FRFs themselves to calculate the FRF sensitivity for damage identification.

Bibliography

1. Sohn, H., Farrar, C.R., Hemez, F.M., Shunk, D.D., Stinemates, D.W. and Nadler, B.R., 2003, "A review of structural health monitoring literature: 1996–2001," Los Alamos National Laboratory Report, LA-13976-MS, Los Alamos, New Mexico.

2. Chang, F.-K., Structural Health Monitoring 2001: The Demands and Challenges–*Proceedings of the 3rd International Workshop on Structural Health Monitoring*, DEStech Publications, 2001.

3. Chang, F.-K., Structural Health Monitoring 2003: From Diagnosis & Prognostics to Structural Health Management–*Proceedings of the 4th International Workshop on Structural Health Monitoring*, DEStech Publications, 2003.

4. Chang, F.-K., Structural Health Monitoring 2005: Advancements and Challenges for Implementation–*Proceedings of the 5th International Workshop on Structural Health Monitoring*, DEStech Publications, 2005.

5. Balageas, D., Structural Health Monitoring 2002: *Proceedings of the 1st European Workshop on Structural Health Monitoring*; SAGE Publications, 2002.

6. Boller, C., and Staszewski, W.J., Structural Health Monitoring 2004: *Proceedings of the 2nd European Workshop on Structural Health Monitoring*; DEStech Publications, 2004.

7. Güemes, A., Structural Health Monitoring 2006: *Proceedings of the 3rd European Workshop on Structural Health Monitoring*; DEStech Publications, 2006.

8. Wu, Z., and Abe, M., Structural Health Monitoring and Intelligent Infrastructure: *Proceedings of the first International Conference on Structural Health Monitoring and Intelligent Infrastructure*, Taylor Francis (UK), 2003.

9. Proceedings of the SPIE Symposium on Nondestructive Evaluation 2006: Vol. 6176 - *Nondestructive Evaluation and Health Monitoring of Aerospace Materials, Composites, and Civil Infrastructure V*, Mufti A.A., et al., Editors; Vol. 6177 - *Health Monitoring and Smart Nondestructive Evaluation of Structural and Biological Systems* V, Kundu, T., Editor, Vol. 6179 - *Advanced Sensor Technologies for Nondestructive Evaluation and Structural Health Monitoring II*, Meyendorf, N., et al., Editors.

10. Proceedings of the SPIE Symposium on Nondestructive Evaluation 2005: Vol. 5767 - *Nondestructive Evaluation and Health Monitoring of Aerospace Materials, Composites, and Civil Infrastructure IV*, Shull, P.J., et al, Editors; Vol. 5768 -

Health Monitoring and Smart Nondestructive Evaluation of Structural and Biological Systems IV, Kundu, T., Editor, Vol. 5770 - *Advanced Sensor Technologies for Nondestructive Evaluation and Structural Health Monitoring*, Meyendorf, N., et al, Editors.

11. Proceedings of the SPIE Symposium on Nondestructive Evaluation 2004: Vol. 5393 - *Nondestructive Evaluation and Health Monitoring of Aerospace Materials and Composites III*, Shull, P.J., Gyekenyesi, A.L., Editors; Vol. 5394 - *Health Monitoring and Smart Nondestructive Evaluation of Structural and Biological Systems III*, Kundu, T., Editor.

12. Proceedings of the SPIE Symposium on Nondestructive Evaluation 2003: Vol. 5046 - *Nondestructive Evaluation and Health Monitoring of Aerospace Materials and Composites II*, Gyekenyesi, A.L., and Shull, P.J., Editors; Vol. 5047 - *Health Monitoring and Smart Nondestructive Evaluation of Structural and Biological Systems III*, Kundu, T., Editor.

13. Proceedings of the SPIE Symposium on Nondestructive Evaluation 2002: Vol. 4702 - *Health Monitoring and Smart Nondestructive Evaluation of Structural and Biological Systems*, Kundu, T., Editor; Vol. 4704 - *Nondestructive Evaluation and Health Monitoring of Aerospace Materials and Civil Infrastructures*, Gyekenyesi, A.L., et al., Editors.

14. Proceedings of the SPIE Symposium on Nondestructive Evaluation 2001: Vol. 4335 – *Advanced Nondestructive Evaluation for Structural and Biological Health Monitoring,* Kundu, T., Editor; Vol. 4336 - *Nondestructive Evaluation of Materials and Composites V,* Baaklini, G.Y., et al., Editors; Vol. 4337 - *Health Monitoring and Management of Civil Infrastructure Systems,* Chase, S.B., and Aktan, A.E., Editors.

15. Cawley, P., 1997, "Long range inspection of structures using low frequency ultrasound," *Proceedings of DAMAS '97*: *Structural Damage Assessment Using Advanced Signal Processing Procedures*, University of Sheffield, UK, pp. 1–17.

16. Sikorsky, C., and Stubbs, N., 1997, "Improving bridge management using NDE and quality management," *Structural Damage Assessment Using Advanced Signal Processing Procedures, Proceedings of DAMAS '97*, University of Sheffield, UK, pp. 399–408.

17. Sikorsky, C., 1997, "Integrating modal based NDE techniques and bridge management systems using quality management," *Smart Systems for Bridges, Structures, and Highways*, *Proceedings of SPIE*, Vol. 3043, pp. 31–42.

18. Sikorsky, C., 1999, "Development of a health monitoring system for civil structures using a Level IV nondestructive damage evaluation method," *Structural Health Monitoring 2000*, Stanford University, Palo Alto, California, pp. 68–81.

19. Bartelds, G., 1997, "Aircraft structural health monitoring, prospects for smart solutions from a European viewpoint," *Structural Health Monitoring, Current Status and Perspectives*, Stanford University, Palo Alto, California, pp. 293–300.

20. Chang, F.K., 1999, "Structural Health Monitoring: A Summary Report on the First International Workshop on Structural Health Monitoring," September 18–20, 1997, *Structural Health Monitoring 2000*, Stanford University, Palo Alto, California.

21. Zak, A., Krawczuk, M., and Ostachowicz, W., 1999, "Vibration of a laminated composite plate with closing delamination," *Structural Damage Assessment Using Advanced Signal Processing Procedures*, *Proceedings of DAMAS '99*, University College, Dublin, Ireland, pp. 17–26.

22. Jacob, P.J., Desforges, M.J., and Ball, A.D., 1997, "Analysis of suitable wavelet coefficients for identification of the simulated failure of composite materials," *Structural Damage Assessment Using Advanced Signal Processing Procedures*, *Proceedings of DAMAS '97*, University of Sheffield, UK, pp. 31–40.

23. Ruotolo, R., and Surace, C., 1997, "Damage assessment of multi-cracked beams using combinatorial optimization," *Structural Damage Assessment Using Advanced Signal Processing Procedures*, *Proceedings of DAMAS '97*, Univeristy of Sheffield, UK, pp. 77–86.

24. Ruotolo, R., and Surace, C., 1997, "Damage assessment of multiple-cracked beams: results and experimental validation," *Journal of Sound and Vibration*, 206(4), pp. 567–588.

25. Rytter, A., and Kirkegaard, P., 1997, "Vibration based inspection using neural networks," *Structural Damage Assessment Using Advanced Signal Processing Procedures*, *Proceedings of DAMAS '97*, University of Sheffield, UK, pp. 97–108.

26. Mares, C., Mottershead, J.E., and Friswell, M.I., 1999, "Damage location in beams by using rigid-body constraints," *Damage Assessment of Structures*, *Proceedings of the International Conference on Damage Assessment of Structures (DAMAS 99)*, Dublin, Ireland, pp. 381–390.

27. Williams, E.J., and Messina, A., 1999, "Applications of the multiple damage location assurance criterion," *Proceedings of the International Conference on Damage Assessment of Structures (DAMAS 99)*, Dublin, Ireland, pp. 256–264.

28. Staszewski, W.J., Biemans, C., Boller, C., and Tomlinson, G.R., 1999, "Impact damage detection in composite structures: recent advances," *Structural Health Monitoring 2000*, Stanford University, Palo Alto, California, pp. 754–763.

29. Garibaldi, L., Marchesiello, S., and Gorman, D.J., 1999, "Bridge dynamics misinterpretations due to low spatial resolution and closeness of frequencies,"

Damage Assessment of Structures, *Proceedings of the International Conference on Damage Assessment of Structures (DAMAS 99)*, Dublin, Ireland, pp. 411–422.

30. Doebling, S.W., Farrar, C.R., and Prime, M.B., 1998, "A summary review of vibration-based damage identification methods," *Shock and Vibration Digest,* 30(2), pp. 91-105.

31. Doebling, S.W., Farrar, C.R., Prime, M.B., and Shevitz, D.W., 1996, "Damage identification and health monitoring of structural and mechanical systems from changes in their vibration characteristics: a literature review," Los Alamos National Laboratory Report LA-13070-MS, Los Alamos, New Mexico.

32. Park, G., Sohn, H., Farrar, C.R., and Inman, D.J., 2003, "Overview of piezoelectric impedance-based health monitoring and path forward," *Shock and Vibration Digest*, 35(6), pp. 451-463.

33. Giurgiutiu, V., and Cuc A., 2005, "Embedded non-destructive evaluation for structural health monitoring, damage detection, and failure prevention," *Shock and Vibration Digest*, 37(2), pp. 83-105.

34. Giurguitiu, V., 2005, "Tuned Lamb wave excitation and detection with piezoelectric wafer active sensors for structural health monitoring," *Journal of Intelligent Material Systems and Structures*, 16(4), pp. 291-305.

35. Epureanu, B.I., 2003, "Nonlinear and chaotic vibration-based damage detection," *Proceedings of the ASME Applied Mechanics Division,* Vol. 254, pp. 163-170.

36. Epureanu, B.I., Yin, S.-H., and Derriso, M.M., 2005, "High-sensitivity damage detection based on enhanced nonlinear dynamics," *Smart Materials and Structures*, 14(2), pp. 321-327.

37. Todd, M.D., Nichols, J.M., Pecora, L.M., and Virgin, L.N., 2001, "Novel nonlinear feature identification in vibration-based damage detection using local attractor variance," *Proceedings of the International Modal Analysis Conference - IMAC*, v 1, pp. 438-444.

38. Livingston, R.A., Jin, A., and Marzougui, D., 2001, "Application of nonlinear dynamics analysis to damage detection and health monitoring of highway structures," *Proceedings of SPIE - The International Society for Optical Engineering*, Vol. 4337, pp. 402-410.

39. Rytter, A., 1993, Vibration Based Inspection of Civil Engineering Structures, Ph.D Dissertation, Department of Building Technology and Structural Engineering, Aalborg University, Denmark.

40. Doherty, J. E., Nondestructive Evaluation, Chapter 12 in Handbook on Experimental Mechanics, A. S. Kobayashi (Ed.), Society of Experimental Mechanics, Inc., 1987.

41. Salawu, O.S., 1997, "Detection of structural damage through changes in frequency: a review," *Engineering Structures*, 19(9), pp. 718-723.

42. Cawley, P., and Adams, R.D., 1979, "The locations of defects in structures from measurements of natural frequencies," *Journal of Strain Analysis*, 14(2), pp. 49–57.

43. Stubbs, N., and Osegueda, R., 1990, "Global non-destructive damage evaluation in solids," *Modal Analysis: The International Journal of Analytical and Experimental Modal Analysis*, 5(2), pp. 67-79.

44. Stubbs, N., and Osegueda, R., 1990, "Global damage detection in solids-experimental verification," *Modal Analysis: The International Journal of Analytical and Experimental Modal Analysis*, 5(2), pp. 81-97.

45. Richardson, M.H., and Mannan, M.A., 1992, "Remote detection and location of structural faults using modal parameters," *Proceedings of the 10th International Modal Analysis Conference*, pp. 502–507.

46. Hearn, G., and Testa, R.B., 1991, "Modal analysis for damage detection in structures," *Journal of Structural Engineering*, 117(10), pp. 3042–3063.

47. Williams, E.J., and Messina, A., 1999, "Applications of the multiple damage location assurance criterion," *Proceedings of the International Conference on Damage Assessment of Structures (DAMAS 99)*, Dublin, Ireland, pp. 256–264.

48. West, W.M., 1984, "Illustration of the use of modal assurance criterion to detect structural changes in an orbiter test specimen," *in Proc. of Air Force Conference on Aircraft Structural Integrity*, pp. 1–6.

49. Kim, J.-H., Jeon, H.-S., and Lee, C.-W., 1992, "Application of the modal assurance criteria for detecting and locating structural faults," *in Proc. of the 10th International Modal Analysis Conference*, pp. 536–540.

50. Salawu, O.S., and Williams, C., 1995, "Bridge assessment using forced vibration testing," *Journal of Structural Engineering*, 121(2), pp. 161–173.

51. Ko, J. M., Wong, C. W., and Lam, H.F., 1994, "Damage detection in steel framed structures by vibration measurement approach," *in Proc. of 12th International Modal Analysis Conference*, pp. 280–286.

52. Pandey, A.K., Biswas, M., and Samman, M.M., 1991, "Damage detection from changes in curvature mode shapes," *Journal of Sound and Vibration*, 145(2), pp. 321–332.

53. Stubbs, N., J.-T. Kim, and K. Topole, 1992, "An efficient and robust algorithm for damage localization in offshore platforms," *in Proc. ASCE 10th Structures Congress*, pp. 543–546.

54. Chance, J., Tomlinson, G.R., and Worden, K., 1994, "A simplified approach to the numerical and experimental modeling of the dynamics of a cracked beam," *in Proc. Of the 12th International Modal Analysis Conference*, pp. 778–785.

55. Ho, Y.K., and Ewins, D.J., 2000, "On the structural damage identification with mode shapes," *European COST F3 Conference on System Identification and Structural Health Monitoring*, Madrid, Spain, pp. 677–686.

56. Wang, A, Lin, R.M., and Lim, M.K., 1997, "Structural damage detection using measured FRF data," *Computer Methods in Applied Mechanics and Engineering*, 147, pp. 187-197.

57. Trendafilova, I., 1998, "Damage detection in structures from dynamic response measurements: an inverse problem perspective," *Modeling and Simulation Based Engineering*, Technical Science Press, pp. 515–520.

58. Agneni, A., Crema, L.B., and Mastroddi, F., 2000, "Damage detection from truncated frequency response functions," *European COST F3 Conference on System Identification and Structural Health Monitoring*, Madrid, Spain, pp. 137–146.

59. Park, N.-G, and Park, Y.-S, 2003, "Damage detection using spatially incomplete frequency response functions," *Mechanical Systems and Signal Processing*, 17(3), pp.519-532.

60. Aktan, A.E., Lee, K.L., Chuntavan, C., and Aksel, T., 1994, "Modal testing for structural identification and condition assessment of constructed facilities," *in Proc. of 12th International Modal Analysis Conference*, pp. 462–468.

61. Pandey, A.K., and Biswas, M., 1994, "Damage detection in structures using changes in flexibility," *Journal of Sound and Vibration*, 169 (1), pp. 3–17.

62. Peterson, L.D., Doebling, S.W., and Alvin, K.F., 1995, "Experimental determination of local structural stiffness by disassembly of measured flexibility matrices," *in Proc. of the 36th AIAA/ASME/ASCE/AHS/ASC Structures, Structural Dynamics, and Materials Conference*, pp. 2756–2766, AIAA-95-1090-CP.

63. Reich, G.W., and Park, K.C., 2000, "Experimental applications of a structural health monitoring methodology," *Smart Structures and Materials 2000: Smart Systems for Bridges, Structures, and Highways*, *Proceedings of SPIE*, Vol. 3988, Newport Beach, California, pp. 143–153.

64. Lin, C. S., 1990, "Location of modeling errors using modal test data," *AIAA Journal*, 28, pp. 1650–1654.

65. Lin, C.S., 1994, "Unity check method for structural damage detection," *in Proc. of 35th AIAA/ASME/ASCE/AHS/ASC Structures, Structural Dynamics and Materials Conference*, pp. 347–354, AIAA-94-1717-CP.

66. Lin, C., 1998, "Unity check method for structural damage detection," *Journal of Spacecraft and Rockets*, 35(4), pp. 577–579.

67. He, J., and D.J. Ewins, 1986, "Analytical stiffness matrix correction using measured vibration modes," *Modal Analysis: The International Journal of Analytical and Experimental Modal Analysis*, 1(3), pp. 9–14.

68. Park, Y.S., Park, H.S., and Lee, S.S., 1988, "Weighted-error-matrix application to detect stiffness damage-characteristic measurement," *Modal Analysis: The International Journal of Analytical and Experimental Modal Analysis*, 3(3), pp. 101–107.

69. Peterson, L.D., Alvin, K.F., Doebling, S.W., and Park, K.C., 1993, "Damage detection using experimentally measured mass and stiffness matrices," *in Proc. of 34th AIAA/ ASME/ASCE/AHS/ASC Structures, Structural Dynamics, and Materials Conference*, pp. 1518–1528, AIAA-93-1482-CP.

70. Salawu, O.S., and Williams, C., 1993, "Structural damage detection using experimental modal analysis - a comparison of some methods," *Proceeding of 11th International Modal Analysis Conference*, pp. 254–260.

71. Ojalvo, I.U., and Pilon, D., 1988, "Diagnostics for geometrically locating structural math model errors from modal test data," *Proceeding of 29th AIAA/ASME/ASCE/AHS/ASC Structures, Structural Dynamics, and Materials Conference*, pp. 1174–1186.

72. Zimmerman, D. C., and Smith, S.W., 1992, Model Refinement and Damage Location for Intelligent Structures, *Intelligent Structural Systems*, H.S. Tzou and G.L. Anderson, Eds., Kluwer Academic Publishers, pp. 403-452.

73. Hemez, F. M., 1993, Theoretical and Experimental Correlation Between Finite Element Models and Modal Tests in the Context of Large Flexible Space Structures, Ph. D. Dissertation, Dept. of Aerospace Engineering Sciences, University of Colorado, Boulder, CO.

74. Kaouk, M., 1993, Finite Element Model Adjustment and Damage Detection Using Measured Test Data, Ph. D. Dissertation, Dept. of Aerospace Engineering Mechanics and Engineering Science, Univ. of Florida, Gainesville, FL.

75. Kabe, A.M., 1985, "Stiffness matrix adjustment using mode data," *AIAA Journal*, 23(9), pp. 1431-1436.

76. Berman, A., and Nagy, E. J., 1983, "Improvement of large analytical model using test data," *AIAA Journal*, 21(8), pp. 1168-1173.

77. Smith, S. W., and Beattie, C. A., 1991, "Model correlation and damage location for large space truss structures: secant method development and evaluation," NASA report NASA-CR-188102.

78. Kammer, D.C., 1988, "Optimal approximation for residual stiffness in linear system identification," *AIAA Journal*, 26(1), pp. 104-112.

79. Zimmerman, D. C., and Kaouk, M., 1994, "Structural damage detection using a minimum rank update theory," *ASME Journal of Vibration and Acoustics*, 116(2), pp. 222-231.

80. Kaouk, M., and Zimmerman, D.C., 1994, "Structural damage assessment using a generalized minimum rank perturbation theory," *AIAA Journal*, 32(4), pp. 836-842.

81. Kaouk, M., and Zimmerman, D.C., 1994, "Assessment of damage affecting all structural properties," *Proceeding of the 9th VPI&SU Symposium on Dynamics and Control of Large Structures*, pp. 445-455.

82. Kaouk, M., and Zimmerman, D. C., 1995, "Structural health assessment using a partition model update technique," *Proceedings of the 13th International Modal Analysis Conference,* pp. 1673–1679.

83. Zimmerman, D. C., Kaouk, M., and Simmermacher, T., 1995, "Structural damage detection using frequency response functions," *Proceeding of the 13th International Modal Analysis Conference*, pp. 179-184.

84. Zimmerman, D. C., Kaouk, M., and Simmermacher, T., 1995, "On the role of engineering insight and judgement structural damage detection," *Proceeding of the 13th International Modal Analysis Conference*, pp. 414-420.

85. Mottershead, J.E., and Friswell, M.I., 1993, "Model updating in structural dynamics: a survery," *Journal of Sound and Vibration*, 167, pp. 347-375.

86. Friswell, M.I., and Mottershead, J.E., 1995, Finite Element Model Updating in Structural Dynamics, Kluwer Academic Publishers, Dordrecht.

87. Link, M., 1999, "Updating of analytical models-review of numerical procedures and application aspects," *Proceeding of Structural Dynamics Forum*, Los Alamos, NM.

88. Haug, E. F., and Choi, K. K., 1984, "Structural design sensitivity analysis with generalized global stiffness and mass matrices," *AIAA Journal*, 22(9), pp. 1299-1303.

89. Fox, R.L., and Kapoor, M.P., 1968, "Rates of change of eigenvalues and eigenvectors," *AIAA Journal*, 6, pp. 2426-2429.

90. Rogers, L.C., 1970, "Derivatives of eigenvalues and eigenvectors," *AIAA Journal*, 8(5), pp. 943-944.

91. Ricles, J. M., 1991, "Nondestructive structural damage detection in flexible space structures using vibration characterization," NASA report CR-185670.

92. Hemez, F. M., 1993, Theoretical and experimental correlation between finite element models and modal tests in the context of large flexible space structures, Ph.D. Dissertation, Department of Aerospace Engineering Sciences, University of Colorado, Boulder, CO.

93. Jung, H., 1992, Structural dynamic model updating using eigensensitivity analysis, Ph.D. Thesis, Department of Mechanical Engineering, Imperial College, London, UK.

94. Lin, R.M., Lim, M.K., and Du, H., 1995, "Improved inverse eigensensitivity method for structural analytical model updating," *ASME Journal of Vibration and Acoustics*, 117(2), pp. 192-198.

95. Lin, R.M., and Ewins, D.J., "Model updating using FRF data," *Proceedings of the 15th International Modal Analysis Seminar*, K.U. Leuven, Belgium, 1990, pp. 141-163.

96. Lin, R.M., and Ewins, D.J., 1994, "Analytical model improvement using frequency response functions," *Mechanical Systems and Signal Processing*, 8(4), pp. 437-458.

97. Minas, C., and Inman, D.J., 1990, "Matching finite element models to modal data," *Journal of Vibration, Acoustics, Stress, and Reliability in Design*, 112(1), pp. 84-92.

98. Zimmerman, D.C., and Widengren, M., 1990, "Correcting finite element models using a symmetric eigenstructure assignment technique," *AIAA Journal*, 28(9), pp. 1670-1676.

99. Zimmerman, D.C., and Kaouk, M., 1992, "Eigenstructure assignment approach for structural damage detection," AIAA Journal, 30(7), pp. 1848-1855.

100. Lim, Tae W., Kashangaki, Thomas A.L., 1994, "Structural damage detection of space truss structures using best achievable eigenvectors," *AIAA Journal*, 32(5), pp. 1049-1057.

101. Lim, Tae W., 1995, "Structural damage detection using constrained eigenstructure assignment," *Journal of Guidance, Control, and Dynamics*, 18(3), pp. 411-418.

102. Gysin, H., 1990, "Comparison of expansion methods for FE modeling error localization," *Proceedings of the 8th International Modal Analysis Conference*, pp. 195-204.

103. Lin, C.S., 1990, "Location of modeling errors using modal test data," *American Institute of Aeronautics and Astronautics Journal*, 28(9), pp. 1650-1654.

104. Dascotte, E., 1990, "Practical application of finite element tuning using experimental modal data," *Proceedings of the 8th International Modal Analysis Conference*, pp. 1032-1037.

105. Friswell, M.I., and Penny, J.E.T., 1997, "The practical limits of damage detection and location using vibration data," *Proceedings of 11th VPI&SU Symposium on Structural Dynamics and Control*, Blacksburg, VA, pp. 31-40.

106. Messina, A., Williams, E.J., and Contursi, T., 1998, "Structural damage detection by a sensitivity and statistical-based method," *Journal of Sound and Vibration*, 216(5), pp. 791-808.

107. Swamidas, A. S. J., and Chen, Y., 1995, "Monitoring crack growth through change of modal parameters," *Journal of Sound and Vibration*, 186(2), pp.325-343.

108. Adams, R. D., Cawley, P., Pye, C. J., and Stone, B. J., 1978, "A vibrational technique for non-destructively assessing the integrity of structures," *Journal of Mechanical Engineering Science*, 20, pp. 93-100.

109. Farrar, C.R., Baker, W.E., Bell, T.M., Cone, K.M., Darling, T.W., Duffey, T.A., Eklund, A., and Migliori, A., 1994, "Dynamic characterization and damage detection in the I-40 bridge over the rio grande," Los Alamos National Laboratory report LA-12767-MS.

110. Trivailo, P., Plotnikova, L.A., and Wood, L.A., 1997, "Enhanced parameter identification for damage detection and structural integrity assessment using "Twin" structures," *Proceedings of the 5th International Congress on Sound and Vibration*, University of Adelaide, SA, pp. 1733-1741.

111. Cha, P.D., and Gu, W., 2000, "Model updating using an incomplete set of experimental modes," *Journal of Sound and Vibration*, 233(4), pp. 587–600.

112. Nalitolela, N.G., Penny, J.E.T., and Friswell, M.I., 1992, "Mass or stiffness addition technique for structural parameter updating," *Modal Analysis: The International Journal of Analytical and Experimental Modal Analysis*, 7(3), pp. 157-168.

113. Lew, J.-S., and Juang, J.N., 2002, "Structural damage detection using virtual passive controllers," *Journal of Guidance, Control, and Dynamics*, 25(3), pp. 419-424.

114. Hagood, N.W., and von Flotow, A., 1991, "Damping of structural vibrations with piezoelectric materials and passive electrical networks," *Journal of Sound and Vibration*, 146(2), pp. 243-268.

115. Wu, S., 1996, "Piezoelectric shunts with a parallel R-L circuit for structural damping and vibration control," *Proceedings of SPIE Symposium on Smart Structures and Materials: Passive Damping and Isolation*, San Diego, CA, Vol. 2720, pp. 259-269.

116. Hollkamp, J.J., 1994, "Multimodal passive vibration suppression with piezoelectric materials and resonant shunts," *Journal of Intelligent Material Systems and Structures*, 5(1), pp. 49-57.

117. Hagood, N.W., Chung, W.H., and von Flotow, A., 1990, "Modeling of piezoelectric actuator dynamics for active structural control," *Proceedings of the 31st AIAA/ASME/ASCE/AHS/ASC Structures, Structural Dynamics and Materials Conference*, long beach, CA, Part 4, pp. 2242-2256.

118. Agnes, G.S., 1995, "Development of a modal model for simultaneous active and passive piezoelectric vibration suppression," *Journal of Intelligent Material Systems and Structures*, 6(4), pp. 482-487.

119. Tsai, M.S., and Wang, K.W., 1999, "On the structural damping characteristics of active piezoelectric actuators with passive shunt," *Journal of Sound and Vibration*, 221(1), pp. 1-22.

120. Tang, J., Liu, Y., and Wang, K.W., 2000, "Semi-active and active-passive hybrid structural damping treatments via piezoelectric materials," *Shock and Vibration Digest*, 32(3), pp. 189-200.

121. Tang, J., and Wang, K.W., 2004, "Vibration confinement via optimal eigenvector assignment and piezoelectric network," *ASME Journal of Vibration and Acoustics*, 126(1), pp. 27-36.

122. Senani, R., 1980, "New tunable synthetic floating inductors," *Electronics Letters*, 16(10), pp. 382-383.

123. Senani, R., 1987, "Generation of new two-amplifier synthetic floating inductors," *Electronics Letters*, 23(22), pp. 1202-1203.

124. Abuelma'atti, M.T., Khan, M.H., 1995, "Current-controlled OTA-based single-capacitor simulations of grounded inductors," *International Journal of Electronics*, 78(5), pp. 881-885.

125. Cicekoglu, M.O., 1998, "Active simulation of grounded inductors with CCII+s and grounded passive elements," *International Journal of Electronics*, 85(4), pp. 455-462.

126. Gift, S.J.G., 2004, "New simulated inductor using operational conveyors," *International Journal of Electronics*, 91(8), pp. 477-483.

127. Wong, C.N., Zhu, W.D., and Xu, G.Y., 2004, "On an iterative general-order perturbation method for multiple structural damage detection," *Journal of Sound and Vibration*, 273(1-2), pp. 363-386.

128. Leissa, A.W., 1974, "On a curve veering aberration," *Journal of Applied Mathematics and Physics (ZAMP)*, 25, pp. 99-111.

129. Kutter, J.R., and Sigillito, V.G., 1981, "On curve veering," *Journal of Sound and Vibration*, 75, pp. 585-588.

130. Perkins, N.G., and Mote, JR C.D., 1986, "Comments on curve veering in eigenvalue problems," *Journal of Sound and Vibration*, 106 (3), pp. 451-463.

131. Pierre, C., 1988, "Mode localization and eigenvalue loci veering phenomena in disordered structures," *Journal of Sound and Vibration*, 126 (3), pp. 485-502.

132. Liu, X.L., 2002, "Behavior of derivatives of eigenvalues and eigenvectors in curve veering and mode localization and their relation to close eigenvalues," *Journal of Sound and Vibration*, 56 (3), pp. 551-564.

133. Ray, L.R., Tian, L., 1999, "Damage detection in smart structures through sensitivity-enhancing feedback control," *Journal of Sound and Vibration*, 227(5), pp. 987–1002.

134. Ray, L.R., Koh, B.H., and Tian, L., 2000, "Damage detection and vibration control in smart plates: towards multifunctional smart structures," *Journal of Intelligent Material Systems and Structures*, 11(9), pp. 725–739.

135. Koh, B.H., and Ray, L.R., 2004, "Feedback controller design for sensitivity-based damage localization," *Journal of Sound and Vibration*, 273(1-2), pp. 317-335.

136. Rogers, L.C., 1970, "Derivative of eigenvalues and eigenvectors," *AIAA Journal*, 8(5), pp. 943-944.

137. Plaut, R.H., and Huseyin, K., 1973, "Derivatives of eigenvalues and eigenvectors in non-self-adjoint systems," *AIAA Journal*, 11(2), pp. 250-251.

138. Garg, S., 1973, "Derivative of eigenvalues and eigenvectors for a general matrix," *AIAA Journal*, 11(8), pp. 1191-1194.

139. Cunningham, T.B., 1980, "Eigenspace selection procedures for closed-loop response shaping with modal control," *Proceedings of the IEEE Conference on Decision and Control*, pp. 178-186.

140. Shelley, F.J., and Clark, W.W., 2000, "Active mode localization in distributed parameter systems with consideration of limited actuator placement, Part 1: Theory," *ASME Journal of Vibration and Acoustics*, 122(2), pp. 160-164.

141. Shelley, F.J., and Clark, W.W., 2000, "Active mode localization in distributed parameter systems with consideration of limited actuator placement, Part 2: Simulations and experiments," *ASME Journal of Vibration and Acoustics*, 122(2), pp. 165-168.

142. Tang, J., and Wang, K.W., 2004, "Vibration confinement via optimal eigenvector assignment and piezoelectric networks," *ASME Journal of Vibration and Acoustics*, 126(1), pp. 27-36.

143. Wu, T.Y., and Wang, K.W., 2007, "Periodic isolator design enhancement via vibration confinement through eigenvector assignment and piezoelectric circuitry," *Journal of Vibration and Control*, 13(7), pp. 989-1006.

144. Yen, J., Liao, J.C., Bogju L., and Randolph, D., 1998, "A hybrid approach to modeling metabolic systems using a genetic algorithm and simplex method," *IEEE Transactions on Systems, Man and Cybernetics*: Part B, 28(2), pp. 173-191.

145. Petsounis, K.A., and Fassois, S.D., 2001, "Parametric time-domain methods for the identification of vibrating structures – a critical comparison and assessment," *Mechanical Systems and Signal Processing*; 15(6), pp. 1031–1060.

146. Ljung, L., Applied System Identification, Prentice Hall PTR, Prentice-Hall Inc., 1994.

147. Ljung, L., System Identification: Theory for the User, Prentice Hall PTR, Prentice-Hall Inc., New Jersey, 1999.

148. Ghanem, R., and Shinozuka, M., 1995, "Structural system identification I: theory," *Journal of Engineering Mechanics*, 121(2), pp. 255–264.

149. Luenberger, D. G., 1964, "Observing the state of a linear system," *IEEE Transactions on Military Electronics*, 8, pp. 74-80.

150. Luenberger, D. G., 1966, "Observers for multivarinble systems," *IEEE Transactions on Automatic Control*, 2, pp. 190-197.

151. Van Overschee, P., and De Moor, B., Subspace Identification for Linear Systems: Theory-Implementation-Applications, Kluwer Academic Publishers, Dordrecht, Netherlands, 1996.

152. Peeters, B., and De Roeck, G., 2001, "Stochastic system identification for operational modal analysis: A review," *Journal of Dynamic Systems, Measurements and Control*, 123(4), pp. 659-667.

153. Akaike, H., 1974, ''Markovian representation of stochastic processes and its application to the analysis of autoregressive moving average processes,'' *Annals of the Institute of Statistical Mathematics*, 26, pp. 363–387.

154. Desai, U. B., Pal, D., and Kirkpatrick, R. D., 1985, ‘‘A realization approach to stochastic model reduction,’’ *International Journal of Control*, 42(4), pp. 821–838.

155. Van Overschee, P., and De Moor, B., 1993, ‘‘Subspace algorithm for the stochastic identification problem,’’ *Automatica*, 29(3), pp. 649–660.

156. Peeters, B., and De Roeck, G., 1999, ‘‘Reference-based stochastic subspace identification for output-only modal analysis,’’ *Mechanical Systems and Signal Processing*, 13(6), pp. 855–878.

157. Kalman, R. E., 1960, “A new approach to linear filtering and prediction problems,” *Journal of Basic Engineering -Transaction of the ASME*, Series D, 82, pp.35-45.

158. Kalman, R. E., and Bucy, R.S., 1961, “New results in linear filtering and prediction theory,” *Journal of Basic Engineering -Transaction of the ASME,* Series D, 83, pp.95-108.

159. Xie, L., and Soh, Y.C., 1994, “Robust Kalman filtering for uncertain systems,” *System Control Letters*, 22(2), pp. 123-129.

160. Sorenson, H.W., 1970, “Least-squares estimation: From Gauss to Kalman,” *Spectrum*, 7(7), pp. 63-68.

161. Dosch, J.J., Inman, D.J. and Garcia, E., 1992, “A self-sensing piezoelectric actuator for collocated control,” *Journal of Intelligent Material Systems and Structures*, 3(1), pp 166-185.

162. Spangler, R.L. and Hall, S.R., 1994, “Broadband active structural damping using positive real compensation and piezoelectric simultaneous sensing and actuation,” *Smart Materials and Structures*, 3(4), pp 448-458.

163. Simmers, G.E., Hodgkins, J.R., Mascarenas, D.D., Park, G. and Sohn, H., 2004, “Improved piezoelectric self-sensing actuation,” *Journal of Intelligent Materials Systems and Structures*, 15(12), pp 941-953.

164. Vipperman, J.S., 2001, “Simultaneous qualitative health monitoring and adaptive piezoelectric sensoriactuation,” *AIAA Journal*, 39(9), pp. 1822-1825.

165. Clark, W.W. and M.J. Ramsay, 2000, “Smart material transducers as power sources for MEMS devices,” *International Symposium on Smart Structures and Microsystems*, Hong Kong, pp. 19–21.

166. Sodano, H., Magliula, E.A., and Inman, D.J., 2002, “Electric power generation using piezoelectric device,” *Proceedings of the 13th International Conference on Adaptive Structures and Technologies*, Oct. 7-9, Berlin, Germany.

167. Ottman, G. K., Hofmann, H.F., Bhatt, A.C., and Lesieutre, G.A., 2002, "Adaptive piezoelectric energy harvesting circuit for wireless remote power supply," *IEEE Transactions on Power Electronics*, 17(5), pp. 669-676.

168. Lesieutre, G.A., Ottman, G.K., and Hofmann, H.F., 2004, "Damping as a result of piezoelectric energy harvesting", *Journal of Sound and Vibration*, 269, pp. 991-1001.

169. Kim, H.W., Batra, A., Priya, S., Uchino, K., Markley, D., Newnham, R.E., and Hofmann, H.F., 2004, "Energy harvesting using a piezoelectric 'cymbal' transducer in dynamic environment", *Japanese Journal of Applied Physics*, 43(9A), pp. 6178-6183.

170. Hagood, N.W. and Ghandi, K. 2003, "Electrical power extraction from mechanical disturbances", U.S. Patent 6,580,177.

171. Wang, Z., Lin, R.M., and Lim, M.K., 1997, "Structural damage detection using measured FRF data," *Computer Methods in Applied Mechanics and Engineering*, 147(1-2), pp. 187-197.

172. Park, N-G, and Park, Y-S, 2003, "Damage detection using spatially incompletely frequency response functions," *Mechanical Systems and Signal Processing*, 17(3), pp. 519-532.

173. Hwang, H.Y., and Kim, C., 2004, "Damage detection using a few frequency response measurements," *Journal of Sound and Vibration*, 270(1-2), pp. 1-14.

174. Furukawa, A., Otsuka, H., and Kiyono, J., 2006, "Structural damage detection method using uncertain frequency response functions," *Computer-Aided Civil and Infrastructure Engineering*, 21(4), pp. 292-305.

VITA

Lijun Jiang was born on November 26, 1977, in Liyang, Jiangsu province, China. He received his B.S. degree in Theoretical and Applied Mechanics in July 1999, from Peking University, Beijing, China. Then he continued his graduate studies at the same university, and received his M.S. degree in Engineering Mechanics in July 2002.

In August 2002, he joined the Pennsylvania State University for the Ph.D. program in Mechanical Engineering. For the first semester, he worked as a teaching assistant at the Department of Mechanical and Nuclear Engineering. After that, he has been a research assistant at the Structural Dynamics and Controls Laboratory (SDCL) under the direction of Professor Kon-Well Wang. The research projects he worked on include multifunctional adaptive piezoelectric sensory network for structural health monitoring, and agent-based negotiation framework for robust design of piezoelectric vibration control network. His research work has been presented on several international conferences organized by SPIE, AIAA and ASME. He has published four journal papers in the IOP journal of Smart Materials and Structures, Journal of Sound and Vibration, ASME Journal of Vibration and Acoustics, and ASME Journal of Computer and Information Science in Engineering, respectively.

He is a member of the National Honor Engineering Society of Tau Beta Pi, the American Society of Mechanical Engineers, American Institute of Aeronautics and Astronautics, Institute of Electrical and Electrical and Electronics Engineers, and the Center of Acoustics and Vibration at the Pennsylvania State University.